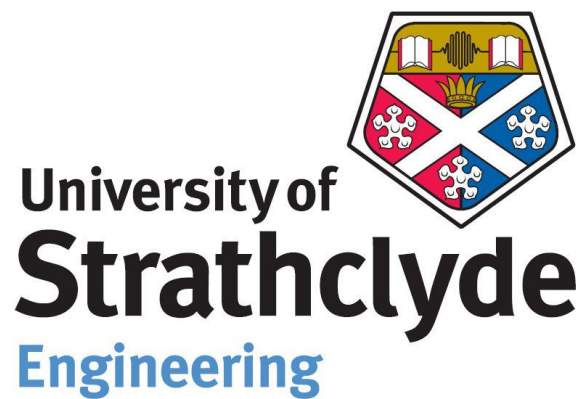


Effect of incremental equal channel angular pressing
(I-ECAP) on the microstructural characteristics and
mechanical behaviour of commercially pure titanium

Muhammad Jawad Qarni



This thesis is submitted to the Department of
Design, Manufacture and Engineering Management

University of Strathclyde

For the degree of Doctor of Philosophy

Glasgow, May - 2017

This thesis is the result of the author's original research. It has been composed by the author and has not been previously submitted for examination which has led to the award of a degree.

The copyright of this thesis belongs to the author under the terms of the United Kingdom Copyright Acts as qualified by University of Strathclyde Regulation 3.50. Due acknowledgement must always be made of the use of any material contained in, or derived from, this thesis.

Signed: Muhammad Jawad Qarni

Date: 02-05-2017

*Dedicated to my wonderful wife, Saman,
who has been a constant source of
motivation, support and love. Thanks for
being so patient during this time. I truly
feel blessed of having you in my life...*

Acknowledgements

First and foremost I am grateful to almighty Allah, The most beneficent and The most merciful. He bestowed up on me the knowledge and the courage to take on this study and complete it.

I would like to express my deepest and sincere gratitude to my supervisor Dr. Andrzej Rosochowski for his continuous guidance, support and constructive criticism. I am thankful to him for allowing me the right level of freedom and independence.

I like to thank my co-supervisor Prof. Jonathan Corney, for his support and input; and for his time spent in progress meetings, especially during the final stages of the PhD.

I like to especially thanks Dr. Giribaskar Sivaswamy, with regards to the technical discussions and for his continuous support in general. I like to appreciate the help from Dr. Sonia Boczkal regarding the EBSD. I also like to thank Dr. Paul Blackwell for his support and mentoring when he was my line manager at AFRC and even to this day.

I like to express thanks to Mr. Mohammad Salamati for the motivational and moral support throughout this time. I also like to thank Mr. Duncan Rodger and Ms. Jacqueline Schramm for the help regarding mechanical testing. I also like to thank Dr. Paul Wood for his guidance in general during the initial stages of the PhD.

I am extremely thankful to my wife, who steadfastly stood by me during all the ups and downs. Thanks for keeping me sane, motivated and well fed during this whole time. Thanks for taking such good care of our baby daughter, while I worked long hours and weekends on the thesis. Thanks to my daughter, Shanza for bringing such blessings and joy in my life. I am also thankful to my two younger sisters and my parents in law for their love, support, understanding and prayers.

Last but not the least, I am sincerely thankful to my parents for their prayers, sacrifice and unconditional love. I am especially grateful to my mother for inculcating the importance of education and hard work from an early age. I could have never reach this stage without her prayers, encouragement and never ending love...

Abstract

Owing to its high specific strength, low density, outstanding corrosion resistance and excellent bio-compatibility titanium and its alloys are a material of choice in many aerospace, military, chemical and biomedical applications. Ti-6Al-4V is the most widely used alloy for medical device applications such as in total replacement implants, where higher strength characteristics are generally a requirement. However, research has suggested that alloying elements such as aluminium and vanadium present in that alloy can be toxic in the long term and are therefore undesirable for full bio-integration. Commercially pure titanium (CP-Ti) has superior biocompatibility but it lacks the strength required for most load bearing implants. One viable solution is to abandon the use of alloying elements and to improve the mechanical strength and performance of CP-Ti by nano-structuring or grain refinement.

Severe plastic deformation (SPD) is an established method for introducing extreme grain refinement in metals. The technique imparts high plastic strain to the material without significantly changing the sample dimensions and is capable of achieving ultrafine grain (UFG) structure in metals. UFG materials are characterized by an average grain size of $<1 \mu\text{m}$ and with mostly high angle grain boundaries. These materials exhibit exceptional improvements in strength, superplastic behaviour and in case for titanium, improved corrosion resistance and enhanced biocompatibility. Among the various available SPD methods, equal channel angular pressing (ECAP) is the most widely used method for obtaining bulk UFG materials. However, ECAP (in its classical form) suffers from low productivity and is not a practical option for commercialization.

Therefore, lately the interest is in the development of continuous SPD techniques, capable of processing very long or continuous billets for use in commercial applications. Incremental ECAP (I-ECAP) developed at the University of Strathclyde, offers such possibility. This promising technique has a strong potential of obtaining the much-needed high strength CP-Ti for biomedical implants on an industrial scale. The aim of the present research work is to investigate the feasibility of the I-ECAP process in improving the mechanical performance of CP-Ti by refining its grain

structure. However, before processing CP-Ti on the I-ECAP experimental rig, it was necessary to eliminate the some existing limitations of the rig and improve the overall process efficiency. Major upgrades and enhancements were implemented as part of the present work. These include: automation of material feeding system, elevated temperature capability, press controller upgrade, data acquisition and process control during experiments. Moreover, finite element analysis was performed to optimize the tooling geometry by studying the billet deformation behaviour and subsequently new I-ECAP dies were designed and manufactured suitable for processing CP-Ti billets.

Using the considerably improved I-ECAP experimental facility, CP-Ti billets were subjected to multiple passes of the I-ECAP process at elevated temperatures. To investigate the effect of different levels of induced shear strain per pass, billets were processed using two separate dies with channel intersection angles of 120 and 90°. Microstructural evolution and textural development in the material was tracked and examined using high-resolution electron backscatter diffraction (EBSD) technique. Twinning and continuous dynamic recrystallization (CDRX) have been observed to act as a grain refinement mechanism during subsequent passes of I-ECAP. Analysis of the microstructure shows that UFG structure was successfully obtained with mostly high angle grain boundaries (HAGB) in the processed billets using the two dies.

Room temperature tensile tests carried out before and after processing show significant increase in strength with some loss in ductility in the processed material. The yield strength and ultimate tensile strength (UTS) of the material after I-ECAP processing using the die angle of 120° was increased by 81% and 25%, respectively. The material processed using the die angle of 90° exhibits an even higher increase in yield strength and UTS i.e. 118% and 33%, respectively. Compression tests conducted at different strain rates at room temperature show increase in strength with a three stage hardening behaviour, though the severely deformed UFG material suffers a loss in its strain hardening ability. Detailed microhardness measurements also show the increase in hardness after processing with a reasonable level of homogeneity. Finally, workability characteristics of UFG titanium is determined by compression testing at room and warm temperature conditions (400 to 600 °C). The work has successfully demonstrated that I-ECAP process is effective in improving the mechanical performance of titanium and has a potential for commercialization.

Table of contents

ACKNOWLEDGEMENTS	I
ABSTRACT	II
TABLE OF CONTENTS	IV
LIST OF FIGURES	VIII
LIST OF TABLES	XVI
1 INTRODUCTION	1
1.1 BACKGROUND.....	1
1.2 RESEARCH AIM AND OBJECTIVES	3
1.3 ORGANIZATION OF THE THESIS.....	4
2 METHODS OF GRAIN REFINEMENT AND THEIR APPLICATION TO TITANIUM..	6
2.1 INTRODUCTION	6
2.1.1 Ultrafine grained (UFG) materials	7
2.2 SYNTHESIS OF UFG MATERIALS.....	8
2.2.1 Bottom-up approach.....	8
2.2.2 Top-down approach	8
2.3 SEVERE PLASTIC DEFORMATION (SPD).....	10
2.4 EQUAL CHANNEL ANGULAR PRESSING (ECAP).....	12
2.5 FUNDAMENTAL PARAMETERS IN ECAP	14
2.5.1 The strain imposed in ECAP	14
2.5.2 Processing routes	17
2.5.3 Multiple turn ECAP	19
2.5.4 Slip systems and shearing patterns for the different processing routes	19
2.5.5 Mechanism of grain refinement in ECAP	22
2.6 CONTINUOUS SPD METHODS	25
2.7 INCREMENTAL ECAP (I-ECAP)	27
2.8 TITANIUM – BACKGROUND	29
2.8.1 Titanium as a commercial material	30
2.8.2 General properties	30
2.8.3 Crystal structure	31
2.8.4 Commercially pure titanium (CP-Ti)	33
2.9 GRAIN REFINEMENT IN CP-TI USING ECAP	35
2.9.1 Microstructures and mechanism of grain refinement	37
2.9.2 Mechanical properties	40

2.9.3	Post ECAP deformation	41
2.10	APPLICATION OF UFG TITANIUM IN BIO-MEDICAL IMPLANTS	42
2.11	SUMMARY	44
3	FE MODELLING OF I-ECAP PROCESS AND DESIGN OF TOOLING.....	46
3.1	INTRODUCTION	46
3.2	FINITE ELEMENT MODELLING.....	48
3.3	RESULTS AND DISCUSSION	52
3.3.1	Influence of channel length on bending behaviour	52
3.3.2	Strain distribution.....	53
3.3.3	Effect of friction.....	55
3.4	OPTIMIZATION OF I-ECAP GEOMETRY	56
3.5	DOUBLE BILLET VARIANT OF I-ECAP PROCESS	58
3.6	DESIGN OF I-ECAP DIE	59
3.7	TOOL MATERIAL	61
3.8	PRE-STRESSING OF I-ECAP DIE.....	62
3.9	STRESS ANALYSIS OF PRE-STRESSING I-ECAP DIE	65
3.9.1	Finite element model.....	65
3.9.2	Procedure for analysis.....	67
3.9.3	Results and discussion	67
3.10	SUMMARY AND CONCLUSIONS	70
4	EXPERIMENTAL SETUP, MATERIAL AND PROCEDURE.....	72
4.1	INTRODUCTION	72
4.2	PREVIOUS CONFIGURATION OF THE I-ECAP RIG	72
4.3	UPGRADATION OF I-ECAP RIG	75
4.3.1	Automation of material feeding system	75
4.3.2	Elevated temperature processing capability.....	78
4.3.3	Digital servo hydraulic control system.....	80
4.3.4	Instrumentation, process control and data acquisition	82
4.3.5	General rig upgrades including safety controls.....	89
4.3.6	The completed setup	89
4.4	AS RECEIVED MATERIAL	91
4.5	BILLET PREPARATION AND LUBRICATION.....	91
4.6	I-ECAP EXPERIMENTAL PROCEDURE	92
4.6.1	Processing using die with channel angle (Φ) of 120°	94
4.6.2	Processing using die with channel angle (Φ) of 90°	96
4.7	MICROSTRUCTURE CHARACTERIZATION	98
4.7.1	Electron back scatter diffraction (EBSD).....	98

4.8	MECHANICAL TESTING.....	99
4.8.1	Tensile testing	100
4.8.2	Fractography	101
4.8.3	Compression testing	101
4.8.4	Hardness measurements	104
4.9	SUMMARY	105
5	MICROSTRUCTURE EVOLUTION AND MECHANISM OF GRAIN REFINEMENT DURING I-ECAP.....	106
5.1	INTRODUCTION	106
5.2	MICROSTRUCTURAL CHARACTERIZATION.....	107
5.3	AS RECEIVED MICROSTRUCTURE.....	107
5.4	PROCESSING USING I-ECAP DIE WITH CHANNEL ANGLE (Φ) OF 120°	110
5.4.1	Microstructural evolution - Flow (Y) plane	110
5.4.2	Microstructural evolution - Transverse (X) plane	117
5.4.3	Texture development - Flow plane	123
5.4.4	Texture development - Transverse plane	125
5.4.5	General characteristics of microstructure through 1 – 6 passes	128
5.4.6	Mechanism of grain refinement during I-ECAP	131
5.4.6.1	Twinning	132
5.4.6.2	Continuous dynamic recrystallization	135
5.5	PROCESSING USING I-ECAP DIE WITH CHANNEL ANGLE (Φ) OF 90°	137
5.5.1	Microstructural evolution – Flow (Y) plane	137
5.5.2	General characteristics of microstructure through 1 to 4 passes	144
5.6	SUMMARY AND CONCLUSIONS	147
6	EFFECT OF I-ECAP ON THE MECHANICAL BEHAVIOUR OF CP-TI.....	149
6.1	INTRODUCTION	149
6.2	PROCESSING USING I-ECAP DIE WITH CHANNEL ANGLE (Φ) OF 120°	149
6.2.1	Loads during processing	149
6.2.2	Tensile properties.....	152
6.2.3	Fractography	155
6.2.4	Hardness evolution.....	157
6.3	PROCESSING USING I-ECAP DIE WITH CHANNEL ANGLE (Φ) OF 90°	161
6.3.1	Loads during processing	161
6.3.2	Tensile properties.....	163
6.3.3	Fractography	165
6.3.4	Hardness evolution.....	167
6.4	COMPARISON OF 120° AND 90° CHANNEL ANGLE CASES	168

6.5	COMPARISON WITH ECAP	171
6.6	HALL – PETCH EFFECT	173
6.7	CONCLUSIONS.....	175
7	WORKABILITY CHARACTERISTICS OF CG AND UFG CP-TI.....	176
7.1	INTRODUCTION	176
7.2	ROOM TEMPERATURE COMPRESSION BEHAVIOUR	177
7.2.1	True stress – true strain curves.....	177
7.2.2	Strain hardening behaviour	179
7.2.3	Flow softening due to adiabatic heating.....	182
7.2.4	Strain rate sensitivity.....	183
7.3	WARM TEMPERATURE DEFORMATION TESTING OF UFG CP-TI.....	184
7.3.1	True stress – true strain curves.....	185
7.3.2	Strain hardening behaviour	187
7.3.3	Microstructures after deformation.....	189
7.3.4	Dynamic grain size.....	194
7.4	CONCLUSION.....	195
8	SUMMARY.....	196
9	CONCLUSIONS.....	199
10	RECOMMENDATIONS FOR FUTURE WORK	201
	REFERENCES.....	204
	APPENDIX A – ENGINEERING DRAWINGS FOR 90° I-ECAP DIE.....	224
	APPENDIX B – ENGINEERING DRAWINGS FOR 120° I-ECAP DIE.....	230
	APPENDIX C – ENGINEERING DRAWINGS FOR COOLING SYSTEM	234
	APPENDIX D – ENGINEERING DRAWING FOR TEST SAMPLES	237

List of figures

Fig. 2.1: The variation of Hall – Petch relationship with varying grain size [24].	6
Fig. 2.2: Illustration of the ECAP process [63].	12
Fig. 2.3: Principle of ECAP where Φ is the angle of intersection between the two channels and Ψ is the angle subtended by the arc of curvature at the point of intersection: (a) $\Psi = 0$, (b) $\Psi = \pi - \Phi$, (c) an arbitrary value of Ψ lying between $\Psi = 0$ and $\Psi = \pi - \Phi$ [71].	15
Fig. 2.4: Variation of the equivalent strain, with the channel angle (Φ) over angle of the arc of curvature (Ψ) for the first pass of ECAP (N=1) [72].	17
Fig. 2.5: Four possible processing routes in ECAP [74].	18
Fig. 2.6: Channel design for multi-turn ECAP: (a) S-shaped two-turn route C, (b) U-shaped two-turn route A, (c) two-turn route B _C and (d) three turn route B _C [79].	19
Fig. 2.7: The slip systems during consecutive passes for different ECAP routes using die with (a) $\Phi = 90^\circ$ and (b) $\Phi = 120^\circ$ [81].	20
Fig. 2.8: The distortions introduced into a cubic element when viewed on the X, Y and Z planes when processing using different ECAP routes [75].	21
Fig. 2.9: (a) The distortion of a cubic element after a single pass [82] and (b) the shearing pattern on the X, Y and Z planes for different processing routes for up to four passes [76].	21
Fig. 2.10: Model of grain refinement in FCC metals processed using ECAP for first pass, second pass and fourth pass corresponding to processing route A, B _C and C [84] on longitudinal (Y) plane.	23
Fig. 2.11: Microstructures and SAED patterns obtained in the X, Y and Z plane in pure aluminium samples after ECAP using 90° die following route B _C , for a total of (a) one, (b) two, (c) three and (d) four passes [74].	24
Fig. 2.12: Schematic of the I-ECAP process (A1 & A2 - die, B – feeding rod and C – punch).	27
Fig. 2.13: Crystal structures of titanium at the atomic level. (a) HCP - Hexagonal close packed; (b) BCC - Body centered cubic [2].	32
Fig. 2.14: Unit cell of (a) alpha (α) and (b) beta (β) phase.	32
Fig. 2.15: CP-Ti grade 2 samples after first pass of ECAP at (a) 25°C and (b) 325°C . The pressing speeds of 0.025, 0.25 and 25 mm/s corresponding to a strain rates of 0.02, 0.2 and 2.0 s^{-1} were used [106].	36
Fig. 2.16: TEM micrographs in the longitudinal (Y) plane of CP-Ti processed billets after eight pass using route (a) B _C , (b) B _A and (c) C. [108].	37
Fig. 2.17: TEM micrograph of CP-Ti after first pass of ECAP showing twins [114].	38
Fig. 2.18: Mechanical properties of CP-Ti after different processing stages reported in [69]	41
Fig. 2.19: Examples of some titanium implants: (a) screw implants made of nano-structured titanium [138], (b) plate implants for bone osteosynthesis made of nano-structured titanium [38] and (c) normal and reduced diameter dental implant made with strengthened CP-Ti after grain refinement [87].	43

Fig. 3.1: (a) FE model showing the initial tool and billet configuration (see Fig. 2.12 for the schematic diagram) and (b) relative movement of punch and feeding rod during the first three cycles of I-ECAP.	48
Fig. 3.2: True stress-strain curves (flow stress data) of CP-Ti (grade 2) obtained from uniaxial compression at 300 °C and at strain rates of 0.01, 0.1 and 1.0 s ⁻¹	50
Fig. 3.3: Deformed mesh (a) coarse mesh, (b) medium mesh, (c) fine mesh and (d) ALE mesh.	51
Fig. 3.4: Equivalent plastic strain distribution along the width of the billet for four different FE meshed model.	51
Fig. 3.5: Equivalent plastic strain distribution for channel length $L_o =$ (a) $0.5w$, (b) $1.0w$, (c) $2.0w$, (d) $3.0w$ and (e) $4.0w$	52
Fig. 3.6: Effect of varying the outer channel length (L_o) on bending	53
Fig. 3.7: Equivalent plastic strain distribution along (a) extrusion direction (left to right) and (b) width direction (top to bottom).	54
Fig. 3.8: Effect of friction on (a) billet bending and (b) strain inhomogeneity ($CV\epsilon_p$).	55
Fig. 3.9: Equivalent plastic strain distribution for a constant punch length $L_p = 0.5w$ and varying die length $L_d =$ (a) $0.5w$, (b) $1.0w$, (c) $2.0w$, (d) $4.0w$ and (e) $10.0w$	56
Fig. 3.10: Equivalent plastic strain distribution for a constant die length $L_d = 10.0w$ and varying punch length $L_p =$ (a) $2.0w$, (b) $3.0w$ and (c) $4.0w$	57
Fig. 3.11: Equivalent plastic strain distribution for a die length $L_d = 10.0w$ and punch length $L_p = 2.0w$ with varying billet length $L_b =$ (a) $10.0w$ and (b) $12.0w$	57
Fig. 3.12: Schematic illustration of the double-billet variant of the I-ECAP process (A = die, B = feeding rod and C = punch). The two billets are marked with B1 and B2.	58
Fig. 3.13: Die insert sub-assembly (a) top view showing the rectangular shaped channel with two billets (B1 and B2), the two longer die inserts (labelled 1) and two shorter die inserts (labelled 2) and (b) cross-sectional cut along A-A.	59
Fig. 3.14: CAD drawing of the I-ECAP tool assembly for (a) $\Phi = 120^\circ$ and (b) $\Phi = 90^\circ$	60
Fig. 3.15: Enlarged 3D view of the punch design for (a) $\Phi = 120^\circ$ and (b) $\Phi = 90^\circ$ (notice the spike in the middle, this is to facilitate the separation of the two billets in opposite direction).	60
Fig. 3.16: Sectioned view of pre-stressing ring is shown with a tapered hole in the centre.	62
Fig. 3.17: Sectioned view of I-ECAP die assembly with geometrical interference.	63
Fig. 3.18: Illustration showing the position of ring before and after pre-stressing.	63
Fig. 3.19: Measurement of I-ECAP channel dimensions along breadth after pre-stressing.	64
Fig. 3.20: Illustration of the tapered profile of the channel breadth after pre-stressing.	64
Fig. 3.21: Parts used in FE model: (a) longer die insert (b) shorter die insert (c) pre-stressing ring and (d) I-ECAP die assembly.	65

Fig. 3.22: (a) Finite element mesh of the whole model and (b) enlarged view of the dense mesh region.	66
Fig. 3.23: Model showing the direction of loading and constraints.	66
Fig. 3.24: Plot of Von Mises stress distribution after press-stressing of the I-ECAP die.....	67
Fig. 3.25: Sectioned plot of Von Mises stress distribution on pre-stressing ring (a) top side and (b) bottom side.....	68
Fig. 3.26: Plot of Von Mises stress distribution on the four die inserts.....	68
Fig. 3.27: FE prediction of force required for pre-stressing the I-ECAP die.	69
Fig. 3.28: Pre-stressing displacement along z-direction (U3).	69
Fig. 4.1: Previous configuration of the I-ECAP rig on the 1000 kN servo hydraulic press.	73
Fig. 4.2: (a) Power jack translating 200 kN screw jack and (b) illustration of the screw jack installation on the I-ECAP rig.....	74
Fig. 4.3: A motor driven system of billet feeding (a) Kollmorgen AKM Synchronous AC servo motor with a 50:1 gear ratio gearhead, (b) SERVOSTAR S300 servo drive, (c) control cabinet to power the servo motor and interface with the I-ECAP rig and (d) cross-section showing how the motor is coupled to screw jack worm shaft.....	76
Fig. 4.4: I-ECAP tooling for material feeding along with the load cell for recording feeding force....	77
Fig. 4.5: I-ECAP tooling with different zones of heating for (a) $\Phi = 120^\circ$ and (b) $\Phi = 90^\circ$	78
Fig. 4.6: Heater control cabinet: (a) outside view and (b) inside connections.....	79
Fig. 4.7: New tooling for maintaining the load cell at low temperature (here blue arrow indicates cool water coming from chiller and red arrow indicates heated water going back to chiller).....	80
Fig. 4.8: (a) The solution from Zwick/Roell: 1 – control cube, 2 – computer based Cubus software, 3 – hand controller for manual actuator control during setup and (b) backside of the control cube, showing options for connections and interfacing.	81
Fig. 4.9: The schematic diagram representing the connections between various elements of the I-ECAP rig.	82
Fig. 4.10: (a) Front screen of the LabVIEW virtual instrument application used to monitor, control and acquire data during the I-ECAP experiments and (b) National Instruments chassis along with the four I/O modules for data acquisition (the numbering on the chart corresponds to the respective I/O module to which it is connected).....	84
Fig. 4.11: Rising and falling edge of the sine wave form signal, (a) first scenario: material feeding starts and stops on the rising edge, (b) second scenario: material feeding starts on rising edge but stops on falling edge.....	85
Fig. 4.12: Automatic material feeding using I-ECAP LabVIEW application based on the first scenario.	86
Fig. 4.13: Example of producer consumer design pattern taken from LabVIEW documentation.....	87

Fig. 4.14: Partial block diagram of the I-ECAP LabVIEW application showing the producer consumer loop.	88
Fig. 4.15: The completed I-ECAP setup after the improvement and upgrades.	90
Fig. 4.16: Billet appearance after different steps of billet preparation (a) 1st step – initial machined billet, (b) 2nd step – sand blasted billet, (c) 3rd step – graphite coated billet and (d) 4th step – anti-seize lubricant applied.	91
Fig. 4.17: Alignment of punch and die slot before I-ECAP experiments.	92
Fig. 4.18: Relative movement of punch and feeding rod during the I-ECAP process.	93
Fig. 4.19: (a) The pair of CP-Ti billets emerging at the end of first I-ECAP pass using $\Phi = 120^\circ$ channel angle die (white arrows indicate direction of material flow), (b) appearance of the CP-Ti billets: unprocessed billet (bottom), billet after first pass of I-ECAP showing bowing (middle) and straightened billet after secondary operation (top) and (c) appearance of CP-Ti billets after first, second, fourth and sixth pass of I-ECAP (second pass billet is straightened in the figure).	95
Fig. 4.20: (a) The pair of CP-Ti billets at the end of first I-ECAP pass using the $\Phi = 90^\circ$ channel angle die, (b) pair of billets (left and right) after first pass processing and (c) appearance of CP-Ti billets after first, second, third and fourth pass of I-ECAP (right hand billets are shown only).	96
Fig. 4.21: Problems encountered during initial processing trials using the $\Phi = 90^\circ$ channel angle.	97
Fig. 4.22: Illustration of the three orthogonal planes (X, Y and Z) representing different sides of the billet.	99
Fig. 4.23: (a) Dimensions (in mm) of the flat tensile sample used in this study and (b) illustration of the three tensile samples cut across the cross-section (X-plane) of the billet.	100
Fig. 4.24: Zwick/Roell Z150 tensile testing machine with the sample held by machine grips.	101
Fig. 4.25: (a) Plan of cutting compression samples from billets, (b) external dimensions of Rastegaev type sample used in the study (see appendix D for detailed drawing) and (c) machined cylindrical compression sample.	102
Fig. 4.26: (a) Zwick/Roell HA250 servo hydraulic testing machine and (b) position of compression sample between the platens (light red background represents the furnace environment).	103
Fig. 4.27: 2D grid style pattern of 11 x 11 equi-spaced points on the surface of the sample used for microhardness measurement study.	104
Fig. 5.1: Illustration of the three orthogonal planes (X, Y and Z) with respect to the billet and the cut plan to obtain samples along flow and transverse plane for microstructure analysis (the polished surface is represented by grey colour in these cut samples).	107
Fig. 5.2: Coloured inverse pole figure (IPF) maps obtained from EBSD analysis showing the microstructure of unprocessed CP-Ti samples in the (a) flow (Y) and (b) transverse (X) plane along with the corresponding misorientation histogram. The colours correspond to the crystallographic orientations shown in the standard stereographic triangle. Colour variations within grains qualitatively represents change in internal orientations.	108
Fig. 5.3: Experimental pole figures illustrating texture on 0001 (left), 1010 (middle) and 1120 (right) planes in un-processed CP-Ti samples in the (a) flow (Y) plane and (b) transverse (X) plane. The texture intensity is represented by the colour scale bar for the corresponding pole figure.	109

Fig. 5.4: Coloured inverse pole figure (IPF) maps obtained from EBSD analysis showing the evolution of microstructure and deformation characteristics in processed CP-Ti samples in the flow (Y) plane after (a) first, (b) second, (c) fourth and (d) sixth pass of I-ECAP at 300 ° C using the die with channel angle (Φ) of 120°. The colours correspond to the crystallographic orientations shown in the standard stereographic triangle (inset). Colour variation within the grains qualitatively represents differences in internal orientations. Note that scale bar used in (a) to (c) is 20 μm whereas in (d) is 5 μm , due to high magnification image. 112

Fig. 5.5: EBSD based grain boundary maps of CP-Ti samples in the flow (Y) plane after (a) first, (b) second, (c) fourth and (d) sixth pass of I-ECAP at 300° C using the die with channel angle (Φ) of 120°. Blue lines represent low angle grain boundaries (LAGB) where $1.5^\circ \leq \theta \leq 15^\circ$, whereas red lines represent the high angle grain boundaries (HAGB) where $\theta > 15^\circ$. Figures on the upper right of each map represent the corresponding histogram of the grain size distribution and cumulative distribution function along with the average grain size (GS). Figures on the bottom right represent the corresponding histogram of the misorientation distribution and the cumulative distribution function along with the percentage of HAGB and LAGB. The arrows indicate the incomplete HAGB. 116

Fig. 5.6: Coloured inverse pole figure (IPF) maps obtained from EBSD analysis showing the evolution of microstructure and deformation characteristics in processed CP-Ti samples in the transverse (X) plane after (a) first, (b) second, (c) fourth and (d) sixth pass of I-ECAP at 300 ° C using the die with channel angle (Φ) of 120°. The colours correspond to the crystallographic orientations shown in the standard stereographic triangle (inset). Colour variation within the grains qualitatively represent differences in internal orientations. Note that scale bar used in (a) to (c) is 20 μm whereas in (d) is 5 μm , due to high magnification image. 118

Fig. 5.7: EBSD based grain boundary maps of CP-Ti samples in the transverse (X) plane after (a) first, (b) second, (c) fourth and (d) sixth pass of I-ECAP at 300° C using the die with channel angle (Φ) of 120°. Blue lines represent low angle grain boundaries (LAGB) where $1.5^\circ \leq \theta \leq 15^\circ$, whereas red lines represent the high angle grain boundaries (HAGB) where $\theta > 15^\circ$. Figures on the upper right of each map represent the corresponding histogram of the grain size distribution and cumulative distribution function along with the average grain size (GS). Figures on the bottom right represents the corresponding histogram of the misorientation distribution and the cumulative distribution function along with the percentage of HAGB and LAGB. 122

Fig. 5.8: The locations of five ideal shear texture components (P, B, Y, C₁ and C₂) developed in HCP metals during ECAP on: (a) (0002) and (b) (**1010**) pole figures. Figure taken from the work of Beausir et al. [175]. 124

Fig. 5.9: Experimental pole figures illustrating the development of texture on the **0001** (left), **1010** (middle) and **1120** (right) crystallographic planes in the flow (Y) plane of the CP-Ti samples after (a) first, (b) second, (c) fourth and (d) sixth pass of I-ECAP carried out at 300 ° C using the die with channel angle (Φ) of 120°. The texture intensity is represented by the colour scale bar for the corresponding pole figure. 126

Fig. 5.10: Experimental pole figures illustrating the development of texture on the 0001 (left), **1010** (middle) and **1120** (right) crystallographic planes in the transverse (X) plane of the CP-Ti samples after (a) first, (b) second, (c) fourth and (d) sixth pass of I-ECAP carried out at 300 ° C using the die with channel angle (Φ) of 120°. The texture intensity is represented by the colour scale bar for the corresponding pole figure. 127

Fig. 5.11: Average values of grain size in CP-Ti samples in the (a) flow (Y) and (b) transverse (X) plane, before and after subsequent I-ECAP passes carried out at 300 ° C using $\Phi = 120^\circ$ channel die. The error bars represent the calculated standard deviation. 129

Fig. 5.12: (a) Average values of grain misorientation angles in CP-Ti samples in the (a) flow (Y) and (b) transverse (X) plane, before and after subsequent I-ECAP passes carried out at 300 °C using $\Phi = 120^\circ$ channel die.	130
Fig. 5.13: (a) Percentage fraction of high angle grain boundaries (HAGBs) in CP-Ti samples in the (a) flow (Y) and (b) transverse (X) plane, before and after subsequent I-ECAP passes carried out at 300 °C using $\Phi = 120^\circ$ channel die.	130
Fig. 5.14: EBSD based band contrast image showing the formation of twin boundaries after the first pass in the flow plane sample. The $\{1012\}$ tensile twin (TT) and $\{1122\}$ compressive twin (CT), are shown in red and green colour, respectively; (b) and (c) magnified IPF map showing CT and TT twin types within grain interiors, respectively and (d) corresponding misorientation histogram and misorientation inverse pole figures at 65° and 85°	133
Fig. 5.15: Higher magnification EBSD map of the second pass sample in the transverse (X) plane after I-ECAP at 300° C, using the die with channel angle (Φ) of 120°. Blue lines represent low angle grain boundaries (LAGBs) where $2^\circ \leq \theta \leq 15^\circ$, whereas red lines represent the high angle grain boundaries (HAGBs) where $\theta > 15^\circ$. The arrows indicate the incomplete HAGB.	136
Fig. 5.16: (a) EBSD based inverse pole figure (IPF) map showing the microstructure of the CP-Ti samples in the flow (Y) plane after first pass (1P) of I-ECAP at 300 °C using the die with a channel angle of 90°, (b) the corresponding grain size histogram with the average grain size and (c) the associated inverse pole figure. Colour variation within grains qualitatively represents differences in internal orientations.	139
Fig. 5.17: (a) EBSD based inverse pole figure (IPF) map showing the microstructure of the CP-Ti samples in the flow (Y) plane after second pass (2P) of I-ECAP at 300 °C using the die with a channel angle of 90°, (b) the corresponding grain size histogram with the average grain size and (c) the associated inverse pole figure. Colour variation within grains qualitatively represents differences in internal orientations.	140
Fig. 5.18: (a) EBSD based inverse pole figure (IPF) map showing the microstructure of the CP-Ti samples in the flow (Y) plane after third pass (3P) of I-ECAP at 300 °C using the die with a channel angle of 90°, (b) the corresponding grain size histogram with the average grain size and (c) the associated inverse pole figure. Colour variation within grains qualitatively represents differences in internal orientations.	142
Fig. 5.19: (a) EBSD based inverse pole figure (IPF) map showing the microstructure of the CP-Ti samples in the flow (Y) plane after fourth pass (4P) of I-ECAP at 300 °C using the die with a channel angle of 90°, (b) the corresponding grain size histogram with the average grain size and (c) the associated inverse pole figure. Colour variation within grains qualitatively represents differences in internal orientations.	143
Fig. 5.20: Average values of grain size in CP-Ti samples in the flow (Y) plane, before and after subsequent I-ECAP at 300 °C using $\Phi = 90^\circ$ channel angle die. The error bars represent the calculated standard deviation.	144
Fig. 5.21: (a) Average values of grain misorientation, (b) Percentage fraction of high angle grain boundaries (HAGB) in CP-Ti samples in the flow plane before and after subsequent I-ECAP at 300 °C using $\Phi = 90^\circ$ channel angle die.	146
Fig. 5.22: Fraction of twin boundaries in the microstructure in CP-Ti samples in the flow plane before and after subsequent I-ECAP processing at 300 °C using $\Phi = 90^\circ$ channel angle die.	146

Fig. 6.1: Experimentally recorded deformation and feeding forces during (a) first, (b) second, (c) third, (d) fourth, (e) fifth and (f) sixth pass of I-ECAP processing at 300 °C using die with a channel angle (Φ) of 120°.....	151
Fig. 6.2: (a) Values of maximum deformation and feeding forces during various passes of I-ECAP at 300 °C using die with a channel angle (Φ) of 120° and (b) illustration of load distribution during the deformation stage.	152
Fig. 6.3: (a) Fractured flat tensile CP-Ti test samples representing the unprocessed condition and after first, second, fourth and sixth pass of I-ECAP at 300 °C using $\Phi = 120^\circ$ channel angle die and (b) stress-strain curves obtained from tensile testing at room temperature and at a strain rate of 0.01 s ⁻¹ . The arrow on each curve indicate the onset of necking.	153
Fig. 6.4: SEM images of the fractured CP-Ti tensile samples showing the fracture morphology at three different magnifications for (a) unprocessed material and I-ECAPed material after (b) first, (c) second, (d) fourth and (e) sixth pass at 300 °C using $\Phi = 120^\circ$ channel angle die.	156
Fig. 6.5: Colour coded contour maps of the microhardness (H_v) recorded in the transverse (X) plane for (a) unprocessed condition, after (b) first, (c) second, (d) fourth and (e) sixth pass of the I-ECAP process at 300 °C using the die with channel angle (Φ) of 120°.....	159
Fig. 6.6: Microhardness (H_v) recorded in the transverse (X) plane along three lines; the centre line and at 1 mm from the top and bottom surfaces after (a) first, (b) second, (c) fourth and (d) sixth pass of the I-ECAP process at 300 °C using the die with channel angle (Φ) of 120° (the dashed line shows average microhardness in the unprocessed condition).....	160
Fig. 6.7: Mean values of Vickers microhardness (H_v) recorded in the X plane before and after subsequent passes of I-ECAP at 300 °C using the die with channel angle (Φ) of 120°. The error bars represent the calculated standard deviation.	160
Fig. 6.8: Deformation and feeding forces recorded during (a) first, (b) second, (c) third and (d) fourth pass of I-ECAP at 300 °C using the die with channel angle (Φ) of 90°.....	162
Fig. 6.9: Values of maximum deformation and feeding forces during consecutive passes of I-ECAP at 300 °C using the with channel angle (Φ) of 90°.	162
Fig. 6.10: True Stress-strain curves obtained from tensile testing at room temperature and at a strain rate of 0.01 s ⁻¹ of the unprocessed and processed CP-Ti samples after first, second, third and fourth pass of I-ECAP at 300 °C using $\Phi = 90^\circ$ channel angle. The arrow on each curve indicate the onset of necking.	164
Fig. 6.11: SEM images of the fractured CP-Ti tensile samples showing the fracture morphology at three different magnifications for (a) unprocessed material and I-ECAPed material after (b) first, (c) second, (d) third and (e) fourth pass at 300 °C using $\Phi = 90^\circ$ channel angle die.....	166
Fig. 6.12: Mean values of Vickers microhardness (H_v) recorded on the X plane before and after subsequent passes of I-ECAP process at 300 °C using the die with channel angle (Φ) of 90°. The error bars represents the calculated standard deviation.....	167
Fig. 6.13: Comparison of the room temperature tensile properties (a) yield strength, (b) ultimate tensile strength (UTS) and (c) percentage ductility (elongation to failure) as a function of induced equivalent strain during I-ECAP processing of CP-Ti using dies with channel angle (Φ) of 120° and 90°.....	170
Fig. 6.14: Representation of yield strength as a function of average grain size to study the Hall – Petch effect in the present study.....	174

Fig. 6.15: Representation of yield strength as a function of average grain size to study the Hall – Petch effect during the final pass in the present study.	174
Fig. 7.1: Flow curves (true stress vs true strain) obtained from uniaxial compression testing at various strain rates for (a) unprocessed (CG) and (b) severely deformed (UFG) CP-Ti.	178
Fig. 7.2: Plots of normalized strain hardening behaviour obtained from room temperature compression testing at various strain rates for (a) unprocessed (CG) and (b) severely deformed material after six passes (UFG).	181
Fig. 7.3: Strain rate sensitivity of CG and UFG material compression tested at room temperature for (a) $\epsilon = 0.05$ and (b) $\epsilon = 0.1$	184
Fig. 7.4: True stress vs true strain plot obtained from the uniaxial compression testing at various strain rates and at temperatures of (a) 400, (b) 500 and (c) 600 °C.	186
Fig. 7.5: Plots of normalized strain hardening behaviour obtained from warm temperature compression testing of UFG CP-Ti at various strain rates and at (a) 400, (b) 500 and (c) 600 °C.	188
Fig. 7.6: EBSD based IPF map with the corresponding grain boundary map (blue and red lines refers to LAGB and HAGB) and the associated grain size histogram for the compression sample at 400 °C and at strain rates of (a) 1.0, (b) 0.10 and (c) 0.01 s ⁻¹	191
Fig. 7.7: EBSD based IPF map with the corresponding grain boundary map (blue and red lines refers to LAGB and HAGB) and the associated grain size histogram for the compression sample at 500 °C and at strain rates of (a) 1.0, (b) 0.10 and (c) 0.01 s ⁻¹	192
Fig. 7.8: EBSD based IPF map with the corresponding grain boundary map (blue and red lines refers to LAGB and HAGB) and the associated grain size histogram for the compression sample at 600 °C and at strain rates of (a) 1.0, (b) 0.10 and (c) 0.01 s ⁻¹	193
Fig. 7.9: Dynamic grain size observed during warm temperature compression testing as a function of temperatures and strain rates.	194

List of tables

Table 2.1: Batch SPD processes [56].	11
Table 2.2: Continuous SPD processes [56]	26
Table 2.3: Physical and mechanical properties of elemental titanium [2].....	31
Table 2.4: ASTM CP-Ti grade classification including their mechanical properties and composition	35
Table 3.1: Composition of tool material - Vanadis 23 (Source Uddeholm).....	61
Table 3.2: Physical properties of Vanadis 23 (Source Uddeholm)	61
Table 3.3: Elastic properties of the materials used in the model	66
Table 3.4: Comparison of FEA results with actual measurement along channel breadth	70
Table 4.1: Chemical composition of as received CP-Ti grade 2 material used in this study (source conformance certificate).....	91
Table 4.2: Summary of processing parameters during I-ECAP experiments using dies with channel angle (Φ) of 120° and 90°.	93
Table 5.1: Grain refining factor (η) at subsequent I-ECAP passes using $\Phi = 120^\circ$ channel die.	129
Table 5.2: Grain refining factor (η) at subsequent I-ECAP pass using $\Phi = 90^\circ$ channel die.	145
Table 6.1: Tensile properties of CP-Ti in unprocessed condition and after subsequent I-ECAP passes at 300 °C using $\Phi = 120^\circ$ channel angle die (0.2% σ_Y — yield strength, σ_{UTS} — ultimate tensile strength, δ_{unif} — uniform elongation, δ_{fail} — elongation to failure and Ψ — reduced cross-area at failure).	154
Table 6.2: Tensile properties of CP-Ti in unprocessed condition and after subsequent I-ECAP passes at 300 °C using $\Phi = 90^\circ$ channel angle die (0.2% σ_Y — yield strength, σ_{UTS} — ultimate tensile strength, δ_{unif} — uniform elongation, δ_{fail} — elongation to failure and Ψ — reduced cross-area at failure).	164
Table 6.3: Summary of CP-Ti processing parameters used in selected ECAP studies and present study, along with the changes in grain size, hardness, strength and ductility. The table is arranged in the order of decreasing processing temperature.	172

Chapter 1

Introduction

1.1 Background

Titanium has high strength, low density, good creep performance and outstanding corrosion resistance. Its strength is comparable to steel but is almost half of its density and therefore titanium has a high specific strength (defined as a ratio of strength to density). This explains its preferential use in many applications such as: aerospace (aero-engines, airframes etc.), chemical processing, power generation, marine applications, automotive components and sports equipment [1, 2].

Titanium is also known for its biocompatibility, compared to other metals, it offers a range of favourable properties. It has good corrosion resistance because of the formation of TiO₂ layer on its surface. It has a lower elastic modulus (compared to stainless steel) which leads to less stress shielding and better compatibility with the bone [3]. Moreover, it is lighter compared to other surgical metals and therefore produces fewer artefacts on computer tomography (CT) scans. Titanium and its alloys are therefore widely used in bio-medical applications [4]. Some of the most common applications include: dental implants, joint replacement implants (for hip, knee, shoulder etc.) and fixation parts (screws, nails etc.).

Ti-6Al-4V (Ti-64), is currently widely used as medical implants due to its good corrosion resistance and high strength, however, long-term performance of Ti-64 has some concerns. This is because, the alloying elements such as Al and V, which are added to enhance the mechanical characteristics of titanium, are considered toxic in the long run and therefore undesirable for full bio-integration [5]. Unalloyed titanium (commercially pure form, CP-Ti) has superior biocompatibility and therefore is an attractive option. However, because of comparatively inferior strength, it is not used in load bearing implants and is only used in very limited applications, such as in dentistry [6].

If CP-Ti is to replace titanium alloys as a major implant material, its strength must be increased without adding harmful alloying elements. One viable solution to abandon the alloying elements but still improve the mechanical performance of CP-Ti is by nano-structuring or grain refinement. Strengthening of metals by reducing the grain size has been demonstrated by numerous studies [7, 8]. Especially in CP-Ti, after attaining ultrafine grain (UFG) structure not only improves its yield and tensile strength but also improves the fatigue and corrosion resistance considerably [9-12]. Grain refinement is also understood to enhance cell response due to changes in titanium surface morphology [13] and grain orientation [14]. Research has also shown that compared to coarse grain titanium, UFG structure in titanium accelerates osseointegration and therefore further enhances its biocompatibility [15, 16].

Severe plastic deformation (SPD) is an established technology for achieving extreme grain refinement and obtaining ultrafine grain (UFG) structure in metals, thereby significantly improving their mechanical properties [17-19]. The technology involves imparting large plastic strain in material, without significantly changing the sample dimensions. Among the various available SPD techniques, equal channel angular pressing (ECAP) is by far the most widely used technique. It is capable of producing bulk UFG material, large enough for practical applications [20]. However, despite the success of the ECAP process, it is not an ideal option from the commercialization viewpoint. Its inability to process very long or continuous billets, due to very high force resulting from friction, is the main limitation. Therefore, there is considerable interest in developing techniques that can overcome the low productivity limitations of the ECAP process.

Incremental ECAP (I-ECAP) process [21], offers the possibility in obtaining UFG structures in long or continuous billets. This promising technique has a strong potential for obtaining the much-needed high strength CP-Ti for biomedical implants on an industrial scale. Investigating the effectiveness of the I-ECAP technique in refining the grain structure in titanium and thereby influencing its mechanical properties is therefore the primary motivation for the present research work.

1.2 Research aim and objectives

Based on the discussion in the previous section it is clear that grain refinement in CP-Ti for the purposes of improving its mechanical performance is crucial to replace the existing titanium alloys in medical applications. It is also essential to use an industrially scalable method such as I-ECAP for processing long or continuous billets of titanium.

The aim of the present research work therefore is:

‘To investigate the feasibility of I-ECAP process in improving the mechanical performance of CP-Ti by refining its grain structure’.

The following five objectives were set to achieve this aim:

- Demonstrate the I-ECAP process as a commercially viable method for grain refinement in titanium. To enable this, the processing capability of the existing I-ECAP rig required some major upgrades and improvements. These includes: (i) automatic material feeding, (ii) addition of elevated temperature processing capability, (iii) commissioning of digital servo press controller, (iv) implementation of process control and instrumentation for data acquisition (v) general rig upgrades including safety controls.
- Demonstrate the I-ECAP process as an effective method of obtaining defect free titanium billets with UFG structure. For this purpose two separate dies with varying channel intersection angles ($\Phi = 120^\circ$ and 90°) are used and compared.
- Understand the complex nature of grain refinement mechanism in titanium during I-ECAP process by studying the evolution of microstructure and texture.
- Characterize the mechanical properties of the processed billets in detail and compare with the unprocessed condition.
- Study the post I-ECAP workability characteristics of UFG titanium by cold and warm compression testing.

1.3 Organization of the thesis

The thesis contains eight chapters in total; following is the brief description of each chapter.

Chapter 1 presents the motivation of the research work, aim and objectives and organization of the thesis.

Chapter 2 introduces the topic of grain refinement in metals and the synthesis techniques for obtaining UFG structure. Severe plastic deformation (SPD), as a method of introducing extreme grain refinement is discussed along with several other SPD techniques, including equal channel angular pressing (ECAP). Principles of the incremental ECAP (I-ECAP) process used in the present work is discussed in detail. The chapter also contains, general background on titanium, its crystal structure and its deformation behaviour. Finally, current state of the art in the grain refinement research work on CP-Ti titanium using ECAP is presented.

Chapter 3 presents the finite element modelling results to study the deformation behaviour of titanium billets during I-ECAP. The chapter also includes the details of optimized die design following FE simulations.

Chapter 4 includes description of the work carried out to improve the processing capability of the I-ECAP experimental rig facility. It defines various elements of the I-ECAP rig and the procedure used to perform experiments using two separate dies with channel intersection angles (Φ) of 120 and 90°. The chapter also includes detail of the test methods and the equipment used to characterize the material.

Chapter 5 attempts to track the evolution of microstructure and texture development using electron backscatter diffraction (EBSD) in titanium during I-ECAP processing. Phenomena such as twinning and continuous dynamic recrystallization (CRDX) are discussed. It also includes the comparison of grain refinement results for the material processed using dies with channel intersection angles (Φ) of 120 and 90°.

Chapter 6 presents the influence of I-ECAP processing using two dies ($\Phi = 120$ and 90°) on the mechanical response of titanium. Results show the enhancements in tensile and hardness properties. Detailed discussion on the ductility and strain hardening

behaviour is also presented. A comparison of mechanical properties in UFG titanium produced by classical ECAP processing is also given in this chapter.

Chapter 7 discusses the workability characteristics of UFG titanium at room and warm temperature conditions during compression testing for various strain rates. Flow stress curves, normalized strain hardening plots, strain rate sensitivity and deformed microstructure for various temperature and strain rate conditions are presented and discussed.

Chapter 8 presents a summary of the research work. It contains important conclusions from the results and discussions presented in chapters 5-7. The chapter also outlines the achievement of the objectives and contribution to knowledge. Finally, recommendations are suggested for future work.

Chapter 2

Methods of grain refinement and their application to titanium

2.1 Introduction

Although the mechanical and physical properties of all polycrystalline metals are determined by several factors, the average grain size of the metals generally plays a very significant and often a dominant role in determining the mechanical behaviour of metals, in particular the yield strength. The strength of polycrystalline metals at low temperatures can be derived from Hall – Petch relationship as follows:

$$\sigma_y = \sigma_o + k_y d_g^{-1/2} \quad \text{Eq. 2.1}$$

where σ_y is the yield strength, σ_o is the friction stress, k_y is a constant known as Hall – Petch slope and d_g is the average grain size [22, 23]. The relationship predicts an increase in the yield stress with decreasing grain size as shown in Fig. 2.1 [24].

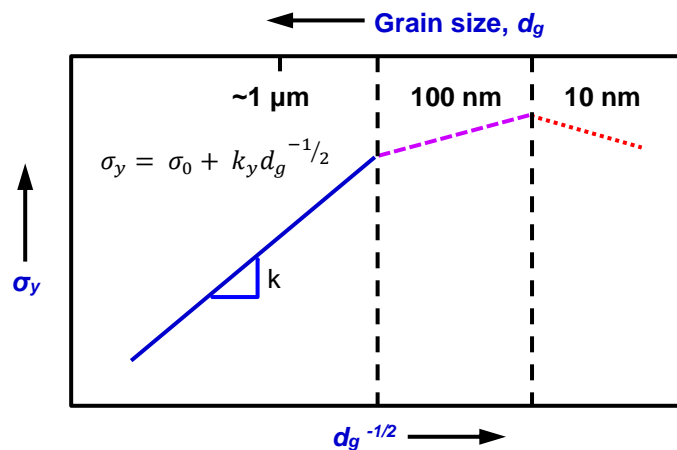


Fig. 2.1: The variation of Hall – Petch relationship with varying grain size [24].

However for grains below a critical size (less than $\sim 25 \text{ nm}$), the relationship may lose its validity leading to a yield strength plateau or even an inverse Hall – Petch

relationship [25] but this still remains to be proved. Nevertheless, for larger grains, the relationship has been investigated for a number of metals and alloys, and good agreement with Eq. 2.1 has been found [26, 27].

The empirical validity of Eq. 2.1 has led to an ever increasing interest in the research and development activities to increase the strength of polycrystalline materials by refining their grain size, which in today's industrial materials can be 5 – 10 μm or even smaller [28].

Grain refinement provides an important tool for improving the properties of metallic materials. The research activities related to ultrafine grain metals began in the 1960s by Embury and Fischer [29], Armstrong et al. [30] and by Erbel in 1970s [31]. The driving force behind this research was the possibility of synthesizing materials with higher strength [7] by reducing their grain size to sub-micron level, a reasonable assumption from the Hall – Petch relationship. A great deal of effort was also geared towards achieving 'superplasticity' in materials, since it is a well-known fact that for finer grain materials, superplastic forming can be performed at higher strain rates and at lower temperatures.

2.1.1 Ultrafine grained (UFG) materials

According to Prangnell et al. [32, 33], materials having an average grain size of less than $\sim 1 \mu\text{m}$ in all directions and having mostly high angle grain boundaries (misorientation angle greater than 15°) are known as ultrafine grained (UFG) materials.

UFG materials are structurally characterized by a large volume fraction of grain boundaries which may significantly alter their physical, mechanical and chemical properties in comparison with conventional coarse-grained polycrystalline materials [34-36], which usually have grain sizes in the range of 10 – 300 μm . Typically, the grain size within UFG materials varies from 100 – 1000 nm and the ratio of high angle grain boundaries to the total boundary area in the material is greater than 70%. The presence of a high fraction of high-angle grain boundaries is important in order to achieve advanced and unique properties, for example, superplasticity [37]. UFG materials are also sometimes referred to as nanocrystalline materials or nanostructured materials, where the grain size is less than 100 nm (0.1 μm).

2.2 Synthesis of UFG materials

Two basic approaches have been developed for the synthesis of UFG materials and these are known as the “bottom-up” and the “top-down” approach [38].

2.2.1 Bottom-up approach

In the “bottom-up” approach, nanostructured / UFG materials are fabricated by assembling individual atoms or by consolidating and sintering of nano-particulate solids. Examples of these techniques include inert gas condensation [39, 40], electrodeposition [41, 42], chemical and physical deposition [43], ball milling with subsequent consolidation and cryomilling with hot isostatic pressing [44, 45]. In practice, these techniques are often limited to the production of fairly small samples that may be useful for applications in fields such as electronic devices but are generally not appropriate for large-scale structural applications.

Furthermore, the finished products obtained by these techniques inevitably contain some degree of residual porosity due to insufficient consolidation, which adversely affects the mechanical properties of the materials [46, 47] and some level of contamination which is introduced during the fabrication procedure. There is also a possibility of imperfect bonding between particles. Finally very fine powder, as produced by ball milling, is difficult to handle and can be perceived as a health hazard.

2.2.2 Top-down approach

The “top-down” approach is based on taking a bulk solid with a relatively coarse grain structure and breaking down its internal structure to produce a UFG microstructure through imposing large strain. This approach is capable of producing bulk quantities of UFG material and also has an advantage of applying it to wide range of metals and their alloys.

Methods of producing UFG materials should meet the following requirements [18]

1. Firstly it is important to obtain ultra-fine grained structures with prevailing high angle boundaries since only in this case can a qualitative change in properties of materials occur.

2. Secondly, the formation of homogenous nano or UFG structures within the whole volume of a sample is necessary for providing uniform properties of the processed materials.
3. Thirdly, though samples are exposed to large plastic deformations they should not have any mechanical damage or cracks.

Conventional procedures of plastic deformation in metal-working, such as rolling or extrusion, do not meet these requirements as they are restricted in their ability to produce UFG microstructure for two reasons. First, the strains are non-uniform and also insufficient to introduce homogenous UFG structures, as the cross-sectional dimensions are normally changed during conventional processing. Secondly, these processes are generally carried at high temperatures which promote grain growth.

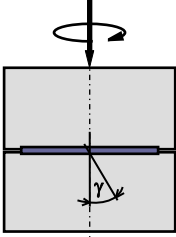
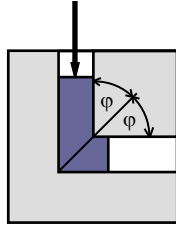
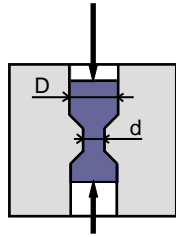
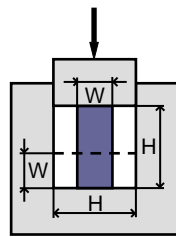
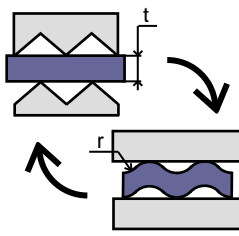
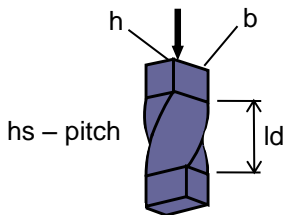
As a consequence, attention has been directed towards development of alternative processing techniques, based on the application of severe plastic deformation (SPD), where extremely high strains are imposed at relatively low temperatures without incurring any significant changes in the cross-sectional dimensions of the samples. Processing bulk UFG / nanostructured materials using SPD is a more economical and practical approach. It results in overcoming a number of difficulties associated with bottom-up approach like residual porosity in compacted samples, impurities from ball milling and addition of costly alloying elements during solidification. Moreover, it enables processing of large scale billets suitable for practical application.

2.3 Severe plastic deformation (SPD)

Formally, processing by severe plastic deformation (SPD) refers to a class of mechanical deformation processes that imparts very large plastic strain in materials [48-50] leading to exceptional grain refinement. A unique feature of SPD processing is that this very large plastic strain is imposed without any significant change in overall dimensions of the work piece. In some SPD techniques, application of high pressure is essential for achieving high strains and introducing the high densities of lattice defect necessary for exceptional grain refinement [51]. To avoid any restoration processes, like recovery and grain growth taking place, SPD processes generally have to be carried out at relatively low temperatures [52-54]. However, in the case of hard to deform materials, SPD is carried out at elevated temperatures, so as to improve ductility and allow the plastic deformation process to take place without fracturing the material.

Developments in processing by SPD were first started at Harvard University in 1935 due to extensive work of Bridgman. In his experiments, metals were subjected to large deformations under high applied pressures in attempt to improve mechanical properties of materials that were inherently brittle. For example, in a series of detailed experiments, subsequently described in a classic text [55], Bridgman subjected thin metal disks (usually thinner than 0.1 mm) to differing high pressures and to simultaneous torsional straining using a methodology that would now be regarded as a classic SPD procedure known as ‘high pressure torsion’. However, although his work demonstrated the potential for achieving improved deformability, it did not shed much light on the microstructural changes taking place in severely deformed metals. Accordingly, despite the evidence of successful potential trends in this early work, the principles of processing by SPD received little attention either in academic sector or in industrial operations to make use of this new technology. Since this early work, many different SPD processing techniques have been proposed, developed and tested (see Table 2.1 [56]). Since the focus of this thesis is ECAP and I-ECAP, these process are described in detail.

Table 2.1: Batch SPD processes [56].

Process name and origin	Schematic representation	Equivalent plastic strain
High pressure torsion (HPT) Valiev et al. [49]		$\varepsilon = \frac{tg\gamma}{\sqrt{3}}$
Equal channel angular pressing (ECAP) Segal et al. [57]		Eq. 2.6
Cyclic extrusion compression (CEC) Korbel et al. [58]		$\varepsilon = n4 \ln\left(\frac{D}{d}\right)$
Multiaxial forging (MF) Ghosh [59]		$\varepsilon = n \frac{2}{\sqrt{3}} \ln\left(\frac{H}{W}\right)$
Repetitive corrugation and straightening (RCS) Huang et al. [60]		$\varepsilon = n \frac{4}{\sqrt{3}} \ln\left(\frac{r+t}{r+0.5t}\right)$
Twist extrusion (TE) Beygelzimer et al. [61]		$\varepsilon = 3.46 \left(\frac{hs}{0.5\sqrt{b^2+h^2}}\right)^{-0.47} \left(\frac{ld}{hs}\right)^{0.55} \left(\frac{h}{b}\right)^{-0.56}$

2.4 Equal channel angular pressing (ECAP)

The process of equal channel angular pressing (ECAP), known also as equal channel angular extrusion (ECAE) was first introduced by Segal and his co-workers in the late 70s and early 80s at an institute in Minsk in the former Soviet Union [57, 62]. The basic objective at that time was to develop a metal forming process capable of imparting high plastic strain to metal billets by simple shear. This early development of a new pressing operation received only limited attention in the scientific community. However the situation changed, when in 1990s reports and reviews began to appear documenting the potential of using ECAP to produce UFG and sub-micrometre metals with new and unique properties [49, 50].

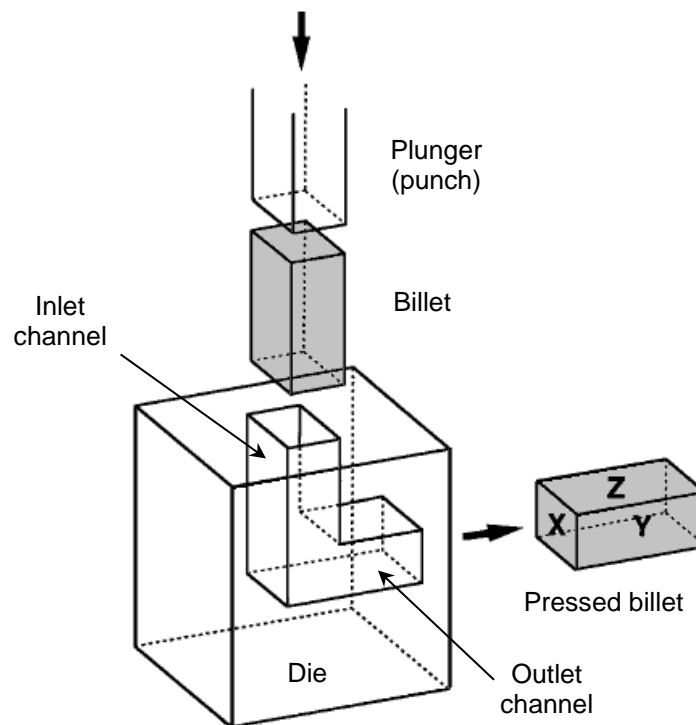


Fig. 2.2: Illustration of the ECAP process [63].

The principle of ECAP is depicted schematically in the illustration in Fig. 2.2 [63]. ECAP tooling consists of a solid die containing two channels, an inlet and an outlet channel having the same cross-sectional area intersecting at an angle near the centre of the die. The billet, which is machined to fit within these channels, is pressed via the inlet channel into the outlet channel using a plunger or punch. As the billet passes through the channel intersection, it changes direction and is subjected to a high level of simple shear strain. In the final stage the billet exits the outlet channel. The

three orthogonal planes are shown in Fig. 2.2, where the X plane is the transverse plane perpendicular to the flow direction and Y and Z planes are the flow and the longitudinal planes parallel to the side face and the top face at the point of exit from the die.

It is evident in the illustration (Fig. 2.2) that the cross-sectional dimensions of the billet are preserved at both inlet and outlet channels. It is important to highlight here that preservation of the cross-sectional dimensions, differentiate processing by the ECAP process in a very significant way from conventional industrial metal working process of rolling, extrusion and drawing, where the dimensions are changed with each consecutive pass. This feature of the ECAP process permits repetitive pressing of the same billet through the die. The grains in the billet are mainly refined due to activation of the slip system, and further passes of the material through the die produce ultrafine grains with high angle grain boundaries. The process is generally carried out at low temperature to avoid grain growth.

Among all SPD techniques developed so far, ECAP has especially drawn a lot of attention from the academic sector as well as from the industrial sector. It is the most promising technique which is capable of producing fully dense bulk billets containing UFG structure in the submicron or nanometer range [64-66] and which are large enough for structural applications [67-69]. Valiev et al. [70] has listed the following reasons why ECAP is specially an attractive processing technique among the other various SPD processes.

1. First, it can be applied to bulk billets so that there is the potential for producing materials that may be used in a wide range of structural applications.
2. Second, it is a relatively simple procedure that is easily performed on a wide range of alloys and, except only for the construction of the die, processing by ECAP uses equipment that is readily available in most laboratories.
3. Third, ECAP may be developed and applied to metals with different crystal structures and to many other materials ranging from precipitation-hardened alloys to inter-metallic and metal–matrix composites.
4. Fourth, reasonable homogeneity is attained through most of the as-pressed billet provided the pressings are continued to a sufficiently high strain.

2.5 Fundamental parameters in ECAP

ECAP is characterized by several fundamental parameters such as strain imposed in each pass on the billet through the die, processing routes, the slip systems operating during the pressing operation and the resulting shearing patterns present within the as-pressed billets. Taken together, these various parameters uniquely define the precise nature of the pressing operation and play a critical role in the resulting grain refinement achieved during ECAP.

2.5.1 The strain imposed in ECAP

A high value of strain is imposed on the material during each pass of the workpiece through an ECAP die. The magnitude of this strain can be computed using an analytical equation which was derived by Iwahashi et al. [71], using the various die configurations illustrated schematically in a two dimensional representation shown in Fig. 2.3.

Here Φ is the angle between the two channels and Ψ represent the angle associated with the arc of curvature where the two parts of the channel intersect. Three conditions are shown in Fig. 2.3, Fig. 2.3(a) corresponds to a limiting case where $\Psi = 0^\circ$, Fig. 2.3(b) corresponds to a second limiting case where $\Psi = (\pi - \Phi)^\circ$ and Fig. 2.3(c) represent an intermediate condition where $0 < \Psi < (\pi - \Phi)^\circ$. To simplify strain calculation frictional effects have not been taken into account, and so it is assumed that the workpiece is very well lubricated.

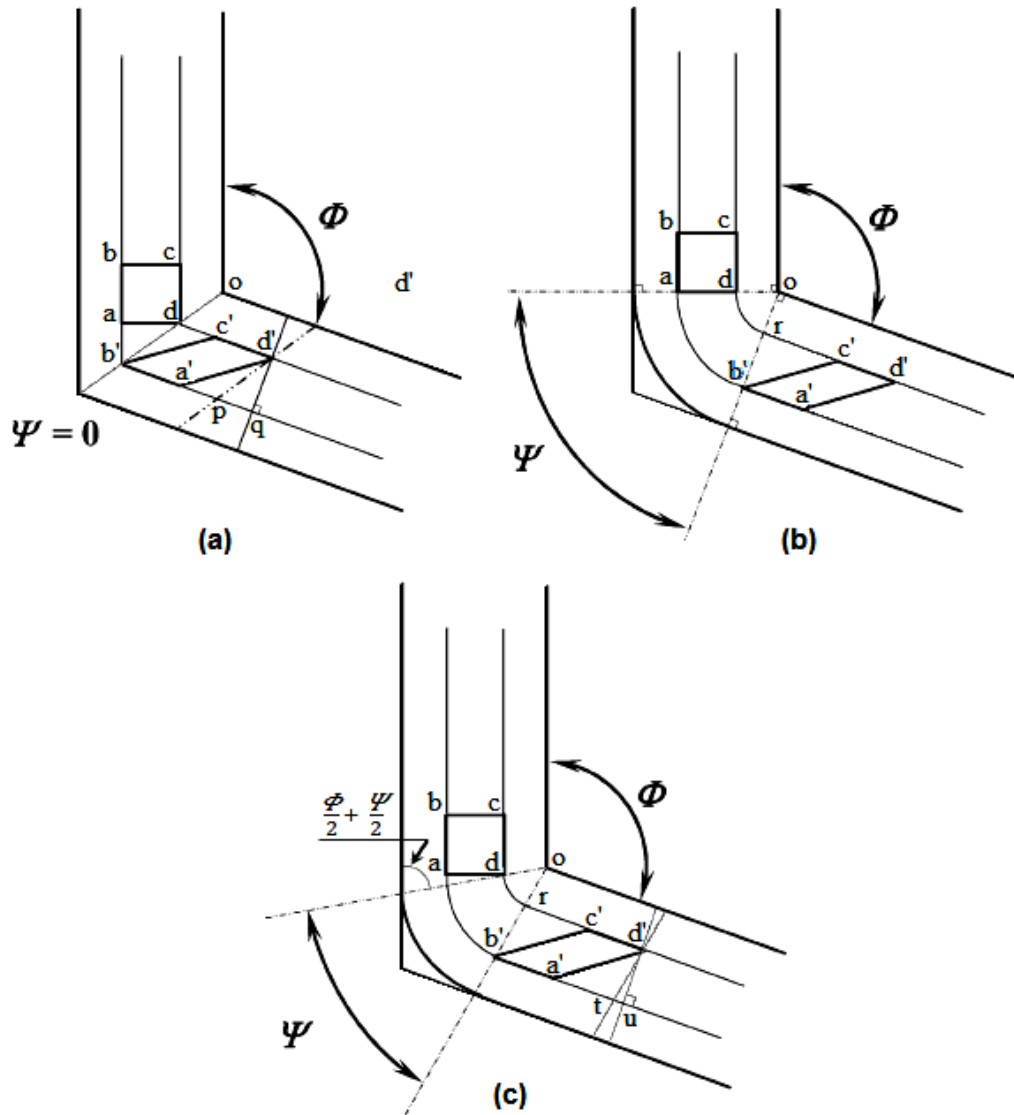


Fig. 2.3: Principle of ECAP where Φ is the angle of intersection between the two channels and Ψ is the angle subtended by the arc of curvature at the point of intersection: (a) $\Psi = 0$, (b) $\Psi = \pi - \Phi$, (c) an arbitrary value of Ψ lying between $\Psi = 0$ and $\Psi = \pi - \Phi$ [71].

For the situation where $\Psi = 0^\circ$ in Fig. 2.3(a), a small square element in the entrance channel, labelled $abcd$, passes through the theoretical shear plane and becomes distorted into the parallelogram labelled $a'b'c'd'$. Using notations from Fig. 2.3 (a) it can be shown that the shear strain, γ , is given by

$$\gamma = \frac{a'q}{qd'}$$

where $qd' = ad$ and $ab' = dc' = a'p = pq = ad \cot\left(\frac{\Phi}{2}\right)$ so that $a'q = 2ad \cot\left(\frac{\Phi}{2}\right)$

Therefore for this condition, where $\Psi = 0^\circ$,

$$\gamma = 2 \cot\left(\frac{\Phi}{2}\right) \quad \text{Eq. 2.2}$$

Using the same approach for Fig. 2.3(b), the shear strain is given by

$$\gamma = \frac{rc'}{rb'}$$

$rb' = da = (oa - od)$ and $ab' = dc' = oa\Psi = (rc' + od\Psi)$ so that $rc' = (oa - od)\Psi$.

Therefore, for this condition, where $\Psi = (\pi - \Phi)^\circ$,

$$\gamma = \Psi \quad \text{Eq. 2.3}$$

Finally, Fig. 2.3(c) where Ψ represent an intermediate situation, the shear strain is given by

$$\gamma = \frac{d'u}{d'u}$$

where $d'u = ad$ and $rb' = da = (oa - od)$

Therefore for this intermediate condition where $0 < \Psi < (\pi - \Phi)^\circ$,

$$\gamma = 2 \cot\left(\frac{\Phi}{2} + \frac{\Psi}{2}\right) + \Psi \operatorname{cosec}\left(\frac{\Phi}{2} + \frac{\Psi}{2}\right) \quad \text{Eq. 2.4}$$

The equivalent strain, ε_{eq} , is represent by

$$\varepsilon_{eq} = \left\{ \frac{2(\varepsilon_x^2 + \varepsilon_y^2 + \varepsilon_z^2) + \left(\frac{\gamma_{xy}^2 + \gamma_{yz}^2 + \gamma_{zx}^2}{2}\right)}{3} \right\}^{\frac{1}{2}} \quad \text{Eq. 2.5}$$

So the strain, ε , after one pass through the ECAP die is

$$\varepsilon_{eq} = \left\{ \frac{2 \cot\left(\frac{\Phi}{2} + \frac{\Psi}{2}\right) + \Psi \operatorname{cosec}\left(\frac{\Phi}{2} + \frac{\Psi}{2}\right)}{\sqrt{3}} \right\} \quad \text{Eq. 2.6}$$

Eq. 2.6 provides a simple and direct way for estimating the strain for any selected die having different values of Φ and Ψ .

Because the same amount of strain is accumulated in the material in each pass through the die, the total strain after N number of passes, ε_N , is given by

$$\varepsilon_N = \frac{N}{\sqrt{3}} \left[2 \cot \left(\frac{\Phi}{2} + \frac{\Psi}{2} \right) + \Psi \operatorname{cosec} \left(\frac{\Phi}{2} + \frac{\Psi}{2} \right) \right] \quad \text{Eq. 2.7}$$

Fig. 2.4 shows a plot of the variation of ε_{eq} after the first pass, with the channel angle (Φ) from 45° to 180° and for Ψ lying in the range of 0° to 90° .

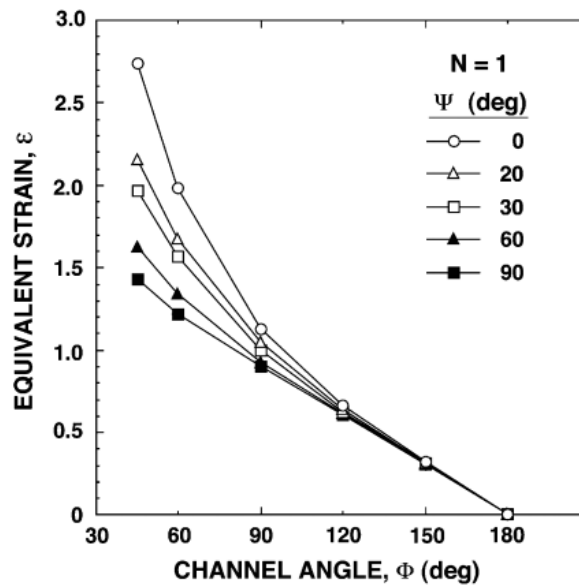


Fig. 2.4: Variation of the equivalent strain, with the channel angle (Φ) over angle of the arc of curvature (Ψ) for the first pass of ECAP ($N=1$) [72]

2.5.2 Processing routes

Since ECAP allows multiple passes of the billet through the die, the direction and number of billet passes are very important for microstructure refinement. Segal [73] first noted that the use of repetitive passes may provide an opportunity to develop different microstructures by rotating the billet about the longitudinal axis between consecutive passes, thereby modifying the shear planes and shear directions.

In particular, four distinct processing routes have been identified for use in ECAP. These routes are designated as route A, route B_A, route B_C and route C and are illustrated in Fig. 2.5. Route A in which the billet is processed repetitively without any rotation, route B_A in which the billet is rotated by 90° clock wise and counter clock

wise alternatively between consecutive passes, route B_C in which the billet is rotated by 90° in the same direction between consecutive passes and route C in which the billet is rotated by 180° between passes.

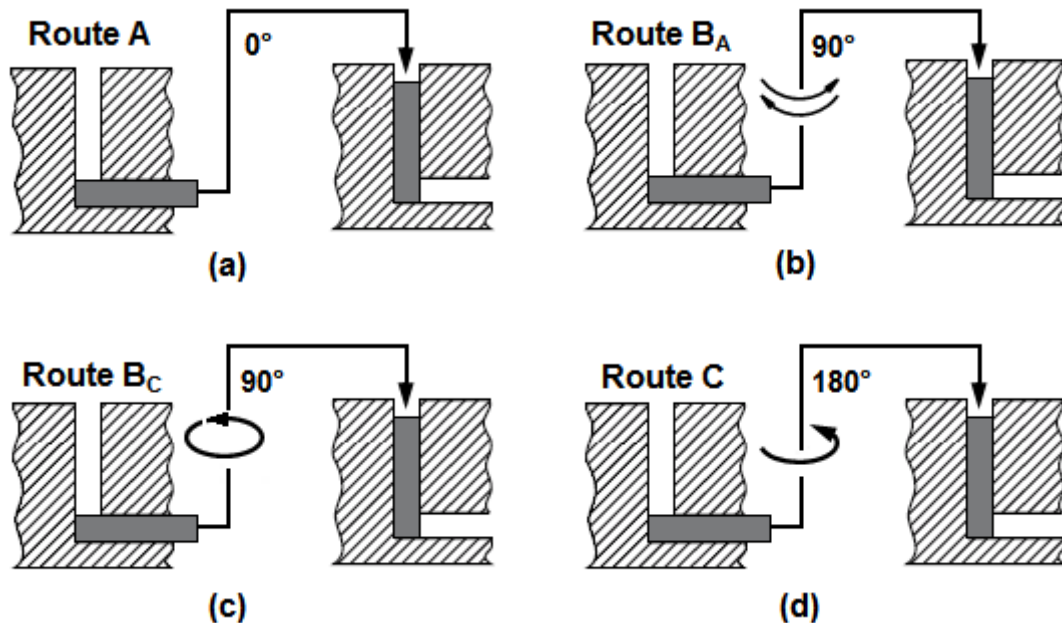


Fig. 2.5: Four possible processing routes in ECAP [74].

These four processing routes were examined in detail in [75]. The distinction between these routes is important, as each route has a different shearing characteristic and therefore each route introduces different shearing patterns [76].

Two more hybrid routes have been proposed in [77], namely, route E and F. Route E represents rotation pattern of 180° after pass one, 90° after pass two and 180° after pass three and so on. While route F consists of rotations about 90° , 180° and 270° after first, second and third pass, respectively. These routes are very rarely used in ECAP process and have not been reported much in the literature. Another route R has been recently proposed in [78] and applied to magnesium alloy AZ61. In route R the billet is inverted/reversed with respect to the original position after each pass.

2.5.3 Multiple turn ECAP

In an attempt to reduce the number of passes, a two turn channel design can be used. Fig. 2.6(a) represent the so called S-shaped channel, one pass using this channel is equivalent to two passes following route C in conventional ECAP die. Similarly, Fig. 2.6(b) shows the U-shaped channel design which is effectively two passes following route A. The Fig. 2.6(c) shows a two-turn shaped design following route B_C and finally Fig. 2.6(d) represents a three-turn design following route B_C.

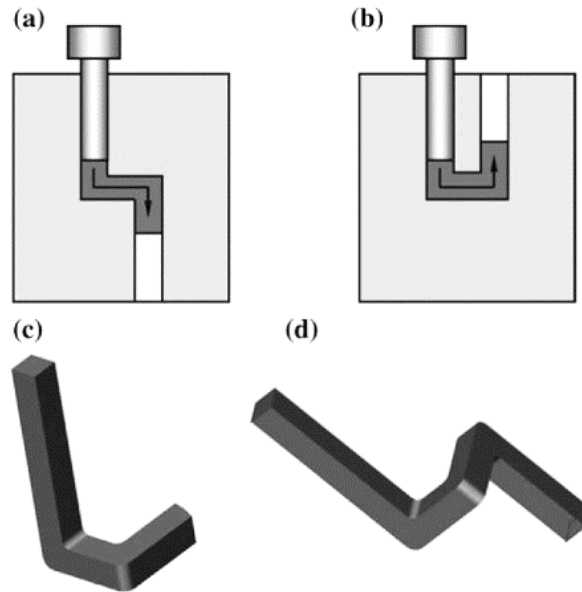


Fig. 2.6: Channel design for multi-turn ECAP: (a) S-shaped two-turn route C, (b) U-shaped two-turn route A, (c) two-turn route B_C and (d) three turn route B_C [79].

Rosochowski and Olejnik [80] performed extensive FE simulation supported by physical modelling to analyse the two-turn S-shaped channel design. Their results show that although a high plastic equivalent strain of 2.3 is induced using this design, the force requirement more than doubles as soon as the billet reaches into the second intersection. Multiple turn ECAP is practically very challenging and therefore multiple passes using a single turn channel as opposed to multiple turn is more widely reported in literature.

2.5.4 Slip systems and shearing patterns for the different processing routes

Each route has a different slip system associated with it. These slip systems are depicted in Fig. 2.7 for different ECAP routes when using a die with (a) $\Phi = 90^\circ$ and

(b) $\Phi = 120^\circ$. In route C, for example, the direction of shear is reversed in each pass and the strain is restored after every even number of passes; that is why route C is also called redundant strain process [70].

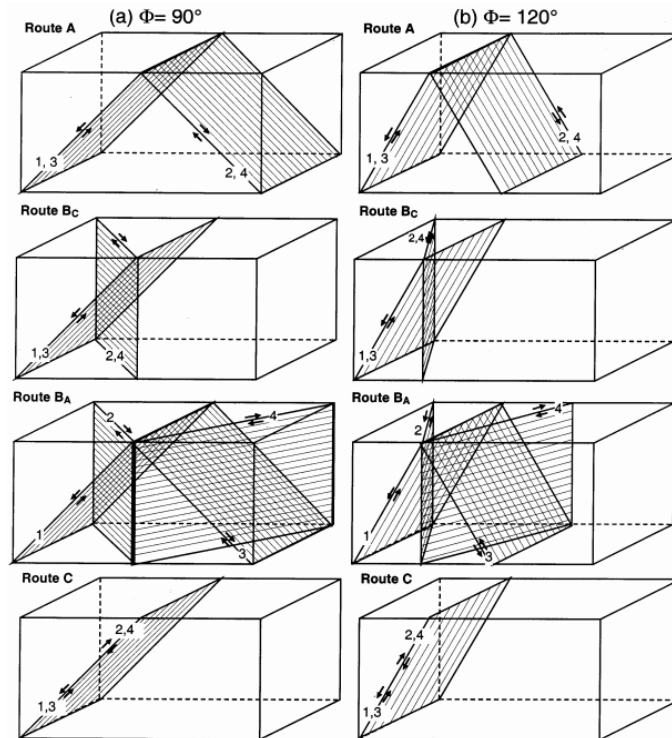


Fig. 2.7: The slip systems during consecutive passes for different ECAP routes using die with (a) $\Phi = 90^\circ$ and (b) $\Phi = 120^\circ$ [81].

The implications of these slip systems are illustrated in Fig. 2.8 [75], which shows the ideal distortions introduced in a cubic element on the X, Y and Z planes, following the four processing routes (A, B_A, B_C and C), up to a total of eight passes using 90° ECAP die. It is apparent that the cubic element is restored to its original form, after every four passes using the route B_C and after every second pass using the route C. Whereas using route A and B_A, the distortions mostly continue to acute [70]. Also notice that no distortions take place in the Z plane when route A and C is used.

Another approach in examining the effect of ECAP is by studying the shearing patterns as shown in Fig. 2.9. The lines are colour coded to represent different passes. These drawings represent that there is considerable variation in the angular range of slip on each plane during ECAP using different routes. Notice that route B_C imposes the largest angular range after four passes.

Route	Plane	Number of pressings								
		0	1	2	3	4	5	6	7	8
A	X	□	▭	▭	▭	▭	▭	▭	▭	▭
	Y	□	▭	▭	▭	▭	▭	▭	▭	▭
	Z	□	□	□	□	□	□	□	□	□
B _A	X	□	▭	▭	▭	▭	▭	▭	▭	▭
	Y	□	▭	▭	▭	▭	▭	▭	▭	▭
	Z	□	□	▭	▭	▭	▭	▭	▭	▭
B _C	X	□	▭	▭	▭	▭	▭	▭	▭	▭
	Y	□	▭	▭	▭	▭	▭	▭	▭	▭
	Z	□	□	▭	▭	▭	▭	▭	▭	▭
C	X	□	▭	▭	▭	▭	▭	▭	▭	▭
	Y	□	▭	▭	▭	▭	▭	▭	▭	▭
	Z	□	□	▭	▭	▭	▭	▭	▭	▭

Fig. 2.8: The distortions introduced into a cubic element when viewed on the X, Y and Z planes when processing using different ECAP routes [75].

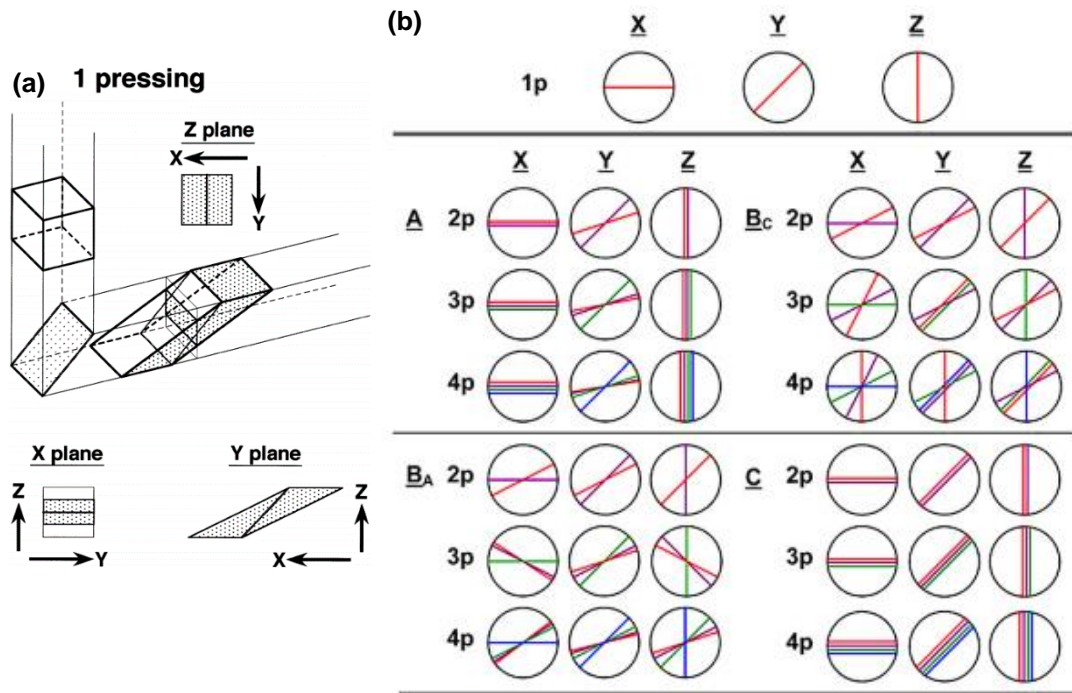


Fig. 2.9: (a) The distortion of a cubic element after a single pass [82] and (b) the shearing pattern on the X, Y and Z planes for different processing routes for up to four passes [76].

2.5.5 Mechanism of grain refinement in ECAP

Although the true nature of the grain refinement mechanism in SPD is still not fully understood [17], it is generally believed that the grains are refined by introducing large number of dislocations. These dislocation accumulates and arrange themselves into a low energy configuration forming sub grains with low-angle grain boundaries (misorientation angle less than 2 degrees). Upon further straining of the material in subsequent passes, the sub-grains continue to evolve and arrange themselves into reasonably homogenous formation of ultrafine grains with high angle grain boundaries (misorientation angle greater than 15 degree) [83].

Fig. 2.10 shows a schematic illustration of a grain refinement model for FCC metals during ECAP processing [84]. FCC was selected because it mainly deforms by slip due to the abundance of slip systems available in its crystal structure. It represents the appearance of the microstructure on the longitudinal (Y) plane. The three rows in the illustration represent the condition after first (1p), second (2p) and fourth (4p) pass of ECAP process while the columns represents the A, B_C and C processing routes. The four colours of red, mauve, green and blue; depict the slip introduced in the first, second, third and fourth pass, respectively. The figure also contains the value of angular range of slip, η , corresponding to each processing route after the representative pass. Furthermore, the width of the sub-grain is set to d for each pass through the die.

The model captures the shearing system introduced in each pass and is consistent with the shearing pattern presented in Fig. 2.9(b). It is readily apparent the route B_C imposes several intersecting slip systems. This results in a high density of dislocations which can rearrange and annihilate in a manner consistent to earlier theories on plastic deformation based on dislocations [85, 86].

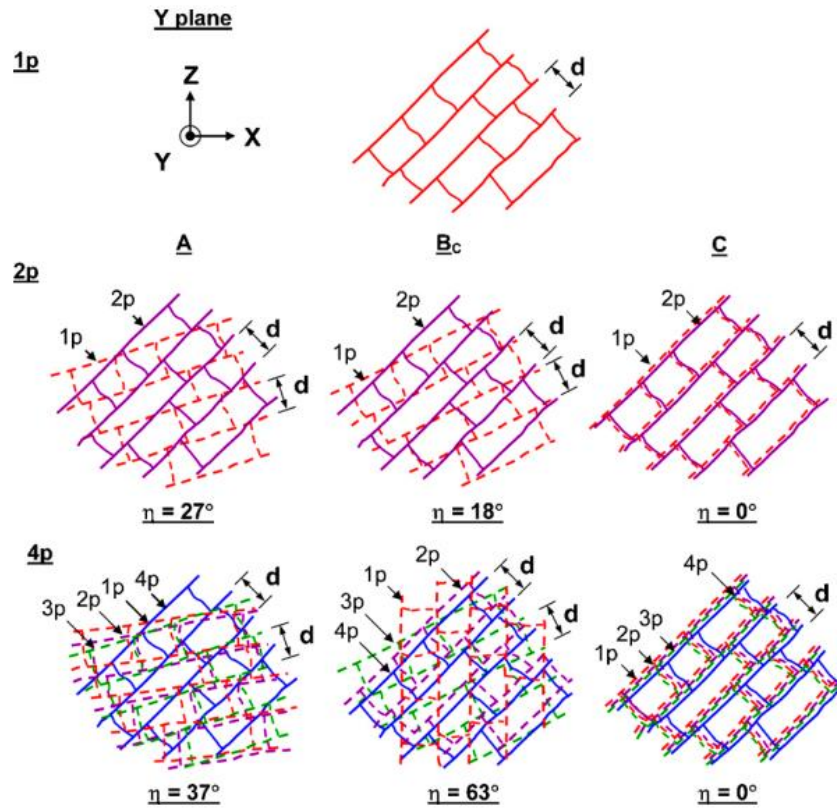


Fig. 2.10: Model of grain refinement in FCC metals processed using ECAP for first pass, second pass and fourth pass corresponding to processing route A, B_c and C [84] on longitudinal (Y) plane.

In order to observe experimentally the grain refinement mechanism, Fig. 2.11(a-d) [74] presents the evolution of microstructure during ECAP processing in pure aluminium (FCC structure) on the X, Y and Z planes of the samples. All samples were processed using a 90° die following B_c for a total of one, two, three and four passes. As can be seen, the microstructures obtained are consistent with the model presented in Fig. 2.10, for example, after first pass along the Y plane, the initial large grains (~1.0 mm) have been divided into array of sub-grains which are elongated and form a banded structure (Fig. 2.11(a)). The SAED pattern shows that the grain boundaries have mostly low angle misorientation after the first pass. Similarly, Fig. 2.11(d) shows that after four passes the microstructure is mostly equiaxed and homogenous on all planes, the SAED pattern demonstrates that the grain boundaries have mostly high angles of misorientation.

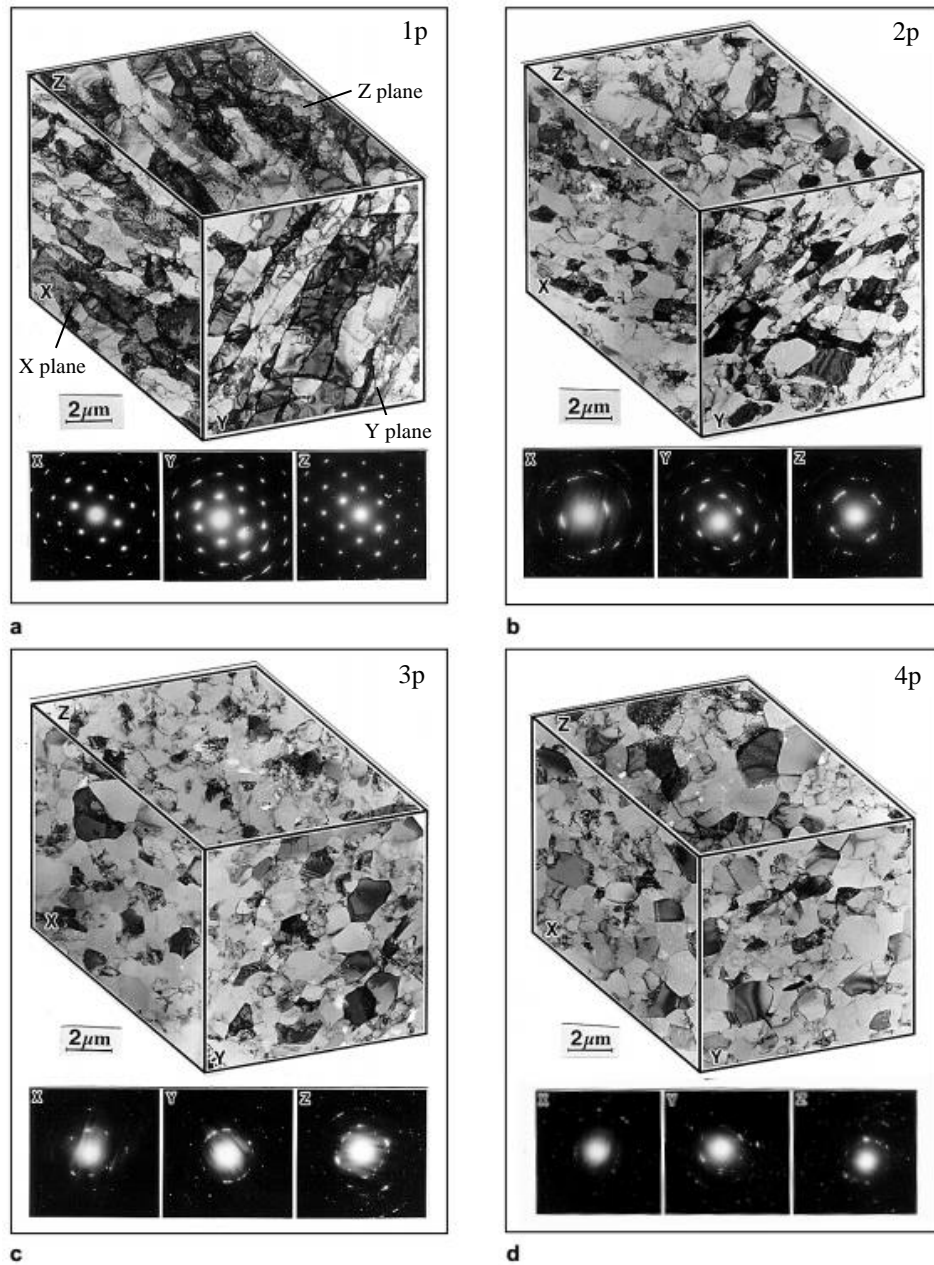


Fig. 2.11: Microstructures and SAED patterns obtained in the X, Y and Z plane in pure aluminium samples after ECAP using 90° die following route Bc, for a total of (a) one, (b) two, (c) three and (d) four passes [74].

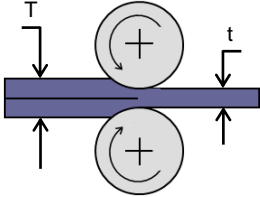
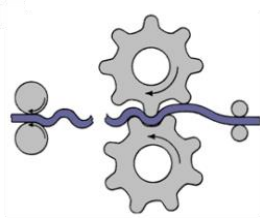
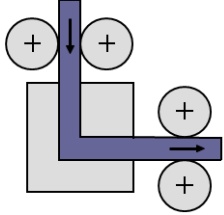
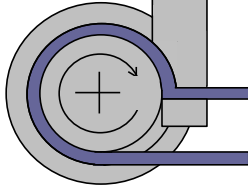
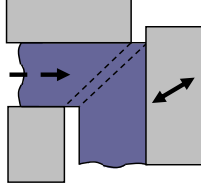
2.6 Continuous SPD methods

Despite the success of the ECAP process, it is not an ideal option from the commercialization perspective in its classical form. Its inability to process very long or continuous billets, due to very high force resulting from friction, is the main limitation. Short billets result in poor utilization of the material due to billet's ends remaining undeformed (so-called end effects).

The important requirement for commercialization of any SPD method is the reduction in processing costs, which includes reduction in the material wastage [87]. This requirement can be fulfilled by developing SPD methods capable of processing continuous billets. Therefore, lately the interest has been focusing on the continuous SPD methods capable of refining very long or continuous billets containing UFG structures.

Several techniques, listed in Table 2.2 [56], have been proposed to enable continuous processing of billets. These include: accumulative roll bonding (ARB) [88], continuous repetitive corrugation and straightening (CRCS) [60], continuous SPD (CSPD) [89], ECAP-Conform (ECAP-C) [90] and Incremental ECAP (I-ECAP) [21]. Some other techniques include: ECAP rolling (ECAR) [91], coshearing [92] and continuous frictional angular extrusion (CFAE) [93]. ECAP-based continuous processes such as CSPD, ECAP-C, ECAR and conshearing do not fundamentally change the nature of ECAP. On the other hand I-ECAP presents a different approach, and attempts to tackle the inherent problem of friction in classical batch ECAP and its continuous variants.

Table 2.2: Continuous SPD processes [56]

Process name and origin	Schematic representation	Equivalent plastic strain
Accumulative roll bonding (ARB) Saito et al. [88]		$\varepsilon = n \frac{2}{\sqrt{3}} \ln \left(\frac{T}{t} \right)$
Continuous repetitive corrugation and straightening (CRCS) Huang et al. [60]		$\varepsilon = n \frac{4}{\sqrt{3}} \ln \left(\frac{r+t}{r+0.5t} \right)$
Continuous SPD (CSPD) Srinivasan et al. [89]		$\varepsilon = n \frac{2}{\sqrt{3}} \cot \varphi$
ECAP-Conform (ECAP-C) Raab et al. [90]		$\varepsilon = n \frac{2}{\sqrt{3}} \cot \varphi$
Incremental ECAP (I-ECAP) Rosochowski and Olejnik [21]		$\varepsilon = n \frac{2}{\sqrt{3}} \cot \varphi$

2.7 Incremental ECAP (I-ECAP)

The incremental ECAP (I-ECAP) process has been developed after extensive FE simulations [94]. The schematic illustration of the process is shown in Fig. 2.12. In the incremental ECAP (I-ECAP) process, the material feeding stage is separated from the deformation stage, as opposed to conventional ECAP where the material feeding and deformation take place simultaneously. Separating the pressing and deformation stages facilitates the material flow and reduces feeding force. Developed by Rosochowski and Olejnik [21], the process is capable of processing very long or even continuous billets, a distinct advantage over the conventional ECAP. I-ECAP can be used for refining grain structures in long bars [95], plates [96] and sheets [97], which makes it an attractive option for industrial implementation.

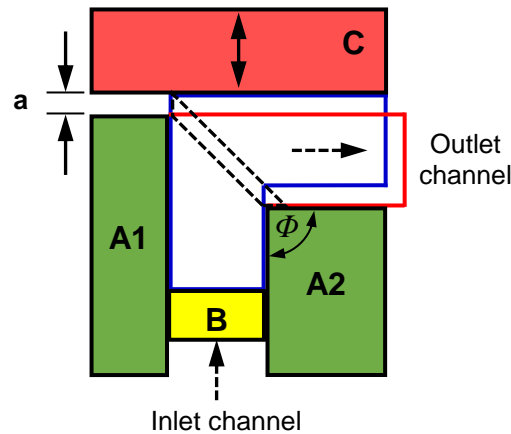


Fig. 2.12: Schematic of the I-ECAP process (A1 & A2 - die, B – feeding rod and C – punch)

There are three main tools in I-ECAP; die – A1 and A2, feeding rod – B and punch – C. During processing, the punch is oscillating with a certain frequency and therefore comes cyclically in contact with the billet top surface. In the material feeding stage, while the punch is retracting, the billet is fed into the deformation zone in increments of ‘a’ by the feeding rod, which is known as feeding stroke. In the deformation stage, the punch comes down and deforms the billet. The blue colour outline of the billet in Fig. 2.12 represents the feeding stage whereas the red colour outline represents the deformation stage with the dashed outline representing the plastically deformed zone. The mode of deformation is similar to that in ECAP, i.e. simple shear, provided the feeding stroke ‘a’ is not too large.

Studies [98, 99] have shown that the contact friction during ECAP plays a critical role with respect to homogenous deformation and good surface quality of processed billets. It is desirable to reduce the contact friction during processing to facilitate optimum processing conditions. However in classical ECAP, it is challenging to provide low friction especially along the bottom wall of the exit channel due to high contact pressure and lubricant removal during processing [98]. The load on pressing tool is mainly dependent on the material shear flow stress, die configuration, billet shape and friction. When a single lubricated billet is processed through a fixed ECAP die, contact friction is present on almost all surfaces of the billet during processing. This contact area increases with increase in billet length. Therefore, the force required to carry out ECAP process not only increases when processing higher strength materials but also increases when the billet length is increased. Consequently, in order to prevent the load on feeding rod (plunger) not to exceed beyond its yield strength, the billet length to width (c/a) ratio is normally limited to 6~10. Thereby limiting the capability of ECAP to process longer billets.

I-ECAP process eliminates this limitation by separating the feeding and deformation stages during processing. This greatly reduces the friction and allows for processing of very long or continuous billets. More information on I-ECAP is provided in the following chapters.

2.8 Titanium – background

Titanium is the ninth most abundant element in the earth's crust (about 0.6%) and the fourth most abundant structural metal after aluminium, iron and magnesium. However, despite being available in such abundance, it is seldom found in high enough concentration and rarely found in pure state. Thus the difficulty of processing it makes titanium expensive. The most important mineral sources of titanium are rutile (TiO_2), ilmenite (FeTiO_3) and leucoxene (an alteration product of ilmenite).

Titanium was first discovered in 1791, by a clergyman and amateur geologist William Gregor in Cornwall, England and named the metal 'manaccanite' [100]. Later in 1795, Martin Heinrich Klaproth, a well-known German chemist, analysed rutile (Ti ore) from Hungary and identified an oxide of an unknown element. He named the new element titanium, after the Titans in Greek mythology.

Many attempts were made by scientists to isolate titanium from its ore but it was not until in 1910 an American chemist Matthew Albert Hunter finally succeeded in isolating titanium in a laboratory. He did this by heating sodium with titanium tetrachloride (TiCl_4) in a pressure cylinder to red heat [101]. This marked the birth of the titanium industry. In 1936, Dr. William Justin Kroll, a metallurgist from Luxembourg extended Hunter's technique and invented the first viable, large scale industrial method of reducing titanium. This process involved the reduction of TiCl_4 with magnesium in an inert gas atmosphere. The resulting titanium is called "titanium sponge" because of its porous and spongy appearance. This famous Kroll process remained essentially unchanged and is the dominant process for titanium production today.

2.8.1 Titanium as a commercial material

Titanium did not become widely used until the second half of the twentieth century. Interest in the properties of titanium started mainly after the Second World War in the 1940's and early 1950's as potential use in high temperature, high strength/weight material in aerospace applications. In the USA, government initiated, large capacity titanium sponge production plants were established. Other countries like UK, France, Japan and Russia (formerly Soviet Union) also started producing titanium in large quantities around that time as well. By late 1970's Russia became the world's leader in titanium sponge production.

With the recognition of adding alloying elements in titanium for strengthening purposes, titanium alloy development progressed rapidly, from about 1950. A major breakthrough was the appearance of the Ti-6Al-4V (Ti64) alloy in the USA in 1954, becoming soon the most important $\alpha + \beta$ alloy, combining excellent properties and good producibility. Today, Ti64 is still the most widely used alloy.

Besides these successful alloy developments and the increasing usage of titanium alloys in aerospace application, there was a steady demand of commercially pure titanium (CP-Ti). Because of its excellent corrosion resistance it was (and still is) increasingly employed in non-aerospace applications.

2.8.2 General properties

Titanium is a strong, low density, nonferrous metal. It's strength is two times that of aluminium, but has approximately only 40% of the density of steel or nickel-base superalloys. It can be strengthened greatly by alloying with elements like aluminium and vanadium and by deformation processing. It is nonmagnetic and has good heat transfer properties. Its coefficient of thermal expansion is somewhat lower than that of steel and less than half of aluminium. Titanium and its alloys have a melting point in excess of 1660 °C (higher than those of steels), although most commercial alloys operate at or below 538 °C to 595 °C [2], depending on the chemical composition. Some of the other physical and mechanical properties of titanium are shown in Table 2.3.

Table 2.3: Physical and mechanical properties of elemental titanium [2]

Property	Value	Property	Value
Crystal structure		Heat of vaporization	9.83 MJ/kg
Alpha α ($\leq 882.5^\circ\text{C}$)	HCP	Thermal conductivity	11.4 W/ m · K
Beta β ($\geq 882.5^\circ\text{C}$)	BCC	Hardness	70 to 74 HRB
Colour	Dark grey	Tensile strength	240 MPa (min)
Density	4.51 g/cm ³	Young's modulus	120 GPa
Melting point	1668 \pm 10 °C	Poisson's ratio	0.361
Specific heat (25 °C)	0.5223 kJ/Kg · K	Thermal expansion coefficient	8.41 $\mu\text{m}/\text{m} \cdot \text{K}$
Heat of fusion	440 kJ/Kg		

2.8.3 Crystal structure

The physical structure of solid materials mainly depends on the arrangements of their atoms and the bonding forces between them. The atoms within solids are normally arranged in a pattern that repeats itself in three dimensions. This most basic and least volume consuming repeating structure of a solid is known as 'unit cell' and the solid itself is said to have a crystal structure, also referred to as a crystalline solid or crystalline material.

Titanium is an allotropic element i.e. it exists in more than one crystallographic form depending upon the temperature. It has got two elemental crystal structures: in the first, atoms are arranged in a close-packed hexagonal (HCP) array; in the second, the atoms are arranged in a body-centred cubic (BCC) array (Fig. 2.13(a) and (b) respectively). These two crystal structures of titanium are also commonly referred to as alpha (α) and beta (β) titanium, α being any hexagonal titanium, pure or alloyed, while β being any cubic titanium pure or alloyed.

Pure titanium, as well as majority of titanium alloys, crystallizes into α titanium at low temperatures. However, it transforms into β titanium at temperatures above 882°C. This transformation temperature from α to all β is known as the β transus temperature (lowest equilibrium temperature at which the material is 100% β) and is of critical importance in deformation processing and heat treatment. Therefore the β titanium or cubic structure is only found above β transus temperature, unless titanium is alloyed with other elements to maintain the cubic structure at lower temperatures.

The exact transformation temperature of titanium is strongly influenced by interstitial and substitutional elements and therefore depends on the purity of the metal.

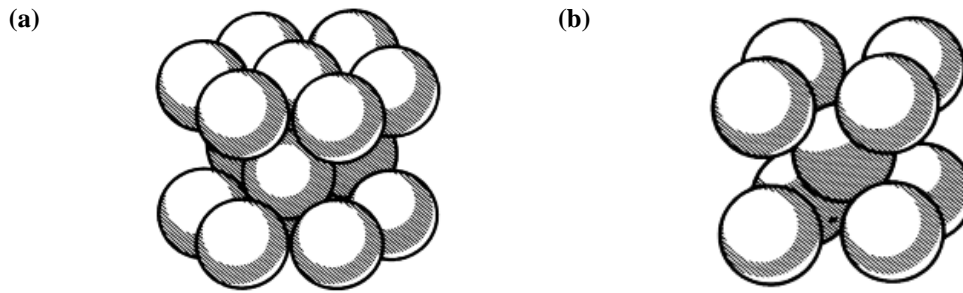


Fig. 2.13: Crystal structures of titanium at the atomic level. (a) HCP - Hexagonal close packed; (b) BCC - Body centered cubic [2].

The isolated HCP unit cell of α titanium (Fig. 2.14(a)) has an equivalent of six atoms per unit cell. Three atoms form a triangle in the middle layer. There are six $1/6$ atoms on both top and bottom corners making an equivalent of two more atoms ($2 \times 6 \times 1/6$). Finally there is one half of an atom in the centre of both the top and bottom layer, making an equivalent of one more atom. The total number of titanium atoms in HCP crystal structure unit cell thus is $3 + 2 + 1 = 6$.

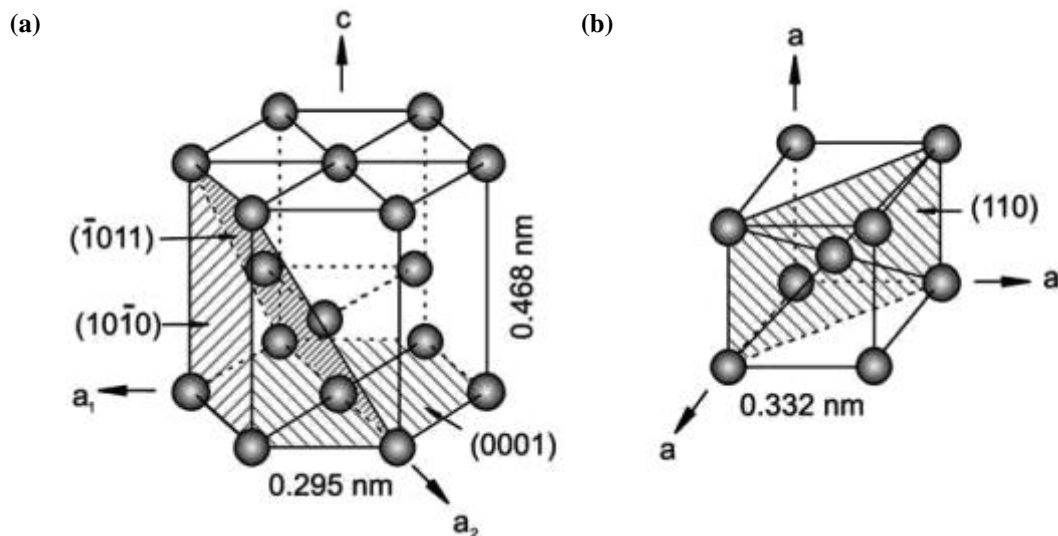


Fig. 2.14: Unit cell of (a) alpha (α) and (b) beta (β) phase.

Illustrated in Fig. 2.14(a), are values of the lattice parameters a (0.295 nm) and c (0.468 nm) at room temperature. The resulting c/a ratio for α titanium is 1.587, smaller than the ideal ratio of 1.633 for the HCP crystal structure. Also indicated in this figure are the three most densely packed types of lattice planes, (0001) plane, also

called the basal plane, one of the three $\{10\bar{1}0\}$ planes, also called prismatic planes and one of the six $\{10\bar{1}1\}$ planes, also called the pyramidal planes.

The isolated BCC unit cell of β titanium (Fig. 2.14(b)), on the other hand, has an equivalent of two atoms per unit cell. One complete atom is located at the centre of the unit cell and there are eight $1/8$ atoms at each corner of the unit cell, making an equivalent of one more atom ($8 \times 1/8$). The total number of titanium atoms in bcc crystal structure unit cell thus is $1 + 1 = 2$. Illustrated in Fig. 2.14(b), are the values of the lattice parameter a (0.332 nm) at 900 °C. Also indicated in this figure is one of the variant of the six most densely packed $\{110\}$ lattice planes.

The existence of the two different crystal structures and the corresponding allotropic transformation is of vital importance since they are the basis for the large variety of properties achieved by titanium alloys. The HCP crystal lattice in particular causes a distinctive anisotropy of mechanical behaviour for the α titanium, this has specially important consequences for the elastic properties of titanium and its alloys. The modulus of elasticity (elastic modulus, E) of pure α titanium single crystal varies between 145 GPa for a load perpendicular to basal plane (along c -axis in Fig. 2.14(a)) and 100 GPa parallel to this plane. A similar variation is observed for the modulus of rigidity (shear modulus, G). However the variations in elastic properties are less pronounced for polycrystalline α titanium with crystallographic texture. The actual variation in properties depends on the nature and density of the texture [100].

2.8.4 Commercially pure titanium (CP-Ti)

The exceptional corrosion resistance of commercially pure titanium (CP-Ti) compared to stainless steel has made it an attractive material for construction of chemical and petrochemical processing equipment [102]. It has also become popular for heat exchangers and other piping applications because of its weld-ability and good general fabricability [103]. Although CP-Ti is more expensive than stainless steel, components made from it often have lower life cycle cost because of the superior durability of CP-Ti in service [104].

CP-Ti is α titanium in structure and as discussed earlier it is based on the low temperature, hexagonal allotropic form of titanium. It is also sometimes called

“unalloyed grade” but can still contain some interstitial alloying elements like oxygen, iron, carbon or nitrogen that are soluble in hexagonal α phase.

There are four materials classified in this group, the grade designations are taken from the American Society for Testing and Materials (ASTM). They include grade 1 (99.5% Ti), grade 2 (99.3% Ti), grade 3 (99.2 Ti) and grade 4 (99.0% Ti). Table 2.4 lists these alloys together with their mechanical properties and composition ranges. Although each material contains slightly different levels of nitrogen, iron and oxygen; carbon and hydrogen are specified at <0.10 wt% and <0.015 wt%, respectively. Hydrogen content above that level will make the metal susceptible to stress corrosion cracking (SCC) and hydrogen embrittlement [105].

A brief description of each of the grades is given below.

- **Grade 1:** is the lowest strength unalloyed titanium with a slightly lower residual content. Although lower in strength, it has the highest ductility with an excellent cold formability. Common application areas include chemical processing, architecture and medical implants.
- **Grade 2:** is regarded as the “workhorse” of the CP-Ti and is the most frequently selected titanium grade in industrial service having moderate strength with excellent weld-ability and fabricability. The strength levels are very similar to those of common stainless steel and its ductility allows for good cold formability.
- **Grade 3:** possesses a slightly higher strength compared to grade 2 due to its slightly higher residual content (primarily oxygen and also nitrogen) with slightly lower ductility. Common application areas include chemical processing, marine and medical implants.
- **Grade 4:** is the highest strength grade of the CP-Ti series; high interstitial version of grade 2 and 3 with reasonable weld-ability and reduced ductility and cold formability. It mainly serves the aerospace/aircraft industry; however other application areas include heat exchangers, cryogenic and surgical equipment.

Table 2.4: ASTM CP-Ti grade classification including their mechanical properties and composition

Designation	σ_{UTS}	σ_y	δ	Residual contents, wt% (max)				
	MPa	MPa	%	N	C	H	Fe	O
Unalloyed grades								
ASTM Grade 1	240	170	24	0.03	0.08	0.015	0.20	0.18
ASTM Grade 2	340	280	20	0.03	0.08	0.015	0.30	0.25
ASTM Grade 3	450	380	18	0.05	0.08	0.015	0.30	0.35
ASTM Grade 4	550	480	15	0.05	0.08	0.015	0.50	0.40

Where σ_{UTS} = tensile strength (min), σ_y = 0.2% yield strength (min) and δ = elongation to fracture

As can be observed from Table 2.4, strength levels of CP-Ti (grade 1~4) are basically controlled by oxygen and iron content. Both of these elements improve the impact strength. Oxygen acts as an interstitial strengthener and iron offers moderate strengthening capabilities. In higher strength CP-Ti grades, oxygen and iron are intentionally added to the residual amounts already in the sponge to provide extra strength. On the other hand, carbon and nitrogen usually are held to minimum residual levels to avoid embrittlement.

2.9 Grain refinement in CP-Ti using ECAP

One of the earliest work on ECAP of titanium was published by Semiantin et al. [106]. The objective of that work was to establish the failure mode and deformation characteristics of several difficult to work alloys including CP-Ti. Because CP-Ti has low ductility among pure metals, the failure was expected to occur due to flow localizations or shear cracking due to the simple shear nature of metal flow during ECAP. Using a 90° channel die, experiments were conducted at various temperatures and processing speeds to determine at which processing conditions uniform flow will occur. For this purpose, CP-Ti grade 2 (hot rolled) square cross-section billets were subjected to first pass of ECAP between 25 and 325 °C and pressing speeds between 0.025 and 25 mm/s (effective strain rates between 0.002 to 2 s⁻¹). At room temperature (25 °C), CP-Ti billets exhibited failure, characterized by the formation of segments along the entire length for all strain rates (see Fig. 2.15(a)). However, when the

temperature was increased, a transition was observed from segmented to uniform flow. At highest tested temperature of 325 °C, uniform flow was obtained for a pressing speed of up to 2.5 mm/s (0.2 s⁻¹), above this speed segmented flow was observed (Fig. 2.15(b)). The extension of this work was presented in [107], where the same CP-Ti billets were subjected to ECAP at 325 °C using route A (no rotation) and route C (rotation by 180° between passes). The billets which were processed using route A were successfully processed up to five passes, while they failed after just two passes when route C was used.

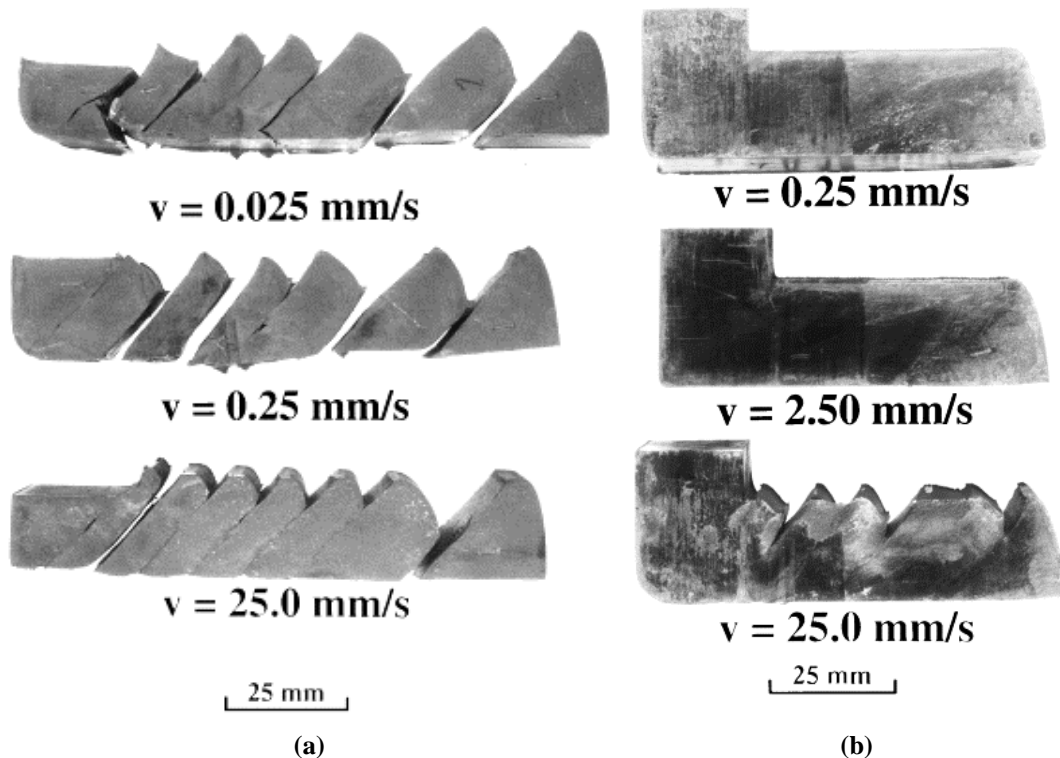


Fig. 2.15: CP-Ti grade 2 samples after first pass of ECAP at (a) 25 °C and (b) 325 °C. The pressing speeds of 0.025, 0.25 and 25 mm/s corresponding to a strain rates of 0.02, 0.2 and 2.0 s⁻¹ were used [106].

Stolyarov et al. [108] studied more ECAP routes, namely route B_C, B_A and C. Experiments were performed on CP-Ti (exact grade not mentioned) at 450 to 400 °C for up to eight passes at a pressing speed of 6 mm/s. To observe the grain morphology and microstructural anisotropy, transmission electron microscopy (TEM) was carried out on both the transverse and the longitudinal plane of the billets. Tensile tests were also carried out on the processed material at room temperature to compare the tensile properties. It was reported that the billets processed via route B_C yielded much higher

surface quality compared to route B_A and C. Moreover, it was revealed that route B_C is the most effective one in terms of grain refinement followed by route C and lastly route B_A. The latter two produced mostly elongated grains (see Fig. 2.16). However, in tensile tests, both the yield and ultimate tensile strength was higher in samples processed using route B_A. It was concluded that the main advantage of using route B_C is that it produces higher surface finish billets and the microstructures achieved are more equiaxed and homogenous than those produced by routes B_A and C.

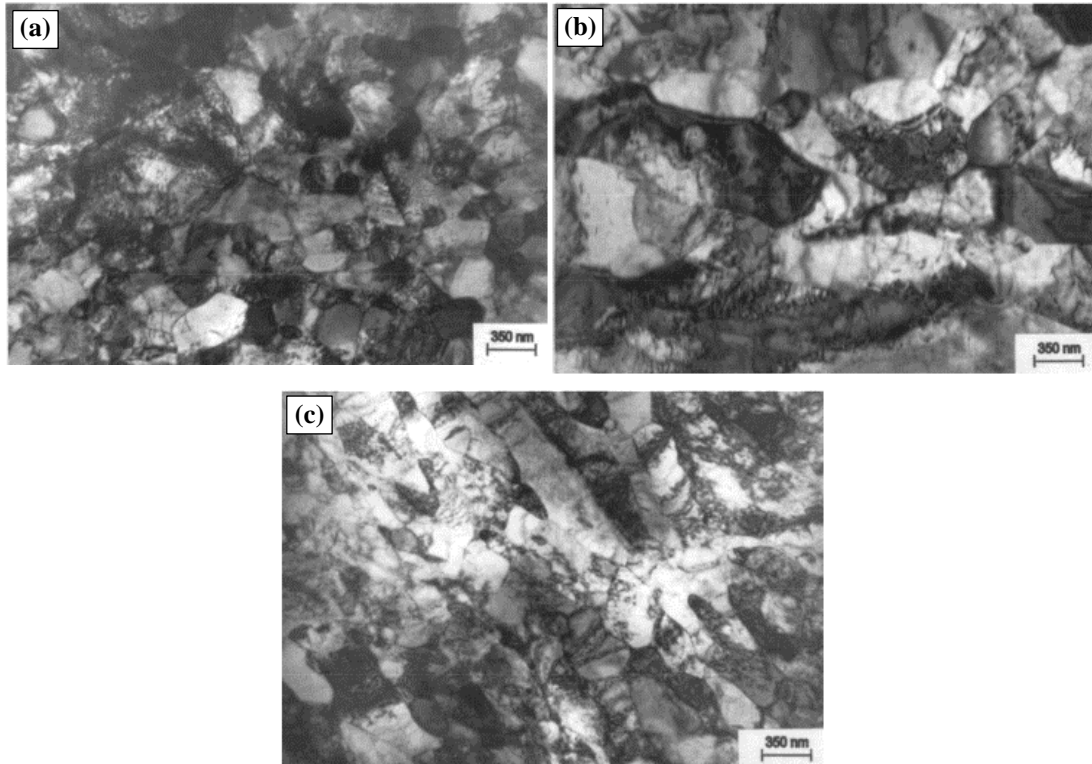


Fig. 2.16: TEM micrographs in the longitudinal (Y) plane of CP-Ti processed billets after eight pass using route (a) B_C, (b) B_A and (c) C. [108].

2.9.1 Microstructures and mechanism of grain refinement

CP-Ti has a hexagonal closed packed (HCP) structure at room temperature. Compared to face-centred cube (FCC) and body-centred cube (BCC) metals, it is regarded as ‘hard-to-deform’ because of its poor ductility. This presents significant challenges in processing this material by ECAP, as it is susceptible to cracking or segmentation during processing [106]. The inferior deformability is mainly due to the limited number of slip systems available in HCP structure. The most common slip modes are the prismatic $\{10\bar{1}0\}$, pyramidal $\{10\bar{1}1\}$ and basal $\{0001\}$ planes along

the $\langle 1120 \rangle$ slip direction [1]. The three slip planes combined with the slip vector constitute a total of four slip systems. However, five independent slip systems are required to satisfy the von-Mises criterion [109]. To accommodate plastic strain during deformation, Ti exhibits various types of twinning alongside dislocation slips [110]. Twinning therefore is an important deformation mechanism, the most observed twins are: $\{10\bar{1}1\}$ and $\{10\bar{1}2\}$ also known as compression and tensile twin, respectively [111-113]. The deformation behaviour of CP-Ti during ECAP therefore is quite complex and is expected to be different from the cubic materials as it involves both dislocation slip and twinning.

Various studies have been performed to describe the microstructure and deformation mechanism during ECAP in CP-Ti. These studies have mainly used transmission electron microscopy (TEM) for investigation. Kim et al. [114] studied the deformation mechanism of CP-Ti during ECAP at 350 °C. TEM micrograph after first pass displayed very thin elongated bands, ~80 nm in wide (Fig. 2.17). Detailed analysis of this band region revealed $\{10\bar{1}1\}$ twin characteristics features. It was concluded that $\{10\bar{1}1\}$ twinning played a critical role in plastic deformation during first pass of ECAP.

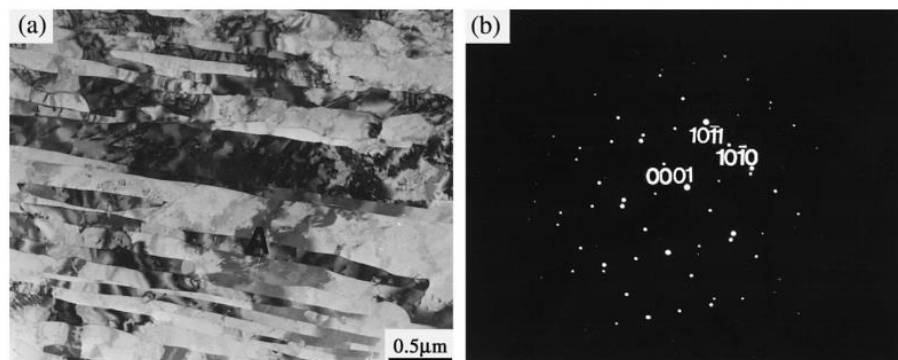


Fig. 2.17: TEM micrograph of CP-Ti after first pass of ECAP showing twins [114].

Later on, the results were also confirmed by higher resolution electron microscopy (HREM) [115]. Using the same die and processing conditions, Shin et al. [116] showed that prismatic α slip was the main deformation mechanism after second pass with route B. In a later work by Kim et al. [117], the effect of processing temperature on the microstructure was also studied. It was revealed that the deformation mechanism was strongly dependant on processing temperature. For

example, processing done at 200 °C resulted in thin parallel bands where slip was the dominant mechanism, in contrast to processing at 350 °C where $\{10\bar{1}1\}$ twinning was found to be more dominant. Moreover, pressing at 600 °C showed some evidence of dynamic recovery and recrystallization alongside twinning. It is important to highlight that the CP-Ti impurity levels mentioned in the work is quite low, which might have enabled processing, using $\Phi = 90^\circ$ at the lowest processing temperature of 200 °C in [117]. Although there is no mention in their work about getting defect free billets without cracks in the work.

Some recent works have utilized electron backscatter diffraction (EBSD) techniques to investigate the microstructure in CP-Ti during ECAP. Chen et al. [118, 119] carried out ECAP on CP-Ti at 450 °C using $\Phi = 90^\circ$ die angle. Investigations were performed using a combination of TEM and EBSD on the 3/4th pass sample. Results showed a weak presence of $\{10\bar{1}2\}$ twin type during the fourth pass, however the overall fraction of twins was very low. It was concluded that continuous dynamic recrystallization (CDRX) was the pre-dominant mechanism of grain refinement. In another study by Chen et al. [120], CP-Ti was processed at 450 °C up to eight passes. Mainly compressive twins $\{10\bar{1}1\}$ with a small fraction of tensile twins $\{10\bar{1}2\}$, were found to be active during the first pass. After pass two, CDRX played a dominant role in grain refinement. And finally more recently, Meredith et al. [121] deformed CP-Ti grade 1 at 275 °C for up to four passes. It was concluded that $\{10\bar{1}1\}$ twinning was active alongside CDRX during the first pass. However, beyond pass two, slip was the dominant deformation mechanism.

2.9.2 Mechanical properties

In one of the early studies in 2001 by Zhernakov et al. [122], the as received CP-Ti (grade not mentioned), which had a yield strength of 400 MPa, ultimate strength of 460 MPa and ductility to failure of 27% was processed using route B_C and C. After ECAP using route B_C the same properties were 800, 816 and 16%. With route C the properties were 732, 772 and 14%.

Several investigations have been performed to refine the grain structure of CP-Ti grade 1 to 4, with the objective of improving the strength characteristics [123-128]. It was established from the review that after multiple passes of ECAP using different die angles (Φ), pressing speeds and temperature conditions, the grain size refinement achieved was in the region of 0.20 to 0.70 μm , with the increase in yield and tensile strength between 1.2 to 2.0 times of the original strength. In order to achieve even higher grain refinement, some additional deformation had also been applied to the billets after ECAP processing.

Zhao et al. [129, 130] have made successful attempts to process titanium at room temperature to suppress grain growth occurring at higher processing temperature, however, these attempts were limited to grade 1 which is considered to be the softest and having the highest formability among commercially available grades of titanium. Using die angles (Φ) of 120° (with eight passes) and 90° (with four passes), it was reported that the grain size reduction achieved at room temperature was between 0.15 to 0.20 μm and the increase in ultimate tensile strength was between 765 to 790 MPa.

Moreover, grain refinement in CP-Ti also improves other properties such as fatigue strength [11, 131] compared to the coarse grain counterparts.

2.9.3 Post ECAP deformation

A number of studies on ECAP of titanium have applied some form of post ECAP deformation. The objective was to further refine the microstructure and to improve mechanical properties. The first attempt, according to author's knowledge, was performed by Stolyarov et al. [69] in 1999, who combined ECAP and HPT. CP-Ti (grade not mentioned) in the form of rod was ECAP processed for seven passes in the temperature range of 500~450 °C following route B_C using a 90° channel intersection die. Disk shaped samples were HPT processed under 1.5 GPa at room temperature or 450 °C, with three rotations. Following TEM analysis in the transverse plane on the ECAP processed samples, the grain size was estimated as 300 nm and was found to be uniform at sample edge and centre. However, since in HPT processing, the strain across the sample disk is not uniform, the TEM micrographs showed that the grain size was refined to 200 nm at the edges whereas in the centre it remained at 300 nm similar to after ECAP. The mechanical properties including yield strength (σ_y), ultimate tensile strength (σ_u), elongation (δ) and hardness (H_v) values reported in the work are shown in Fig. 2.18. As can be seen, the properties were increased due to HPT deformation following ECAP.

Processing State	H_v (MPa)	σ_u (MPa)	σ_y (MPa)	δ (%)	H_v/σ_y	H_v/σ_u
Hot-rolled rod	1800	480	440	24	4.09	3.75
ECAP (500–450°C)	2350	540	520	16	4.52	4.35
ECAP (500–450°C) +HPT (450°C)	2700	640	530	30	5.09	4.22
ECAP (500–450°C) +HPT (20°C)	3120	730	625	25	4.99	4.27

H_v is the microhardness. σ_u is the ultimate strength and σ_y is the yielding strength obtained from tensile test.

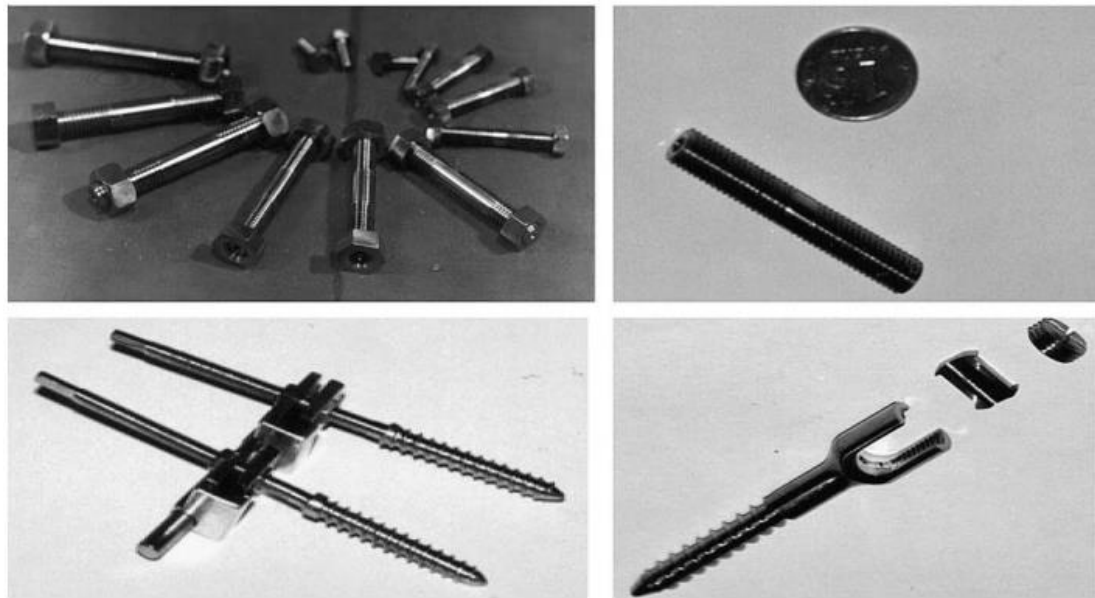
Fig. 2.18: Mechanical properties of CP-Ti after different processing stages reported in [69]

Since HPT can only produce very small disc shaped sample which are not suitable for practical applications, Stolyarov and co-workers in [132] applied cold extrusion following warm ECAP processing of CP-Ti. The ECAP increased the yield strength to 640 MPa while the second step, cold extrusion introduced higher dislocations density and increased the strength to 970 MPa. It was also reported that the microstructure was stable upto 300 °C. Similarly in [133, 134] post ECAP deformation steps such as cold rolling and cold extrusion on CP-Ti were performed.

This yielded significant increase in grain size refinement level through the introduction of more dislocations; this subsequently increased the strength characteristics even further. It was reported in [135], that after warm ECAP processing of CP-Ti (grade 2) and additional cold rolling the increase in yield and tensile strength exceed that displayed by conventional Ti-6Al-4V alloy. However, these post deformation steps change the sample dimensions significantly and therefore reduce the freedom and flexibility of processing provided by billets produced directly by ECAP. On the other hand it is expected that some post ECAP change of billets' shapes and dimensions might be inevitable when producing preforms for further manufacturing operations.

2.10 Application of UFG titanium in bio-medical implants

Pure titanium (CP-Ti) has excellent bio-compatibility and therefore is an ideal choice for use in bio-medical implants. However, its usage is restricted due to limited strength, therefore Ti-6Al-4V and other titanium alloys are used in load bearing implants. As discussed in Chapter 1, alloying elements in titanium alloys such as aluminium and vanadium can be toxic in the long run. If CP-Ti is to replace the currently used alloys in medical implants, its strength must be improved. Improving the strength characteristics using SPD methods in particular ECAP, has generated a lot of interest [12, 15, 38, 87, 119, 125, 136-138]. It is also worth mentioning that grain refinement in CP-Ti improves the corrosion resistance, which is a desirable property for implant materials [9, 10]. Examples of some UFG / nano structured titanium implants taken from the literature are shown in Fig. 2.19.



(a)



(b)



(c)

Fig. 2.19: Examples of some titanium implants: (a) screw implants made of nano-structured titanium [138], (b) plate implants for bone osteosynthesis made of nano-structured titanium [38] and (c) normal and reduced diameter dental implant made with strengthened CP-Ti after grain refinement [87].

2.11 Summary

The chapter introduces the topic of grain refinement in metals. The two synthesis approaches for achieving ultrafine grain (UFG) structure i.e. bottom-up and top-down approaches were presented. Severe plastic deformation (SPD), a top-down approach, was discussed in detail as a method of introducing extreme grain refinement in metals by inducing large plastic strain. The working principle of equal channel angular pressing (ECAP) was presented and its fundamental parameters such as: strain induced in each pass, processing routes, slips systems and shearing patterns in different routes and a simplified model of grain refinement mechanism. It was discussed that despite the success of ECAP in grain refinement in metals, the classical ECAP method is not suitable for processing of long or continuous billets. The grain refinement method used in the present study, the incremental ECAP (I-ECAP) was presented and its advantages as a continuous SPD method was discussed.

Since the present work focuses on processing of titanium, some details including general background on titanium, its crystal structure and the various available commercial grades of pure titanium (CP-Ti) were presented. A brief review on the current state of the art in the grain refinement research work on CP-Ti using ECAP was also presented.

As discussed, CP-Ti has superior biocompatibility but it lacks the strength required for most load bearing implants. Currently Ti-6Al-4V is widely used in medical device applications such as in total replacement implants, where higher strength characteristics is generally a requirement. However, research has suggested that alloying elements such as aluminium and vanadium present in the alloy can be toxic in the long term and are therefore undesirable for full bio-integration. If CP-Ti is to replace Ti-6Al-4V in medical application, its strength characteristics has to be improved without adding alloying elements. The mechanical strength and performance of CP-Ti can be greatly improved by grain refinement. The existing research has already shown that achieving ultrafine grain (UFG) structure in CP-Ti can significantly improve its strength characteristics. However, majority of the work has utilized classical ECAP which suffers from low productivity and is not a practical option for industrialisation. For commercial availability of UFG CP-Ti, there exists a need to

refine its grain structure and thereby improve the strength characteristics by using a industrially viable method such as I-ECAP.

I-ECAP is a promising SPD technique capable of processing continuous billets containing UFG structure. Due to the incremental nature of the process which separates the material feeding and the deformation stages, it effectively reduces friction considerably. Separation of feeding and deformation stages, essentially allows processing of very long or continuous billets. So far I-ECAP technique has not been studied in detail for CP-Ti. The present research work is aimed to demonstrate I-ECAP as an viable method for industrialisation and to exhibit its effectiveness in processing CP-Ti grade 2 billets.

Chapter 3

FE modelling of I-ECAP process and design of tooling

3.1 Introduction

Creating the tooling for any SPD process which can impart large plastic strain to material is a challenging and technically formidable task [17]. It requires a considerable investment in tool design, which on one hand should be durable enough to sustain repetitive high loads and on the other hand should not cause damage to the material. It is therefore crucial to optimize the tooling and select appropriate processing conditions during any SPD process by investigating their effects on the deformation behaviour of the material. In particular during ECAP several factors such as: die geometry, material properties and processing conditions greatly influence the shear deformation behaviour during processing. These factors in turn govern the microstructure and mechanical properties of the processed materials.

Although analytical techniques [71, 73] based on slip line and upper bound theories can predict an idealized plastic strain during ECAP processing, these techniques do not offer flexibility to account for realistic conditions such as friction, strain hardening behaviour of material and processing speed. These conditions often give rise to complex non-homogenous plastic strain distribution within the billet [139]. Numerical modelling based on finite element (FE) analysis can easily take into account these factors and therefore it is considered the most appropriate technique to analyse the deformation behaviour of processed materials during ECAP.

Prangnell et al. [140] in 1997 was the first to carry out FE analysis of the ECAP process. Using compression test data from an aluminium alloy (Al-0.15%Mn), two dimensional plain strain analysis was performed to simulate the shear deformation during first pass of an ECAP process. The effect of die angles ($\Phi = 90$ and 100°) and friction on the effective plastic strain distribution in the billets was studied. Their results show that the inhomogeneous deformation at the billet ends increases with

friction and a sharper die angle. Moreover, in the case of 90° die angle, simulations predicted the development of a dead zone in the die corner.

Since then, several studies have employed FE analysis to investigate the deformation behaviour of the billet during ECAP and to design the appropriate tooling. FE has been applied to study factors that affect the deformation, including (i) die geometry (Φ , Ψ) [139, 141-146], (ii) material behaviour (strain hardening, softening and strain rate sensitivity) [139, 143, 147, 148], (iii) processing conditions (friction, speed, backpressure and thermal conditions) [141, 143, 149-155] and (iv) multiple turns [80, 156-158]. The primary concerns in these investigations were the conditions that can give rise to incomplete die fillings and also the plastic strain inhomogeneity in the billets after processing [159].

However to date, little work has been published to the effects that cause billets to bend during and after processing, occurrence of which is generally observed in strain rate sensitive materials [160]. Moreover, existing work only considers hypothetical elasto-plastic material models [139, 161, 162]. This bending in billets creates significant problems in the subsequent pass i.e. when re-inserting billet in the inlet channel for the next pass. Therefore, secondary operations such as: machining and/or straightening are carried out to resolve the problem which requires additional resources and time.

This chapter has two parts, first parts, presents a systematic FE study to evaluate the deformation behaviour of CP-Ti grade 2 during the I-ECAP process. The effects of outlet channel length and friction on the bending behaviour of billet and resulting plastic strain distribution is investigated. Objective is to optimize the I-ECAP tooling geometry in order to minimize or eliminate billet bending and to process billets with long steady state section wherein the strain distribution is uniform along the extrusion direction. The second part of this chapter is concerned with the I-ECAP die design based on the FE optimized tooling geometry.

3.2 Finite element modelling

In the present study, commercial FEM code Abaqus/Explicit v6.13-2 was employed to carry out 2D plain strain simulation for the first pass of an I-ECAP process using CP Ti grade 02 material. The system of units used during the simulation was mm, N and sec. The FE model of I-ECAP process is represented in Fig. 3.1(a), which represents the schematic (see Fig. 2.12) of the I-ECAP process. It shows the initial position of the billet with respect to the two die elements (A1 and A2), feeding rod (B) and punch (C).

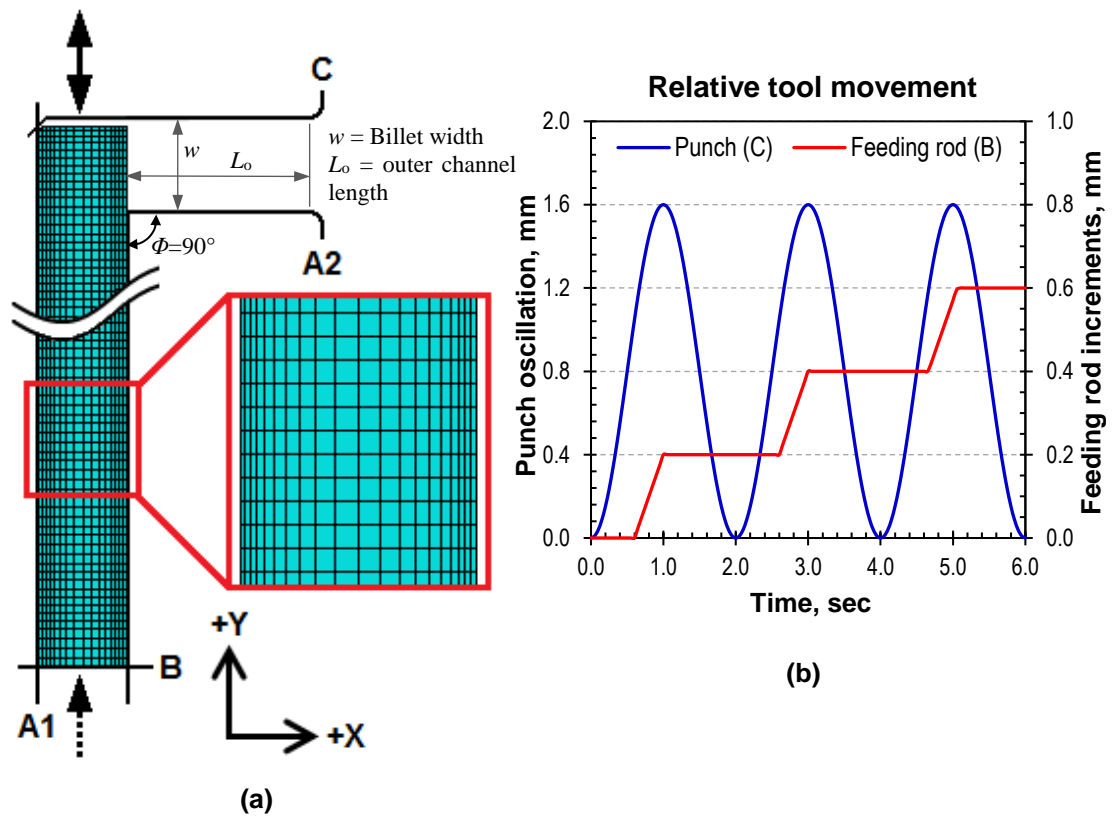


Fig. 3.1: (a) FE model showing the initial tool and billet configuration (see Fig. 2.12 for the schematic diagram) and (b) relative movement of punch and feeding rod during the first three cycles of I-ECAP.

The billet width denoted by w , is 10 mm and the billet length (L_b) is $8.0w$. The length of the inlet channel was L_b plus $0.5w$ to accommodate the billet, while the outlet channel length (L_o) was varied to study its effect on billet deformation. A small chamfer of $0.1w$ was created at the top left corner of the billet head in order to facilitate the material flow and to permit smooth convergence during the start of simulation. The angle of intersection (Φ) between the inlet and outlet channel was 90° ; and the inner

corner die radius was $0.05w$. The inlet channel had a constant width of w (same as billet), whereas the width of the outlet channel varied during cycles because of punch oscillation. However, at the end of each deformation cycle, the width of the outlet channel was equal to inlet channel; this was accomplished by adjusting the mean position of the punch oscillation.

For the billet, CPE4R element type was selected from Abaqus element library. This is a plain strain 2D four noded reduced integration element, with controls to minimize hour glass effects. For the sake of simplicity and to minimize the computation time, all tools were assumed to be analytical rigid parts i.e. non-deformable and were made with line elements. The die elements A1 & A2 were fixed by applying constrains in all degrees of freedom, however the feeding rod (B) and punch (C) were allowed to translate along the Y-direction. The feeding rod incremental motion was defined using the tabular data input, whereas the punch oscillatory motion was defined as a Fourier series (Eq. 3.1) using a periodic function in Abaqus.

$$a = A_0 + \sum_{n=1}^N [A_n \cos n\omega(t - t_0) + B_n \sin n\omega(t - t_0)] \quad \text{Eq. 3.1}$$

where A_0 is the initial amplitude, t_0 is the initial time, t is the current time, $n\omega$ is the circular frequency (radian per second); A and B are the coefficients of cosine and sine terms respectively. The representative boundary conditions for the punch and feeding rod for the first three cycles of the simulation are shown in Fig. 3.1(b). Here the punch frequency is $f = 0.5$ Hz, peak to peak amplitude of oscillation is 1.6 mm and the feeding stroke is 0.2 mm/cycle (0.10 mm/s). This equates to $A_0 = 0$, $A = 0$, $B = 0.8$ mm, $n\omega = 2\pi f = 3.14$ radians/s and $t_0 = 0$ being used with Eq. 3.1 which becomes $a = \sin(2\pi ft)$

To improve the formability of titanium and other such hard to deform materials, ECAP processing is normally carried out at elevated temperature. For CP-Ti grade 2, a processing temperature of 300 °C is considered appropriate to avoid failure or segmentation in the processed billets [106, 107]. The material flow stress data in the present study was determined through compression testing using cylindrical samples following the ASTM E209 standard [163]. The tests were conducted at 300 °C and at three different strain rates of 0.01, 0.1, 1.0 s⁻¹ to account for strain rate sensitivity of the material. Fig. 3.2 shows the true stress and true strain curves obtained from the

testing. It is clear that material is strain rate sensitive, as the flow stress increases with increase in strain rate. The flow stress also exhibits the typical three stage hardening behaviour in titanium under compression [113]. The flow stress data was inputted in Abaqus as a look up table. The default elastic plastic von-Mises material model with isotropic hardening was used. The Young Modulus was defined as 95 GPa and poisson ratio as 0.32 [164].

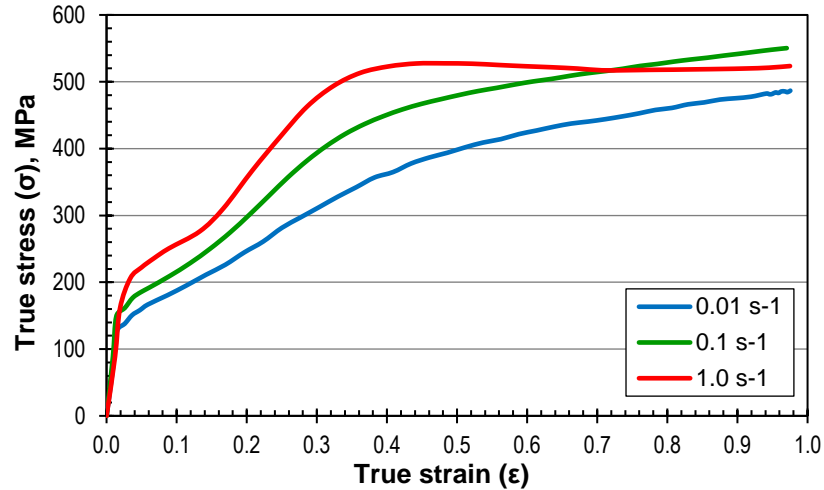


Fig. 3.2: True stress-strain curves (flow stress data) of CP-Ti (grade 2) obtained from uniaxial compression at 300 °C and at strain rates of 0.01, 0.1 and 1.0 s⁻¹.

Contact interaction between tool-billet interfaces was defined using the Coulomb friction law for which the co-efficient of friction (μ) was taken as 0.10, this represented graphite based lubrication condition. However, interaction at tool-tool interface was ignored. Heat generated due to friction and plastic work (adiabatic heating) was also ignored during the present work. The simulations were performed on a Dell workstation computer with 96 GB of RAM and with two hexa-core Intel Xeon processors (clock speed of 3.46 GHz). All simulation was performed using double precision to minimize the truncation error during calculations. It took approximately 1 hour and 45 minutes to solve the model.

Before running the simulations, a convergence test was carried out to assess the sensitivity of the results to mesh density. For this purpose, different models were created with 10, 20 and 40 elements along the billet width (w), as shown in Fig. 3.3 (a), (b) and (c) respectively. This corresponded to a total of 610, 1240 and 4840 elements within the billet, respectively. A model was also created with adaptive re-meshing using the arbitrary Lagrangian-Eulerian (ALE) method with 20 elements

along the billet width (w) as shown in Fig. 3.3 (d). Fig. 3.4 shows the equivalent plastic strain distribution after first pass of I-ECAP along the billet width (A - top to B - bottom) for all the cases. Although the coarse meshed model shows deviation from the medium and the fine meshed model, the trend is similar. In comparison, the ALE model significantly over predicts and under predicts the strains near the top and bottom of the billet width, respectively. However, it can be seen that there is no significant difference between the medium and the fine mesh model. Therefore, the medium meshed model with no re-meshing technique was selected for all remaining simulations.

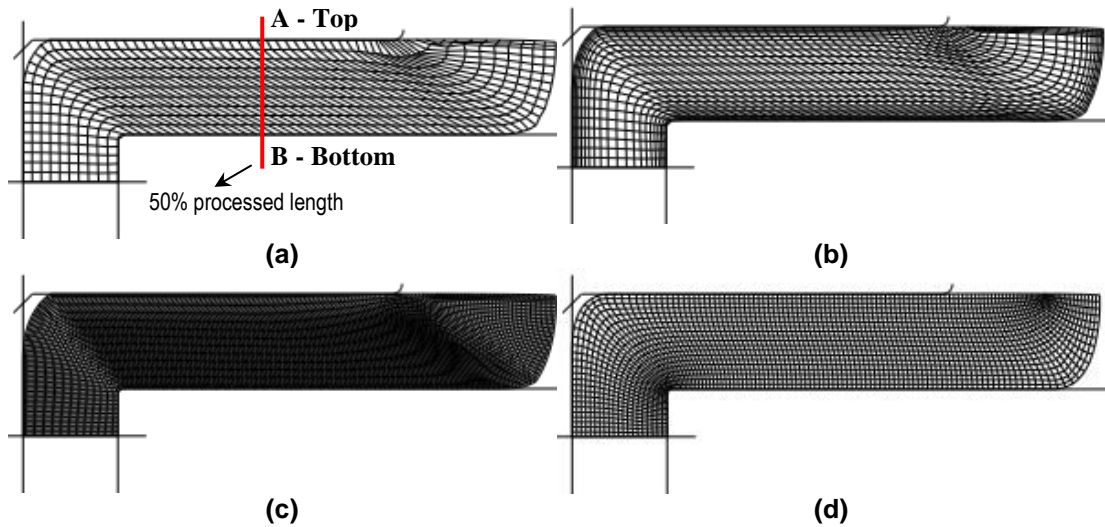


Fig. 3.3: Deformed mesh (a) coarse mesh, (b) medium mesh, (c) fine mesh and (d) ALE mesh.

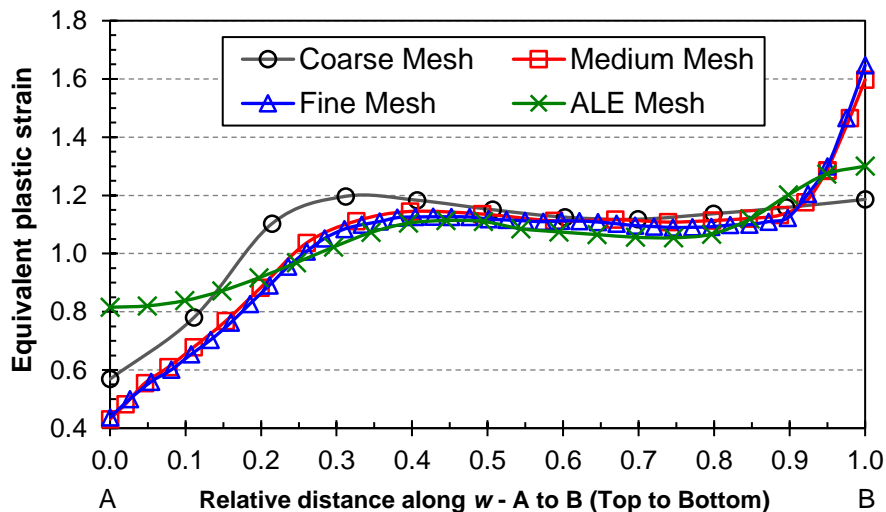


Fig. 3.4: Equivalent plastic strain distribution along the width of the billet for four different FE meshed model.

3.3 Results and discussion

In order to obtain detailed information about the deformation behaviour of CP-Ti during I-ECAP process, the influence of the outlet channel length (L_o), billet length (L_b) and friction is investigated in a systematic manner.

3.3.1 Influence of channel length on bending behaviour

The effect of L_o on the billet deformation during I-ECAP was investigated. For this purpose, different L_o lengths measuring $0.5w$, $1.0w$, $2.0w$, $3.0w$ and $4.0w$ were simulated with a constant $L_b = 8w$ and $\mu = 0.1$. Fig. 3.5 (a-e) shows the distribution of equivalent plastic strain in the billet corresponding to different L_o at 95% processed state. It is fairly obvious from the plots, that smaller L_o of $0.5w$ and $1.0w$ generates significant bending in the billets. This bending is measured as a vertical distance as shown in Fig. 3.5 (a). This non desirable bending is however greatly reduced for $L_o = 2.0w$ and above. Fig. 3.6 shows the measured amount of bending for each case.

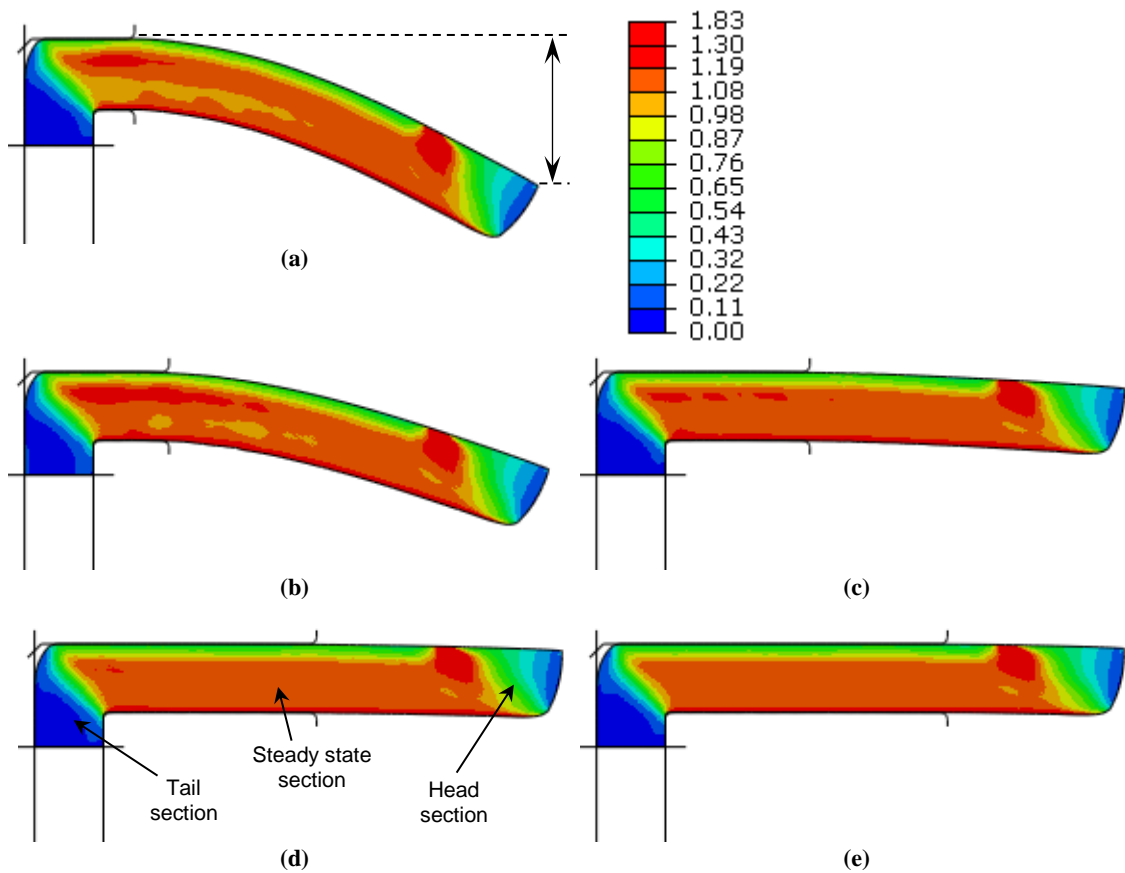


Fig. 3.5: Equivalent plastic strain distribution for channel length $L_o =$ (a) $0.5w$, (b) $1.0w$, (c) $2.0w$, (d) $3.0w$ and (e) $4.0w$

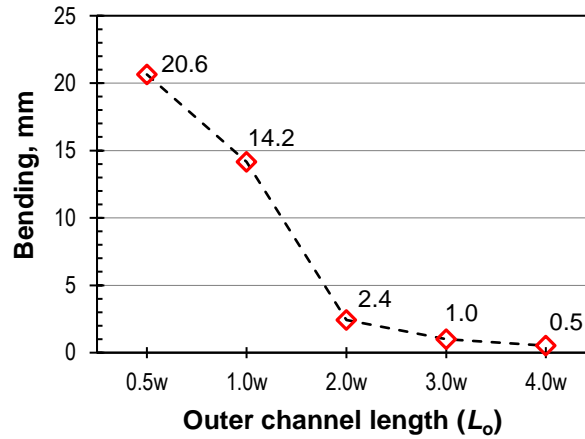


Fig. 3.6: Effect of varying the outer channel length (L_o) on bending

3.3.2 Strain distribution

For all the cases (Fig. 3.5 (a-e)), along the billet length from left to right there are three distinct strain gradient sections: tail, steady state and head. The equivalent plastic strain distribution measured at the centre of the billet width along the entire length is plotted for different L_o in Fig. 3.7(a). It can be seen that the length of the non-uniformly deformed tail section is not influenced by the different L_o , as it looks similar for all the cases. The length of the head section is also not significantly influenced by the different L_o and roughly measures $1.4w$ for all cases. Between the non-uniformly deformed head and the tail section, lies a steady state section. The plastic strain is uniformly distributed along the extrusion direction in this steady state section.

However, for all cases, the plastic strain distribution when measured along the normal direction (i.e. from top surface to bottom surface) within this steady state section is non-uniform. The plot of equivalent plastic strain distribution as a function of billet width (w) from top surface to bottom surface (A to B in Fig. 3.3 (a)) is shown in Fig. 3.7 (b). The plot can be divided into three regions; top, middle and bottom. The equivalent plastic strain in the top part has lower values. This is because, at the intersection of two channels, the billet does not completely fill the die resulting in a corner gap. The formation of this corner gap causes, little or no intense shearing near the top of the billet. This corner gap is however not changed significantly for different L_o as can be seen in Fig. 3.5 (a-e). The plastic strain within the middle region is more

or less uniform and does not change much for all cases. In the bottom 10% of the billet width, higher values of equivalent plastic strain can be observed.

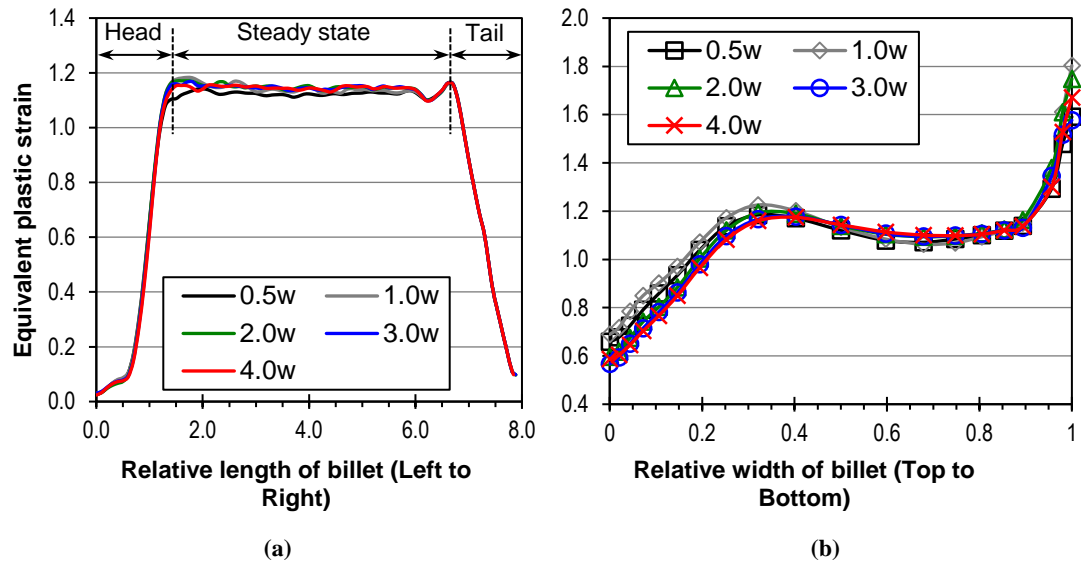


Fig. 3.7: Equivalent plastic strain distribution along (a) extrusion direction (left to right) and (b) width direction (top to bottom).

3.3.3 Effect of friction

Until now, the effect of outlet channel length (L_o) on the deformation behaviour during first pass of the I-ECAP process under a fixed friction co-efficient of $\mu = 0.10$ have been discussed. In order to investigate the effect of friction during I-ECAP, a lower value of $\mu = 0.05$ and a higher value $\mu = 0.20$ is also simulated with $L_b = 8w$ and with L_o varying from 0.5 to $4.0w$. In order to quantify the strain inhomogeneity within the billet resulting from varying friction condition, a statistical analysis parameter known as coefficient of conformance ($CV\bar{\epsilon}_p$) [165] is used. It is defined as:

$$CV\bar{\epsilon}_p = \frac{\text{Stdev } \bar{\epsilon}_p}{\text{Avg } \bar{\epsilon}_p} = \frac{\sqrt{\frac{\sum(\bar{\epsilon}_p^i - \text{Avg } \bar{\epsilon}_p)^2}{N}}}{\text{Avg } \bar{\epsilon}_p} \quad \text{Eq. 3.2}$$

where $\bar{\epsilon}_p^i$ is the plastic strain magnitude in the i th element and N is the number of elements measured. The elements in the head and the tail region were excluded in the measurements. Higher values of $CV\bar{\epsilon}_p$ means greater inhomogeneity.

Fig. 3.8 (a) and (b) shows the effects of the different friction coefficients on the billet bending and the $CV\bar{\epsilon}_p$ respectively. In the case of billet bending, increasing friction reduces the bending for all friction coefficients simulated, however the effects are negligible when L_o is increased to $2.0w$ and above. Strain inhomogeneity, $CV\bar{\epsilon}_p$, on the other hand is not influenced when μ is increased from 0.05 to 0.10 . However, the strain inhomogeneity is increased to more than twice when μ is increased to 0.20 , as seen by the bar levels in Fig. 3.8(b).

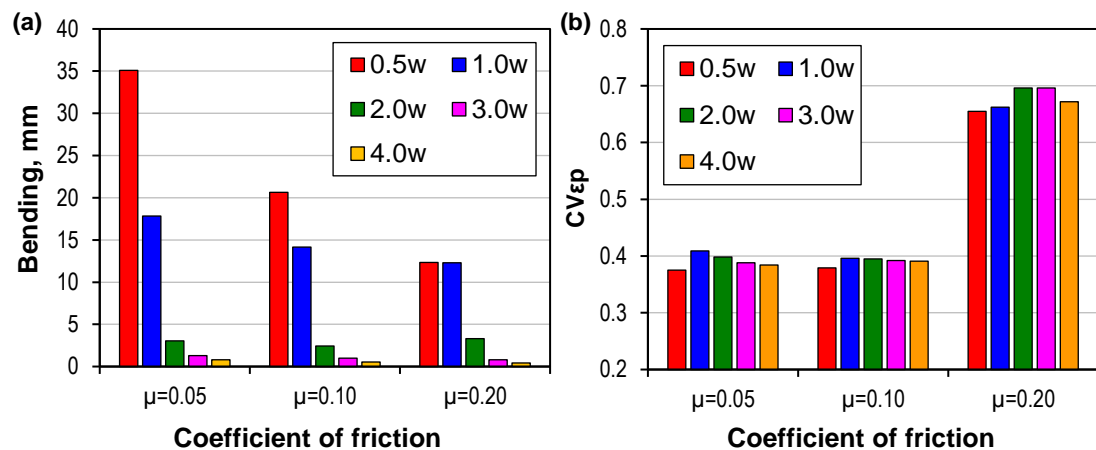


Fig. 3.8: Effect of friction on (a) billet bending and (b) strain inhomogeneity ($CV\bar{\epsilon}_p$).

3.4 Optimization of I-ECAP geometry

Unlike in the classical ECAP process, where the tooling is composed of a solid single die and therefore the outer channel length has a fixed length, the I-ECAP tooling is made up of two tools, a static die and an oscillating punch. This allows the I-ECAP process to have different die and punch length, referred to as L_d and L_p respectively in the following discussion. The effect of varying L_d on the billet bending was investigated by considering a worst case scenario of minimum punch length. Fig. 3.9 (a-e) shows the effect of varying L_d from $0.5w$ to $10.0w$ while maintaining L_p of $0.5w$. It is fairly evident that by increasing the L_d reduces billet bending at the same time it increases the steady state section length even though in all cases a minimum punch length was used. The die length (L_d) seems to have a much bigger effect in minimizing the billet bending.

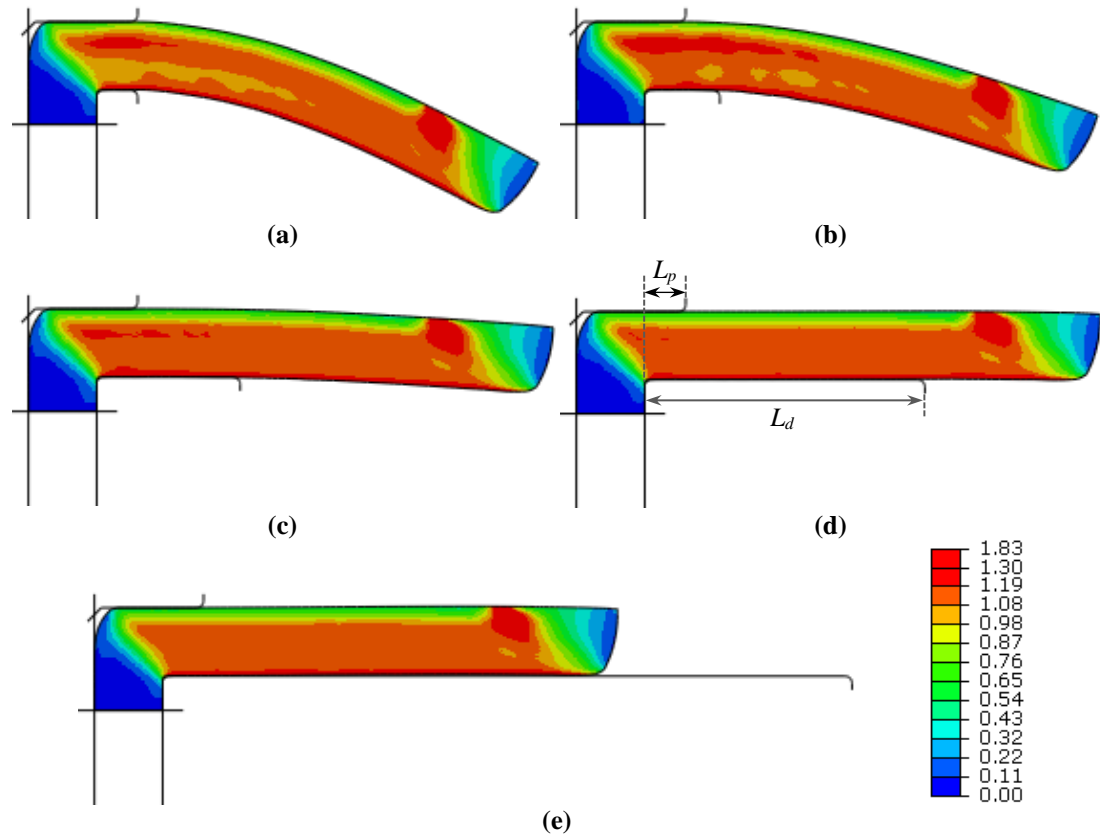


Fig. 3.9: Equivalent plastic strain distribution for a constant punch length $L_p = 0.5w$ and varying die length $L_d =$ (a) $0.5w$, (b) $1.0w$, (c) $2.0w$, (d) $4.0w$ and (e) $10.0w$.

For practical purposes however, punch length of $L_p = 0.5w$ would be too small, and as such the punch surface would experience a pressure of up to 560 MPa

(according to loads predicted by FE). Although this is still well below the compressive yield strength of the tool material used, it is desirable to minimize this pressure. Therefore longer punch lengths are considered. Fig. 3.10 (a-d) shows the effect of varying L_p from $2.0w$ to $4.0w$ while keeping L_d constant at $10.0w$. It can be seen that the plastic strain distribution and the deformation behaviour is similar in all three cases.

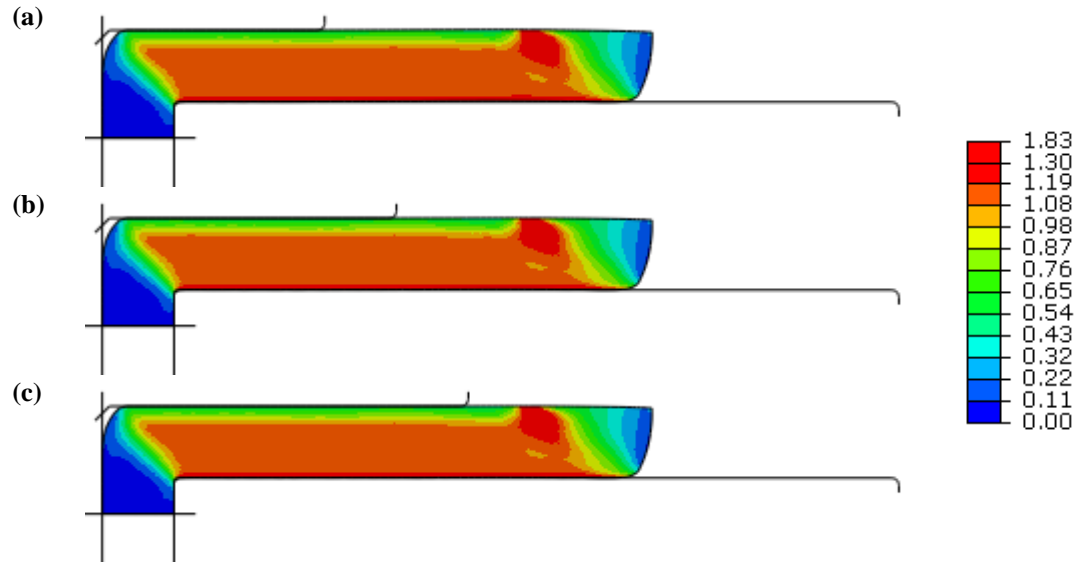


Fig. 3.10: Equivalent plastic strain distribution for a constant die length $L_d = 10.0w$ and varying punch length $L_p =$ (a) $2.0w$, (b) $3.0w$ and (c) $4.0w$.

Furthermore, the effect of processing longer billets was also studied. Fig. 3.11 (a) and (b) shows the plastic strain distribution for $L_p=2.0w$, $L_d=10.0w$ with $L_b = 10.0w$ and $12.0w$ respectively. As can be seen, the simulation results predict that a punch length (L_p) of $2.0w$ and a die length (L_d) of $10.0w$ are optimal values for tool design in order to minimize billet bending and to achieve a longer uniform plastic strain distribution region during I-ECAP processing.

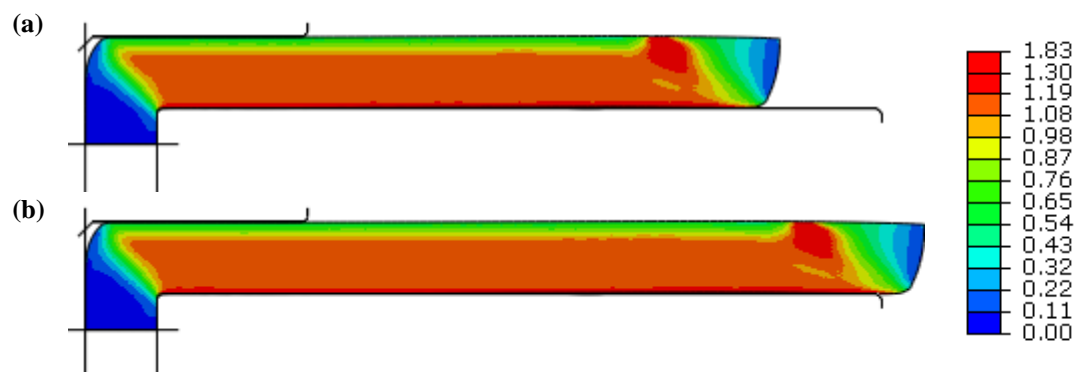


Fig. 3.11: Equivalent plastic strain distribution for a die length $L_d = 10.0w$ and punch length $L_p=2.0w$ with varying billet length $L_b =$ (a) $10.0w$ and (b) $12.0w$.

3.5 Double billet variant of I-ECAP process

Although FE analysis was performed for the first pass and assuming plain strain conditions, the results were promising enough to design and manufacture the I-ECAP die using the optimized tooling geometry. The double-billet variant [95] of the I-ECAP process was used in the present study. The working principle is similar to the single billet I-ECAP as explained in section 2.7, except only two billets are simultaneously processed. To investigate the effect of channel angle on the processed material, two separate I-ECAP dies with channel angle (Φ) of 120° and 90° were designed and manufactured. The schematic illustration of the two I-ECAP designs is shown in Fig. 3.12. As the name suggests, the advantage of using the double billet variant over the conventional ECAP procedure (other than capability to process longer billets) is that, it can process two billets simultaneously and therefore has twice the productivity. Also, due to symmetry, any lateral forces should cancel each other.

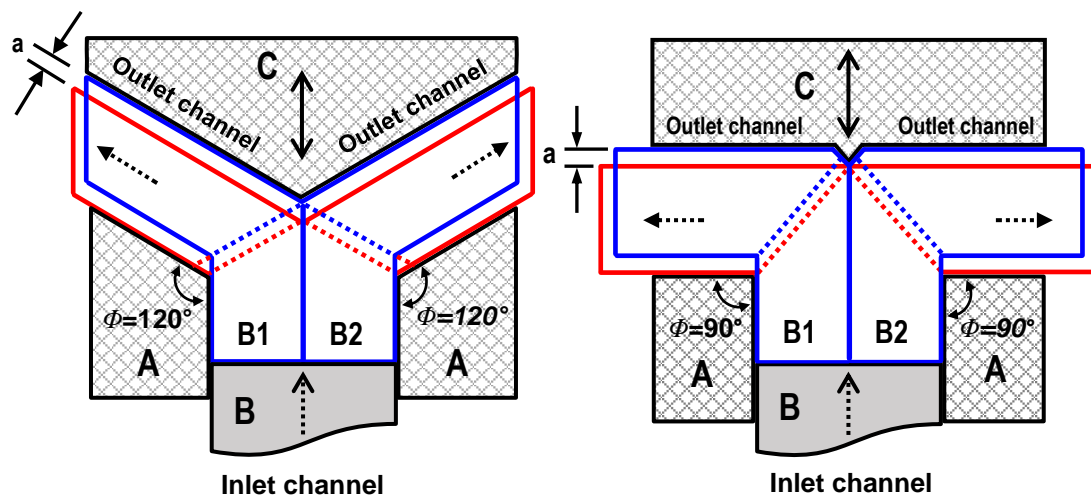


Fig. 3.12: Schematic illustration of the double-billet variant of the I-ECAP process (A = die, B = feeding rod and C = punch). The two billets are marked with B1 and B2.

3.6 Design of I-ECAP die

The design of the double billet I-ECAP die is based on a split die concept. The main die is composed of four die inserts (two longer and two shorter inserts), forming an inlet channel having a rectangular shape to accommodate two square cross-section billets (B1 and B2), as shown in Fig. 3.13. The die inserts are assembled together using lateral dowel pins and a pre-stressing ring (discussed below). The purpose of using a pre-stressing ring is to apply high compressive stress in the radial direction and to minimize the tangential stress generated in the die during processing.

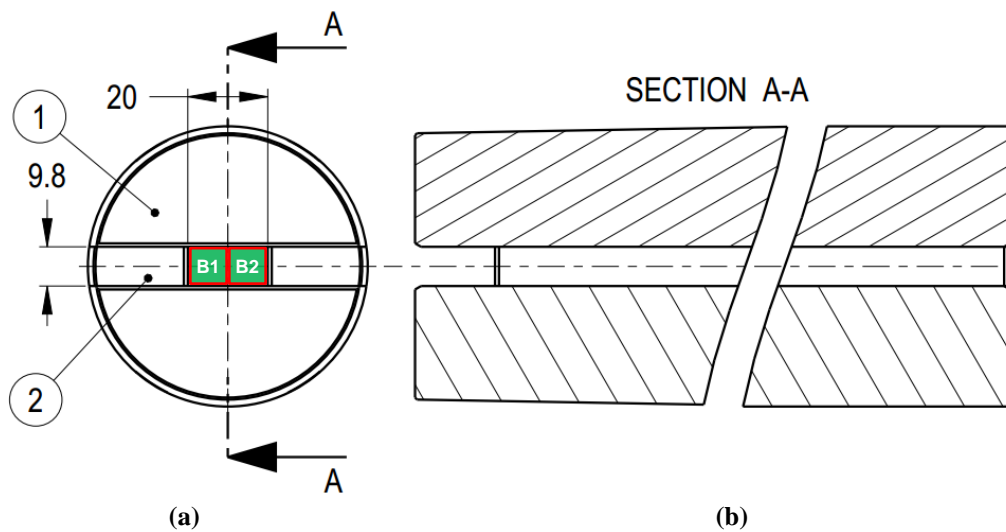


Fig. 3.13: Die insert sub-assembly (a) top view showing the rectangular shaped channel with two billets (B1 and B2), the two longer die inserts (labelled 1) and two shorter die inserts (labelled 2) and (b) cross-sectional cut along A-A.

Fig. 3.14 shows the cross section of the full assembly model representing the various tooling elements of the I-ECAP die-set. It shows the two I-ECAP dies used in the present work, i.e. dies with channel angle (Φ) of (a) 120° and (b) 90° . Fig. 3.15 shows the enlarged 3D view of the punch for the (a) 120° and (b) 90° designs. Both punches have a cylindrical top to fit inside the punch holder (as shown in Fig. 3.14) and a cut-out bottom to fit inside the I-ECAP die slot. For the $\Phi = 90^\circ$ in Fig. 3.15(b), notice the spike in the middle of the punch; this is to facilitate flow of the two billets in opposite direction.

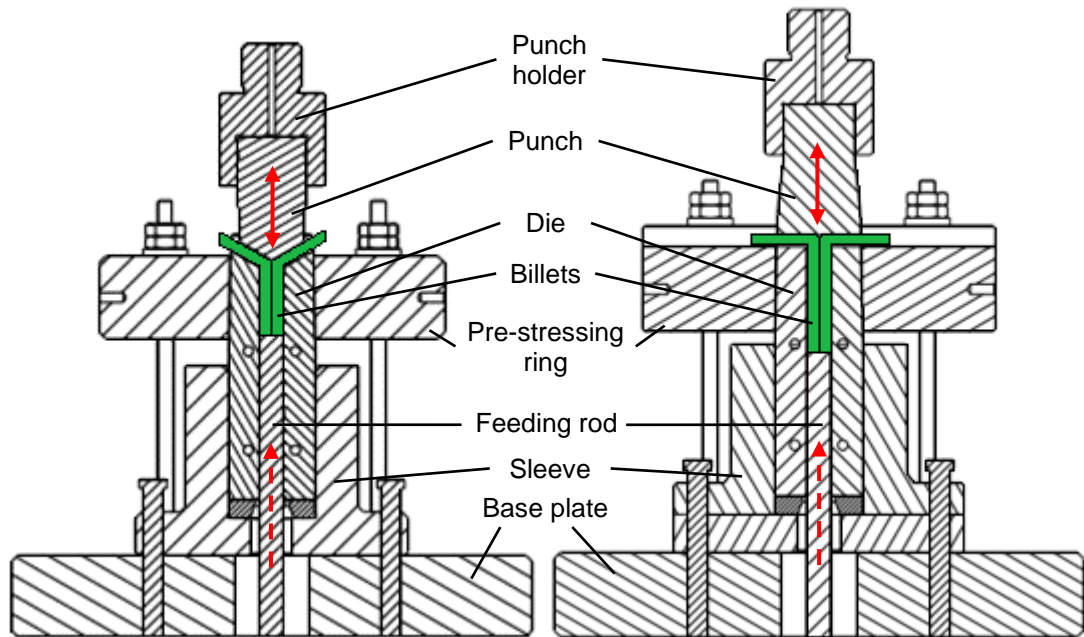


Fig. 3.14: CAD drawing of the I-ECAP tool assembly for (a) $\Phi = 120^\circ$ and (b) $\Phi = 90^\circ$.

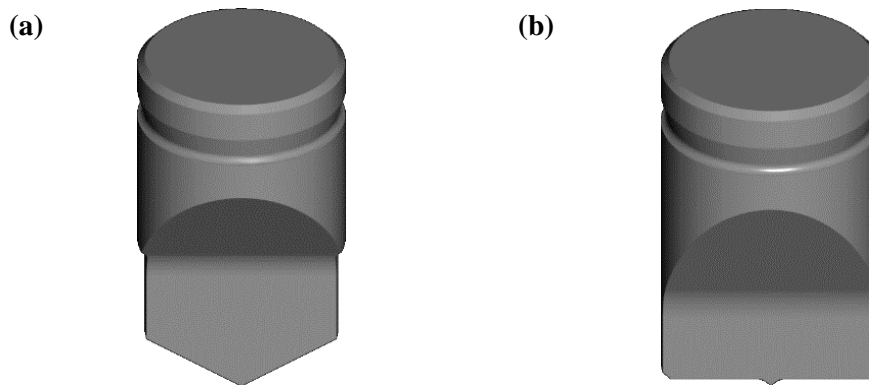


Fig. 3.15: Enlarged 3D view of the punch design for (a) $\Phi = 120^\circ$ and (b) $\Phi = 90^\circ$ (notice the spike in the middle, this is to facilitate the separation of the two billets in opposite direction).

All parts, assembly models and the associated manufacturing drawings in the present work were generated by the author in PTC Pro/Engineer Wildfire 4.0 which is a 3D CAD program. The design follows the guidelines for design for manufacture (DFM) and geometric dimensioning and tolerancing (GD&T). The detailed manufacturing drawings for die angle (Φ) of 90 and 120° can be found in Appendix A and B, respectively.

3.7 Tool material

Note that the I-ECAP die-set with $\Phi = 120^\circ$ was designed based on engineering judgment and the die geometry is not optimized using FE simulations. However, because of the similarities in design configurations both are presented together.

The die inserts were made of Vanadis 23 supplied by a Swedish company, Uddeholm. Uddeholm is a leading supplier of high strength, wear and corrosion resistant tool steels. Vanadis 23 is a powder metallurgy high speed tool steel corresponding to AISI M3:2 offering excellent combination of wear resistance and toughness. It is a chromium-molybdenum-tungsten-vanadium alloy (see Table 3.1 for composition) and is characterized by:

- High wear resistance
- High compressive strength
- Good toughness
- Very good dimensional stability on heat treatment
- Good machinability

Table 3.1: Composition of tool material - Vanadis 23 (Source Uddeholm)

Composition	C	Cr	Mo	W	V
%	1.28	4.2	5.0	6.4	3.1

Some of the physical properties of Vanadis 23 are shown in Table 3.2

Table 3.2: Physical properties of Vanadis 23 (Source Uddeholm)

Temp °C	Density Kg/m ³	Modulus of elasticity GPa	Thermal expansion co- efficient (20°C) 1/°C	Thermal conductivity W/m. °C	Specific heat J/Kg. °C
20	7980	230	-	24	420
400	7870	205	12.1 x 10 ⁻⁶	28	510
600	7805	184	12.7 x 10 ⁻⁶	27	600

The material was heat treated to achieve a hardness of 62 HRC. At this hardness level the compressive yield strength of the material is above 2500 MPa. This is desired to withstand high compressive forces during I-ECAP processing.

The other components of I-ECAP tooling assembly such as pre-stressing ring, sleeve and base plate were made with P20 material, heat treated to 40 HRC. P20 is a tool steel material which offers good machinability and wear resistance properties.

3.8 Pre-stressing of I-ECAP die

The pre-stressing of extrusion dies is a well-established practice. This is mainly done to improve the service life of the extrusion dies. The design of pre-stressing systems, aims at obtaining a high compressive pre-stress in the critical area of the die, leading to reduced stresses under full process pressure. A single ring system, which is the most commonly used pre-stressing system, was used to pre-stress the I-ECAP die-set in the radial direction.

The pre-stressing of I-ECAP die-set involves two main components (i) the die insert sub-assembly and (ii) the pre-stressing ring. The pre-stressing ring has central hole with a one degree draft. Because of this, the diameter of its hole at the top side is slightly smaller than the diameter at the bottom side, thereby forming a cone (see Fig. 3.16 for illustration). Similarly, the top half of the die insert sub-assembly has an outer tapered profile to match the hole in the pre-stressing ring. The pre-stressing ring also has a slot to allow the material to exit after I-ECAP processing.

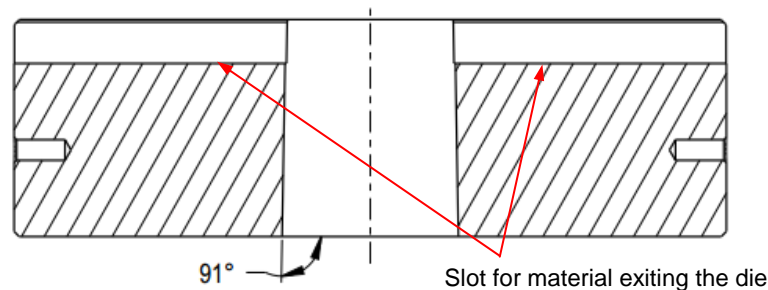


Fig. 3.16: Sectioned view of pre-stressing ring is shown with a tapered hole in the centre.

Compared to the extrusion die, pre-stressing of the I-ECAP die was done partially, i.e. only the top half of the die insert sub-assembly was pre-stressed. This is the region where the actual billet deformation takes place and where the highest amount of counter force is required to prevent die opening.

To create pre-stressing condition, interference type fit is required between the pre-stressing ring and the die insert sub-assembly. A design rule was followed which

recommends using 0.3 to 0.5% of the die diameter for interference; 0.35% was used in this case. Since the diameter of the die insert sub-assembly was 70 mm, the total interference between the pre-stressing ring and die insert sub-assembly was calculated as 0.245 mm ($0.35\% \times 70 \text{ mm}$). This resulted in 0.123 mm interference per side as illustrated in Fig. 3.17.

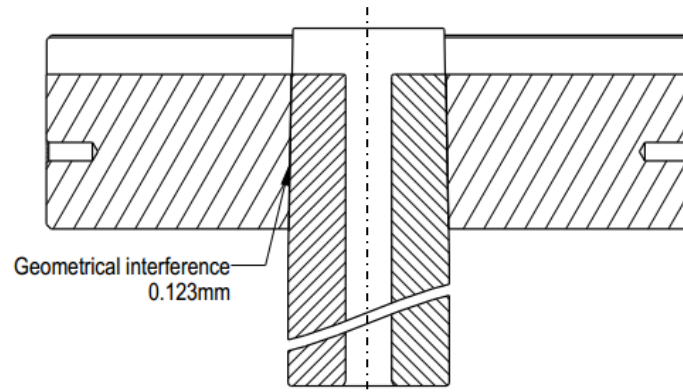


Fig. 3.17: Sectioned view of I-ECAP die assembly with geometrical interference.

To pre-stress I-ECAP die set, the pre-stressing ring was pushed onto the die insert sub-assembly. A sleeve part (see Fig. 3.14) was used to prevent the die insert sub-assembly from opening at the bottom side while pre-stressing is done on the top.

The pre-stressing ring was initially placed on the die insert sub-assembly and allowed to go down freely under its own weight. Once there was zero clearance between the two components, the pre-stressing ring stopped. After this point, the pre-stressing ring had to go further down by 7 mm to achieve the required interference fit.

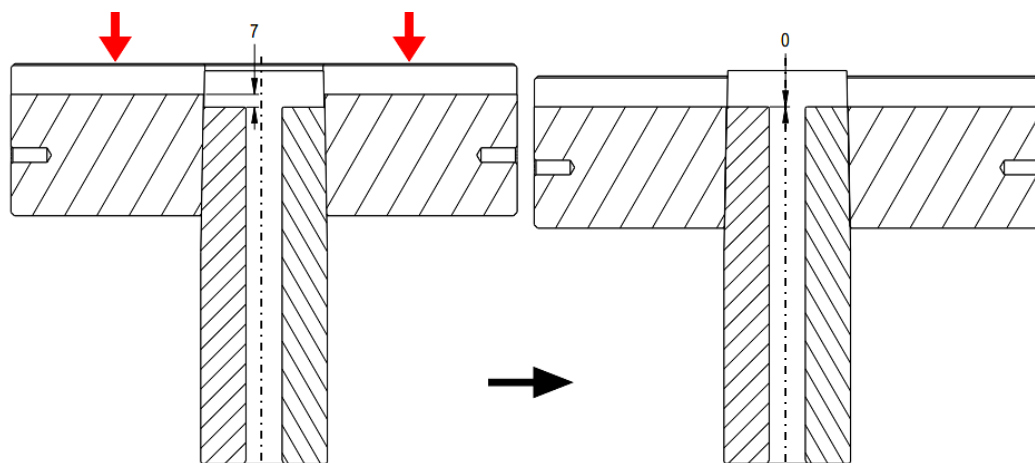


Fig. 3.18: Illustration showing the position of ring before and after pre-stressing.

The pre-stressing procedure was performed on a 1000 kN press using the displacement control mode. The hydraulic actuator gradually applied downward force and pressed the pre-stressing ring onto the die insert sub-assembly. To prevent any catastrophic fracture of the ring or die, the pressing was done very slowly and in increments of 0.5 mm. The force value from the load cell was continuously monitored. At the final stage of the pre-stressing the load cell recorded a value of ~750 kN.

After pre-stressing the I-ECAP die, a problem was encountered with the die channel dimensions. The original channel dimension was reduced from 9.8 to 9.6mm, see Fig. 3.19. By carefully measuring the breadth of the inlet channel, it was discovered that the channel opening had become tapered after pre-stressing. Machining was performed on the top part of the inlet channel to remove the taper. Red region shown in the Fig. 3.20 was removed through machining, to make the channel walls parallel. Some machining was also performed on the punch and the feeding rod.

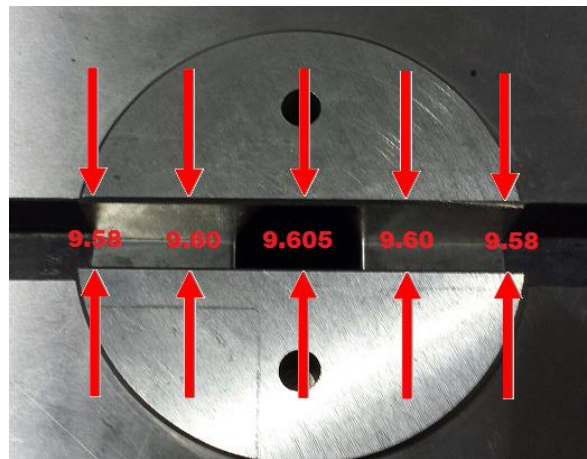


Fig. 3.19: Measurement of I-ECAP channel dimensions along breadth after pre-stressing.

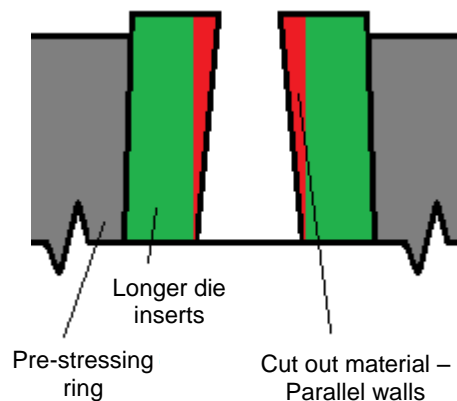


Fig. 3.20: Illustration of the tapered profile of the channel breadth after pre-stressing.

3.9 Stress analysis of pre-stressing I-ECAP die

In order to understand the effects of pre-stressing on the I-ECAP die, elastic stress analysis using FE was performed. A 3D model of the pre-stressing ring and die insert sub-assembly was developed using commercial FE code Abaqus/Standard to predict the deformations and the level of stresses after pre-stressing. The individual part geometry which was created in Pro/Engineer CAD software, was exported to Abaqus using an IGES file format. For simplification, all the extra features like, radii, chamfers and holes were removed from the CAD model before exporting. After importing into Abaqus, the parts were partitioned to enable mapped meshing and assembled together to form a three dimensional die insert sub-assembly and the pre-stressing ring (as can be seen in Fig. 3.21).

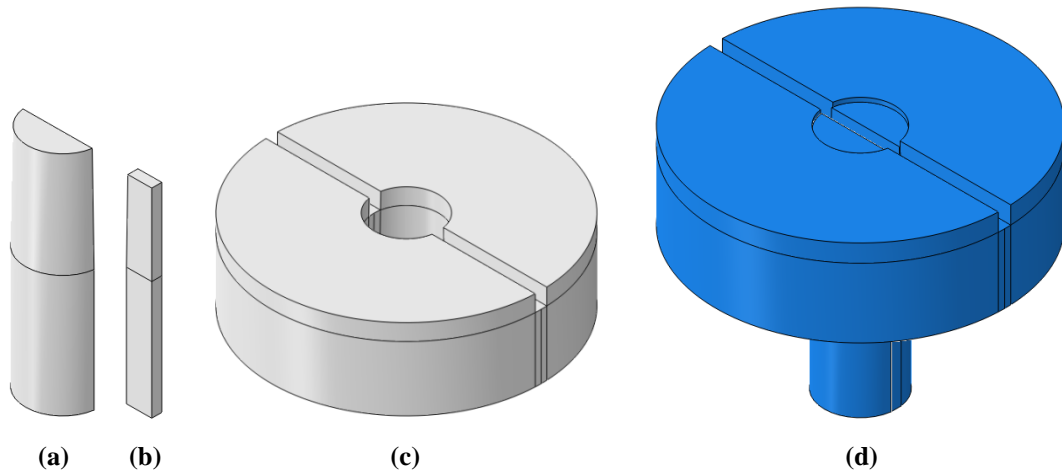


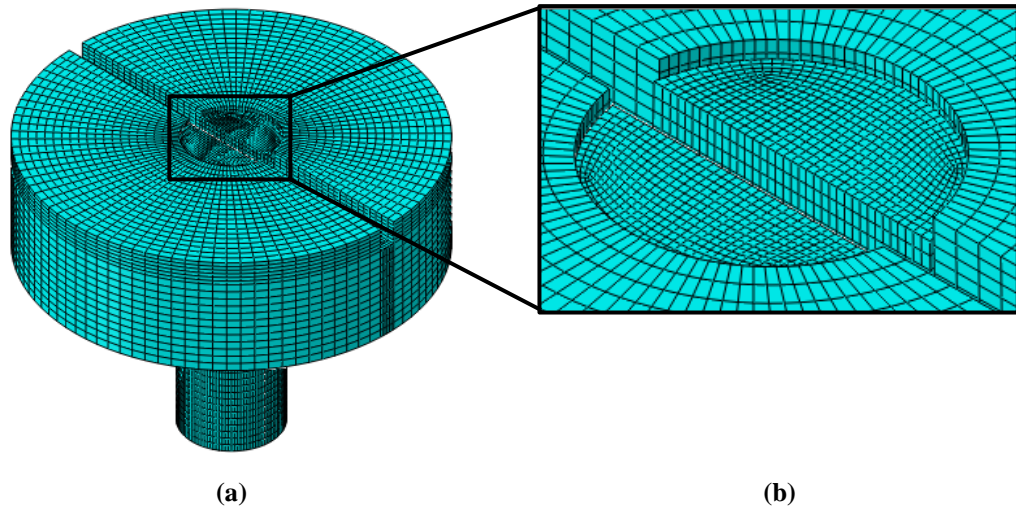
Fig. 3.21: Parts used in FE model: (a) longer die insert (b) shorter die insert (c) pre-stressing ring and (d) I-ECAP die assembly.

3.9.1 Finite element model

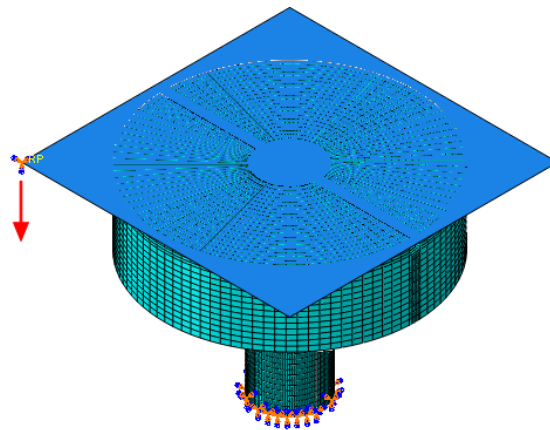
Eight noded linear brick element (C3D8R) with reduced integration was used to create the mesh. As can be seen in Fig. 3.22, the element size is smaller near the area of interest. In total there were 100,112 elements and 112,488 nodes in the model. Special care was taken to create a regular mapped mesh using the sweep meshing technique. Table 3.3 shows the value of Young's modulus and Poisson's ratio used in the model.

Table 3.3: Elastic properties of the materials used in the model

Parts	Material	Young's Modulus (E)	Poisson's ratio (ν)
Die inserts	Vanadis 23	230 GPa	0.3
Pre-stressing ring	P20	199.95 GPa	0.27

**Fig. 3.22: (a) Finite element mesh of the whole model and (b) enlarged view of the dense mesh region.**

The nodes at the bottom of the die insert sub-assembly were constrained in all translation and all rotation degrees of freedom throughout the analysis (Fig. 3.23). A rigid analytical plane surface was used to push the pre-stressing ring into the die insert sub-assembly. A downward displacement was applied at the reference point of this rigid plane. The pre-stressing ring was pushed by a value of 7 mm onto the die insert sub-assembly following a linear displacement ramp profile.

**Fig. 3.23: Model showing the direction of loading and constraints.**

A friction co-efficient value of 0.12 was considered between the contacting bodies. This value was achieved after trial and error method. Different friction co-efficient values were tried until the corresponding reaction force on the rigid plane was approximately 750 kN, the value measured on the load cell during the actual pre-stressing.

3.9.2 Procedure for analysis

Two steps were defined to solve the FE problem; in the first step contact was initiated, this was done by applying a very small displacement to the pre-stressing ring via the rigid plane. In second step the actual pre-stressing was performed, time duration of 7 seconds was defined for this step. The 7 mm displacement was applied as a ramp profile therefore the speed of the pressing was 1 mm/s. Time incrementation was carefully selected so as to allow convergence of solution. It took approximately 25 minutes to solve the pre-stressing problem.

3.9.3 Results and discussion

The Fig. 3.24 shows the Von Mises stress distribution along different section of the I-ECAP die set. As both the pre-stressing ring and the die insert sub-assembly were modelled using deformable geometry, stresses are produced in both components. As predicted, the maximum stress is occurring in the shorter die inserts.

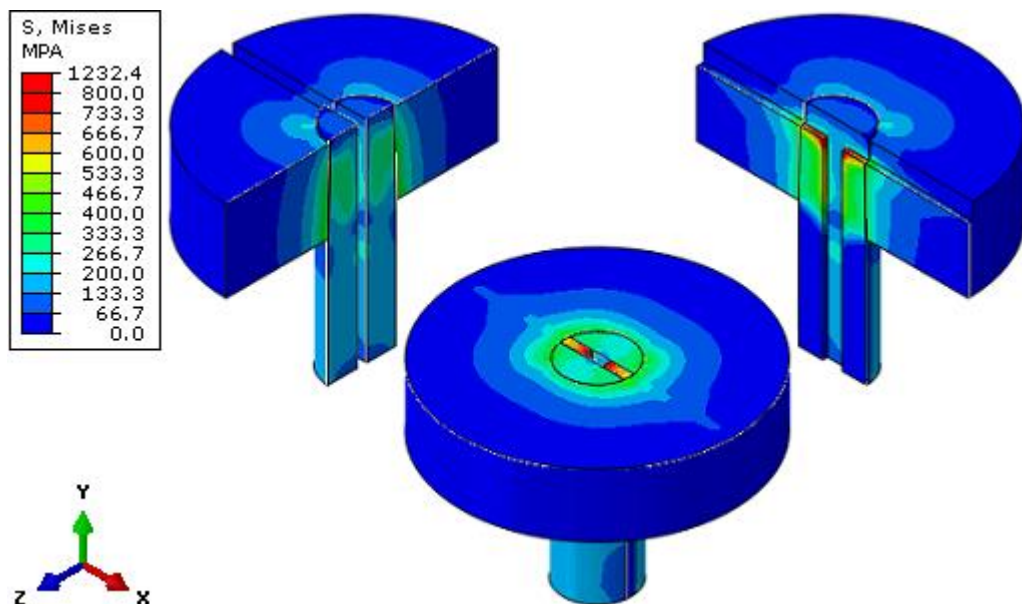


Fig. 3.24: Plot of Von Mises stress distribution after press-stressing of the I-ECAP die.

Fig. 3.25 shows the stress distribution for the upper and lower sides of the pre-stressing ring, the views have been sectioned to see the stresses on the tapered hole.

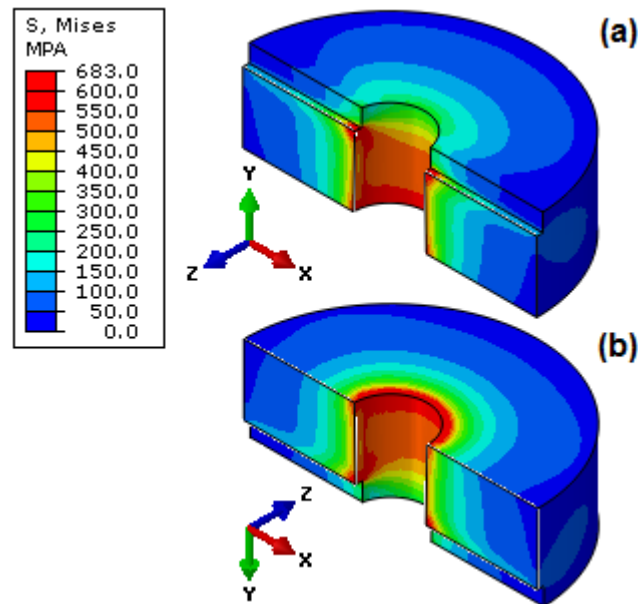


Fig. 3.25: Sectioned plot of Von Mises stress distribution on pre-stressing ring (a) top side and (b) bottom side.

The following (Fig. 3.26) shows the stress distribution on the individual components of the die insert sub-assembly. It should be mentioned here that the material for die insert is Vanadis 23, which has a yield stress values of 2500 MPa at 62 HRC. The maximum stress predicted by the FE simulation is 1232.4 MPa which is well below the yield strength of the material, so as far the pre-stressing is concerned the design is safe.

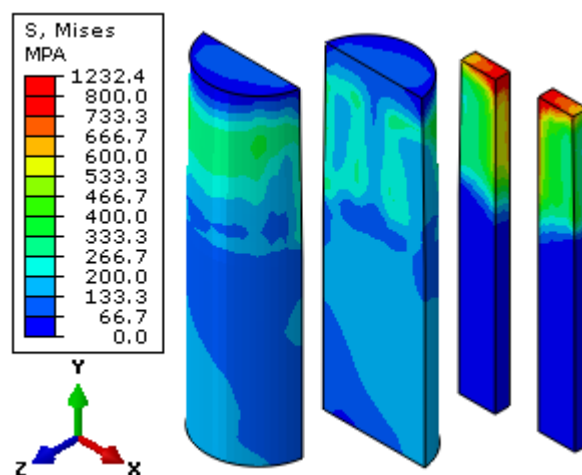


Fig. 3.26: Plot of Von Mises stress distribution on the four die inserts.

The force predicted by FE model during pre-stressing is shown in Fig. 3.27; it increases linearly with the displacement. As mentioned earlier, the co-efficient of friction was carefully selected to achieve the final force value equal to the experimental measured one.

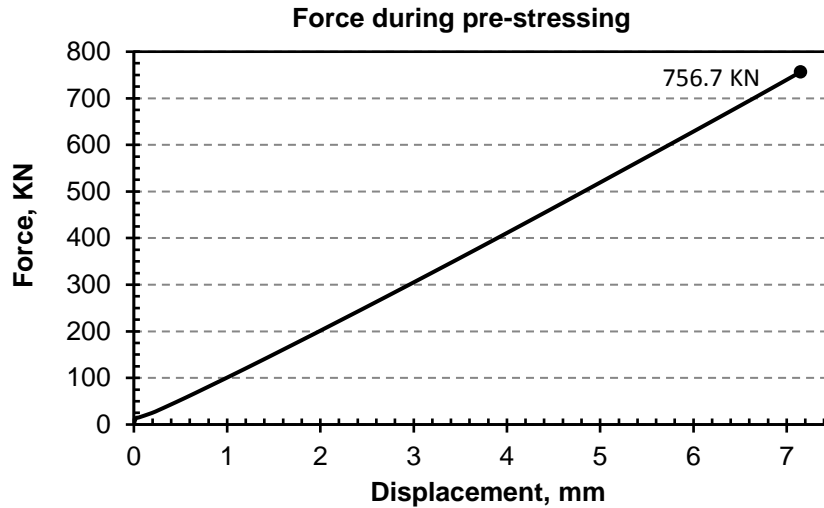


Fig. 3.27: FE prediction of force required for pre-stressing the I-ECAP die.

The effect of pre-stressing on the channel width (z-direction) is shown in Fig. 3.28. Because of the global coordinate system used, the displacement appears to have positive and negative values (red and blue colour in the results).

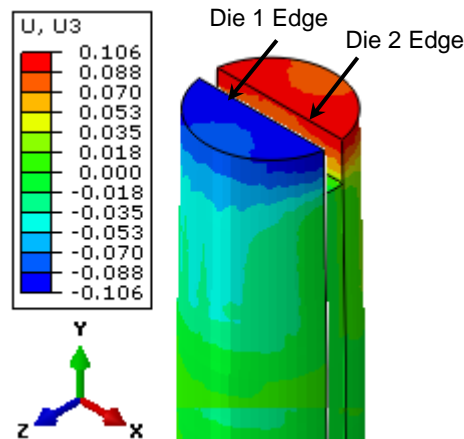


Fig. 3.28: Pre-stressing displacement along z-direction (U3).

A comparison was done between the FE results and the actual measurement obtained through gauge blocks. As can be seen from the Table 3.4 below, FE predictions are in good agreement with the actual measurements.

Table 3.4: Comparison of FEA results with actual measurement along channel breadth

Channel Gap	Left corner	Middle section	Right corner
Actual	9.580	9.605	9.580
FEA	9.594	9.612	9.594

3.10 Summary and conclusions

Finite element simulation using Abaqus/Explicit has been carried out to study the billet deformation behaviour during the first pass of I-ECAP using a single CP-Ti grade 2 billet. The purpose of the study was to optimize the I-ECAP tooling geometry to minimize or eliminate billet bending and to achieve uniform strain distribution. Investigations were performed to study the effect of tool length, billet length and friction on the bending behaviour of billet during processing and to study the resulting plastic strain distribution. The following conclusions are drawn from the study:

1. The phenomenon of billet bending is an inherent nature of the I-ECAP process. Increasing the outlet channel length greatly reduces the non-desirable bending effect within the billets.
2. Increasing the friction from 0.05 to 0.2 reduces the tendency of billet bending. However the effect is negligible beyond channel length of $2w$. Friction, significantly increases the strain inhomogeneity within the steady state section of the billet. Therefore the billet should be well lubricated to minimize friction and avoid galling.
3. Unlike the classical ECAP process, the I-ECAP process owing to its unique tool design allows using unequal tool lengths (punch and die length can be different). Simulation results predict that even for longer billet lengths, an optimum punch and die length of 20 and 100 mm respectively can be used.

The stress analysis of pre-stressing the I-ECAP die has been carried out. The maximum stress predicted by the FE simulation is well below the yield strength of the die material, so the design is considered to be safe. The FE results are in good agreement with the actual measurements. The stress state in tools during I-ECAP process has not been studied here, although it is believed that the high strength high speed steel used for tools will easily withstand these loads.

Following the FE analysis, the optimized tooling geometry was successfully incorporated into the die design of the double billet I-ECAP process. Details of the experiments performed on CP-Ti billets using the new I-ECAP dies are presented in the following chapter.

Chapter 4

Experimental setup, material and procedure

4.1 Introduction

The experimental part of this research work consists of the following three main activities:

1. Processing of CP-Ti grade 2 billets using the I-ECAP experimental rig
2. Microstructural characterization of the processed material to investigate grain refinement process
3. Mechanical testing of the processed material to evaluate the changes in its properties

This chapter describes in detail the I-ECAP experimental setup, sample preparation method and the experimental procedure. It also describes the international test standards used for performing mechanical testing, the sample geometry, the equipment used and the method of data analysis.

4.2 Previous configuration of the I-ECAP rig

The I-ECAP process for billets and sheets uses a 1000 kN laboratory press equipped with a servo hydraulic actuator controlled using an analogue servo control module (SCM) by ESH. The rig consists of three main elements; the press actuator, the I-ECAP die-set mounted on the press bed, and a manually driven screw jack for material feeding.

It is worthwhile recalling the principle of I-ECAP from Chapter 2. In I-ECAP the material feeding stage and the deformation stage are separated as opposed to classical ECAP procedure where the material feeding and deformation take place simultaneously. To enable this, the process employs an oscillating punch and an incremental feeding device to feed billets into the die channel.

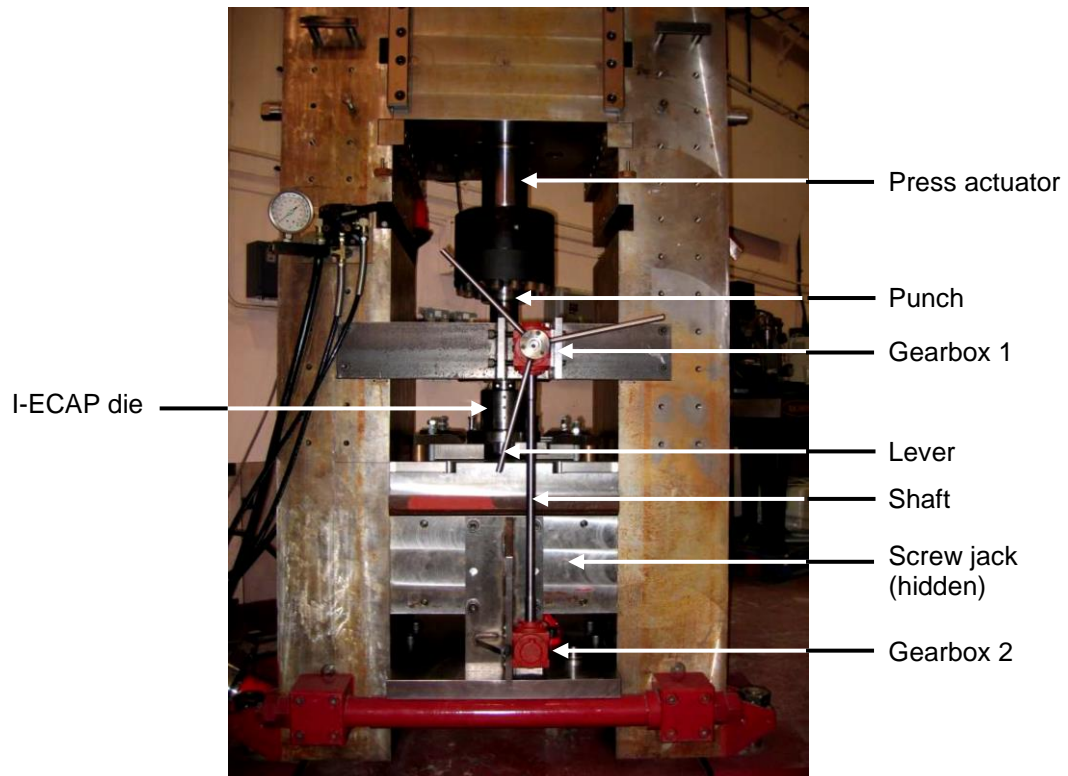


Fig. 4.1: Previous configuration of the I-ECAP rig on the 1000 kN servo hydraulic press.

To realize punch oscillations, the previous setup utilized an external waveform generator to generate a sine wave signal. The frequency and amplitude of this sine wave signal defined the processing parameters, which was monitored in real time using an analogue oscilloscope. This external signal was fed into the SCM, which causes the oscillatory movement of the punch attached to the press actuator.

The incremental feeding of the billets was accomplished via a 200 kN self-locking screw jack (Fig. 4.2(a)). It was mounted on a supporting plate (see Fig. 4.2(b)) fitted at the bottom of the press. To move the lifting screw of the screw jack, levers positioned at the front of the press were manually turned. Turning the lever, rotated a system of shafts connected by two gearboxes (gearbox 1 and 2 in Fig. 4.1). The gear ratios of the two gearboxes, together with the gear ratio of the screw jack, resulted in one complete rotation of the input shaft moving the lifting screw by approximately 0.2 mm.

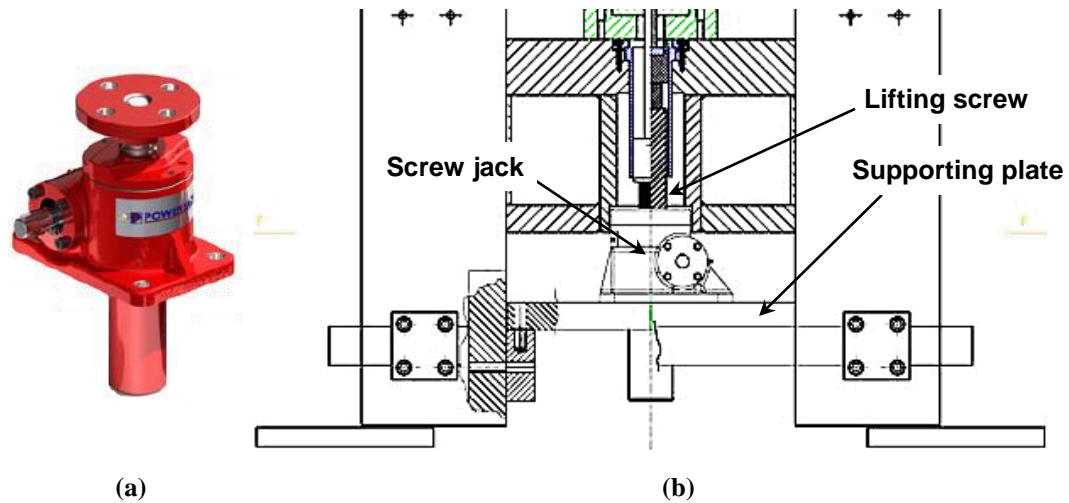


Fig. 4.2: (a) Power jack translating 200 kN screw jack and (b) illustration of the screw jack installation on the I-ECAP rig

The procedure for carrying out experiments in the previous configuration was as follows. First of all some setup operations were performed. These included: aligning the punch with respect to the die, moving the screw jack to the bottom position by manually turning the levers (to create space to insert billets), setting up the punch oscillations using the external waveform generator, introducing the lubricated billets into the inlet channel and heating the tooling if necessary.

To start processing, the billets were fed manually (using screw jack) into the deformation zone so that a small load reading began to appear on a LED display on the control cabinet. This indicated that the billets were starting to make contact with the punch. At this point, the feeding process had to be synchronized with the punch oscillatory movement. A dial gauge attached to the punch served as a reference for feeding. When the punch was retracting away from the billet, the lever of the feeding mechanism was given one full turn. This caused the billet to be pushed into the deformation zone by ~ 0.2 mm, where it was locked in position by the self-locking screw of the screw jack. In the next cycle the punch came down and plastically deformed the billets. This cycle of feeding and deformation was repeated until the entire billet length was processed, at which point the experiment was stopped and billets were removed and prepared for the next I-ECAP pass.

4.3 Upgradation of I-ECAP rig

The above described procedure for performing experiments on the I-ECAP rig was a major cause of user's fatigue. Besides, the manually operated feeding mechanism resulted in: less productivity (limited to ~0.2 mm per feeding cycle only), low level of repeatability and sometimes out of synchronize feeding with punch oscillatory motion. The previous configuration of the I-ECAP rig was therefore not reliable and not appropriate at all especially if I-ECAP process is to be considered for industrialization purposes.

A major program of work was undertaken as part of this PhD to upgrade the I-ECAP rig. The objective was to demonstrate the I-ECAP rig as a viable method for industrial usage and also to make the I-ECAP process more efficient, repetitive and to enable robust process control and data acquisition during processing.

The following aspects of the I-ECAP rig were selected for improvement and upgrading purposes.

- Automation of material feeding system
- Elevated temperature processing capability
- Digital servo hydraulic control system
- Instrumentation, process control and data acquisition
- General rig upgrades including safety

4.3.1 Automation of material feeding system

The first and the most important upgrade was to eliminate the problems with manually feeding of the billets during processing and the inefficiencies associated with it. As discussed earlier, manual feeding of the billets by rotating the levers during processing was a major drawback of the previous I-ECAP experimental procedure. To demonstrate I-ECAP as an industrially viable option, an automatic material feeding system was an essential requirement.

A new motor driven automatic system of billet feeding was implemented to replace the previous manual system of levers and gearboxes. The new system shown in Fig. 4.3 consisted of (a) Kollmorgen AKM Synchronous AC servo motor with a

50:1 gear ratio gearhead, (b) SERVOSTAR S300 servo drive, (c) control cabinet to power motor and interface with the I-ECAP rig and (d) mechanical coupling to interface motor with screw jack worm shaft.

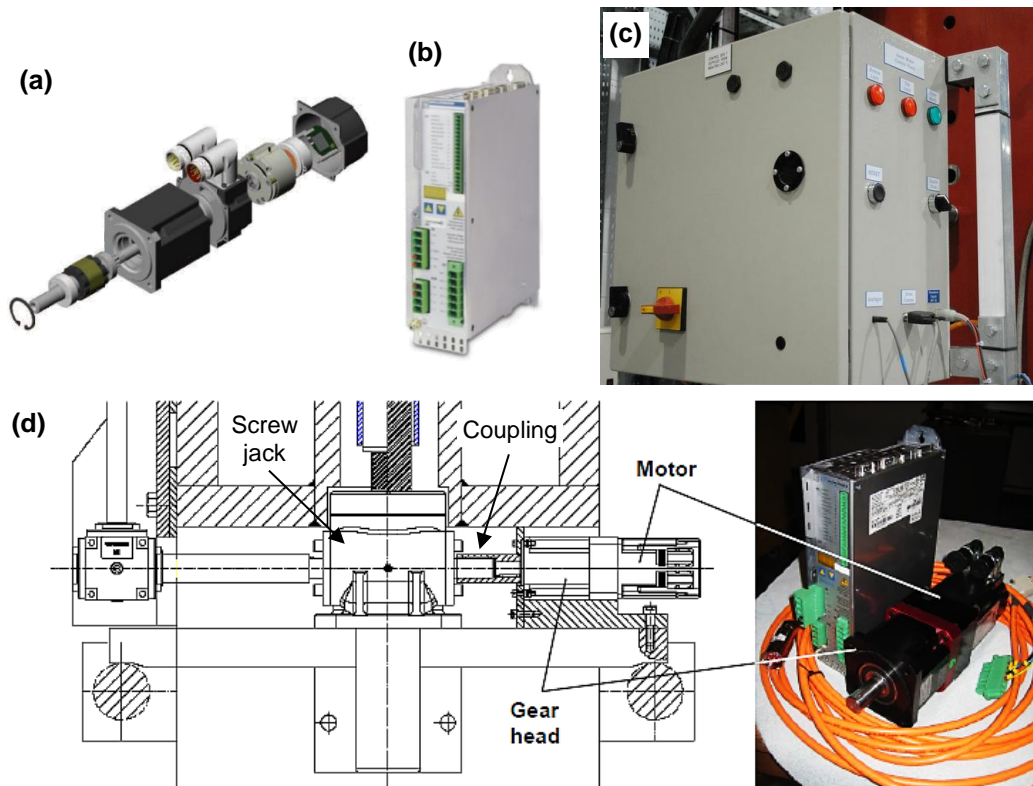


Fig. 4.3: A motor driven system of billet feeding (a) Kollmorgen AKM Synchronous AC servo motor with a 50:1 gear ratio gearhead, (b) SERVOSTAR S300 servo drive, (c) control cabinet to power the servo motor and interface with the I-ECAP rig and (d) cross-section showing how the motor is coupled to screw jack worm shaft.

To investigate the I-ECAP process in detail an important parameter is feeding force. During I-ECAP, the feeding stage is separated from the deformation stage, therefore it is believed that the force required to feed the material is considerably lower compared to classical ECAP. To practically measure the feeding force during experiments, a load cell was required within the existing tooling responsible for billet feeding. For this purpose, a full 3D CAD model of the whole I-ECAP rig including screw jack, press table, I-ECAP die set and punch attached to the press actuator was developed. The main challenge was to find a load cell which was compact enough to fit within the existing tooling and also capable of measuring loads up to 200 kN (maximum allowable load for screwjack). A 300 series compact type load cell from Richmond Industries was selected, as it satisfied these requirements. Design changes

were made in the existing tooling and some new tools were made to house the load cell just above the screw jack, as shown in Fig. 4.4. Designing the new tooling for billet feeding and installing the load cell, enabled monitoring and recording feeding forces during processing.

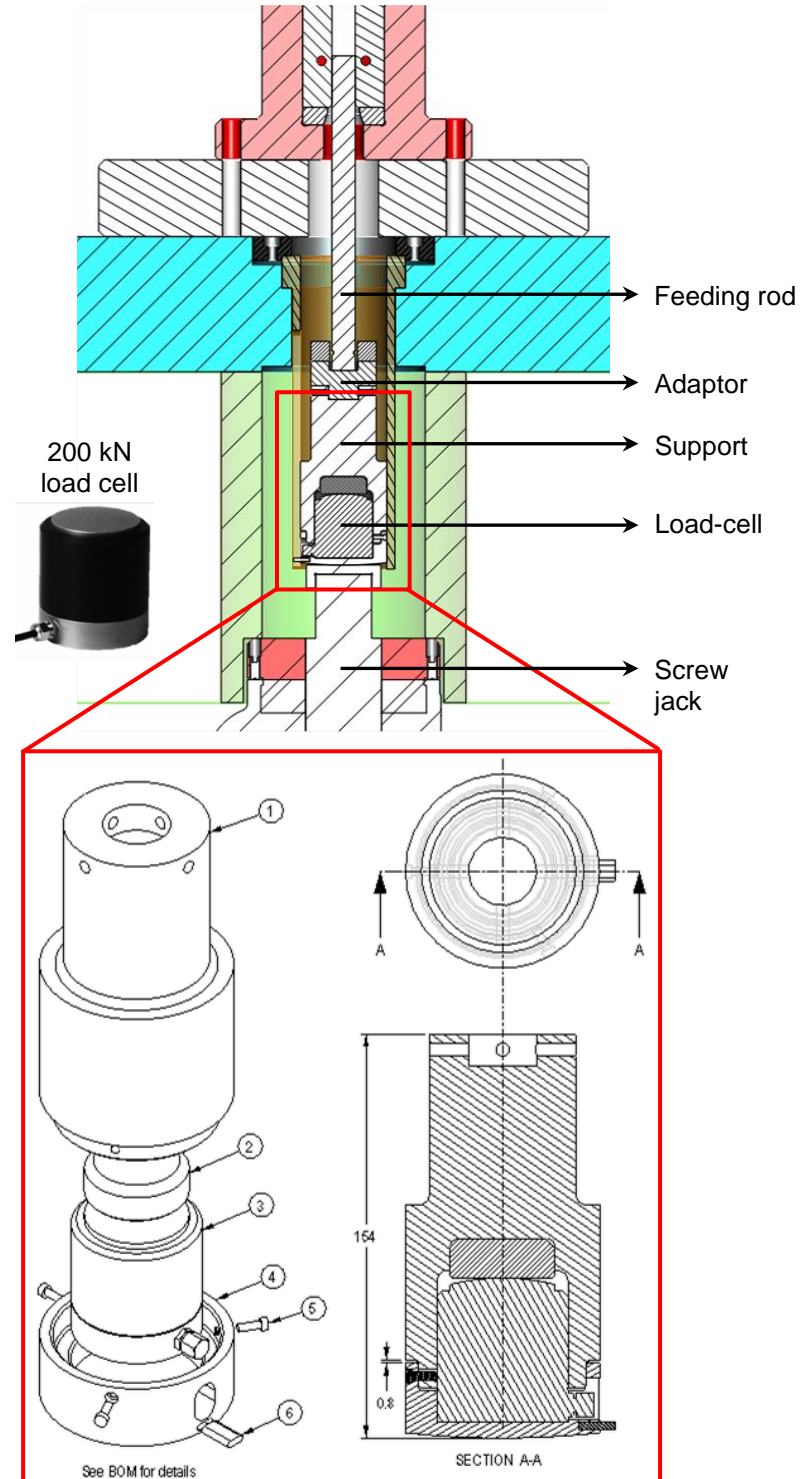


Fig. 4.4: I-ECAP tooling for material feeding along with the load cell for recording feeding force.

4.3.2 Elevated temperature processing capability

In order to avoid cracking and segmentation of billets during processing of difficult to deform materials like titanium, the process has to be carried out at elevated temperature. To enable this, the I-ECAP rig was installed with three zones of heating as shown in Fig. 4.5.

Zone 1 consists of a 600 watts heater band attached to the punch holder. Zone 2 features a split type aluminum heating block fitted with six fire-rod heaters of 250 watts each and finally Zone 3 is a large band heater attached to the outer surface of the pre-stressing ring with a power of 3000 watts. There is a K-Type thermocouple close to the deformation zone which is used to monitor and maintain the processing temperature within accuracy of ± 2.0 °C during I-ECAP processing. Fig. 4.6 shows the heater control cabinet which is used to power and control the various heaters.

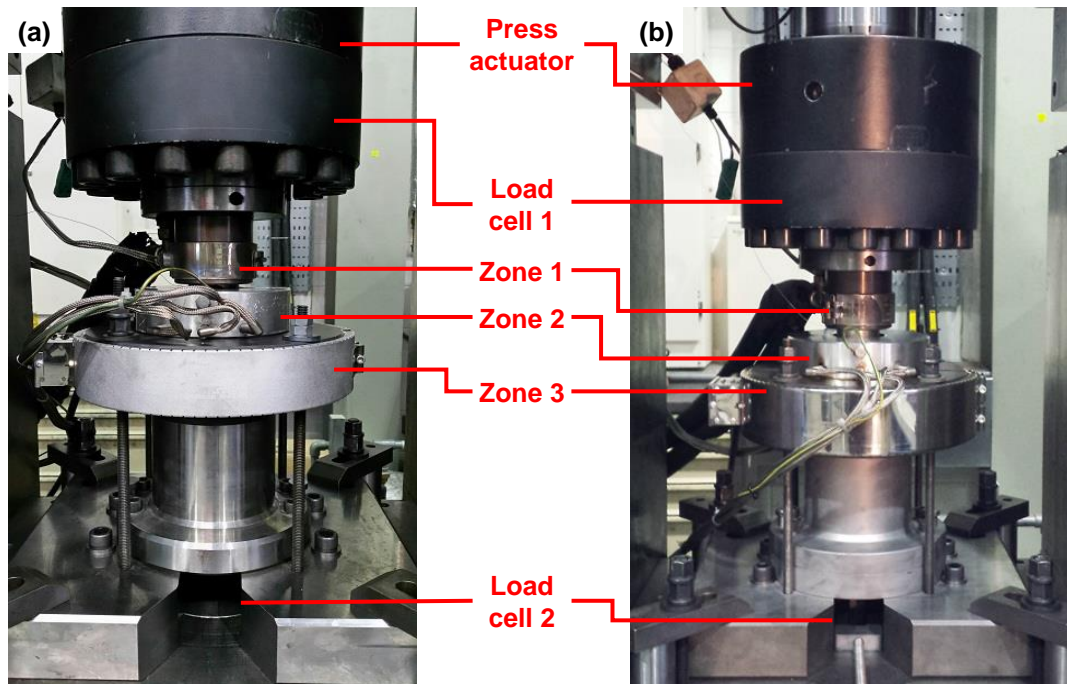


Fig. 4.5: I-ECAP tooling with different zones of heating for (a) $\Phi = 120^\circ$ and (b) $\Phi = 90^\circ$

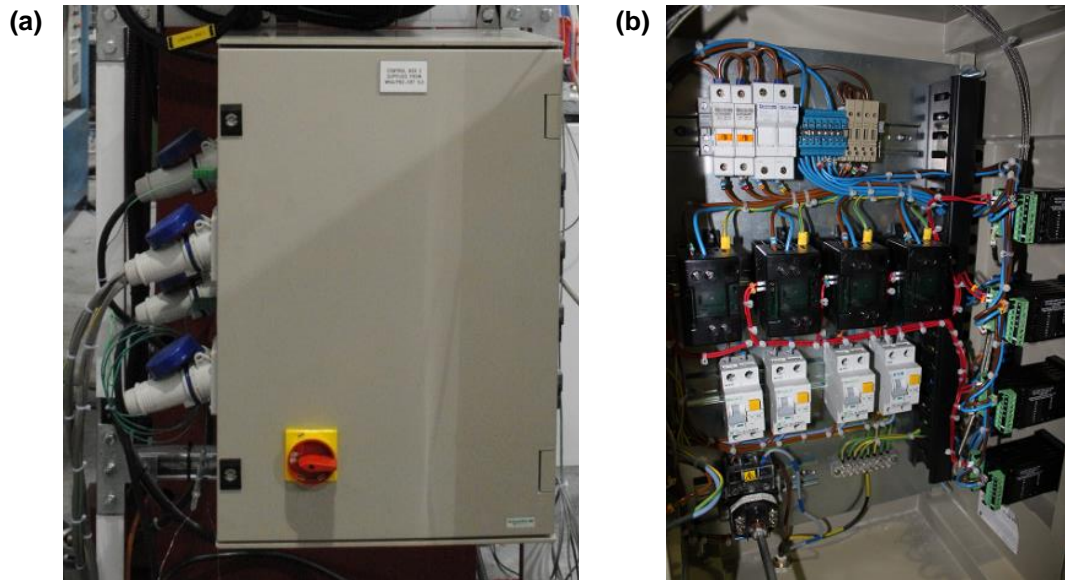


Fig. 4.6: Heater control cabinet: (a) outside view and (b) inside connections.

However, the elevated temperature processing itself presented a problem. Due to high temperature, there is a potential of heat reaching into the load cell which measures deformation force (load cell 1 in Fig. 4.5). The load-cell installed on the press is a general-purpose load cell and it is not meant to be operated at temperatures in excess of 70 °C. At elevated temperature, the reliability of the data from load cell is compromised. In extreme case, the load cell can be damaged permanently. To avoid this problem a cooling system was designed and installed. The system comprised of an industrial chiller (used also to cool the oil in the press power pack) and some new tooling between punch holder and the load cell. Three designs were developed for this new tooling and the best designed was selected and manufactured based on the criteria of design for manufacture (DFM), reusability of the existing tools and the cost . The design is shown in Fig. 4.7 (see Appendix C for detailed drawings).

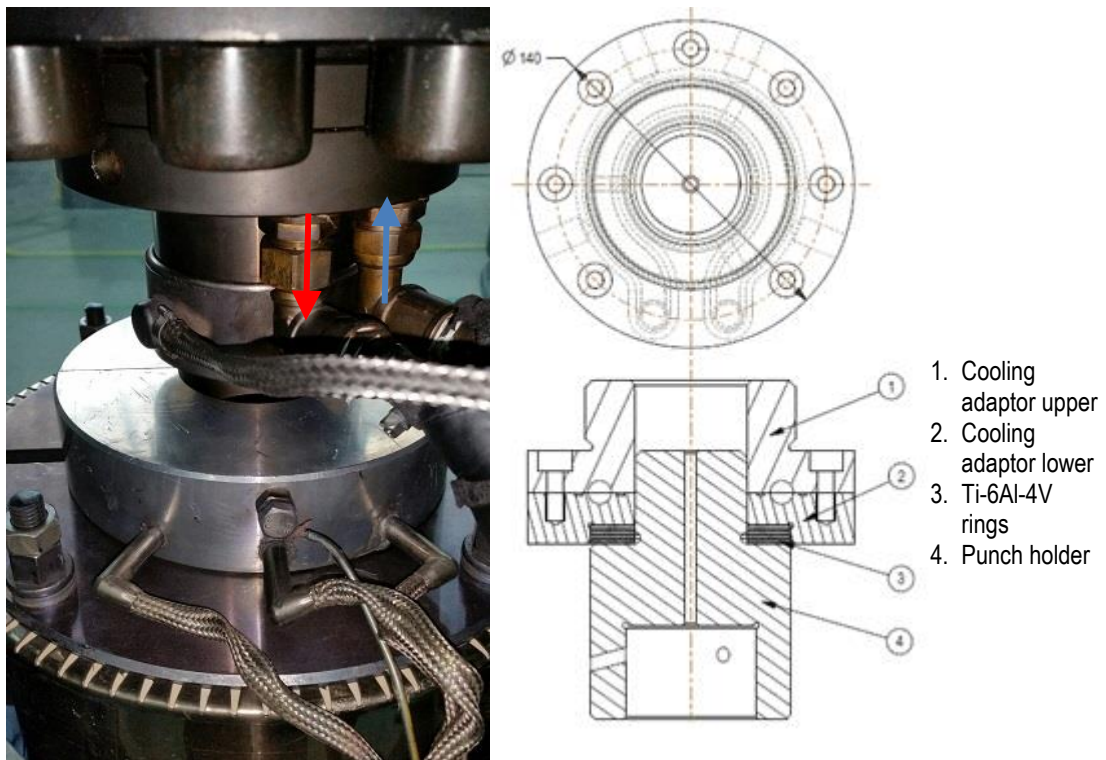


Fig. 4.7: New tooling for maintaining the load cell at low temperature (here blue arrow indicates cool water coming from chiller and red arrow indicates heated water going back to chiller).

4.3.3 Digital servo hydraulic control system

The previous servo hydraulic controller for the press from ESH, was based on an obsolete analogue technology. It offered very limited options, for example, an external waveform generator was used to generate the sine wave required for oscillating the punch during the I-ECAP process. The system was very bulky and lacked some essential safety features in case the load reached a dangerous level during operation.

In order to make the I-ECAP rig efficient and robust, it was essential to replace the old control system with a modern one. For this purpose, major press control suppliers including MOOG, Instron and Zwick/Roell were contacted for a solution. After product demonstrations from these suppliers and after detailed analysis in terms of specification, flexibility, robustness, future upscaling and cost; the solution from Zwick/Roell was selected. The solution (as shown in Fig. 4.8) comprises a state of the art digital servo hydraulic controller known as ‘control cube’ along with its computer based ‘Cubus’ software interface. The solution provided several enhancements in terms of controls and safety, however following are some of the noteworthy features:

1. Cubus displays critical information in real time such as command (displacement or load) and the actual feedback in the form of text and charts.
2. Sine wave signal generation via a cyclic module so the external generator is not required.
3. Options to create complex test sequences with the help of a block program module and options to save and recall programs.
4. Easy interface and integration options with external data acquisition system.

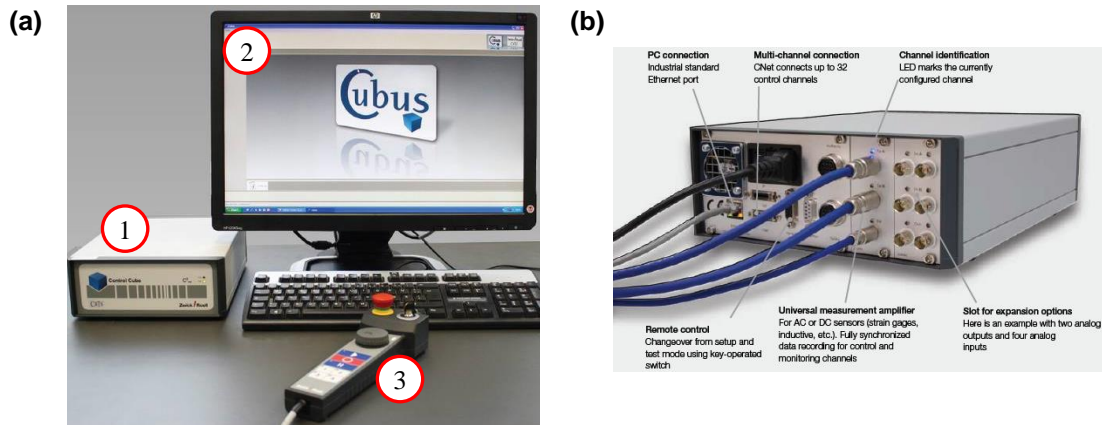


Fig. 4.8: (a) The solution from Zwick/Roell: 1 – control cube, 2 – computer based Cubus software, 3 – hand controller for manual actuator control during setup and (b) backside of the control cube, showing options for connections and interfacing.

4.3.4 Instrumentation, process control and data acquisition

For a robust process control and data acquisition during experiments, a dedicated LabVIEW virtual instrument application was programmed and implemented as part of the upgradation work. The objective of creating this application was mainly for the automatic synchronization of material feeding during processing. The application serves as a central point from where one can monitor, control and record data during experiments. To understand how this application is integrated into the overall experimental rig, a schematic diagram in Fig. 4.9 is presented to show the various elements of the I-ECAP rig and their connections.

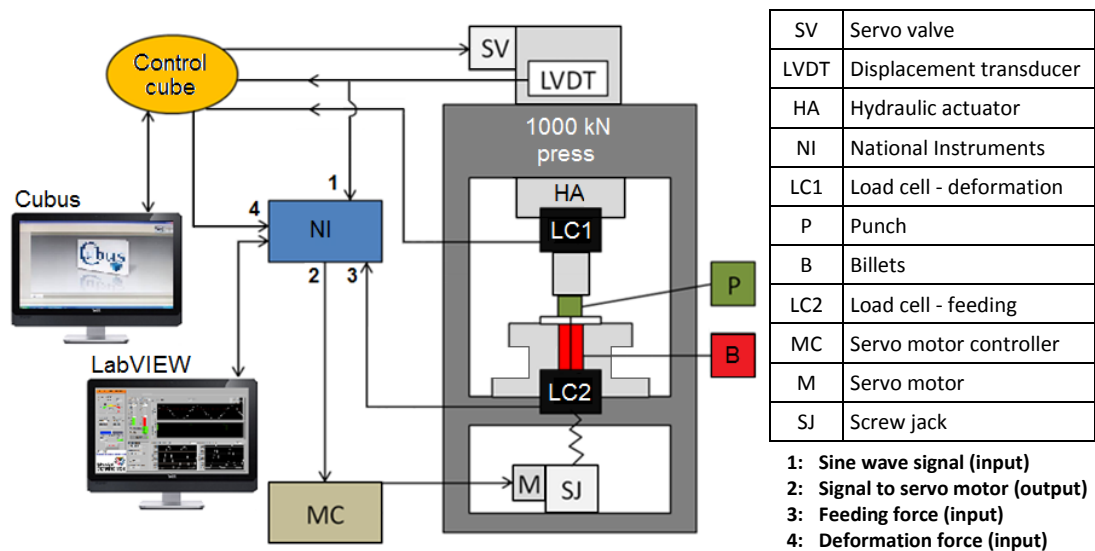


Fig. 4.9: The schematic diagram representing the connections between various elements of the I-ECAP rig.

There are two modes of the operation: synchronous mode and manual mode. Synchronous mode is used during the actual experiments to control, monitor and record data, whereas the manual mode is used during press setup and to eject the billet at the end of processing. The manual mode has two modes: jog mode and continuous mode. Jog mode is used during setup when precise and fine screw jack movements are needed, whereas continuous mode is used for rapid and long duration movements of screw jack.

The following Compaq DAQ input and output modules from National Instruments were used for instrumentation purposes (shown in Fig. 4.10(a)):

1. NI-9215:

An input module with 100 kS/s/ch, 16-bit, simultaneous input and 4-channels. This was used to acquire sine waveform signal commands from Cubus software for punch oscillations.

2. NI-9263:

An output module with 100 kS/s/ch, 16-bit, simultaneous input and 4-channels. This was used to send start and stop signals to servo motor via the control cabinet to drive the screw jack and to synchronize the billet feeding.

3. NI-9237

An input module with 50 kS/s/ch, bridge analogue input and 4-channels. This module was used to acquire feeding force values.

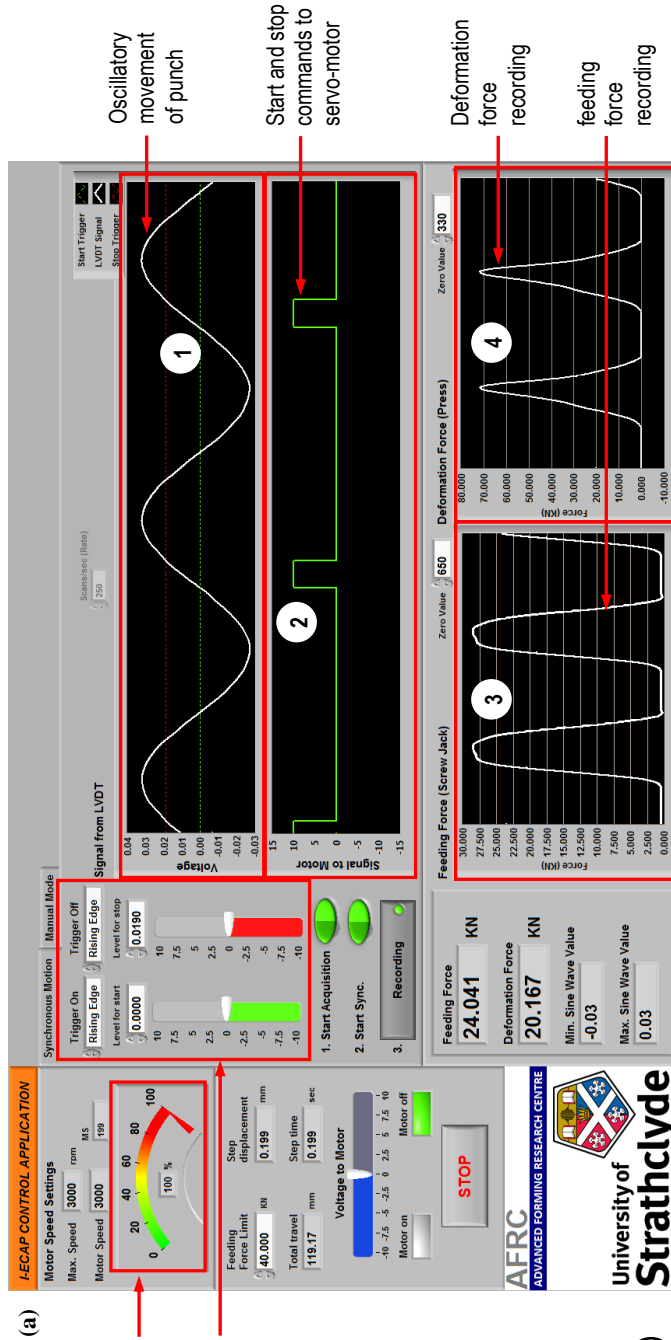
4. NI-9201:

An input module with 500 kS/s, 12-bits and 8-channels. This module was used to acquire deformation force values.

Note: Here *kS/s/ch* means *kilo scans per second per channel*

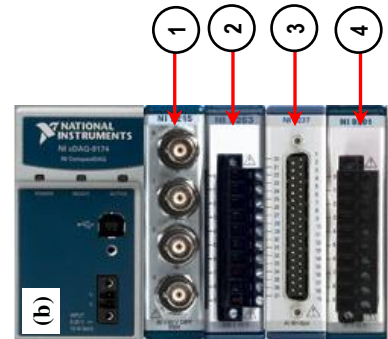
Fig. 4.10(a) shows the front screen of the LabVIEW application in synchronous mode. There are four display charts, the number on each chart corresponds to the respective I/O module to which it is connected. These display charts are used to monitor the sine wave signal (punch oscillations), start and stop commands to servo motor (for screw jack movement), feeding force and deformation force. The application also provide various other controls such as: controlling the rpm of the servo motor (via a dial control), setting the maximum upper limit of feeding force beyond which feeding is stopped to prevent any damage to the feeding force load cell and controls to setup the feeding stroke (defined as 'a' in Fig. 3.12).

Fig. 4.10: (a) Front screen of the LabVIEW virtual instrument application used to monitor, control and acquire data during the I-ECAP experiments and (b) National Instruments chassis along with the four I/O modules for data acquisition (the numbering on the chart corresponds to the respective I/O module to which it is connected).



Servo motor speed control

Controls to adjust the feeding stroke



The application acquires the sine wave form signal and uses it to synchronize the screw jack movement by sending motion start and stop command to the servo motor. Before explaining how the material feeding is synchronized, it is important to understand how the displacement profile of the punch oscillation (sine wave signal) is handled in the application. A full cycle of the sine wave is shown in Fig. 4.11. The sine wave is considered to be split into two parts: rising edge part (when the punch is moving up, blue colour line) and falling edge part (when the punch is coming down, red colour line).

To synchronize the material feeding, the user is required to setup the feeding stroke 'a' in the application. This is done by selecting either the rising or the falling edge of the sine wave for triggering motor start and stop commands. The application also requires defining levels on the sine wave form at which to trigger start and stop commands to the motor. The start and stop trigger levels are shown as square and diamond in Fig. 4.11, respectively.

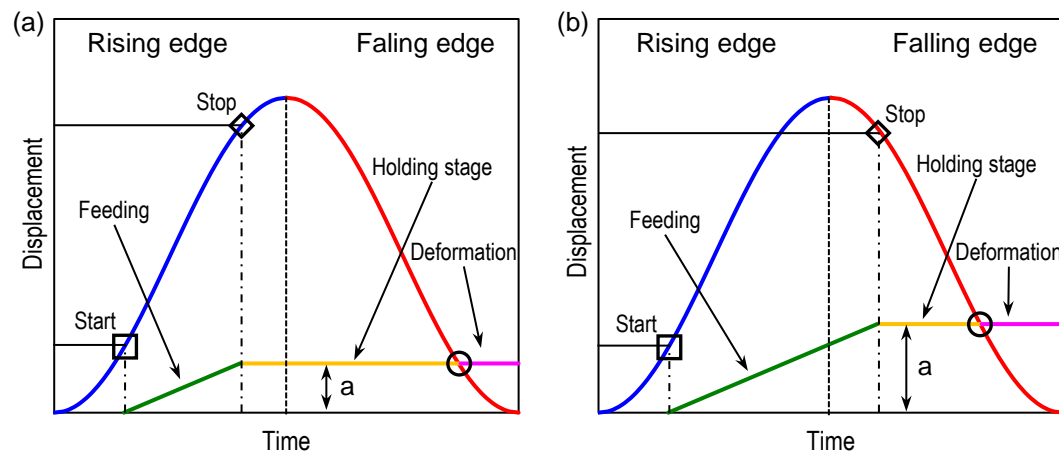


Fig. 4.11: Rising and falling edge of the sine wave form signal, (a) first scenario: material feeding starts and stops on the rising edge, (b) second scenario: material feeding starts on rising edge but stops on falling edge.

The figure also shows the displacement profile of the screw jack movement (solid straight lines) realized by the servo motor. The displacement profile is split into three regions shown in different colours. Green region of the line, represents the material feeding stage, the orange region represents the holding stage and the pink region represents the deformation stage (the small circle represents the initiation of deformation stage).

Two scenarios are shown in Fig. 4.11. Fig. 4.11(a) represents the first scenario, in which material feeding take place only during the rising part of the punch movement. However, since the amplitude of punch oscillations is normally set at higher values (between 1.2 and 2.0 mm), compared to the feeding stroke ('a' is between 0.2 and 0.5 mm), some initial portion of the falling edge can also be used for material feeding. As can be seen in Fig. 4.11(b), this second scenario enables higher values of feeding stroke compared to in first scenario.

Fig. 4.12 shows how the first scenario of material feeding is implemented using the I-ECAP LabVIEW application. Notice that signal to motor represents the voltage signal, level of which is seen to rise when the motor 'start trigger' condition is met and fall to zero once the 'stop trigger' condition is met.

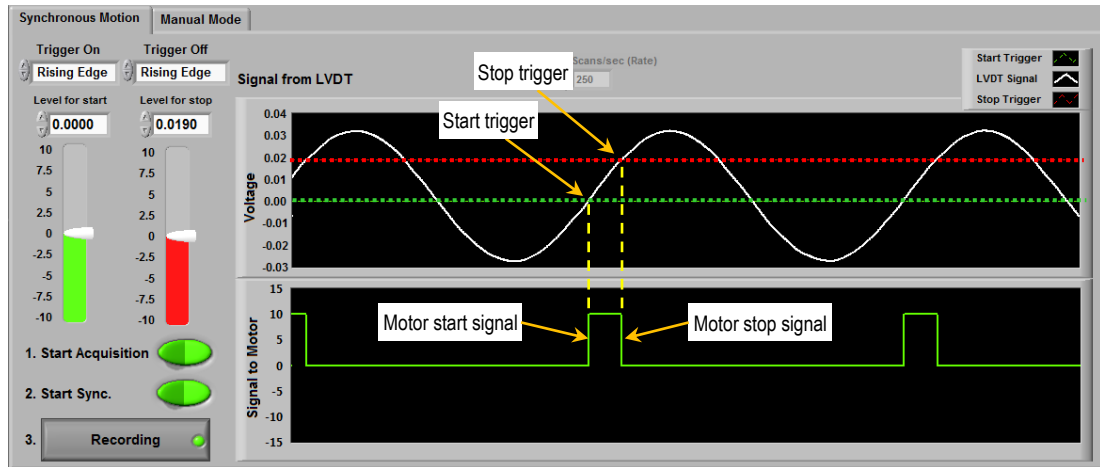


Fig. 4.12: Automatic material feeding using I-ECAP LabVIEW application based on the first scenario.

The I-ECAP LabVIEW application performs two major tasks. The first task is to perform data acquisition and analysis. The second task involves processing data (converting voltage values into actual load values) and writing it on the hard disk. Acquiring data takes place at a much faster rates compared to writing data. During the initial stages of application development, both processes were performed in a signal continuous loop. This immediately caused problems, as the data acquisition was waiting until the processed data was written to the hard drive which resulted in incomplete data acquisition. To overcome this problem, an efficient design

pattern/architecture known as ‘producer/consumer’ was programmed and implemented in LabVIEW (see Fig. 4.13).

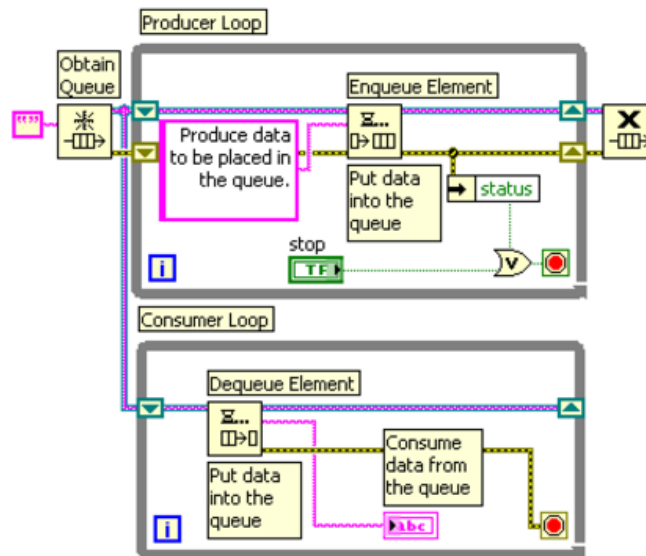


Fig. 4.13: Example of producer consumer design pattern taken from LabVIEW documentation

The producer/consumer design pattern is based on the Master/Slave pattern. The idea is to have two parallel loops running together, the master loop which ‘produces’ data constantly and passes the data to the slave loop which ‘consumes’ the data. Using this architecture, the data acquisition and analysis are implemented in the producer loop, which is followed by data being passed, using a system of queues to the consumer loop. The consumer loop processes the data and stores it in an internal buffer. Once the buffer is full, the data is dumped onto a hard disk. This way, the two processes can take place simultaneously but at different speeds.

It is important to mention here the readings from load cells connected to punch for measuring deformation force and to screwjack for measuring feeding force, were carefully calibrated in order to convert the raw signals in to actual load values in kN.

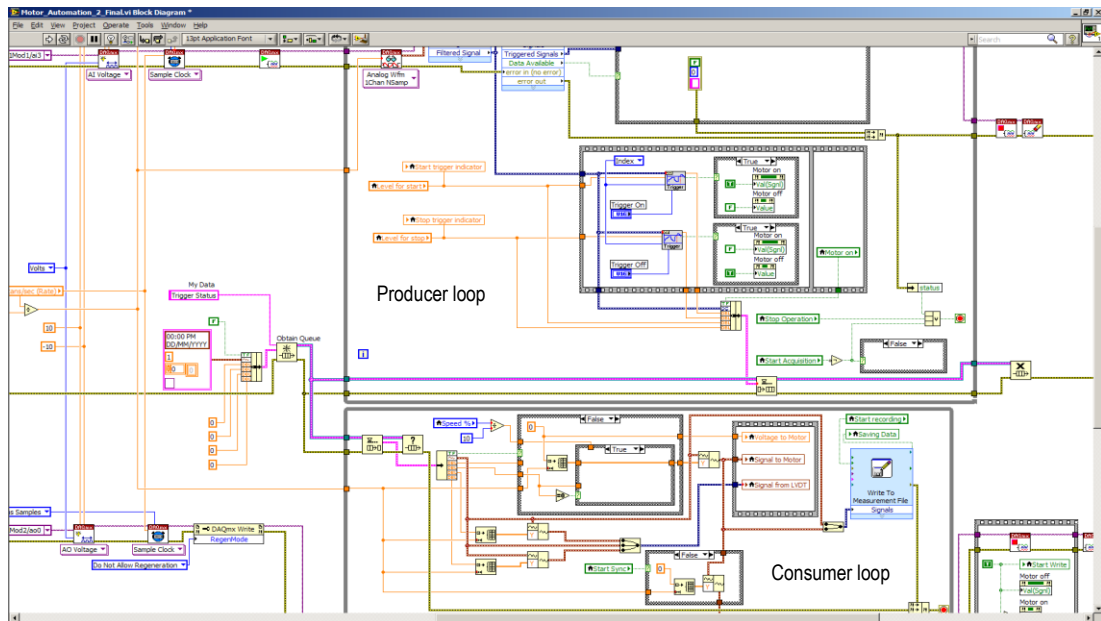


Fig. 4.14: Partial block diagram of the I-ECAP LabVIEW application showing the producer consumer loop.

The producer loop acquires the sine wave form signal coming from the NI-9215 module at a rate of 250 scans/s. Since I-ECAP is mostly performed at low frequencies between 0.5 to 2 Hz, a low pass filter with a cut off frequency of 10 Hz is applied to filter out any higher frequency signals. The application also applies some smoothing to the signal before the analysis. The data is processed in real time and as soon as the trigger start condition is met, the application sends voltage signal via NI-9263 module to the servo motor to enable material feeding. This is done until the sine wave form reaches the stop trigger condition at which point a ‘zero’ voltage signal is sent to stop the servo motor. Fig. 4.14 shows the partial block diagram implementation of the ‘producer/consumer’ loop.

4.3.5 General rig upgrades including safety controls

Other general rig upgrades included the following tasks:

1. Installation and commissioning of a MOOG servo valve on the 1000 kN press
2. Installation of a new hydraulic accumulator (pressure storage reservoir)
3. Installation and commissioning of an industrial chiller for cooling hydraulic oil and punch tooling.
4. General servicing of the hydraulic power pack
5. Installation of E-stops on the press for safety purpose and integration with servo motor controller.
6. Installation of a limit switch to impose hard limits on the upper and lower position of screw jack.

4.3.6 The completed setup

The completed I-ECAP experimental rig is shown in Fig. 4.15 after the upgrades and improvements. The figure shows the 1000 kN hydraulic press and all the other elements of the rig together.

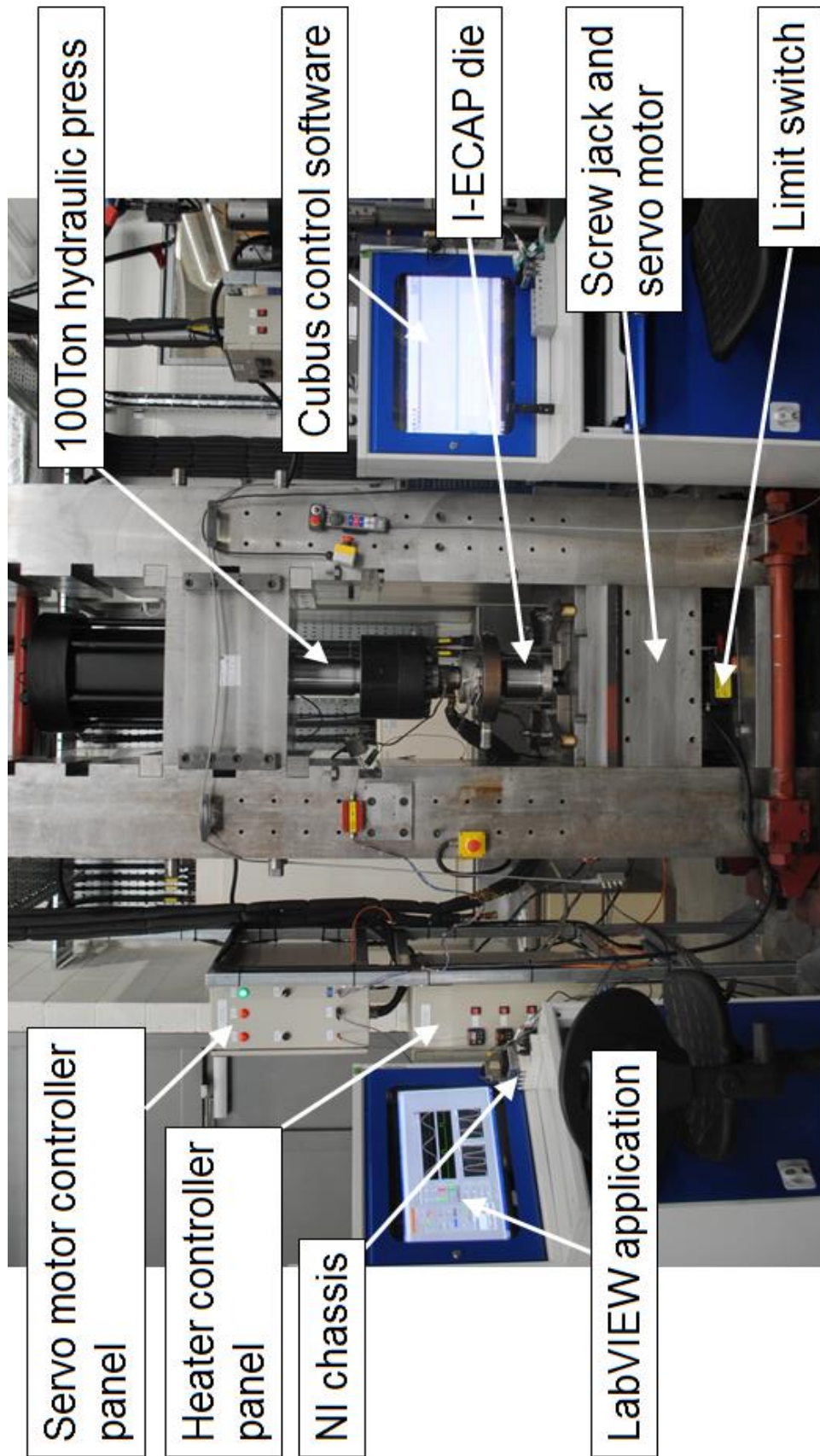


Fig. 4.15: The completed I-ECAP setup after the improvement and upgrades.

4.4 As received material

The as received material used in the present study was commercial purity titanium (CP-Ti), grade 2 in the form of a 12.5 mm thick rolled plate from Dynamic Metals Ltd (UK). The chemical composition of this material as reported in the conformance certificate is shown in Table 4.1.

Table 4.1: Chemical composition of as received CP-Ti grade 2 material used in this study (source conformance certificate)

Element	C	N	O	H	Fe	Ti
wt% (Max)	0.08	0.03	0.18	0.015	0.20	Balance

4.5 Billet preparation and lubrication

Square cross-section billets measuring 10 x 10 mm² (nominal value) and 120 mm in length were cut using wire electric discharge machining (EDM) such that the length of the billet was parallel to the rolling direction of the plate. A small 1 mm chamfer was machined at the top edge of the billet, to facilitate the flow of material during the initial stage of processing.



Fig. 4.16: Billet appearance after different steps of billet preparation (a) 1st step – initial machined billet, (b) 2nd step – sand blasted billet, (c) 3rd step – graphite coated billet and (d) 4th step – anti-seize lubricant applied.

As titanium is very susceptible to galling on the die walls, it was necessary to perform some steps related to billet preparation prior to I-ECAP experiments. These steps included sandblasting of billets, spray coating a thin layer of lubricant (2 parts graphite and 1 part water, mixed together) on the billets, drying in an oven at 100 °C

and finally brushing a thin coating of anti-seize lubricant Loctite 8009 from Henkel Ltd. This method of billet preparation and lubrication was the most effective to avoid any billet seizing during operation. The appearance of billet after different preparatory steps is shown in Fig. 4.16.

4.6 I-ECAP experimental procedure

The first step before starting the experiment is to centre the punch and align it with the I-ECAP die. The punch is fitted inside a punch holder which is attached to the press actuator, while the I-ECAP die-set is clamped onto the press bed. The alignment of punch and die is a crucial step, to avoid any wear or damage of tools during operation. Fig. 4.17 shows the importance of aligning the tools. The alignment is performed by adjusting the position of I-ECAP die on the press table and clamping it to the table to prevent any movement during processing. The setup mode of the Cubus software is used during the alignment phase.

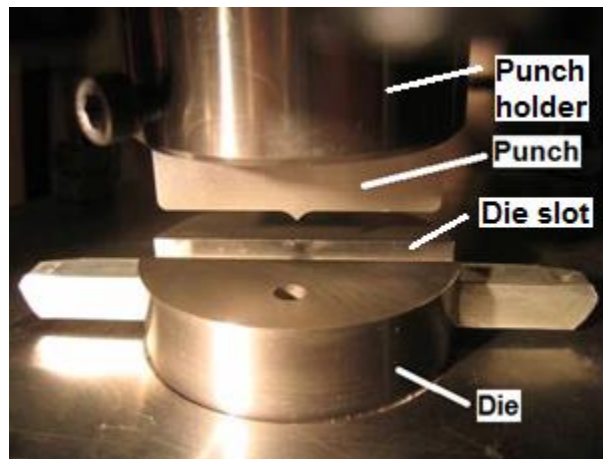


Fig. 4.17: Alignment of punch and die slot before I-ECAP experiments.

After alignment of punch and die, the heating is switched on and tools are allowed to heat up to the test temperature of 300 °C for about 3 hours. Once the die temperature is stable, the pair of lubricated billets is introduced inside the die vertical (inlet) channel. The billets are left inside the die for 15 mins, in order to achieve homogenous temperature distribution. It is important to mention here that the choice of 300 °C as processing temperature was based on literature review. This temperature

is believed to be high enough to enable processing of grade 2 titanium without failure and also low enough to minimize grain growth during processing.

Experiments were performed using a feeding stroke of 0.2 mm/cycle (0.1 mm/sec), punch oscillatory movement of 0.5 Hz with a peak to peak amplitude of 1.6 mm (Fig. 4.18). Table 4.2 shows the summary of processing parameter during I-ECAP experiments.

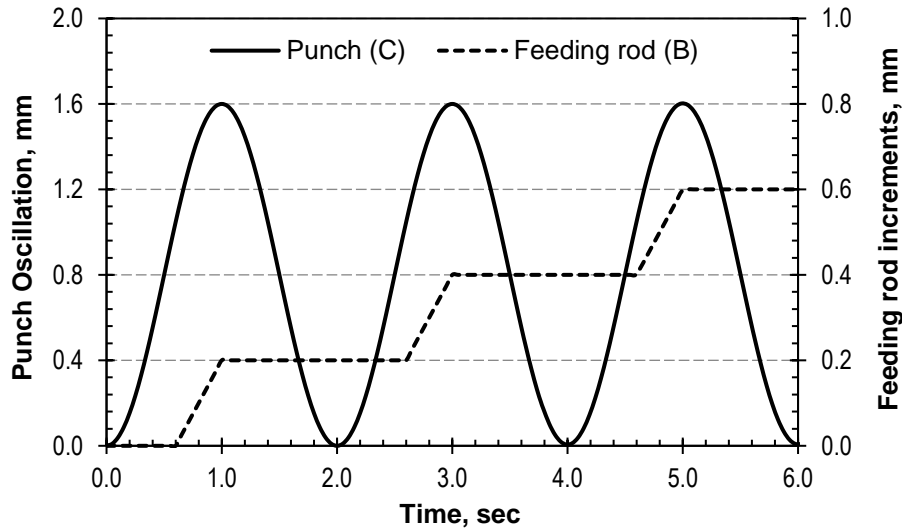


Fig. 4.18: Relative movement of punch and feeding rod during the I-ECAP process.

Table 4.2: Summary of processing parameters during I-ECAP experiments using dies with channel angle (Φ) of 120° and 90° .

No.	Variable	Category	Value	Unit
1	Outer corner angle (Ψ)	<i>Die geometry</i>	0° for $\Phi = 120^\circ$ die 15° for $\Phi = 90^\circ$ die	$^\circ$
2	Temperature		300	$^\circ\text{C}$
3	Processing route		B_C	-
4	No. of passes	<i>Processing conditions</i>	6 for $\Phi = 120^\circ$ die 4 for $\Phi = 90^\circ$ die	-
5	Strain induced per pass (Eq. 2.7)		0.67 for $\Phi = 120^\circ$ die 1.07 for $\Phi = 90^\circ$ die	-
6	I-ECAP variant		Double billet	-
7	Frequency of punch oscillation		0.5	Hz
8	Amplitude of punch oscillation	<i>I-ECAP parameters</i>	1.6 (peak to peak)	mm
9	Feeding stroke increment (feeding speed)		0.2 (0.1)	mm/cycle (mm/s)

4.6.1 Processing using die with channel angle (Φ) of 120°

The die configuration with channel angle (Φ) of 120° , presented in Fig. 3.12, led to an imposed strain of ~ 0.67 per pass Eq. 2.7. The billets were processed repeatedly and were subjected to a total of six passes giving a maximum strain of ~ 4.02 . Processing route B_C was followed in which the billet is rotated by 90° about its longitudinal axis in the same direction after each pass. Route B_C is considered to be the most effective in achieving homogenous microstructure in which grains are separated by high angle boundaries [166]. Compared to other routes, route B_C in Ti yields finer equi-axed grains, produces better surface quality billets [108] and also superior corrosion resistance [10]. Table 4.2 presents summary of processing parameters during I-ECAP experiments with 120° channel die. After each pass, the billets were quenched in cold water immediately, in order to suppress grain growth.

In Fig. 4.19 (a), the pair of CP-Ti billets can be seen emerging out of the I-ECAP 120° channel die at the end of the first pass. The process uniformly deformed billets and the macroscopic appearance of the processed billets was smooth with no visible signs of defects or surface cracks. However, the processed billets exhibited slight bowing, which prevented the same pair of billets to be re-inserted in the inlet channel for next pass. Therefore, a secondary straightening operation was performed by pressing the pair of billets on a 5000 KN hydraulic press between two flat dies heated to 200°C . Fig. 4.19 (b) shows the appearance of the billets at different stages: unprocessed billet before I-ECAP (bottom), after I-ECAP (middle) and after straightening operation (top).

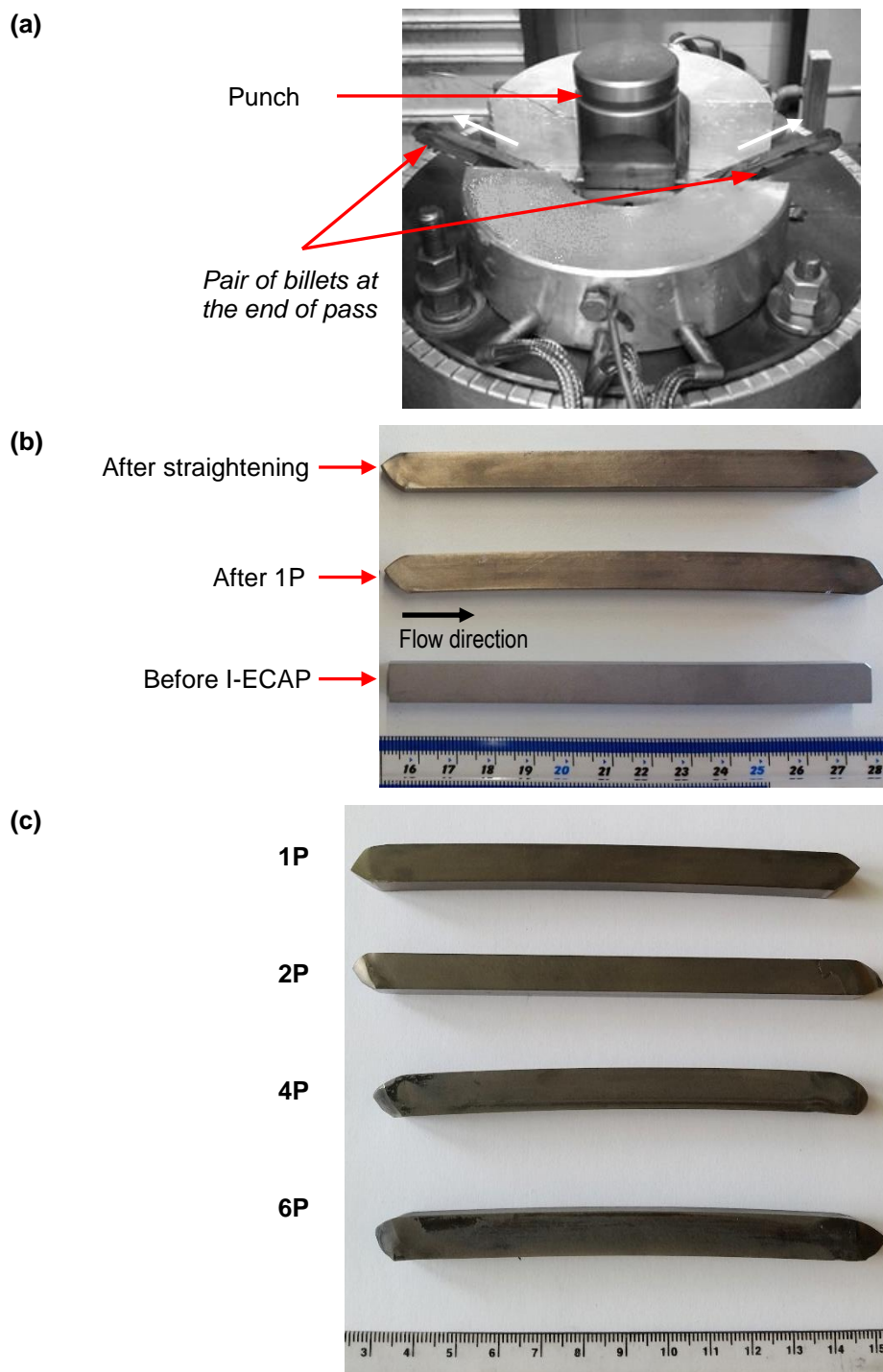


Fig. 4.19: (a) The pair of CP-Ti billets emerging at the end of first I-ECAP pass using $\Phi = 120^\circ$ channel angle die (white arrows indicate direction of material flow), (b) appearance of the CP-Ti billets: unprocessed billet (bottom), billet after first pass of I-ECAP showing bowing (middle) and straightened billet after secondary operation (top) and (c) appearance of CP-Ti billets after first, second, fourth and sixth pass of I-ECAP (second pass billet is straightened in the figure).

4.6.2 Processing using die with channel angle (Φ) of 90°

The billet preparation and experimental procedure for the channel angle of 90° was similar to experiments using the channel angle of 120° , the only difference was in the total number of passes, which was four. The channel configuration of 90° lead to an imposed strain of ~ 1.07 per pass leading to a total strain of ~ 4.28 after four passes. Fig. 4.20 shows the appearance of the billets after first, second, third and fourth pass of I-ECAP processing using the channel angle (Φ) of 90° . Notice that the billets are perfectly straight and therefore no straightening was required. This confirms that the optimized tooling geometry finalized after FE analysis was quite effective in eliminating any bending in billets.

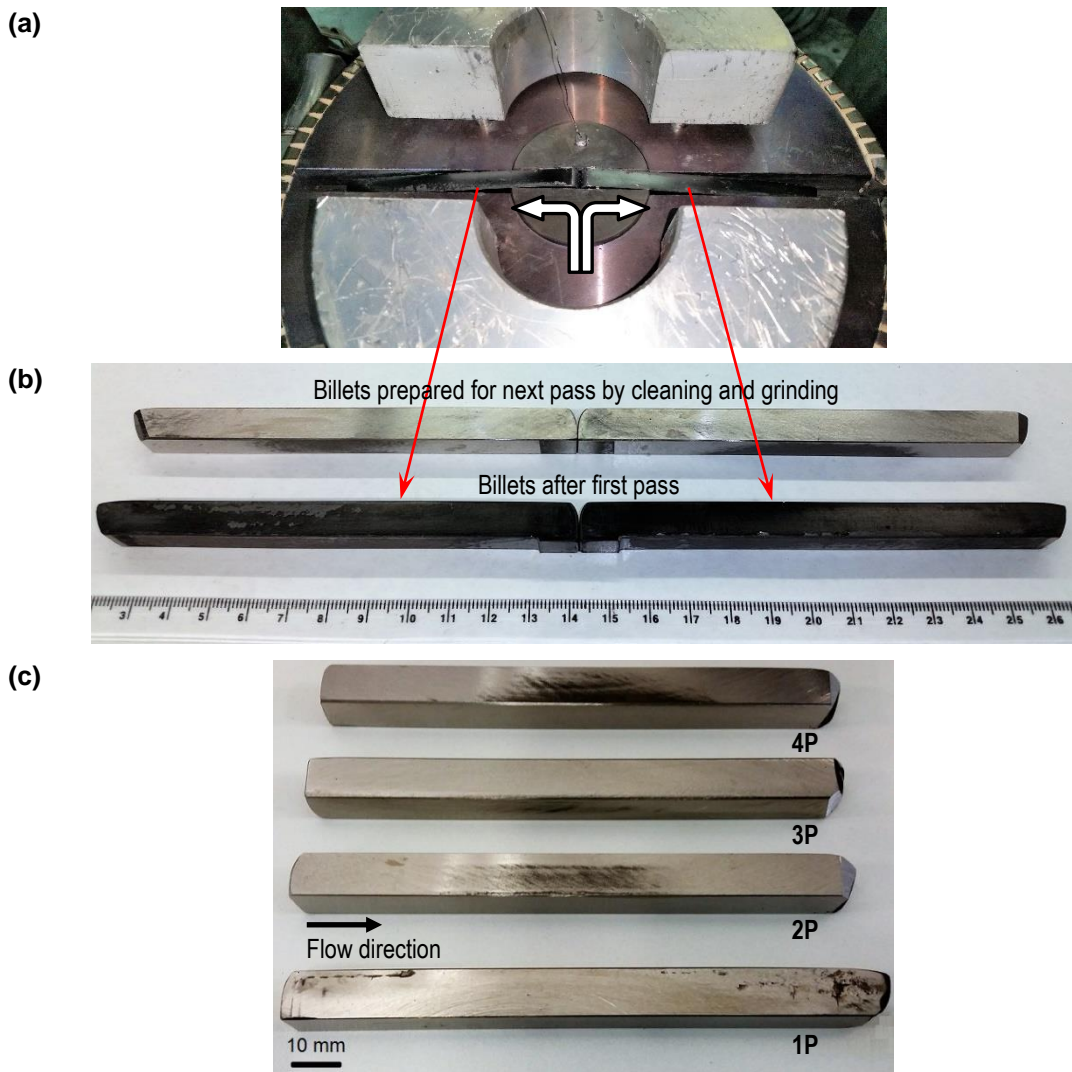


Fig. 4.20: (a) The pair of CP-Ti billets at the end of first I-ECAP pass using the $\Phi = 90^\circ$ channel angle die, (b) pair of billets (left and right) after first pass processing and (c) appearance of CP-Ti billets after first, second, third and fourth pass of I-ECAP (right hand billets are shown only).

There were some problems encountered during the initial trials with $\Phi = 90^\circ$ die (see Fig. 4.21 for illustration). Because of the pre-stressing of the die the internal channel dimensions were reduced. Although the unlubricated billets could still fit the channel however when billets were coated with lubricant and processed for the first time, they got badly stuck in the channel. This resulted in severe galling and titanium sticking to the channel walls. In an attempt to push the billets out of the die using feeding rod, the feeding rod got jammed inside the die channel. So the only way was to disassemble the whole die i.e. remove the pre-stressing ring and open the die-insert subassembly. The inside surface of the die-inserts (die walls) was re-ground to remove the residual titanium and to achieve the desired surface finish. The dies were assembled and pre-stressed again and a new feeding rod was manufactured as it was damaged when trying to force it out. The billet dimensions excluding the length were reduced all around by 0.1 mm to allow sufficient clearance after applying lubrication. The billets were processed again after the tool re-work was carried out. As seen in Fig. 4.20, billets were processed successfully and the problems encountered earlier were eliminated.



Fig. 4.21: Problems encountered during initial processing trials using the $\Phi = 90^\circ$ channel angle.

4.7 Microstructure characterization

4.7.1 Electron back scatter diffraction (EBSD)

Electron backscatter diffraction (EBSD) was used to characterize the microstructure in the unprocessed condition and after subsequent passes of I-ECAP. For characterization purposes, a slice of material was cut from the middle of the billet to avoid end effects. Initially, several attempts were made to prepare the samples for EBSD analysis by the author. These involved various combination of mechanical grinding, polishing, polishing using VibroMet machine and electro polishing. However, all such attempts to prepare samples and acquire EBSD data on the FEI's Quanta FEG 250 scanning electron microscope (SEM) failed.

Finally, it was decided to send the samples to Institute of Non-Ferrous Metals in Gliwice, Poland because of their ion milling facility. The surface of each sample was grinded on Buehler machines using 180, 320, 1000 and 4000 grit SiC papers. Polishing was done with colloidal silica using DP-Mol and OP-Chem. Finally, on RES101 ion milling machine, the sample surface was prepared for EBSD test according to the scheme: equalization, polishing and cleaning. The SEM used was an HRSEM FEI Inspect F50 with an EDAX TSL EBSD detector. The sample was tilted 70° from the horizontal plane for EBSD data collection, at a 20 kV accelerating voltage and 200 mA beam current. A step size of 0.40 µm was used for the unprocessed material and 0.08 µm for the processed material. The EBSD data with an average confidence index between 0.15 to 0.40 (for various samples) was analysed using TSL OIM software.

4.8 Mechanical testing

Various mechanical tests were performed on the unprocessed and processed billets to study the effect of I-ECAP processing on the mechanical performance of CP-Ti. The mechanical tests were performed on the samples, which were cut from the billets. For the purposes of identification it was necessary to first establish three orthogonal planes; X, Y and Z with respect to the billet. As illustrated in Fig. 4.22, X plane is the cross-sectional or transverse plane perpendicular to the longitudinal axis of the billet whereas Y and Z plane are flow and longitudinal planes parallel to the side face and the top face of the billet at the point of exit from the die, respectively.

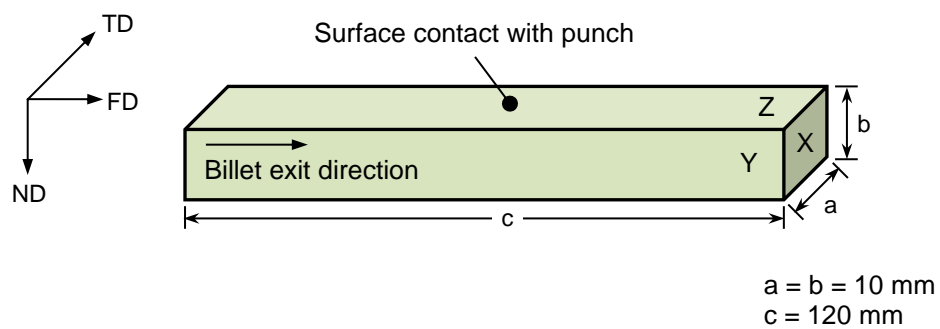


Fig. 4.22: Illustration of the three orthogonal planes (X, Y and Z) representing different sides of the billet.

4.8.1 Tensile testing

Tensile tests were carried out following the ASTM E8 standard [167], to evaluate the strength and ductility of the material in the unprocessed condition and after subsequent I-ECAP passes. For this purpose, flat tensile samples with a 14 mm gauge length and $3 \times 2 \text{ mm}^2$ cross-section (see Fig. 4.23 (a) for detailed dimensions), were cut parallel to longitudinal axis (Y plane) of the processed billet using 0.5 mm wire EDM. A set of three samples were cut from each billet across the width (a). To avoid the effect of any surface defect, the samples were cut 1 mm away from the side faces (see Fig. 4.23(b) for illustration).

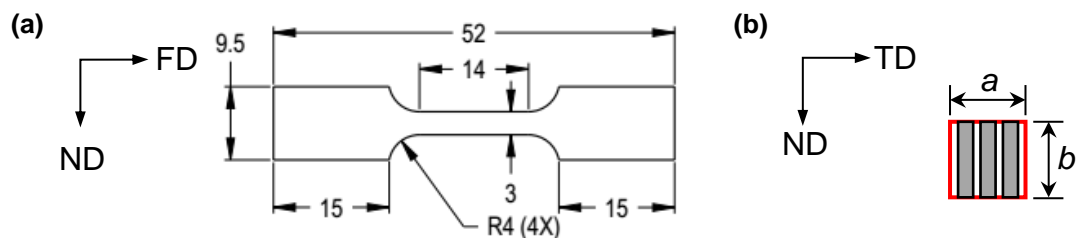


Fig. 4.23: (a) Dimensions (in mm) of the flat tensile sample used in this study and (b) illustration of the three tensile samples cut across the cross-section (X-plane) of the billet.

All tensile tests were performed on the Zwick/Roell Z150 test machine (shown in Fig. 4.24) with testXpert control software. The tensile sample was loaded and gripped between the wedge clamps of the machine. During testing the sample was pulled from the bottom at a constant strain rate until fracture. The elongation was measured as a displacement of the machine cross-head. The load-displacement data from each test was converted into true stress-strain curve. For each material condition, three separate tests were performed to ensure repeatability so the final stress-strain curve for each condition represents the average of the three tests.

4.8.2 Fractography

Following tensile testing, fracture surface of the samples was examined to study the fracture morphology, using the FEI's Quanta FEG 250 scanning electron microscope (SEM), operating at 20 kV and with secondary electron (SE) mode.



Fig. 4.24: Zwick/Roell Z150 tensile testing machine with the sample held by machine grips.

4.8.3 Compression testing

To investigate workability characteristics and deformation behaviour of the material after I-ECAP, uniaxial compression tests were performed both at room temperature and at elevated temperature. Samples for compression testing were precision machined from the billet by turning, such that the axis of the compression sample was parallel to the longitudinal axis of the billet, as shown in Fig. 4.25(a).

During compression testing it is necessary for the sample to deform under uniaxial condition, which means that sample should be able to maintain its cylindrical shape during tests. This situation is however difficult to achieve due to friction between sample surfaces and machine platens. Such friction can cause 'barrelling effect' in samples, wherein the sample does not deform under ideal uniaxial condition. A simple but effective method to reduce friction is to use so called Rastegaev type samples

[168]. These samples have a shallow cavity (recess) at top and bottom surface of the sample, as shown in Fig. 4.25(b). The idea is to fill the cavity with lubricant, the cavity will then act a lubricant reservoir and prevent lubricant being squeezed out during the compression testing. This approach reduces friction and substantially minimizes barrelling during compression testing. A machined cylindrical compression sample is shown in Fig. 4.25(c).

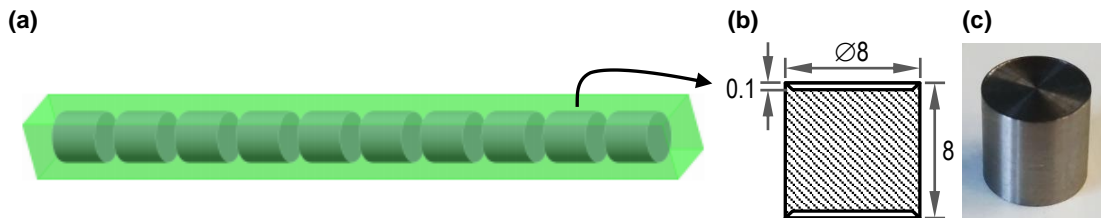


Fig. 4.25: (a) Plan of cutting compression samples from billets, (b) external dimensions of Rastegaev type sample used in the study (see appendix D for detailed drawing) and (c) machined cylindrical compression sample.

Room temperature compression testing was performed following the ASTM E9 – 09 standard [169] whereas, elevated temperature testing was performed following the ASTM E209-00 standard [163]. For room temperature tests, the top and bottom surface of the compression samples were coated with molybdenum-disulphide (MoS_2). For elevated temperature tests, the sample surfaces were coated with graphite. For both conditions, the anvil surfaces were coated with a boron nitride.

Both type of tests were performed on the Zwick/Roell HA250 servo hydraulic testing machine with a 250 KN load cell (shown in the Fig. 4.26(a)). The machine is equipped with a high speed data acquisition system and a temperature controller. The machine has a fixed lower platen and a movable upper platen, both made of high strength material. To enable elevated temperature experiments, tooling can be enclosed inside a split type furnace installed on the machine. The arrangement of these different components is shown in Fig. 4.26(a). During compression testing, cylindrical sample is compressed between the two platens; see Fig. 4.26(b).

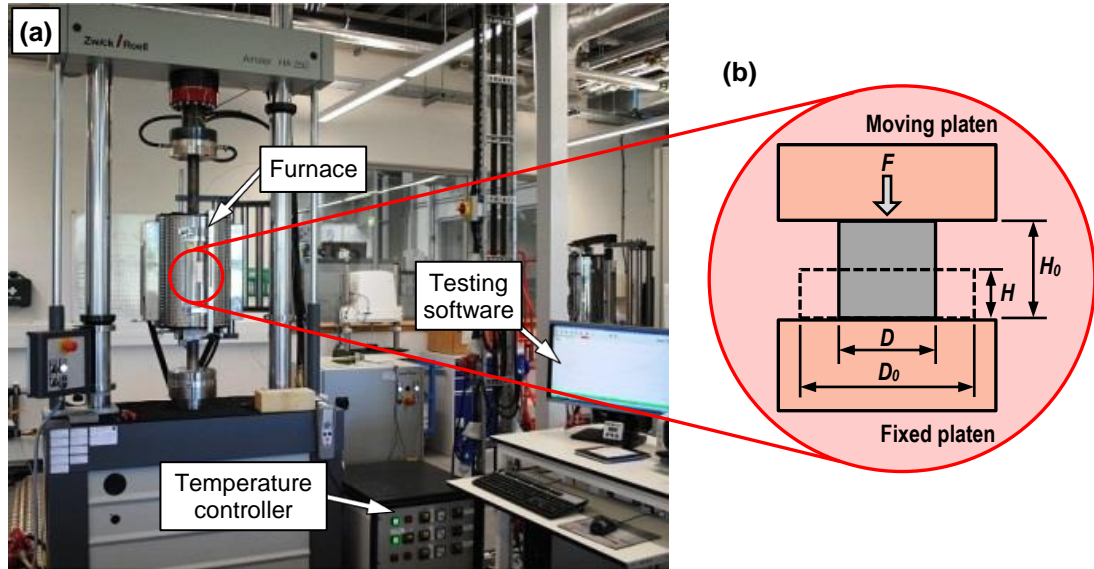


Fig. 4.26: (a) Zwick/Roell HA250 servo hydraulic testing machine and (b) position of compression sample between the platens (light red background represents the furnace environment).

Because of high forces experienced during the test, machine elements were also deformed elastically and became part of the force-deformation curve obtained from the test. To eliminate this error, compliance testing was performed at each test conditions in which the machine platens were pressed without any sample between them. The correction curve obtained from the compliance testing was then subtracted from the original curve to obtain true deformation values for the test sample.

The true stress and strain values were then derived from the force and deformation measurements, and were calculated using the Eq. 4.1 and Eq. 4.2

$$\sigma_e = \frac{F}{A_0}; \quad \epsilon_e = \frac{\delta H}{H_0} = \frac{(H - H_0)}{H_0} \quad \text{Eq. 4.1}$$

$$\sigma_t = \sigma_e(1 + \epsilon_e); \quad \epsilon_t = \ln(1 + \epsilon_e) \quad \text{Eq. 4.2}$$

where σ_e and ϵ_e are the engineering stress and strain, respectively; σ_t and ϵ_t are the true stress and strain, respectively; F , A_0 , H_0 and H are the compression force, original area, original and instantaneous height, respectively. Note that because of the form of Eq. 4.2, the ϵ_e will appear as negative values and consequently ϵ_t will be negative as well. So for plotting flow stress curves (true stress-strain), the function $\text{abs}(\epsilon_t)$ is used in excel.

4.8.4 Hardness measurements

Hardness measurements were performed to investigate the evolution of hardness and to examine the homogeneity of strain distribution during I-ECAP processing. Samples measuring 10 mm in thickness, were cut from the centre of the unprocessed billet and from first, second, fourth and sixth pass billets across the transverse (X) plane. Each sample was then mounted and polished to a mirror-like finish using 600, 1200, 2500 and 4000 grit SiC papers. Vicker's micro-hardness (H_v) measurements were taken on the surface of each sample using Zwick ZHV μ micro hardness tester equipped with Vickers indenter. For each measurement, a load of 1000 gf was applied for a dwell time of 10 secs. The measurements were taken on a 2D grid style pattern of 11 x 11 equi-spaced points (as shown in Fig. 4.27) along TD and ND directions respectively, after leaving a gap of 0.5 mm from all four side walls. This resulted in a total of 122 measurement points across the sample surface. A detailed contour map was subsequently generated representing the hardness distribution profile for each sample condition.

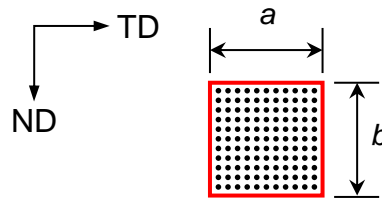


Fig. 4.27: 2D grid style pattern of 11 x 11 equi-spaced points on the surface of the sample used for microhardness measurement study.

4.9 Summary

The chapter outlined the details about the I-ECAP experimental rig. The previous I-ECAP experimental configuration was not ideally suited for research and possible industrialization. Apart from being old and bulky, there were issues resulting from the manual feeding of the billets during experiments. To demonstrate the I-ECAP process as a viable method for commercialization, major upgrades and improvement were carried out. New features implemented by the author as part of this work, such as automatic material feeding and data acquisition and process control via the LabView application are expected to make the I-ECAP process more efficient, robust and repeatable.

The upgrades and improvements of the rig have greatly enhanced the operational efficiency of the process. The improved I-ECAP rig has been successfully demonstrated to process CP-Ti billets during multiple passes. Experiments were performed using die with a channel angle (Φ) of 120° and 90° . Processing was done at 300°C following route B_C, used in both cases. For $\Phi = 120^\circ$ case, the billets were subjected to a total of six passes, whereas for $\Phi = 90^\circ$ case the billets were subjected to four passes. In the case of $\Phi = 120^\circ$, the billets obtained were slightly bent and to which straightening was carried out before next pass processing. However, the billets were uniformly deformed and the macroscopic appearance of the billet surface was smooth, with no visible signs of defects or surface cracks. After some initial problems, similar results were obtained in the case of $\Phi = 90^\circ$. It is important to emphasize here that the new 90° I-ECAP die produced straight billets (no bending or bowing). The processed billets required very little preparation for the next pass. Thus the 90° I-ECAP die geometry which was optimized after FE simulations, proved to be very effective in experimental trials.

To investigate the effect of I-ECAP processing on the material, microstructural characterization and different mechanical testing were performed. The details of the equipment, test samples, test conditions and the standards used were presented. The obtained results are discussed in Chapter 5 to 7.

Chapter 5

Microstructure evolution and mechanism of grain refinement during I-ECAP

5.1 Introduction

With the exception of a few studies mentioned in section 2.9.1, all the other studies have characterized CP-Ti after only a certain pass, moreover the choice of TEM limits the scanned area under observations. Therefore, there exists a requirement for carrying out detailed investigation to observe the deformation process and to study the microstructural evolution and textural development during processing of CP-Ti.

The aim of the chapter is to perform such investigation by employing EBSD analysis to study relatively large scan areas. Moreover, in this work, processing is carried out using two different I-ECAP dies with a varying channel angle (Φ) of 120° and 90°.

The chapter is organized in three sections:

1. First section contains the microstructural details of the as-received CP-Ti.
2. Second section contains a complete study on the microstructure evolution and textural development along both flow and transverse direction of CP-Ti samples processed at 300 °C using an I-ECAP die with channel angle (Φ) of 120°. In depth discussion is also presented in this section, to explain the mechanism of grain refinement during I-ECAP.
3. Third section includes the microstructural observations and deformation characteristics during I-ECAP processing of CP-Ti using $\Phi = 90^\circ$ die.

5.2 Microstructural characterization

It is convenient to recall the reference system (three orthogonal planes); X, Y and Z with respect to the billet presented in 4.7.1. As illustrated in Fig. 5.1, X-plane is the cross-sectional or transverse plane perpendicular to the longitudinal axis of the billet whereas Y and Z-plane are flow and longitudinal planes parallel to the side face and the top face of the billet at the point of exit from the die, respectively. Samples from the unprocessed and processed billets were cut using a linear precision saw, following the cut plan as shown in Fig. 5.1.

Microstructural observations along the flow direction were made on the Y-plane (FD-ND), while observations along the transverse directions were made on the X-plane (TD-ND). Here FD, TD and ND represents the flow, transverse and normal directions respectively. Note that in the I-ECAP process, the billet is pressed/fed from the bottom as opposed to being pressed from the top in conventional ECAP, the ND direction is therefore shown to point downwards to make it consistent.

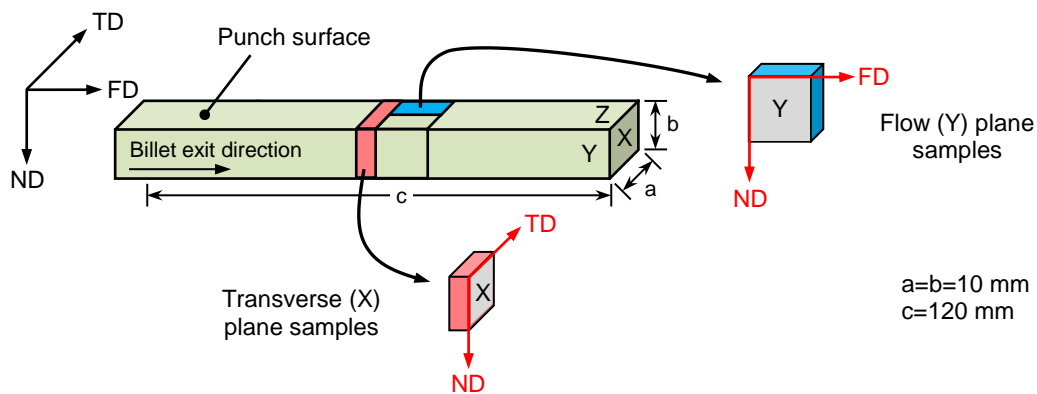


Fig. 5.1: Illustration of the three orthogonal planes (X, Y and Z) with respect to the billet and the cut plan to obtain samples along flow and transverse plane for microstructure analysis (the polished surface is represented by grey colour in these cut samples).

5.3 As received microstructure

Microstructural characteristics of CP-Ti before and after I-ECAP processing were analysed using SEM based EBSD technique. Fig. 5.2 shows the coloured inverse pole figure (IPF) map of the unprocessed material, in the (a) flow (Y) and (b) transverse (X) plane of the as received samples along with the corresponding misorientation histogram. The RGB colour code: red for (0001), green for $(2\bar{1}\bar{1}0)$ and blue for $(10\bar{1}0)$ as shown in the standard stereographic triangle (inset in Fig. 5.2(a)),

corresponds to the crystallographic orientation of each grain. The colour variations within the grains qualitatively represents difference in internal orientations.

It appears that the grains are more or less equiaxed in morphology and the grain size analysis reveals an average grain size of 20 and 22 μm , on the flow and transverse planes, respectively. A small fraction of twins are also seen in the microstructure. The grain boundary maps obtained from the EBSD analysis (not shown here) confirm that the boundaries of the grains in both flow and transverse plane are high angle ($\theta > 15^\circ$) in nature with minor misorientation variation within the grain interiors. This minor misorientation is also evident in the IPF maps which show slight colour variations within the grain interiors.

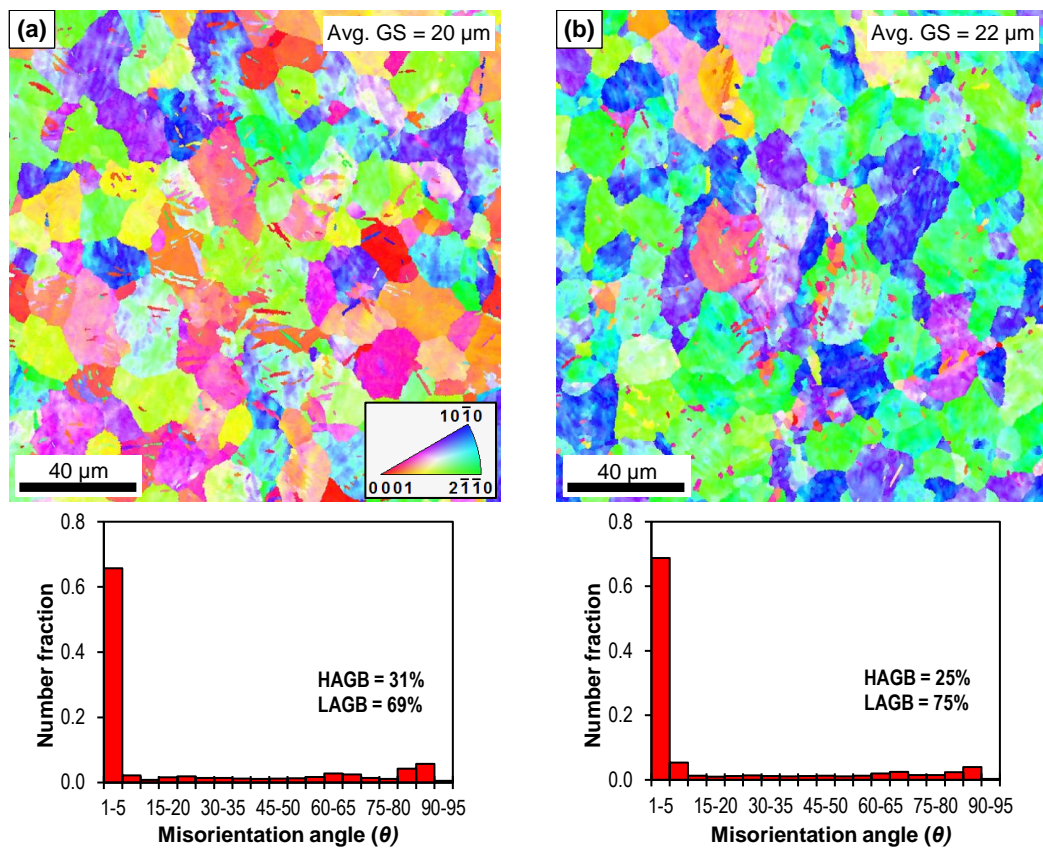


Fig. 5.2: Coloured inverse pole figure (IPF) maps obtained from EBSD analysis showing the microstructure of unprocessed CP-Ti samples in the (a) flow (Y) and (b) transverse (X) plane along with the corresponding misorientation histogram. The colours correspond to the crystallographic orientations shown in the standard stereographic triangle. Colour variations within grains qualitatively represents change in internal orientations.

Fig. 5.3 shows the relevant pole figures recorded on basal (0001), prismatic ($10\bar{1}0$) and pyramidal ($11\bar{2}0$) planes representing the texture of the unprocessed material in the (a) flow and (b) transverse plane. These textures were recorded on the samples at the same measurement areas as used for the IPF maps. Fig. 5.3(a) represents the texture characteristics of the grains in the flow plane, which exhibits typical rolling texture as observed in HCP materials [170]. (0001) pole figure shows the presence of a basal texture with the c -axis of the majority of grains inclined at an angle ± 30 - 60° from TD towards FD. The ($10\bar{1}0$) and ($11\bar{2}0$) pole figures indicates that a -axis of the HCP lattice is randomly oriented in the rolling plane, and there is no preferred orientation for prismatic and pyramidal planes (Fig. 5.3(a)). The estimated textures show that the basal planes of the grains are preferentially oriented parallel to the rolling direction. As a result, a ring texture is formed in the (0001) pole figure, where the basal pole densities are distributed 360° non-uniformly at the periphery of the pole figure (Fig. 5.3(b)).

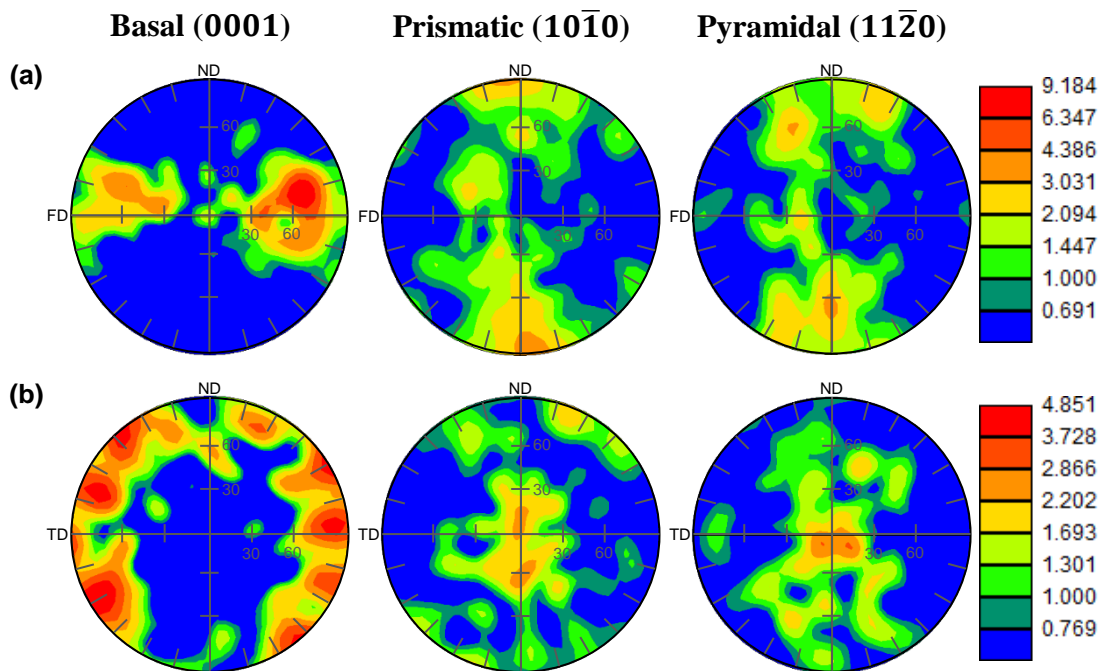


Fig. 5.3: Experimental pole figures illustrating texture on 0001 (left), $10\bar{1}0$ (middle) and $11\bar{2}0$ (right) planes in un-processed CP-Ti samples in the (a) flow (Y) plane and (b) transverse (X) plane. The texture intensity is represented by the colour scale bar for the corresponding pole figure.

5.4 Processing using I-ECAP die with channel angle (Φ) of 120°

5.4.1 Microstructural evolution - Flow (Y) plane

The post deformation microstructure was examined using high resolution SEM-EBSD technique. Fig. 5.4 shows the coloured IPF maps, representing the evolution of microstructure and deformation characteristics in the flow (Y) plane of the samples subjected to (a) first (b) second (c) fourth and (d) sixth pass of I-ECAP process. As mentioned earlier, each pass gives a strain of ~ 0.67 so these IPF maps correspond to a total strain of 0.67, 1.34, 2.68 and 4.02, respectively. The FD and ND directions are shown in Fig. 5.4(a) and are applicable for all the IPF maps in flow plane. It is also important to emphasize that the samples for EBSD analysis were taken from the centre region of the processed billets to avoid any end effects and surface defects due to friction.

EBSD scan of the sample subjected to first pass of I-ECAP in Fig. 5.4(a) shows that most of the grains are elongated and forming a typical banded style microstructure due to the shearing process. The metal flow pattern is similar with those developed in other metals after first pass of ECAP processing [166]. This pattern is mainly influenced by the channel intersection angle (Φ) during the first pass. In general, the microstructure is heterogeneous and three regions can be identified similar to those seen in [171]. Region 1 is a coarse grain which has been elongated and appears to be largely deformation free with the size similar to pre-existing coarse grains. Colour variation within this coarse grain suggests minor misorientations are accumulated within the grain. With further straining, these misorientations will increase, which is likely to result in formation of new smaller grains with high angle boundaries. Region 2 consists of a comparatively thin banded structure, which have likely deformed to form new elongated grains. The bands measure tens of micrometres in length and a few micrometres in width, therefore, are not considered to be of the ultrafine scale. Region 3 consists of fine equiaxed grains in the size range less than 3 μm ; it is also seen that some of these fine grains have nucleated along the grain boundaries of larger elongated grain. Microstructure having such fine grains along the grain boundaries is termed as necklace structure. The smallest grains are about ~ 500 nm in size, however

their fraction is quite low. This shows that ultrafine grains have already begun to form after the first pass.

As seen in Fig. 5.4(b), after second pass of I-ECAP processing, the microstructure is further refined compared to the first pass. As a result, many more fine grains have formed while the number of elongated grains has decreased considerably. Also, the length and width of the remaining elongated grains have been greatly reduced due to the total amount of strain induced. The majority of these elongated grains have orientations, which range from basal plane 0001 (red) to either half way to $10\bar{1}0$ (pink) or less than half way to $2\bar{1}\bar{1}0$ (orange).

Fig. 5.4(c) represents the microstructure after the fourth pass of I-ECAP processing. The microstructure has significantly changed from the first pass microstructure as the banded nature has been lost completely alongside the tilted material flow pattern. It is observed that a great amount of grain refinement has taken place, this is confirmed by the almost non-existence of elongated grains and the domination of equiaxed fine grains.

Fig. 5.4(d) shows the EBSD microstructure of the sample after six passes. Notice the use of higher magnification for the image, as indicated by 5 μm scale bar compared to 20 μm in previous three images. The grains here are mostly equiaxed, however it is seen that some grains are slightly elongated and generally oriented in the billet extrusion direction (considered to be the characteristic of route B_C). Although tremendous grain refinement has taken place, it seems that with further passes more refinement in grain size is possible.

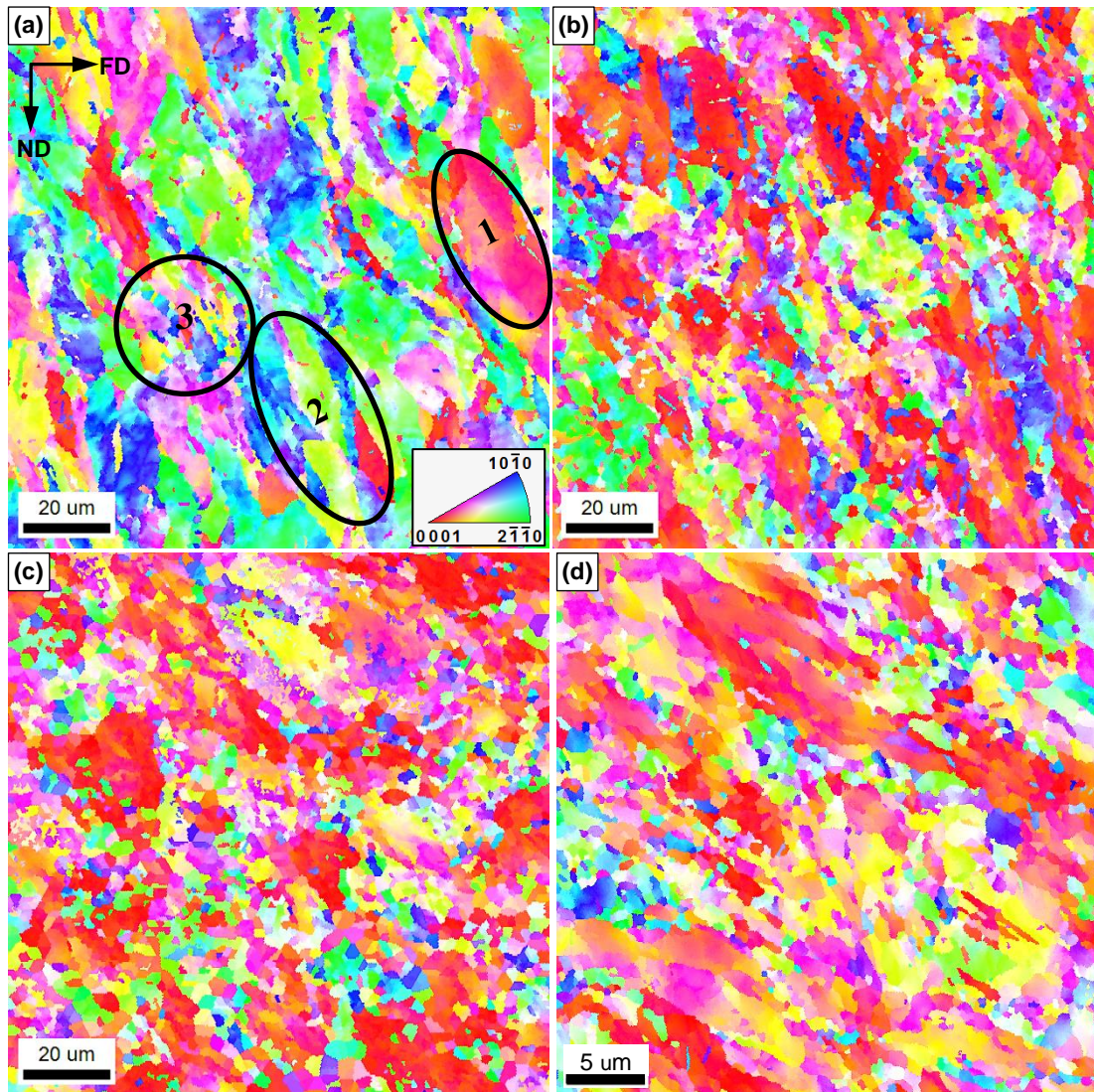


Fig. 5.4: Coloured inverse pole figure (IPF) maps obtained from EBSD analysis showing the evolution of microstructure and deformation characteristics in processed CP-Ti samples in the flow (Y) plane after (a) first, (b) second, (c) fourth and (d) sixth pass of I-ECAP at 300 ° C using the die with channel angle (ϕ) of 120°. The colours correspond to the crystallographic orientations shown in the standard stereographic triangle (inset). Colour variation within the grains qualitatively represents differences in internal orientations. Note that scale bar used in (a) to (c) is 20 μm whereas in (d) is 5 μm , due to high magnification image.

Fig. 5.5(a-d) shows grain boundary maps of the IPF maps presented in Fig. 5.4 (a-d). In these figures, the light blue lines represent the low angle grain boundaries (LAGB) with misorientation angle (θ) between 1.5 to 15°, whereas the thick red lines represent the high angle grain boundaries (HAGB) with misorientation angle (θ) greater than 15°. The figure on the upper right of each grain boundary map shows the corresponding histogram of grain size (equivalent circle diameter) with the solid line representing the cumulative grain size distribution function. The figure also includes

the value of calculated average grain size (GS). Accordingly, the figure on the bottom right of each grain boundary map shows the corresponding histogram of grain misorientation with the solid line representing the cumulative grain misorientation distribution function. The figure also includes the calculated fraction of LAGB and HAGB as a percentage. Note that 1P, 2P, 4P and 6P in the Fig. 5.5(a-d) represents the respective I-ECAP pass numbers.

These plots in Fig. 5.5(a-d) demonstrate a very clear evolution of microstructure in the flow plane with the increasing number of passes. In general, the grain size histogram shows that the bars are shifting towards the left, indicating the increase in grain refinement achieved due to subsequent processing. Moreover, the grain misorientation histogram reveals that the fraction of HAGB is gradually increasing with the increasing number of passes.

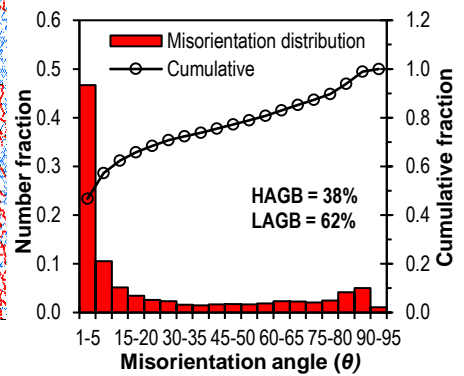
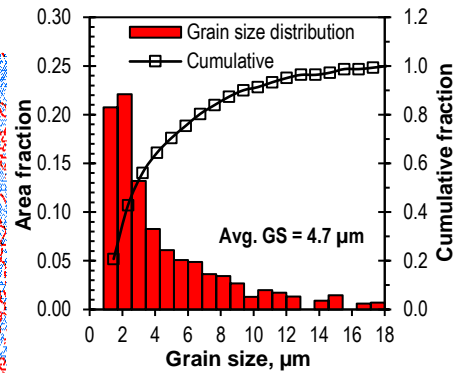
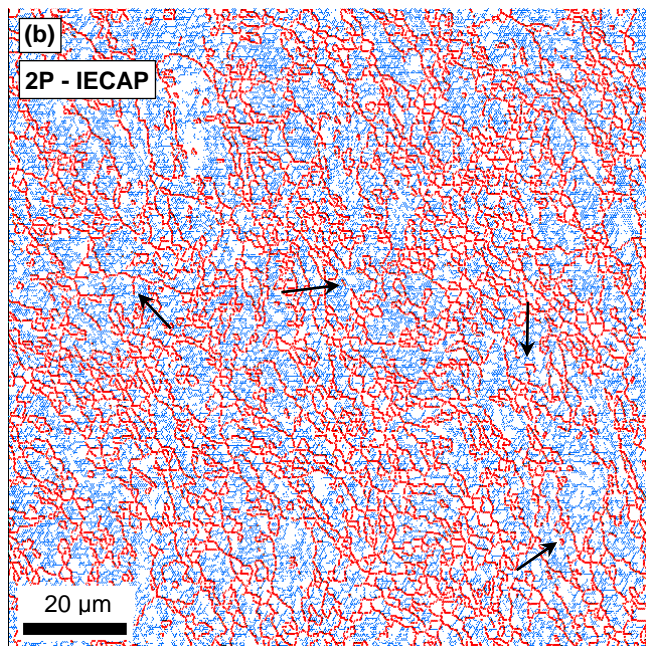
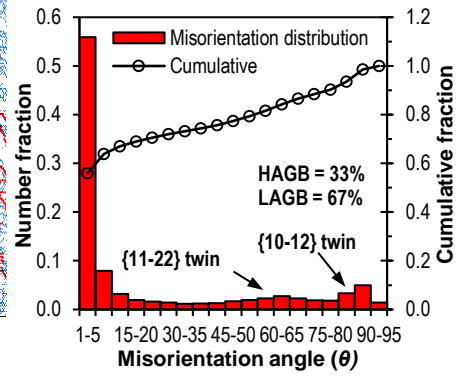
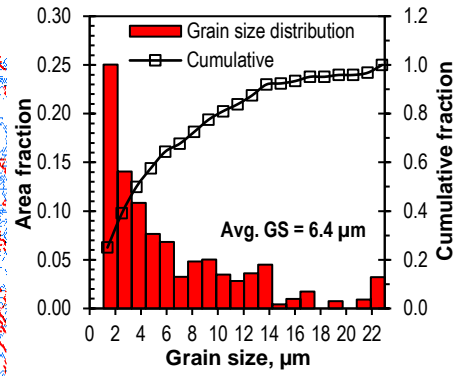
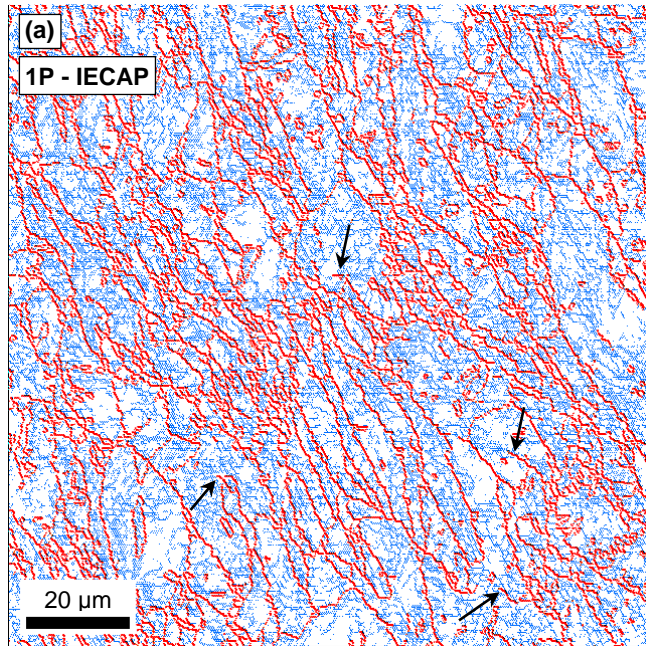
The grain boundary map in Fig. 5.5(a) confirms the existence of mostly elongated grains with small fraction of fine grains in the microstructure. There is some evidence of these fine grains situated alongside the boundaries of larger elongated grains. The corresponding grain size histogram of Fig. 5.5(a) reveals a tiny fraction of grains which are above 20 μm . This confirms the presence of pre-existing deformation free coarse grains, which was seen as an elongated grain (circled as 1) in Fig. 5.4(a). The grain boundary map also reveals that the microstructure has mostly low angle grain misorientations, as evident by the abundance of blue lines after the first pass of I-ECAP. The corresponding grain misorientation histogram confirms this as well. By examining the grain boundary misorientation histogram carefully, twinning behaviour during the deformation can be observed. The histogram shows a noticeable peak of misorientation at around 85° , which would indicate that these boundaries correspond to the $\{10\bar{1}2\}$ tensile twin boundary [110]. There is also a minor peak in the misorientation histogram at $\sim 65^\circ$, signalling that the $\{11\bar{2}2\}$ twins were also operative during deformation. Twinning behaviour will be discussed further in the following section.

The grain boundary map after second pass in Fig. 5.5(b) shows that the grains have been further refined with more than 90% of the grains smaller than 10 μm and with 40% of the grains between 0.7 to 2.0 μm size. The fraction of elongated grain has been reduced considerably. Careful observation of the grain boundary maps reveals

that some of the grains contains incomplete HAGB segments, the individual location of these incomplete HAGB are pointed by a black arrow. These HAGB does not seems to be fully enclosed. These boundary segments are believed to be arising due to continuous dynamic recrystallization (CRDX) process. It is also seen that the fraction of LAGB has been reduced whereas the fraction of HAGB has been increased, compared to the first pass. Similar to first pass, the corresponding histogram for the second pass also shows a misorientation peak around 85° , which would indicate the presence of $\{10\bar{1}2\}$ tensile twins. However, the peak around $\sim 65^\circ$ misorientation has been reduced, indicating a much decreased activity of $\{11\bar{2}2\}$ twins.

Fig. 5.5(c), which represents the grain boundary map after fourth pass, shows that majority of grains have been refined, with close to 80% of the total area fraction between 1 to 4 μm . As can be seen, the grains are now mostly equiaxed and the size distribution is becoming homogenous. Examination of the corresponding misorientation histogram does not show any preferential peak for suspected twins. This is consistent with the experimental results reported in literature, whereby finer sized grains hinder deformation twinning [172]. As the grain size decreases the stress required to activate deformation twinning increases greatly compared to the stress required for slip type dislocations [173]. Therefore for higher passes as the grain size continue to decrease, deformation by slip mode becomes more favourable.

Fig. 5.5(d) continue to exhibit the remarkable trend towards grain refinement; notice again the use of a higher magnification image. The average grain size after six passes have reduced the initial size of 20 μm to 1.3 μm only. Moreover, the percentage fraction of HAGB has been increased to 51%. It is also interesting to note from the grain boundary map, that the sub-grains formed having LAGB have mostly clustered towards the HAGB. As explained in detail later, this is a feature of CDRX, whereby, existing HAGB act as nucleating sites for sub-grain formation.



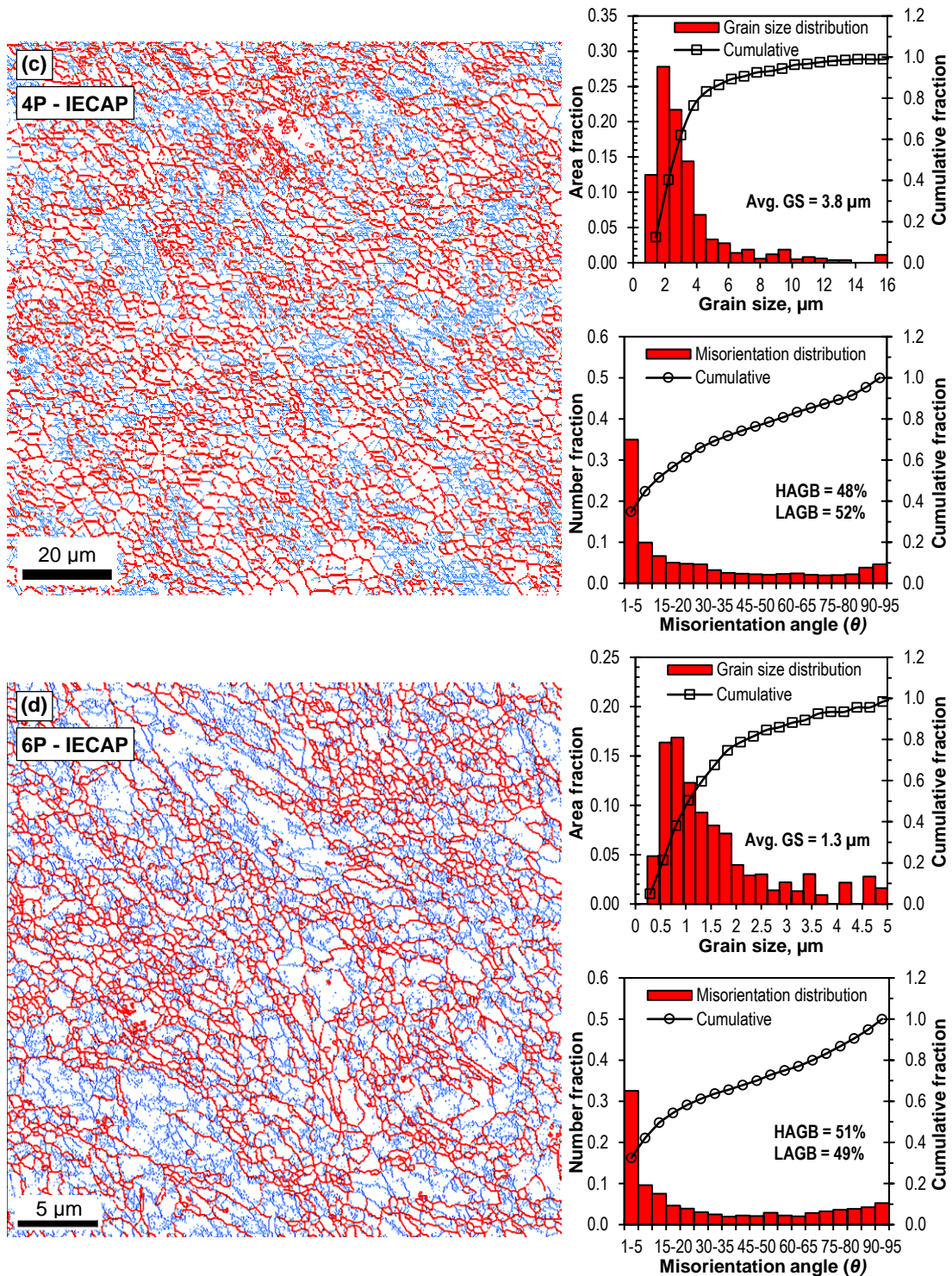


Fig. 5.5: EBSD based grain boundary maps of CP-Ti samples in the flow (Y) plane after (a) first, (b) second, (c) fourth and (d) sixth pass of I-ECAP at 300° C using the die with channel angle (Φ) of 120°. Blue lines represent low angle grain boundaries (LAGB) where $1.5^\circ \leq \theta \leq 15^\circ$, whereas red lines represent the high angle grain boundaries (HAGB) where $\theta > 15^\circ$. Figures on the upper right of each map represent the corresponding histogram of the grain size distribution and cumulative distribution function along with the average grain size (GS). Figures on the bottom right represent the corresponding histogram of the misorientation distribution and the cumulative distribution function along with the percentage of HAGB and LAGB. The arrows indicate the incomplete HAGB.

5.4.2 Microstructural evolution - Transverse (X) plane

In order to study the homogeneity of microstructure during I-ECAP processing, the microstructure is also analysed in the transverse plane. Fig. 5.6 shows the coloured inverse pole figure (IPF) maps obtained using SEM-EBSD technique, representing the evolution of microstructure and deformation characteristics along transverse (X) plane of the samples, subjected to (a) first, (b) second, (c) fourth and (d) sixth pass of the I-ECAP process. The TD and ND directions are shown in Fig. 5.6(a) and are applicable to all the IPF maps in transverse plane.

IPF map of the sample subjected to first pass is shown in Fig. 5.6(a), it differs immensely from the microstructure observed in the flow plane sample (Fig. 5.4(a)). There is no tilt in material flow along any direction and as a consequence there is no occurrence of elongated grains. Unlike in the flow plane, here majority of the grains are more or less equiaxed in morphology with the boundaries of some grains decorated by fine grains. Evidence of some twin boundaries is also seen in the microstructure. The microstructure can be regarded as being highly anisotropic (heterogeneous), because it consists of large grains, fine grain and twins after the first pass.

IPF map in Fig. 5.6(b) reveals further grain refinement of the microstructure after second pass. As expected, material flow is observed at a tilt (see the black arrows), this is consistent with second pass processing with route B_C in the transverse plane [75]. It is also observed that most of the larger grains have been broken down into fine grains with size range of 1 to 5 μm. The heterogeneity of the microstructure in terms of grain size has been greatly reduced. However, most of the grains after second pass are in green colour which suggests that the crystallographic orientation is close to pyramidal (2 $\bar{1}\bar{1}$ 0) plane.

Fig. 5.6(c) represents the microstructure after the fourth pass of I-ECAP processing. It is seen that the microstructure has been again completely transformed compared to after the first pass. After fourth pass, there is abundance of fine grains which results in a relatively homogenous microstructure. Majority of the grains after the fourth pass are still green in colour, however careful examination of the microstructure reveals that colour code of the fine grains is different from green. This suggests that the new grains which are being formed as a result of grain refinement process have mostly HAGB.

Fig. 5.6(d) shows the EBSD microstructure after the sixth pass. To better appreciate the fine grain structure, higher magnification is employed again as evident by 5 μm scale bar compared to 20 μm in previous three images. The grains are mostly equiaxed in morphology with the formation of UFG structure. Weakening of the texture has however taken place due to the significant grain refinement in grain sizes as evident by the variation of colour across the grains in microstructure.

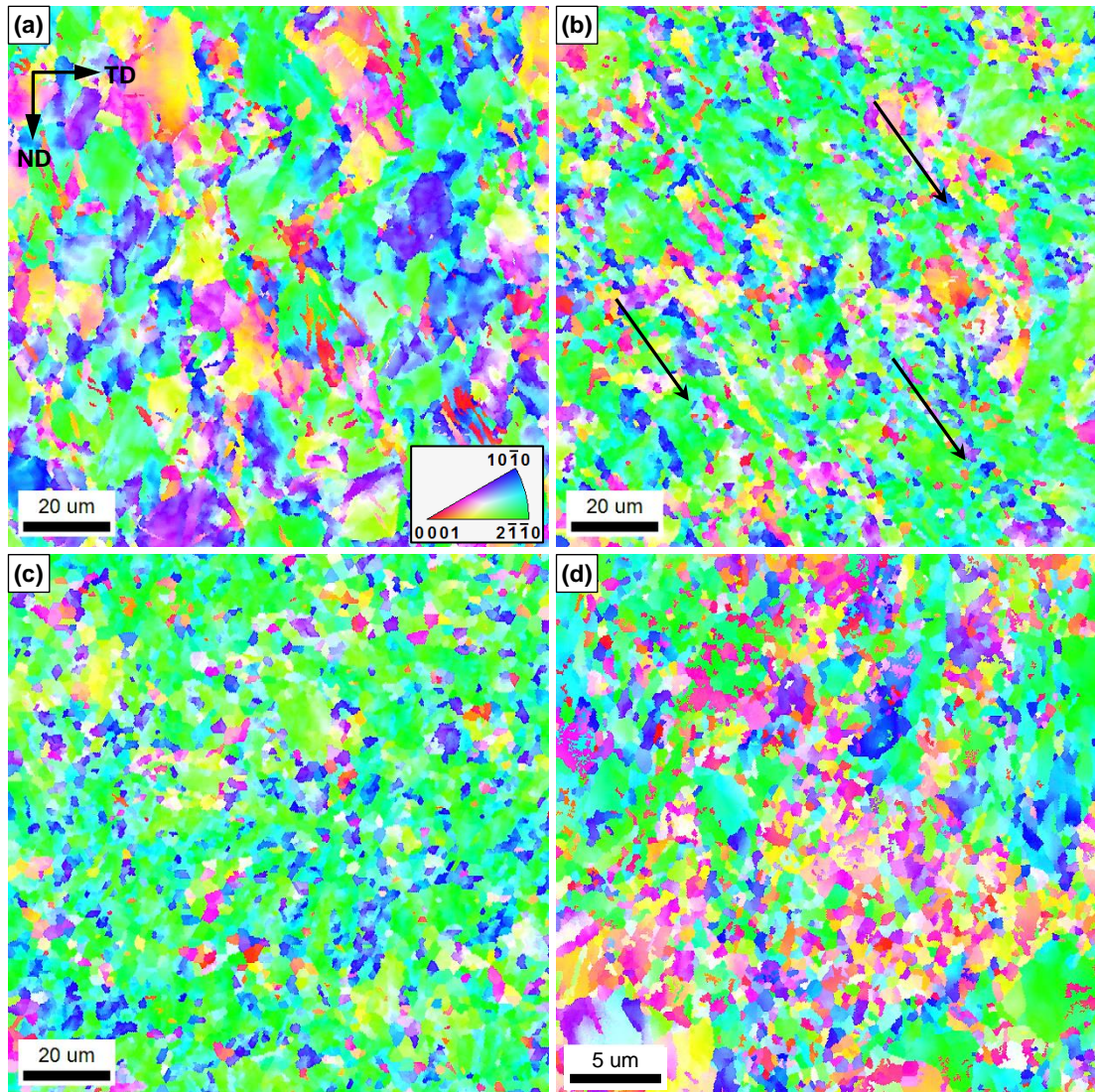


Fig. 5.6: Coloured inverse pole figure (IPF) maps obtained from EBSD analysis showing the evolution of microstructure and deformation characteristics in processed CP-Ti samples in the transverse (X) plane after (a) first, (b) second, (c) fourth and (d) sixth pass of I-ECAP at 300 ° C using the die with channel angle (Φ) of 120°. The colours correspond to the crystallographic orientations shown in the standard stereographic triangle (inset). Colour variation within the grains qualitatively represent differences in internal orientations. Note that scale bar used in (a) to (c) is 20 μm whereas in (d) is 5 μm , due to high magnification image.

Fig. 5.7(a-d) shows grain boundary maps of the IPF maps presented in Fig. 5.6(a-d). As previously presented, the figure on the upper right of each grain boundary map shows the corresponding histogram of grain size (equivalent circle diameter) with the solid line representing the cumulative grain size distribution function. The figure also includes the value of calculated average grain size (GS). Accordingly, the figure on the bottom right of each grain boundary map shows the corresponding histogram of grain misorientation with the solid line representing the cumulative misorientation distribution function. The figure also includes the values of calculated fraction of LAGB and HAGB as a percentage.

As was the case with the microstructure in the flow plane, the plots here also demonstrate a very clear evolution of microstructure in the transverse plane with increasing number of passes. As previously, in general, the grain size histogram shows that the bars are shifting towards the left, indicating the increasing level of grain refinement achieved due to subsequent processing. On the other hand, the misorientation histogram is gradually shifting towards the right, indicating the increase in fraction of HAGBs with the increasing number of passes.

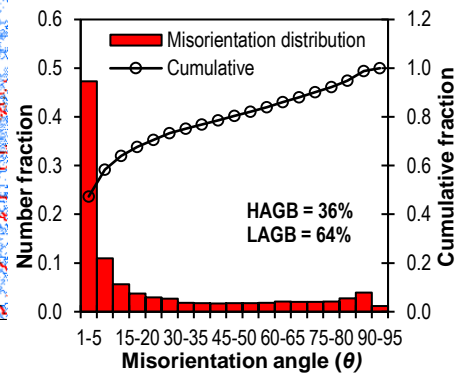
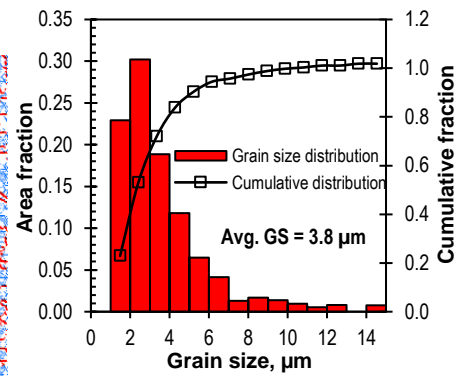
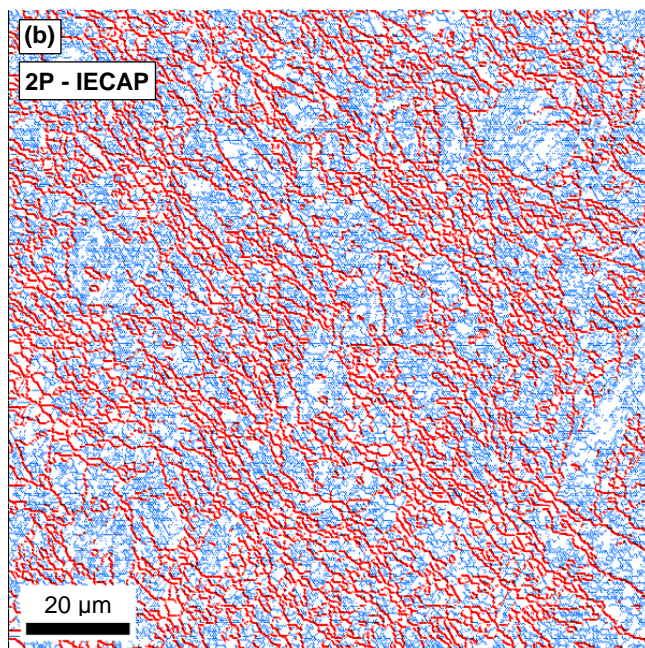
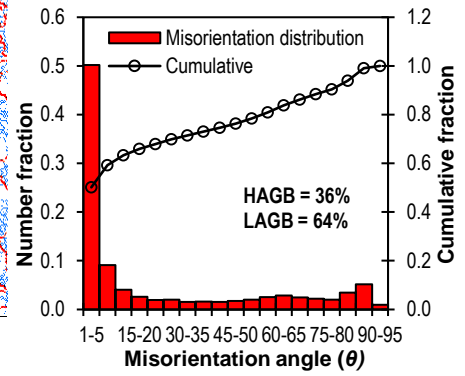
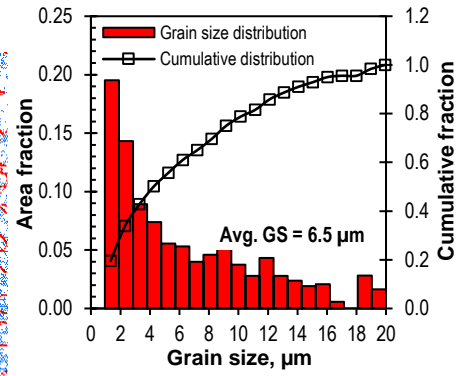
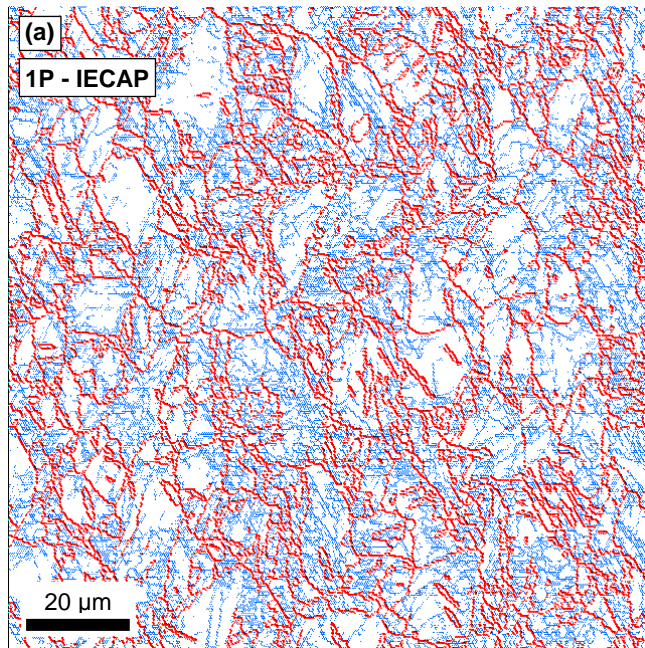
Fig. 5.7(a) represents the grain boundary map after the first pass of I-ECAP process. It is evident that although the microstructure is heterogeneous (coarse and fine grains co-existing), still majority of the grains are equiaxed in morphology. Moreover, formation of fine grains around the grain boundaries (necklace structure) is apparent as well. These fine grain contributing to the formation of necklace structure are less than $2\ \mu\text{m}$ in size and account for 20% of the area fraction after the first pass. It is very interesting to mention that the grain boundary map analysed for the sample in the transverse plane prior to any processing, displayed an even distribution of LAGB across the entire scanned area including within the grains. However, it is seen that after the first pass, the LAGB are starting to cluster around the HAGB of large grains to form sub-grains. The corresponding misorientation histogram again suggests the presence of $\{10\bar{1}2\}$ and $\{11\bar{2}2\}$ twins because of the observed peaks around 85° and 65° misorientation angle, respectively.

The grain boundary map after second pass in Fig. 5.7(b) shows grain refinement in action, with the formation of large regions of fine grains. Here grains less than $2\ \mu\text{m}$ in size occupy 45% of the total area fraction. This is reflected by the sharp initial rise

in the black line representing the cumulative distribution function. The grain boundary maps again reveals that some of the grains contains incomplete HAGB segments (pointed by black arrows). In terms of the twinning, similar behaviour is observed as flow plane sample. The peak around 65° has diminished, with a peak (although reduced) still exists around 85° misorientation. This suggest that there is some fraction of $\{10\bar{1}2\}$ twins in the microstructure. However interestingly after the second pass as the microstructure is refined, it appears that LAGB have been re-distributed fairly evenly across the whole scanned area including inside of the grains (compare the blue background in Fig. 5.7(b) with Fig. 5.7(a)). This indicates increase in the number of sub-grain formation. Also, as seen by the grain misorientation histogram that although the overall fraction of LAGB has remained same at 64%, the fraction of sub-grains with LAGB less than 5° has actually slightly decreased and LAGB between 5° and 15° has slightly increase, compared to the first pass.

Fig. 5.7(c), which represents the grain boundary map after the fourth pass, shows that the majority of grains have been refined. Similar to the flow plane, up to 80% of the grain size fraction lies between 1 to 6 μm . The grain misorientation histogram shows a reduction in percentage of LAGBs and an increase in HAGBs. Moreover, there are no noticeable peaks at misorientation angles corresponding to any twins, which again suggests that there is no noticeable twins fraction present in the microstructure as the grain size is refined.

Finally, the grain boundary map following the sixth pass shown in Fig. 5.7(d) displays substantial further grain size refinement. The fraction of grains above 2 μm has been greatly reduced with only less than 15% accounting for larger size. The average grain size in the transverse plane after the six passes of processing have been reduced from an initial size of 22 μm to 1.1 μm only, with an increase in HAGB as indicated by the misorientation histogram. It is again interesting to note from the grain boundary map, that the LAGBs have been significantly reduced and they are again mostly accumulated in the vicinity of HAGB.



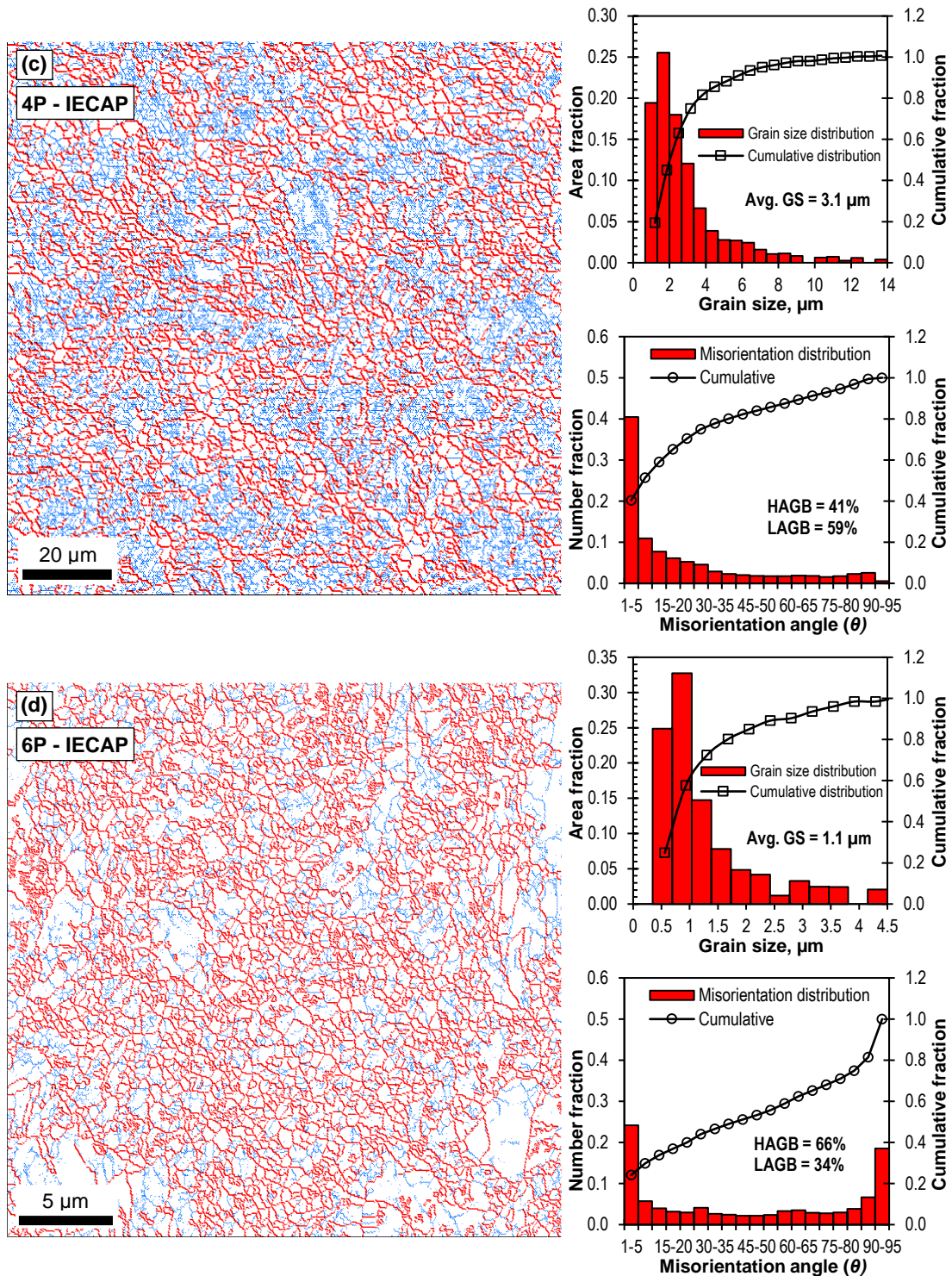


Fig. 5.7: EBSD based grain boundary maps of CP-Ti samples in the transverse (X) plane after (a) first, (b) second, (c) fourth and (d) sixth pass of I-ECAP at 300° C using the die with channel angle (Φ) of 120°. Blue lines represent low angle grain boundaries (LAGB) where $1.5^\circ \leq \theta \leq 15^\circ$, whereas red lines represent the high angle grain boundaries (HAGB) where $\theta > 15^\circ$. Figures on the upper right of each map represent the corresponding histogram of the grain size distribution and cumulative distribution function along with the average grain size (GS). Figures on the bottom right represents the corresponding histogram of the misorientation distribution and the cumulative distribution function along with the percentage of HAGB and LAGB.

5.4.3 Texture development - Flow plane

Evolution of crystallographic textures was tracked by obtaining pole figures via EBSD analysis after I-ECAP processing. Fig. 5.9 shows the experimental textures recorded on basal (0001), prismatic ($10\bar{1}0$) and pyramidal ($11\bar{2}0$) crystallographic planes of the samples in the flow plane, processed through (a) first, (b) second, (c) fourth and (d) sixth pass of I-ECAP process, respectively. The texture intensities are represented by the colour scale bar corresponding to the representative pole figure. These experimental pole figures have been recorded at the same measurement areas where the IPF maps shown in Fig. 5.4 were obtained.

As evident from the pole figure in Fig. 5.9(a), the off-basal texture present in the unprocessed material (as seen in Fig. 5.3(a)) has been weakened, this is mainly due to the significant changes in microstructure caused by shear deformation in the first pass. The peak intensity value in Fig. 5.9(a) is considerably lower than in Fig. 5.3(a). This intensity however gradually increases with increase in the number of passes, reaching a maximum strength after fourth pass (see the maximum value in the colour scale bars).

In particular, it is also seen that the basal texture is dominant after second and fourth pass, see the (0001) pole figures provided in Fig. 5.9(b) and (c). Most of the grains in the scanned area shown by IPF maps in Fig. 5.4(b) to (c) are also seen to be red in colour, which indicates the development of stable orientation during shear deformation towards basal plane. Fig. 5.9(b), which represents the pole figures after second pass revealed the development of basal fibre $\{0001\}\langle 11\bar{2}0\rangle$ as a prominent texture component. Possible texture components and their characteristics in the case of HCP materials are listed in [174]. Also the pole figures obtained after second pass, suggest that majority of grains reoriented their c -axis parallel to TD. Moreover the $\langle 11\bar{2}0\rangle$ direction and the $\{10\bar{1}0\}$ planes of the grains observed in the flow plane became parallel to shear direction and shear plane, respectively. Beausir et al. [175] identified five ideal shear texture components (P, B, Y, C_1 and C_2) in the case of HCP materials subjected to ECAP process. ($10\bar{1}0$) and ($11\bar{2}0$) pole figures of the second, fourth and sixth pass samples also shows the development of ideal shear texture components. Increase in the intensities close to ideal locations on the pole figures confirmed the development of P fibre. Note that the positions are slightly rotated from

the ideal locations as indicated by dotted lines in $(10\bar{1}0)$ pole figure, this is consistent with the finding reported in [175] after second pass and beyond. There is also some evidence of the formation of B fibre component after sixth pass (see $(10\bar{1}0)$ plane pole figure in Fig. 5.9(d)). Among the five ideal shear texture components P and B are known to occur more commonly during ECAP of HCP materials [176].

Development of six clusters at an angle interval of 60° is noticed in the $(10\bar{1}0)$ and $(11\bar{2}0)$ pole figures of the second, fourth and sixth pass samples in Fig. 5.9(b) to (d). It was reported that these clusters are introduced by the crystallographic symmetry of $\{10\bar{1}0\}$ family of planes (six) and $\langle 11\bar{2}0 \rangle$ family of directions (six) in the case of pure titanium subjected to shear deformation [177]. Slight reduction in the intensity of texture is observed after sixth pass which indicates weakening of the texture. This is also supported by the IPF map in Fig. 5.4(d), which shows the reduction in the fraction of grains in red colour. Formation of fine grains with HAGBs after sixth pass is attributed to this.

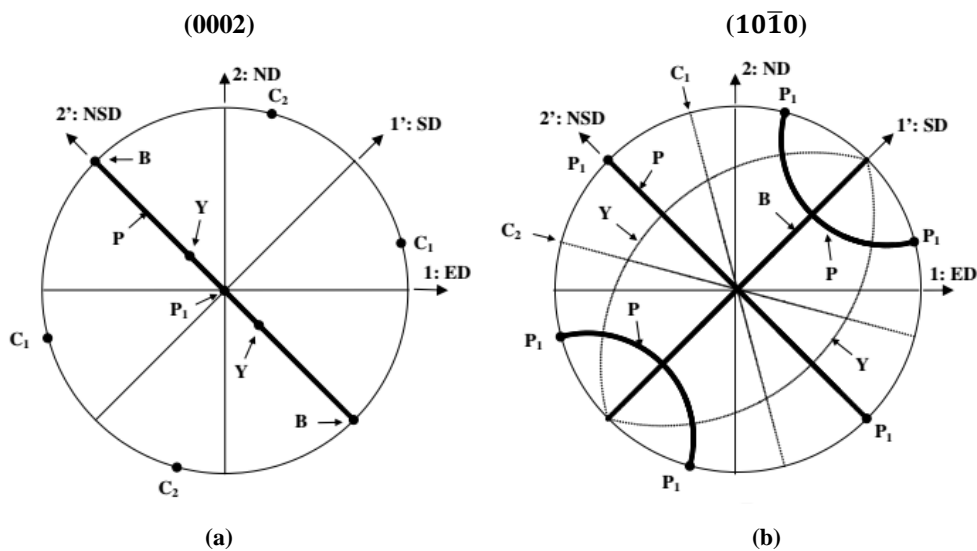


Fig. 5.8: The locations of five ideal shear texture components (P, B, Y, C₁ and C₂) developed in HCP metals during ECAP on: (a) (0002) and (b) $(10\bar{1}0)$ pole figures. Figure taken from the work of Beausir et al. [175].

5.4.4 Texture development - Transverse plane

Fig. 5.10 shows the experimental textures recorded on basal (0001), prismatic ($10\bar{1}0$) and pyramidal ($11\bar{2}0$) crystallographic planes of the samples in the transverse plane, processed through (a) first, (b) second, (c) fourth and (d) sixth pass of I-ECAP process, respectively. These experimental pole figures have been recorded at the same measurement locations where the IPF maps shown in Fig. 5.6 were obtained.

After the first pass, in contrast to the flow (Y) plane pole figures which showed a decrease in peak intensity values compared to the unprocessed material, here the values have actually increased. This was also observed by the presence of mostly green coloured grains as shown in Fig. 5.6(a), which indicates strengthening of texture after first pass. After second pass, it is seen that the peak intensity does not change much in value. However, the peak intensity value reaches a maximum after fourth pass, whereby texture is strengthened drastically followed by significant weakening after sixth pass. This is also confirmed by the presence of mostly green coloured grains as seen in Fig. 5.6(c), followed by the formation of new fine grains of random orientation after sixth pass (Fig. 5.6(d)).

The pole figures also suggest the development of $\{11\bar{2}0\}$ fibres. These fibres started to evolve after second pass and are seen to be getting stronger upto fourth pass. Compared to the second pass pole figures, the three pole figures in Fig. 5.10(c) show that the intensity of the peaks are now appearing at ideal locations of the fibre texture components. Normally the $\{11\bar{2}0\}$ fibres in HCP materials are expected to occur at certain ideal locations irrespective of the c value as reported in [174].

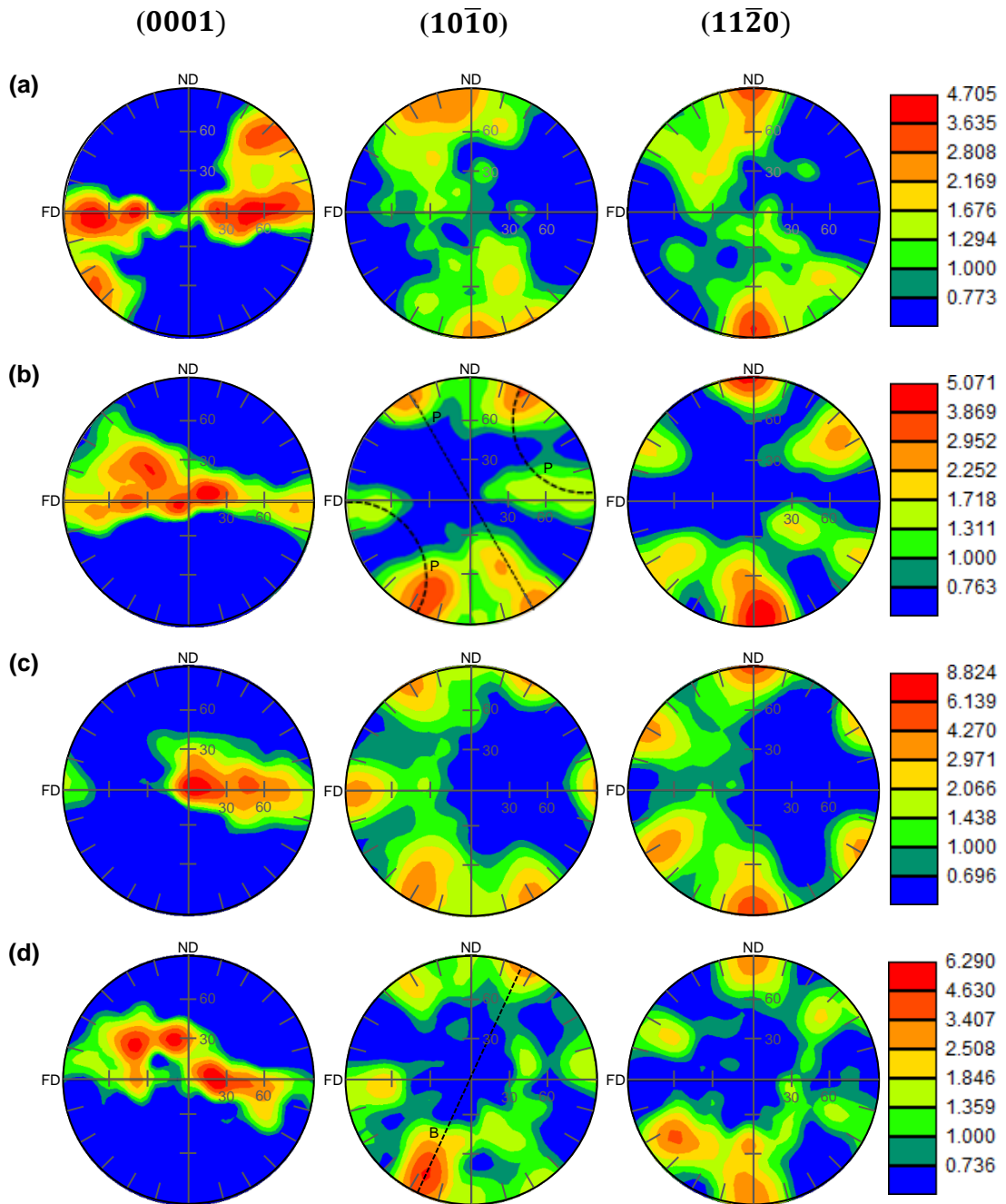


Fig. 5.9: Experimental pole figures illustrating the development of texture on the 0001 (left), $10\bar{1}0$ (middle) and $11\bar{2}0$ (right) crystallographic planes in the flow (Y) plane of the CP-Ti samples after (a) first, (b) second, (c) fourth and (d) sixth pass of I-ECAP carried out at 300°C using the die with channel angle (Φ) of 120° . The texture intensity is represented by the colour scale bar for the corresponding pole figure.

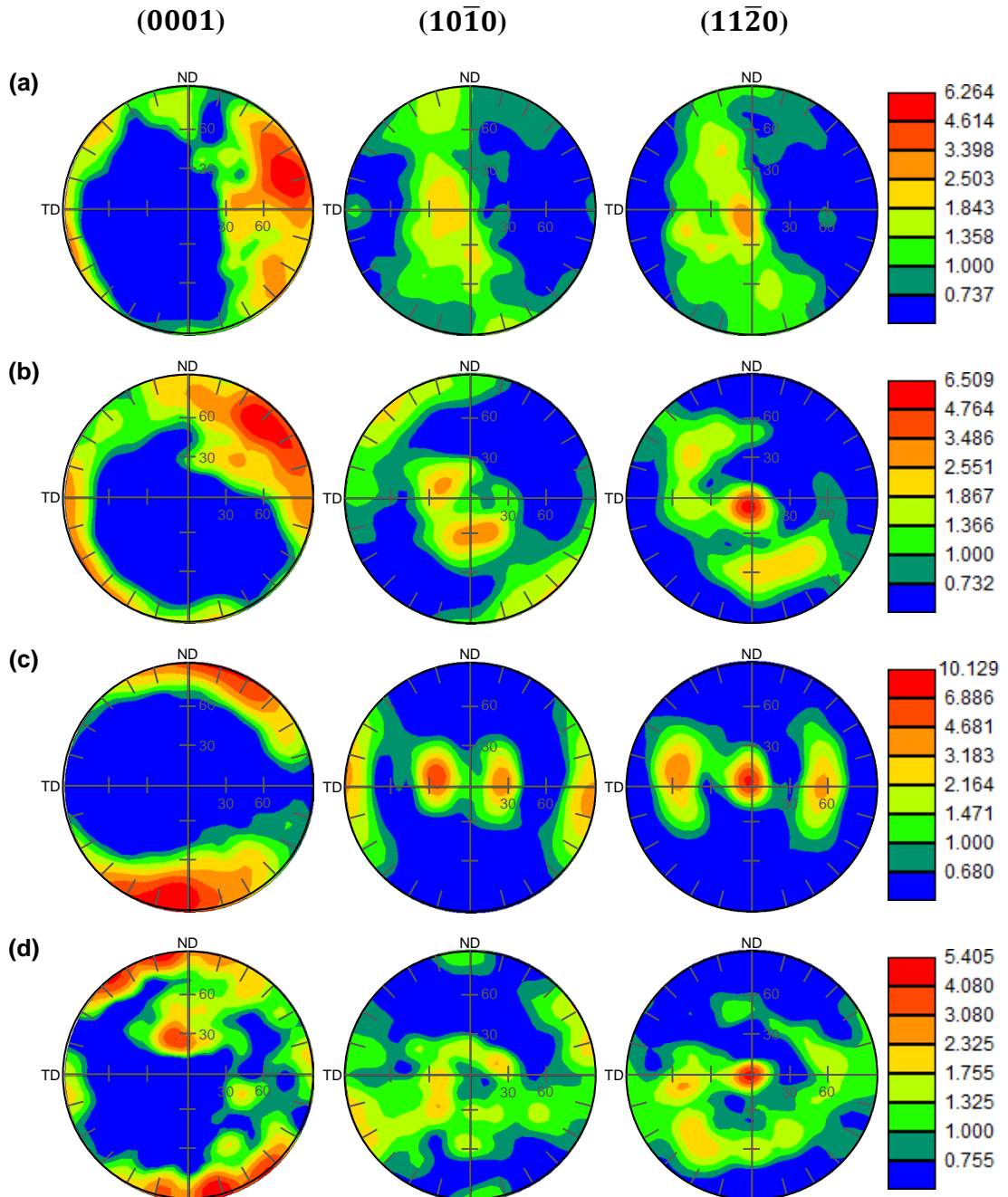


Fig. 5.10: Experimental pole figures illustrating the development of texture on the 0001 (left), $10\bar{1}0$ (middle) and $11\bar{2}0$ (right) crystallographic planes in the transverse (X) plane of the CP-Ti samples after (a) first, (b) second, (c) fourth and (d) sixth pass of I-ECAP carried out at 300°C using the die with channel angle (Φ) of 120° . The texture intensity is represented by the colour scale bar for the corresponding pole figure.

5.4.5 General characteristics of microstructure through 1 – 6 passes

The study provides a thorough investigation documenting the microstructural and textural evolution in CP-Ti grade 2 billets subjected to six passes of I-ECAP at 300 °C using a die with $\Phi = 120^\circ$ following route B_C. Exceptional grain refinement was achieved in both flow and transverse plane of the samples. To appreciate the level of grain refinement achieved during I-ECAP processing, Fig. 5.11 (a) and (b) presents the average grain size prior to any processing and after subsequent I-ECAP processing for flow and transverse planes, respectively. The average values were obtained from the histogram of grain size distribution (Fig. 5.5 and Fig. 5.7) following the EBSD analysis. The error bars in the graph represents the standard deviation, which is an indication of the level of dispersion in the grain size from the average value. These figures confirm the remarkable microstructural changes taking place during I-ECAP. The graphs displays the level of grain refinement taking place during I-ECAP processing, evident by the rapidly decreasing average grain size value as the number of passes increases. More importantly, the graphs also shows that the size of the error bars is noticeably decreasing with the increasing number of passes. This highlights that the microstructure is evolving into a more homogenous state after each pass.

It is convenient to use a refining factor (η) to understand the efficiency of grain refinement during I-ECAP processing, which is given by Eq. 5.1 [120]:

$$\eta = \frac{d_0 - d}{d_0} \quad \text{Eq. 5.1}$$

where d_0 and d are the average grain sizes of the previous and current pass, respectively. The calculated values of η in flow and transverse plane are listed in Table 5.1. As can be seen, the first pass sees the highest values of η , after which the value decrease gradually until pass four. However, it can be seen that the value of η at the final sixth pass for both planes is relatively high, this suggests that grain refinement has not reached a saturation point. With further processing, even more grain refinement should be possible. This is in sharp contrast to results reported in [120], where processing of CP-Ti grade 2 was done up to eight passes and saturation in η was seen after sixth pass. The difference in die channel angle of 90° and processing temperature are likely to be the reason. Overall, the η values for the flow and transverse planes are

more or less similar to each other in the current study which shows that refinement is taking place at a similar rate across both planes.

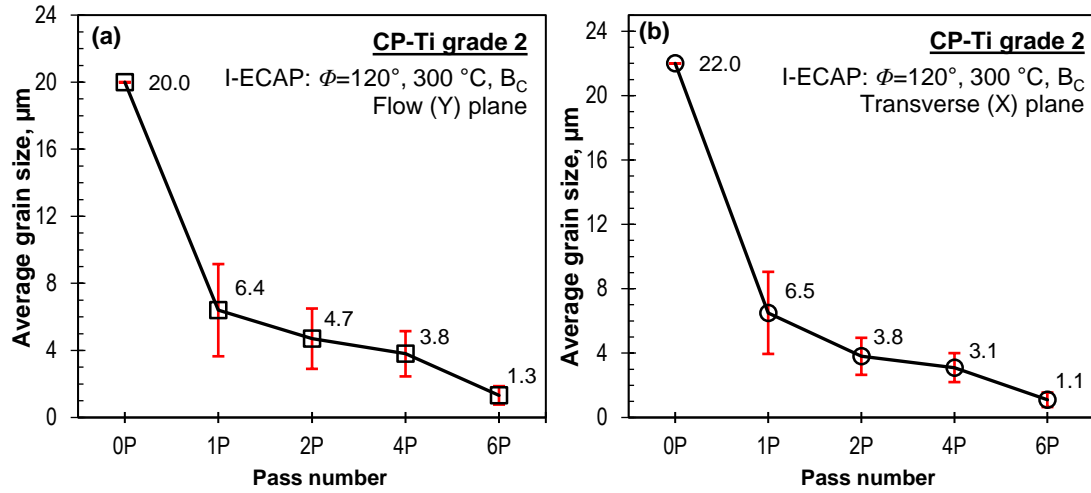


Fig. 5.11: Average values of grain size in CP-Ti samples in the (a) flow (Y) and (b) transverse (X) plane, before and after subsequent I-ECAP passes carried out at 300°C using $\Phi = 120^\circ$ channel die. The error bars represent the calculated standard deviation.

Table 5.1: Grain refining factor (η) at subsequent I-ECAP passes using $\Phi = 120^\circ$ channel die.

I-ECAP pass #	Equivalent strain (ϵ_{eq})	Refining factor (η)	
		Flow (Y) plane	Transverse (X) plane
1P	0.67	0.68	0.70
2P	1.34	0.27	0.42
4P	2.68	0.19	0.18
6P	4.02	0.64	0.65

For bulk UFG materials, it is usually not enough to achieve extreme grain refinement; the microstructure should also consist of grains with HAGBs [70]. The high fraction of HAGBs in UFG material is important in order to achieve improved properties [19]. To assess the evolution of misorientation during I-ECAP processing, two measures, average misorientation and the fraction of HAGBs, as a function of the number of passes, are presented in Fig. 5.12 and Fig. 5.13 for (a) flow and (b) transverse planes. It is seen that the average misorientation in the flow plane increases gradually over the subsequent passes, with a maximal value reaching 33° in the end. Meanwhile, in the transverse plane, the value initially rises sharply after the first pass and does not change much until the fourth pass. Beyond fourth pass the value rises rapidly and reaches a relatively high average misorientation value of 47° in the sixth

pass. Regarding the percentage fraction of HAGBs in the flow plane, the value is seen to increase gradually except between second and fourth pass, where there is a jump of 10% in the fraction of HAGBs. Fraction of HAGB in the transverse plane displays a similar trend as the average misorientation. Here again, there is an increase beyond fourth pass with the HAGB fraction abruptly increasing by as much as 25% and reaching a considerably high value of 66% after sixth pass. In general, it is seen that both the value of average misorientation and the fraction of HAGBs are considerably higher in the transverse plane.

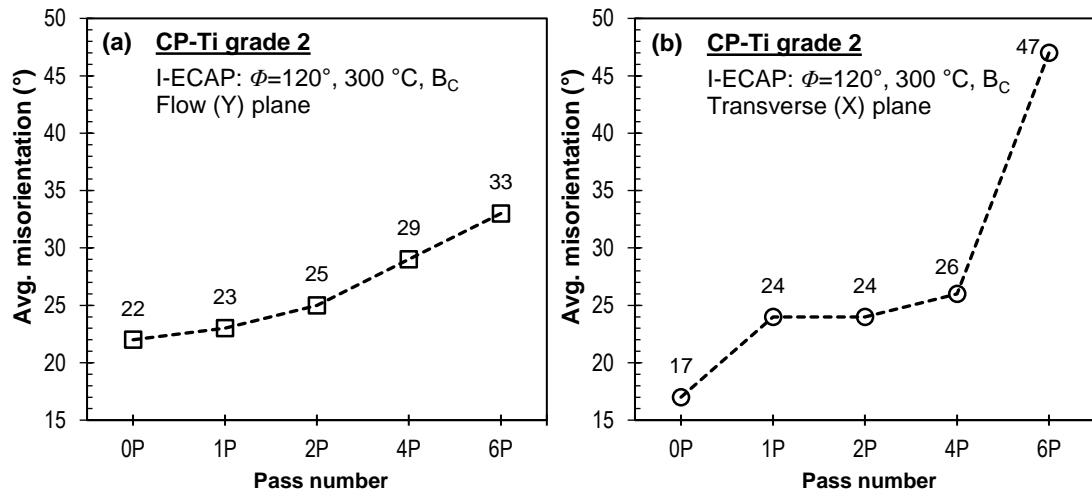


Fig. 5.12: (a) Average values of grain misorientation angles in CP-Ti samples in the (a) flow (Y) and (b) transverse (X) plane, before and after subsequent I-ECAP passes carried out at 300°C using $\phi = 120^\circ$ channel die.

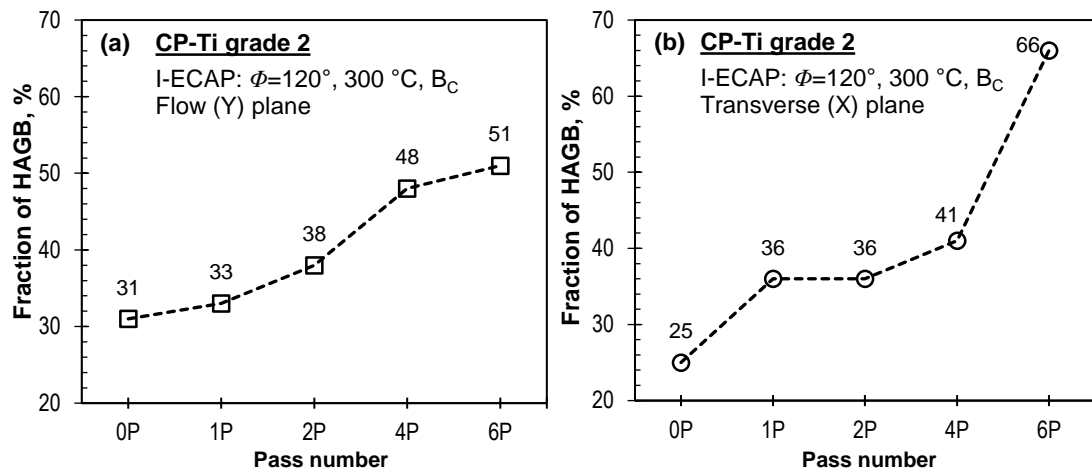


Fig. 5.13: (a) Percentage fraction of high angle grain boundaries (HAGBs) in CP-Ti samples in the (a) flow (Y) and (b) transverse (X) plane, before and after subsequent I-ECAP passes carried out at 300°C using $\phi = 120^\circ$ channel die.

5.4.6 Mechanism of grain refinement during I-ECAP

Pure Ti has an axial (c/a) ratio of 1.587, which is markedly different from the ideal value of 1.633 for HCP crystal structure. This, together with the limited number of slip systems present in its crystal lattice, results in a complex deformation mechanism consisting of both slip and twinning modes. Studies have shown that the microstructural evolution of CP-Ti during ECAP is quite different compared to FCC and BCC metals. During ECAP deformation, cubic metals normally form shear bands due to slip being the dominant mechanism [81]. However in CP-Ti, twinning has been observed to accommodate the plastic deformation during ECAP [114-117]. On application of stress, perpendicular to the basal plane during deformation, the role of twinning in HCP metals is to orient substantial portions of the grain along twin orientation. A slip type deformation is then possible along any favourable re-orientations [178]. Moreover, as twinning alone cannot accommodate the large plastic strain during ECAP, it is normally accompanied by dislocation slip.

As mentioned earlier, most of the work related to studying grain refinement mechanism during ECAP of CP-Ti has relied on TEM. Although TEM is a powerful tool for analysing the microstructure, however, the scan area under observation is limited in size. Therefore, the mechanism observed can just be local and may not entirely represent the general deformation behaviour. It was only recently when studies conducted by Chen et al. [118-120] and Meredith et al. [121] using SEM-EBSD, established CDRX accompanying twinning during the initial passes of the ECAP process. In the last decade, EBSD measurement technology has evolved considerably. The advantage of using EBSD is the ability to scan large areas for observing and quantitatively analysing the LAGBs, HAGBs, grain size and evolution of texture, as presented in this work. Moreover, statistical analysis of the boundary misorientation data can reveal presence of twin fraction in the microstructure. The $\{10\bar{1}2\}$ and $\{11\bar{2}1\}$ tensile twins are associated with misorientation peaks around 85 and 35° misorientation angles, whereas $\{10\bar{1}1\}$ and $\{11\bar{2}2\}$ compressive twins are associated with peaks around 57 and 65° angles, respectively [110]. Here the term compressive and tensile relates to the contraction and extension of c-axis in the HCP crystal.

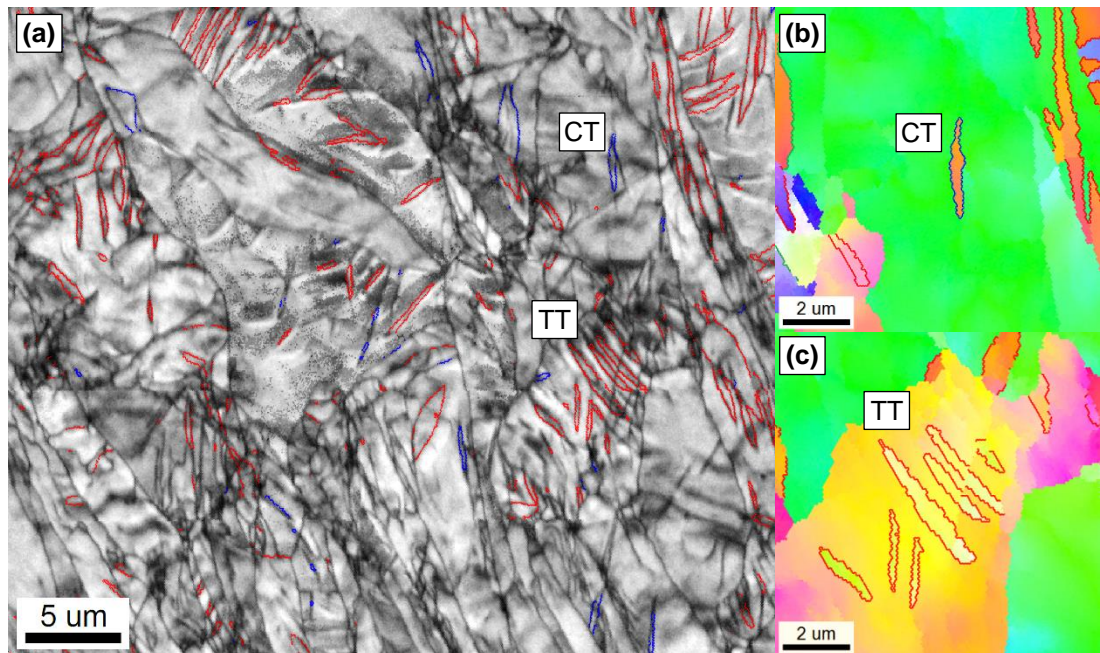
5.4.6.1 Twinning

Twinning during the first pass is evident as the microstructure obtained across both flow and transverse plane is heterogeneous and has high anisotropic grain morphology. Similar microstructural results were obtained in [171], which reported twinning to be active alongside slip during the first pass. In FCC metals such as aluminium where twinning does not exist and where the deformation mechanism is mainly by slip, all grains are extremely elongated and forms shear bands after first pass [179].

In the present study, the grain misorientation histogram obtained from the samples after first I-ECAP pass in the flow and transverse planes, shows peak around 85° and a minor peak around 65° misorientation angle, suggesting the presence of $\{10\bar{1}2\}$ and $\{11\bar{2}2\}$ twins, respectively. To establish the occurrence of twinning during I-ECAP of CP-Ti, a high magnification band contrast image is generated from the flow plane of the first pass sample and is shown in Fig. 5.14(a). As evident by the image, $\{10\bar{1}2\}$ tensile twin (TT) and $\{11\bar{2}2\}$ compressive twin (CT) type were activated in the microstructure, boundaries of which are shown as red and blue colour, respectively. Fig. 5.14(b) and (c) presents an enlarged view of the selected grains to show the boundaries of CT and TT twin types. Fig. 5.14(d) shows the grain misorientation histogram of the microstructure, the preferential misorientation peak for the contribution of twins are again noticed at around 65° and 85° . The corresponding inverse pole figure at $65^\circ \pm 5^\circ$ shows cluster in misorientation axes at around $\langle 10\bar{1}0 \rangle$ which confirms $\{11\bar{2}2\}$ twin boundary. Similarly, the corresponding inverse pole figure at $85^\circ \pm 5^\circ$ shows cluster in misorientation axes at around $\langle 2\bar{1}\bar{1}0 \rangle$ which confirms $\{10\bar{1}2\}$ twin boundary. Note that in Fig. 5.14(b) and (c), the twin boundaries appearing inside the grains are HAGB, therefore they seems to be dividing the grain from the inside. By doing so, they are playing a key role in the grain refinement process.

In comparison to $\{10\bar{1}2\}$ twins, the fraction of $\{11\bar{2}2\}$ twins is much smaller during the first pass. According to the literature survey, the presence of $\{11\bar{2}2\}$ twins was only reported very recently by Meredith et al. [121], who provided some evidence for the existence of such twins following EBSD analysis of the first pass microstructure. Similar to current results, the fraction of $\{11\bar{2}2\}$ twins observed was

very low in that study. Therefore, although twinning act as a dominant deformation mechanism during the initial passes of I-ECAP, compared to $\{11\bar{2}2\}$ twin, the $\{10\bar{1}2\}$ twin specifically play a greater role in the grain refinement process of CP-Ti.



Boundaries: Twin (Axis-Angle with K1 Plane)

	Plane Normal	Direction	Angle	Tolerance	K1 Plane	K1 Tolerance	Fraction	Number	Length
—	2 -1-10	2 -1-10	85	5°	10 -12	5°	0.136	9436	435.83 microns
—	10 -10	10 -10	65	5°	11 -22	5°	0.014	987	45.59 microns

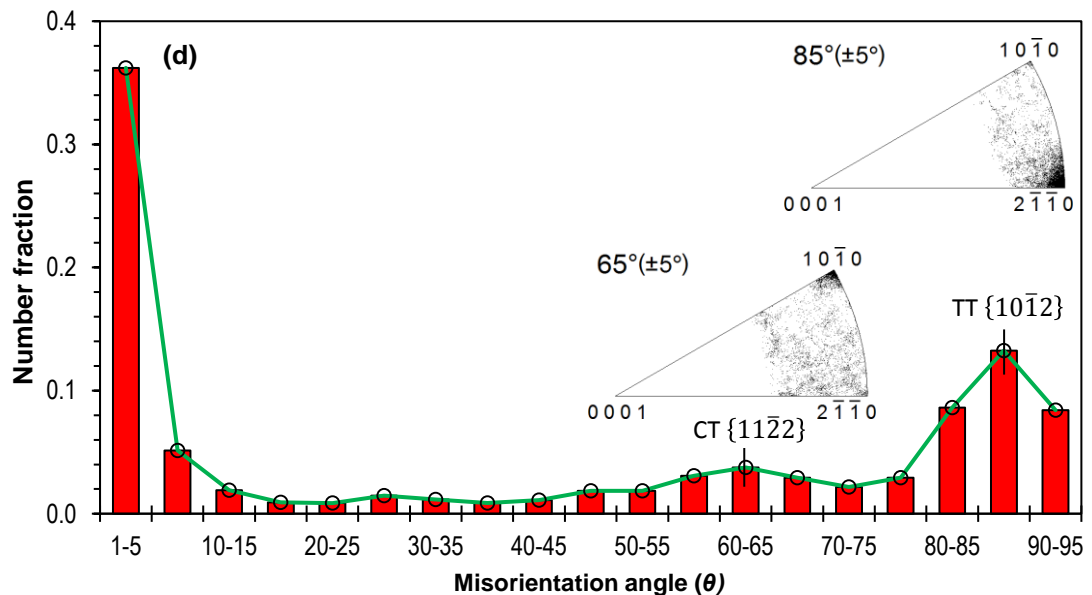


Fig. 5.14: EBSD based band contrast image showing the formation of twin boundaries after the first pass in the flow plane sample. The $\{10\bar{1}2\}$ tensile twin (TT) and $\{11\bar{2}2\}$ compressive twin (CT), are shown in red and green colour, respectively; (b) and (c) magnified IPF map showing CT and TT twin types within grain interiors, respectively and (d) corresponding misorientation histogram and misorientation inverse pole figures at 65° and 85° .

Other studies on ECAP of CP-Ti have reported the presence of $\{10\bar{1}1\}$ twins during the first pass [114, 117, 120], such twins were not observed in the present study. $\{10\bar{1}2\}$ twins observed here, were previously reported to be found in small fraction during the first pass processing of CP-Ti alongside $\{10\bar{1}1\}$ twins [120]. Analysis of the second pass microstructure in [121], suggested small occurrence of $\{10\bar{1}2\}$ twin boundary as well. Moreover, during the 3/4th pass, a weak presence of such twins were also observed to accommodate the deformation strains [118, 119]. $\{10\bar{1}1\}$ twin is known to occur at above 400 °C [178], it is believed that due to the use of a lower temperature (300 °C) compared to the above mentioned studies, $\{10\bar{1}1\}$ twin is not found here.

With the evolution of microstructure after second pass, twinning activity is greatly suppressed. As the microstructure is refined, the $\{11\bar{2}2\}$ twins are no longer apparent in the misorientation histogram. The 85° peak relating to the $\{10\bar{1}2\}$ is also greatly suppressed after second pass. This indicates that beyond second pass as the grain size is decreasing, slip is becoming the dominant deformation mechanism. The $\{11\bar{2}2\}$ twin has been shown to be very sensitive to grain size [110], which explains its early demise compared to $\{10\bar{1}2\}$ twin in the present study. With subsequent processing and grain refinement in fourth pass and beyond, the $\{10\bar{1}2\}$ twin activity is also no longer noticeable. This is consistent with other studies on conventional ECAP processing on CP-Ti, which also claimed that deformation by twinning was replaced or taken over by deformation by slip after the initial passes [116, 180, 181].

It is generally accepted that the twinning activity in titanium is strongly dependent on the grain size, it decreases with the reduction in grain size [182]. It is important to highlight, that although twinning has been observed during I-ECAP processing of titanium but compared to room temperature deformation of titanium [110, 182], the overall fraction of twinning observed here is significantly lower. This is attributed to the use of elevated temperature processing at 300 °C, which would facilitate slip type deformation.

5.4.6.2 Continuous dynamic recrystallization

Titanium is a high stacking fault energy (SFE) metal and is expected to exhibit continuous dynamic recrystallization (CDRX) during elevated temperature deformation processes. Recent studies on ECAP of CP-Ti have reported CDRX as one of the grain refinement mechanisms [119, 121]. CDRX is a recovery dominated process whereby progressive accumulation of dislocations within grains near grain boundaries generates subgrains with low angle grain boundaries (LAGB) [183]. Upon further straining the material, the subgrains continue to rotate and the misorientations angles (θ) around the LAGBs continue to increase. Consequently, when the misorientation reaches the LAGB/HAGB cut-off (15°) value, new fine grains are originated with high angle grain boundaries (HAGB).

To observe CDRX in the present study, a high magnification EBSD map is generated in the transverse plane from the second pass processed sample, as shown in Fig. 5.15. In the EBSD map, the thin blue lines represent the LAGBs with misorientation angle θ between 2 to 15° , whereas the thick red lines represent the HAGBs with θ greater than 15° . Incomplete HAGB segments, which do not form a fully enclosed grain, were frequently observed in the grain boundary maps of samples in the flow and transverse plane (Fig. 5.5 and Fig. 5.7). These incomplete HAGBs can be seen clearly in Fig. 5.15 (as indicated by black arrows) and is a strong indication of the CDRX process. These incomplete HAGBs have evolved from the LAGBs by the progressive accumulations of dislocations near the grain boundaries. Careful analysis of two of these incomplete HAGBs, labelled as L1 and L2 reveals that the misorientation is just over 15° (see the corresponding graphs in Fig. 5.14). This confirms that these HAGBs have evolved from LAGBs. Further accumulation of dislocation in subsequent passes will lead to the extension of these incomplete HAGBs segments to form fully enclosed refined grains.

Another characteristic feature associated with CDRX is the formation of necklace structure, i.e. fine grains decorated around the coarse grains [118]. Fig. 5.15 also shows that most of the LAGBs (subgrains) development is around HAGBs. Since existing HAGBs act as nucleating sites for subgrains, it is expected that the grain refinement takes place at the exterior of coarse grains and spreads towards grain interior [121].

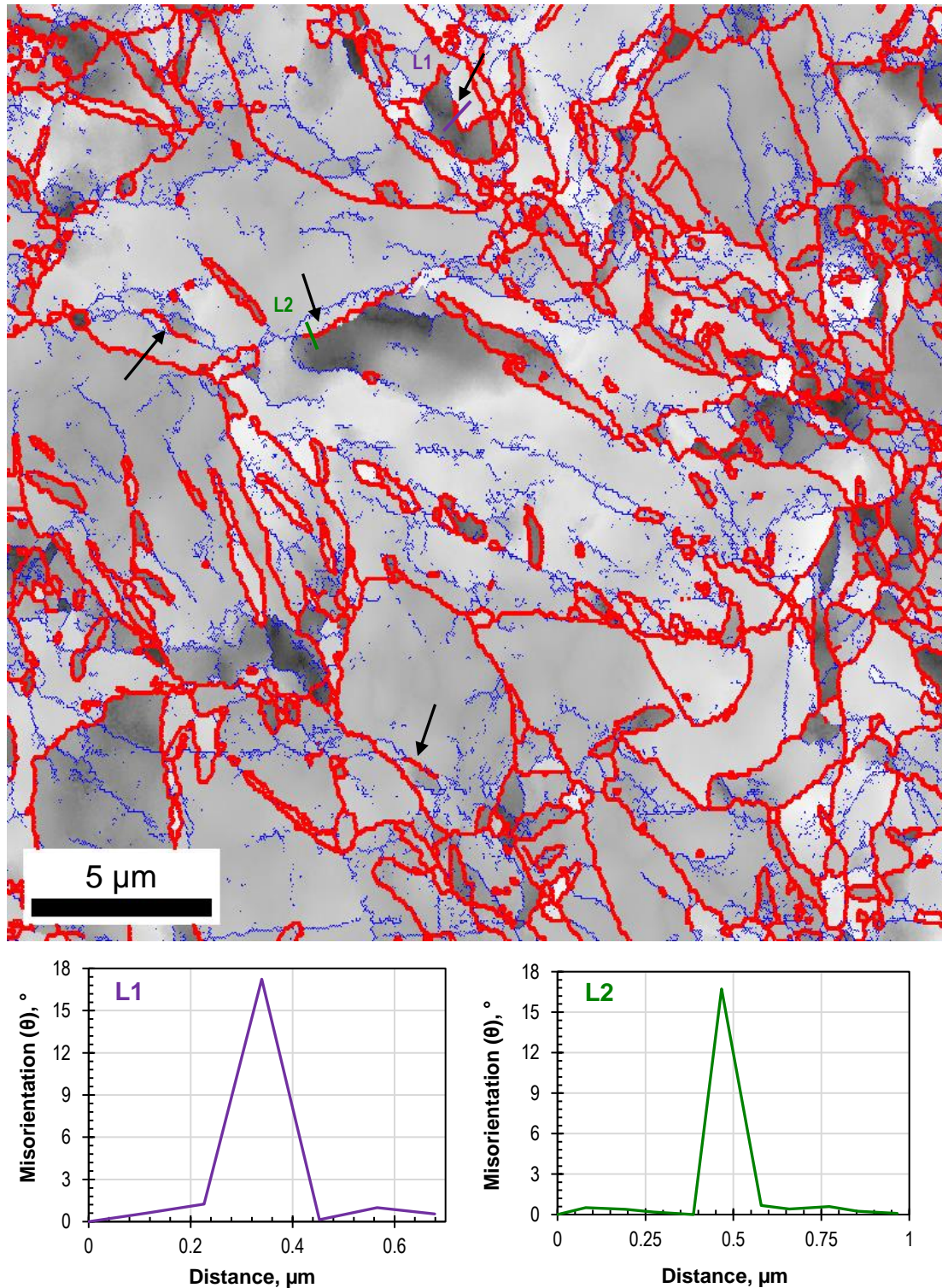


Fig. 5.15: Higher magnification EBSD map of the second pass sample in the transverse (X) plane after I-ECAP at 300 $^\circ$ C, using the die with channel angle (Φ) of 120 $^\circ$. Blue lines represent low angle grain boundaries (LAGBs) where $2^\circ \leq \theta \leq 15^\circ$, whereas red lines represent the high angle grain boundaries (HAGBs) where $\theta > 15^\circ$. The arrows indicate the incomplete HAGB.

5.5 Processing using I-ECAP die with channel angle (Φ) of 90°

5.5.1 Microstructural evolution – Flow (Y) plane

Fig. 5.16(a) to 5.18(a) shows the IPF maps representing the post deformation microstructural characteristics in the flow (Y) plane of the samples after first, second, third and fourth pass. The FD and ND direction shown in Fig. 5.16 is applicable for all maps presented. Each pass of I-ECAP gives an equivalent strain of ~ 1.07 , so these IPF maps corresponds to a total strain of ~ 1.07 , ~ 2.14 , ~ 3.21 and ~ 4.28 . Fig. 5.16(b) to 5.18(b) shows the corresponding grain size histogram along with the average grain size. Fig. 5.16(c) to 5.18(c) represent the associated inverse pole figures representing the texture. These plots demonstrate a very clear evolution of microstructure in the flow plane with the increasing number of passes. Note that, all samples for EBSD analysis were taken from the centre region of the processed billets.

The IPF map of the sample subjected to first pass of I-ECAP in Fig. 5.16(a) shows the grain refinement in action. Most of the grains are elongated and forming a banded style microstructure due to shearing process. The metal flow is at a tilt with a value of 24° with respect to FD. This tilt is also referred to as ‘grain elongation angle (β)’, and is a characteristic feature of the ECAP shearing process in the flow (Y) plane [75]. The angle observed in the present study is in good agreement with the theoretical calculated value and is similar to the value reported by Suwas et al. [180], who also performed ECAP on CP-Ti using a die with $\Phi = 90^\circ$. In the first pass, this angle (β) is about 26.6° , and for second pass using route B_C the value is 19° , as calculated by Zhu and Lowe in [81].

Large clusters of very fine grains ($<1 \mu\text{m}$) are also seen in the microstructure after first pass (regions marked with white circles). The fine grains are also observed along the boundaries of large elongated grains, forming the so-called necklace structure. According to the grain size histogram (Fig. 5.16(b)), these submicron grains constitute $\sim 30\%$ of the total scanned area. Twinning is an important deformation mechanism for CP-Ti during ECAP; careful analysis of the microstructure revealed presence of mainly $\{10\bar{1}2\}$ tensile twins. The twin boundaries are shown as black lines in Fig. 5.16(a). The microstructure therefore is heterogeneous with a mixture of twins, large elongated grains and fine grains. This heterogeneity in the microstructure after

first pass processing in CP-Ti is consistent with other similar studies [117, 120]. The average grain size after first pass is 3.16 μm , a reduction of nearly 84% compared to the unprocessed material.

Fig. 5.17(a) represents the microstructure after second pass of I-ECAP. It is evident that further refinement has taken place as the average grain size is reduced to 2.41 μm . Moreover, the bars in the grain size histogram in Fig. 5.17(b) are shifted more towards the left. The fraction of submicron grains have increased to 38% and the smallest grains are around 0.32 μm . The metal flow is still observed at a tilt, with grain elongation (β) of $\sim 21^\circ$, which is quite close to the theoretical value of 19° . The microstructure is still banded in nature due to the presence of mostly elongated grains. However, the thickness of the elongated grains has been reduced compared to the first pass. Similar to $\Phi = 120^\circ$ results, the majority of these elongated grains have orientation which range from basal plane 0001 (red) to either half way to $10\bar{1}0$ (pink) or less than half way to $2\bar{1}\bar{1}0$ (orange). This is also evident from the corresponding inverse pole figure in Fig. 5.17(c), which shows the intensity near the above mentioned planes. It is interesting to note that the colour of the fine grains is different from the above mentioned colours; this suggests that the new grains which are being formed as a result of grain refinement process are surrounded by HAGBs.

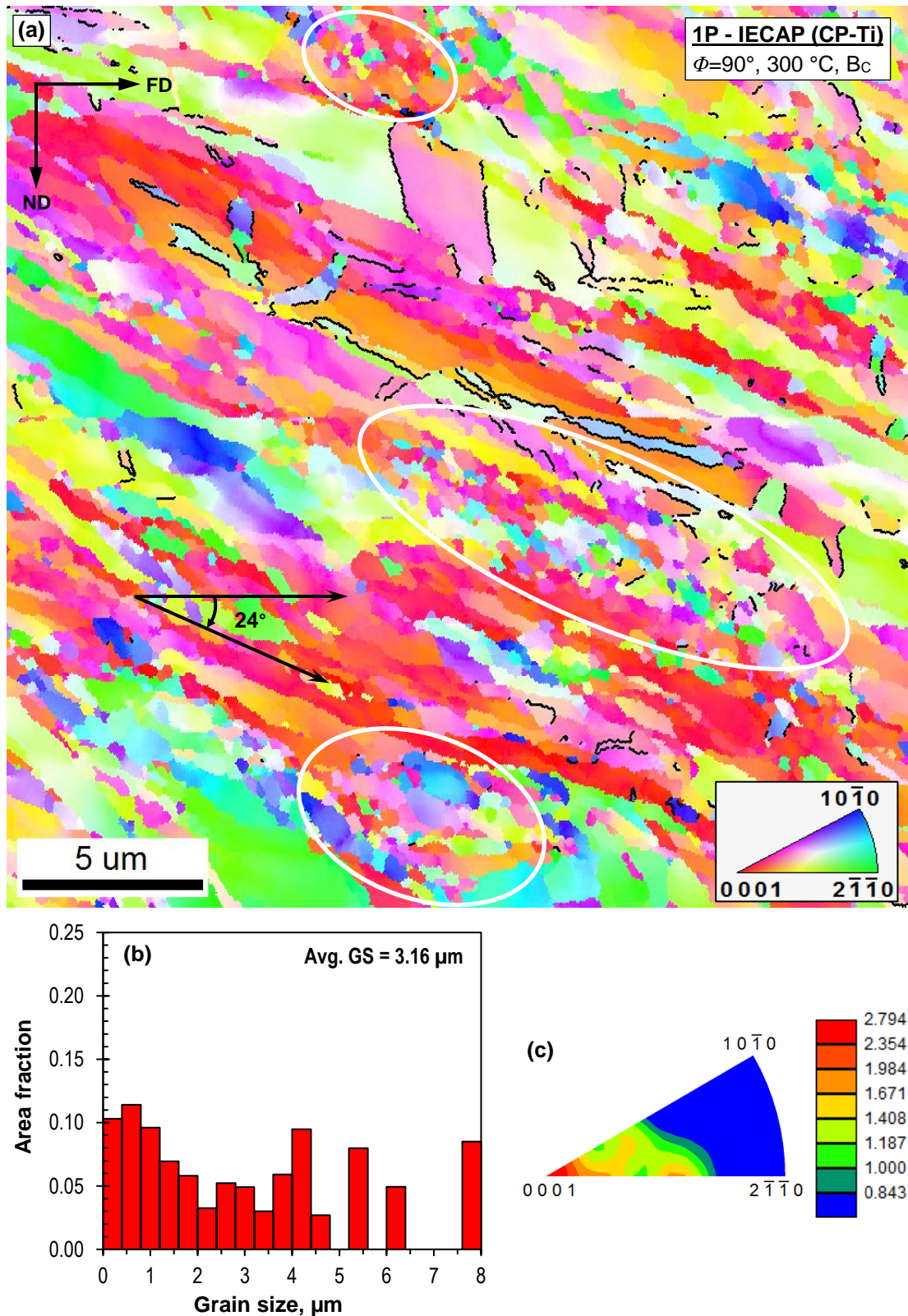


Fig. 5.16: (a) EBSD based inverse pole figure (IPF) map showing the microstructure of the CP-Ti samples in the flow (Y) plane after first pass (1P) of I-ECAP at 300 °C using the die with a channel angle of 90°, (b) the corresponding grain size histogram with the average grain size and (c) the associated inverse pole figure. Colour variation within grains qualitatively represents differences in internal orientations.

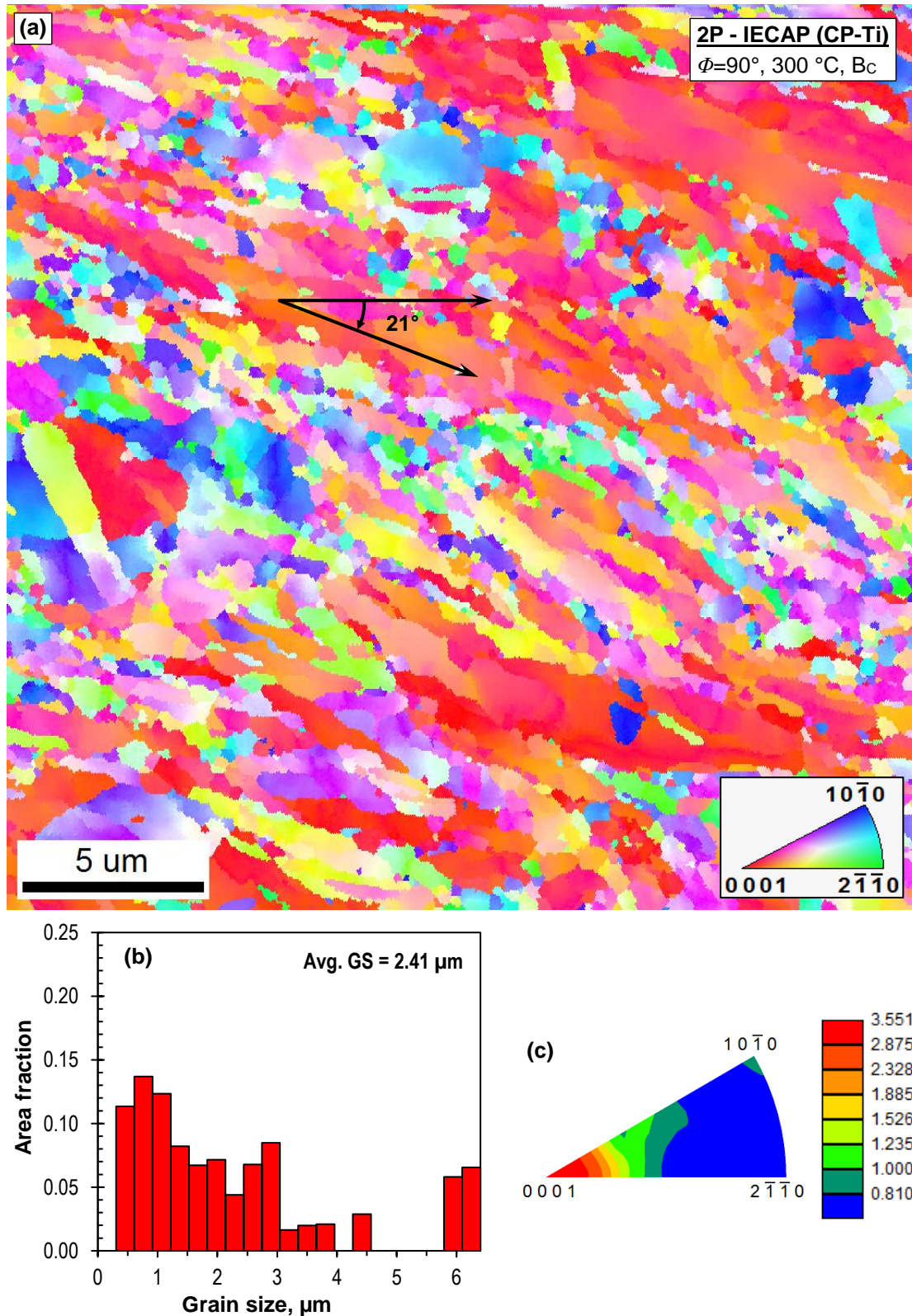


Fig. 5.17: (a) EBSD based inverse pole figure (IPF) map showing the microstructure of the CP-Ti samples in the flow (Y) plane after second pass (2P) of I-ECAP at 300 °C using the die with a channel angle of 90°, (b) the corresponding grain size histogram with the average grain size and (c) the associated inverse pole figure. Colour variation within grains qualitatively represents differences in internal orientations.

Fig. 5.18(a) shows the EBSD based IPF map in the flow plane after three passes of I-ECAP. The microstructure is significantly different from the first two passes, as there is no tilt and the banded style structure does not exist anymore. Here elongated grains are no longer observed and they have been replaced by newly formed equiaxed grains. According to the grain size histogram in Fig. 5.18(b), 90% of the grains are below 3 μm in size with sub-micron grains comprising nearly 70% of the total area fraction.

Fig. 5.19(b) represents the microstructure after four passes of I-ECAP. It is evident that tremendous grain refinement has been achieved and the average grain size is 0.86 μm . The heterogeneity has been completely lost and the microstructure is homogenous with mainly equi-axed grains. The percentage of HAGB is 79% of the total grain boundary fraction in the microstructure. The inverse pole figure in Fig. 5.19(c), shows that the texture strength has weakened significantly due to grain refinement. This is also seen by the random distribution of colours in the IPF map.

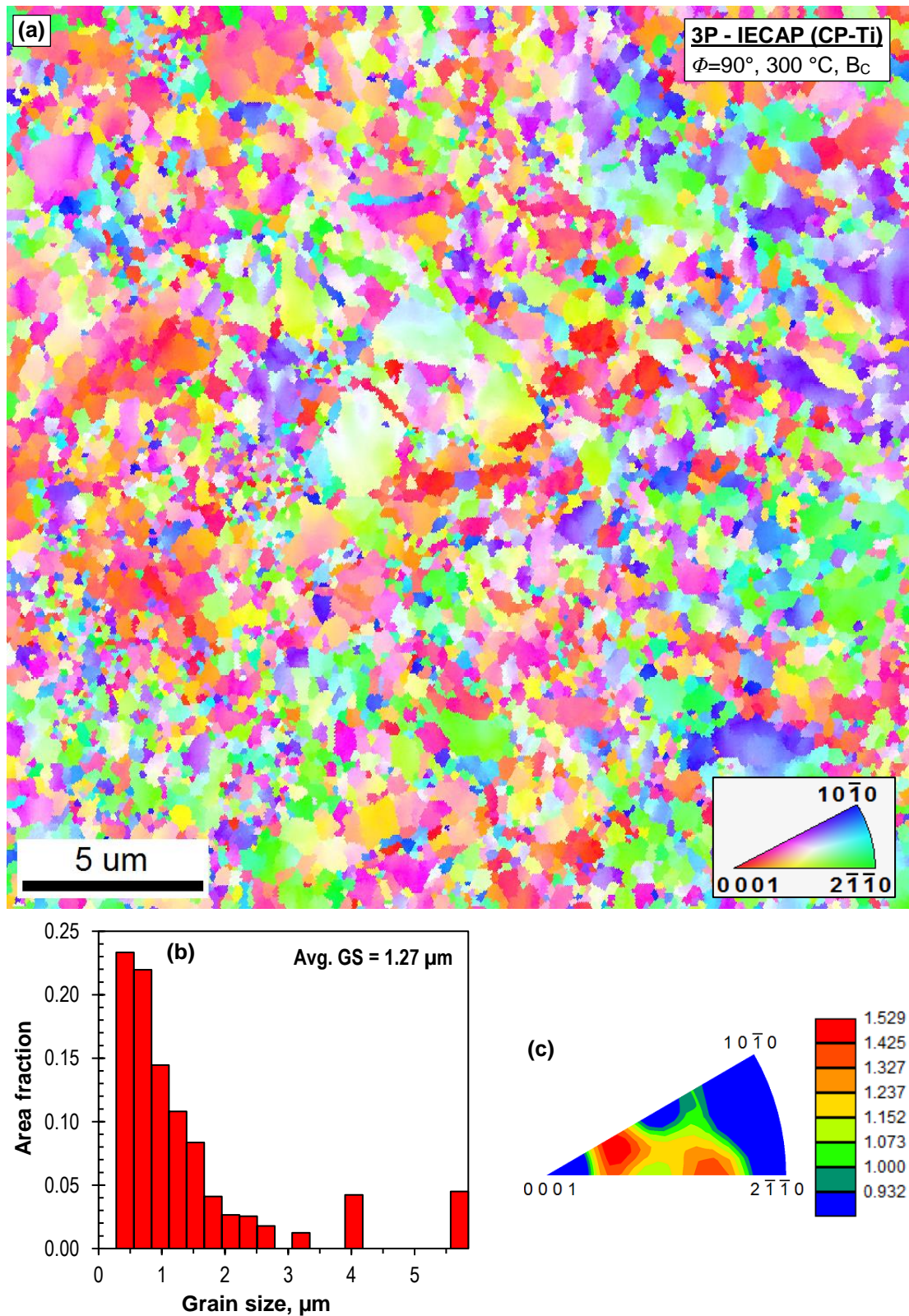


Fig. 5.18: (a) EBSD based inverse pole figure (IPF) map showing the microstructure of the CP-Ti samples in the flow (Y) plane after third pass (3P) of I-ECAP at 300 °C using the die with a channel angle of 90°, (b) the corresponding grain size histogram with the average grain size and (c) the associated inverse pole figure. Colour variation within grains qualitatively represents differences in internal orientations.

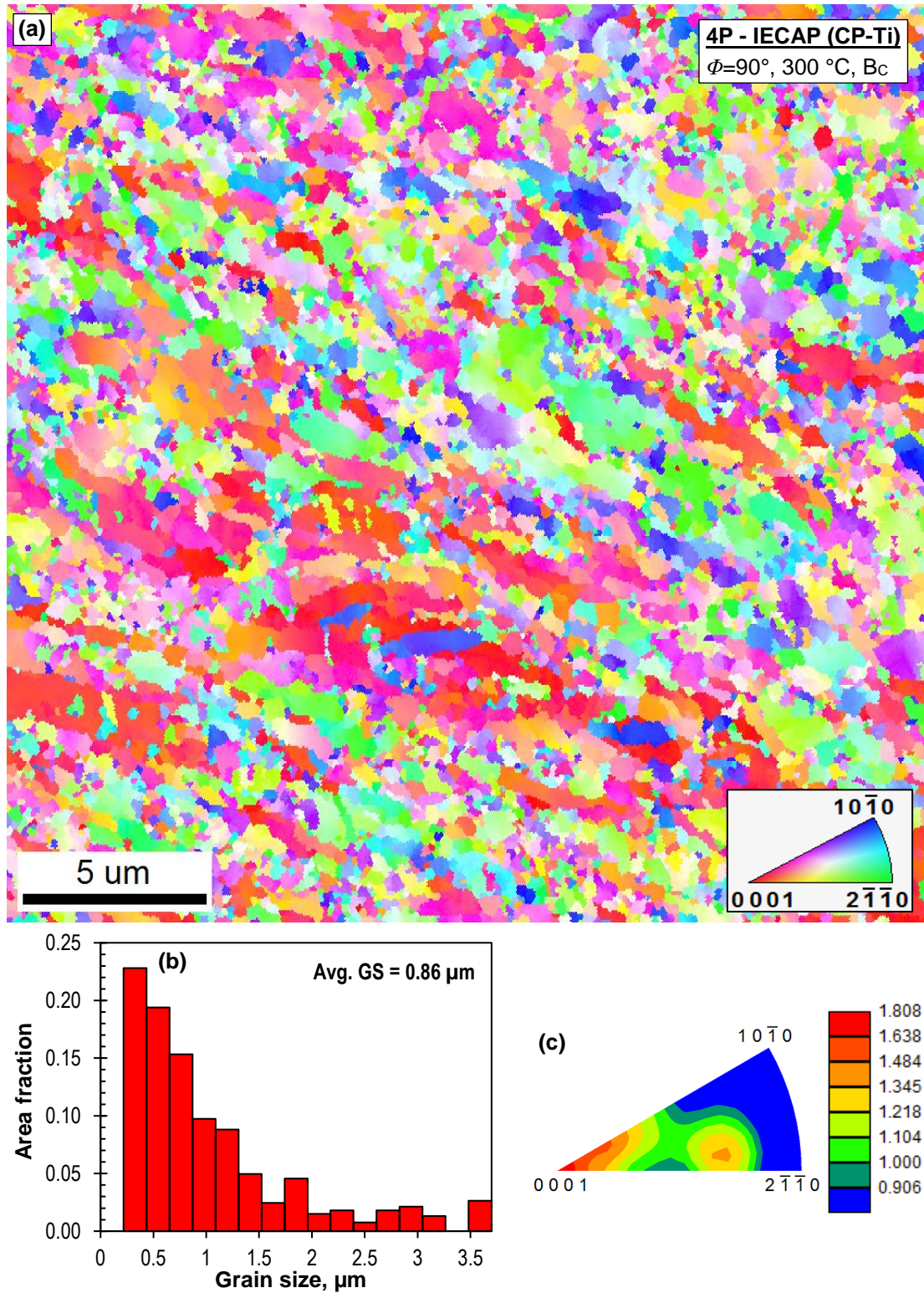


Fig. 5.19: (a) EBSD based inverse pole figure (IPF) map showing the microstructure of the CP-Ti samples in the flow (Y) plane after fourth pass (4P) of I-ECAP at 300 °C using the die with a channel angle of 90°, (b) the corresponding grain size histogram with the average grain size and (c) the associated inverse pole figure. Colour variation within grains qualitatively represents differences in internal orientations.

5.5.2 General characteristics of microstructure through 1 to 4 passes

Microstructural evolution and deformation characteristics were studied for CP-Ti grade 2 billets subjected to four passes of I-ECAP at 300 °C using a die with $\Phi = 90^\circ$ following route B_C. Extraordinary grain refinement was achieved with increasing number of passes (Fig. 5.16 to Fig. 5.19). To appreciate the level of grain refinement during I-ECAP process, Fig. 5.20 presents the average grain size prior to any processing and after subsequent I-ECAP processing. The average values were obtained from the histograms of grain size distribution following the EBSD analysis. The error bars in the graph represent the standard deviation, which is an indication of the level of dispersion in the grain size from the average value. These figures confirm the remarkable microstructural changes taking place during I-ECAP process. The graph displays the grain refinement taking place as the number of passes increases, evident by the rapidly decreasing value of average grain. More importantly, it also displays that the size of the error bars is decreasing noticeably with subsequent processing, this highlights the fact that the microstructure is becoming more homogenous with increase in the number of passes.

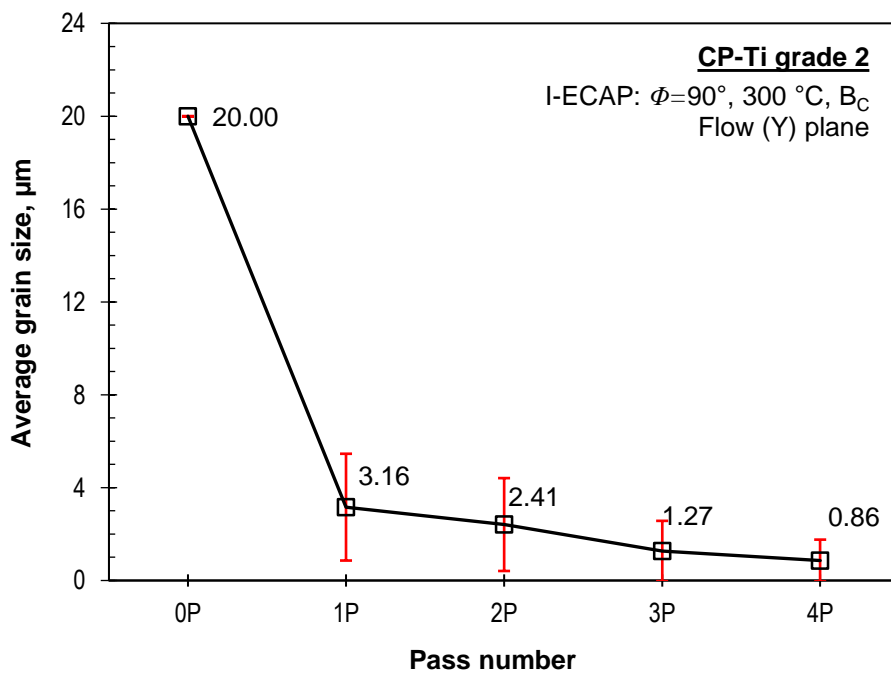


Fig. 5.20: Average values of grain size in CP-Ti samples in the flow (Y) plane, before and after subsequent I-ECAP at 300 °C using $\Phi = 90^\circ$ channel angle die. The error bars represent the calculated standard deviation.

The grain refining factor (η) has been calculated using Eq. 5.1 and presented in Table 5.2. After first pass processing, the average grain size was refined from 20 to 3.16 μm , which gives a high factor of 0.84 for this pass. During second pass, the factor is 0.24, a somewhat lower value compared to the first pass. During the third pass, the level of refinement increases as the factor increases to 0.47. Subsequently the factor decreases to 0.32 during the final fourth pass. It is expected that further passes would bring this factor to a saturation value.

Table 5.2: Grain refining factor (η) at subsequent I-ECAP pass using $\Phi = 90^\circ$ channel die.

I-ECAP pass #	Equivalent strain (ϵ_{eq})	Refining factor (η)
		Along flow (Y) plane
1P	1.07	0.84
2P	2.14	0.24
3P	3.21	0.47
4P	4.28	0.32

As mentioned earlier, in order to classify a material as UFG structure, two requirements have to be met. Firstly, majority of the grains should be below 1 μm . The EBSD results confirmed that the average grain size value after four passes is 0.86 μm ; this fulfils the first requirement. The second requirement is that majority of grains should be surrounded by HAGBs (misorientation greater than 15°). In order to see the evolution of HAGBs during subsequent passes, average value of grain misorientation and percentage fraction of HAGBs are presented in Fig. 5.21(a) and (b). Similar trends are observed in both graphs. After first pass, both average misorientation and fraction of HAGB increase sharply. During the second pass, there is not much change in these values. However, the values increases moderately during third pass and then increases again sharply during the fourth pass. With a 79% fraction of HAGB, the material also satisfies the second requirement and therefore classified as UFG material.

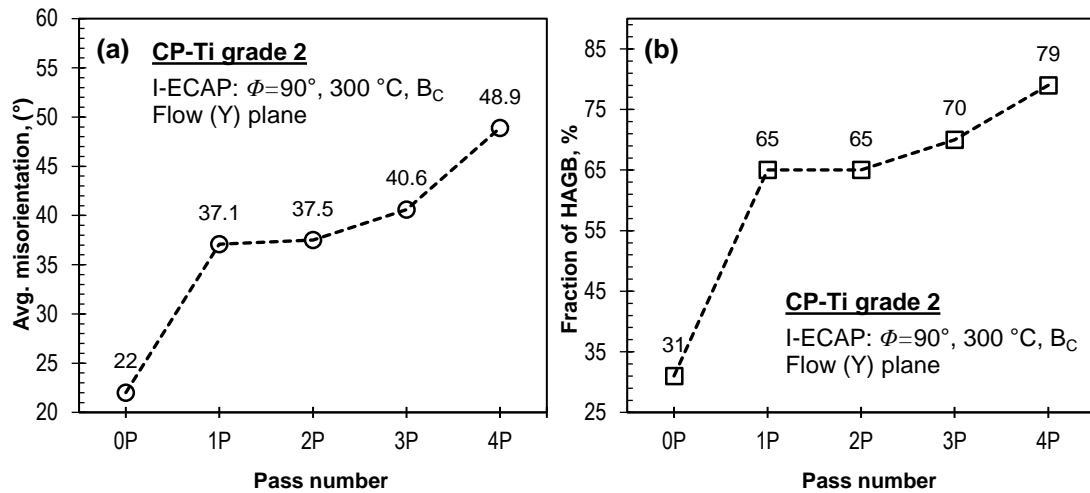


Fig. 5.21: (a) Average values of grain misorientation, (b) Percentage fraction of high angle grain boundaries (HAGB) in CP-Ti samples in the flow plane before and after subsequent I-ECAP at 300 °C using $\Phi = 90^\circ$ channel angle die.

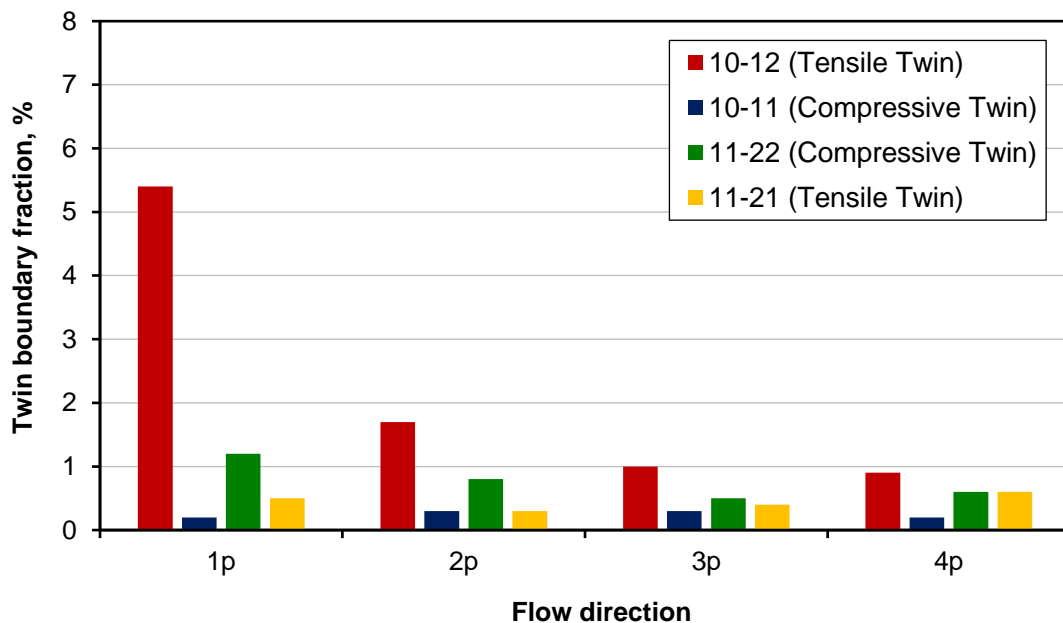


Fig. 5.22: Fraction of twin boundaries in the microstructure in CP-Ti samples in the flow plane before and after subsequent I-ECAP processing at 300 °C using $\Phi = 90^\circ$ channel angle die.

A quantitative analysis of the twin boundary fraction present in the microstructure after different I-ECAP passes is presented in Fig. 5.22. Similar to processing with $\Phi = 120^\circ$, during I-ECAP processing with $\Phi = 90^\circ$, two main twin types were observed, namely: $\{10\bar{1}2\}$ tensile twin and $\{11\bar{2}2\}$ compressive twin. However, $\{10\bar{1}2\}$ twin type was present in a relatively higher fraction in microstructure during processing compared to $\{11\bar{2}2\}$ twin. As evident from the

graph, twinning activity is greatly reduced with increasing number of passes as grain size becomes smaller.

5.6 Summary and conclusions

I-ECAP process was performed on CP-Ti grade 2 billets at 300 °C following route B_C, using die with a channel angle (Φ) of 120° and 90°. For $\Phi = 120^\circ$ case, the billets were subjected to a total of six passes, whereas for $\Phi = 90^\circ$ case the billets were subjected to four passes. The evolution of microstructure and deformation characteristics was studied and tracked by using relatively large scan areas obtained via EBSD. For the $\Phi = 120^\circ$ case, analysis was performed in both flow and transverse planes and for $\Phi = 90^\circ$ case, investigation was performed only in flow plane of the processed billet. Moreover, for $\Phi = 120^\circ$ case, texture development through subsequent I-ECAP processing was also investigated using pole figures in both planes.

For processing using die with channel angle (Φ) of 120°

1. Microstructure after first pass of I-ECAP was heterogeneous. It consisted of elongated grains, fine grains and a small fraction of undeformed pre-existing grains. Moreover, the grain misorientation histogram for both planes, showed peaks around 85 and 65° which suggested the presence of $\{10\bar{1}2\}$ and $\{11\bar{2}2\}$ in the microstructure. Beyond second pass, twinning activity was greatly suppressed with only a very small fraction of $\{10\bar{1}2\}$ twins appearing in the microstructure. Both twin types were confirmed by carrying detailed analysis in the present study.
2. Remarkable grain refinement was achieved after further passes of I-ECAP. After six passes the average grain size in flow plane was reduced from 20 to 1.3 μm . In transverse plane, the average grain size was reduced from 22 to 1.1 μm . The final microstructure after sixth pass was mostly homogenous and equiaxed. Moreover, it mostly consisted of HAGBs, in flow (Y) plane the fraction of HAGB was 51% and in transverse (X) plane the fraction was 66%.
3. Pole figures indicated that the strength of basal texture increased during processing up to fourth pass, beyond which it is seen to be weakened due to significant grain refinement.

4. Careful analysis of the second pass sample in transverse (X) plane revealed incomplete HAGB segments with misorientation angle slightly above 15° . This is a strong evidence for the occurrence of continuous dynamic recrystallization (CDRX) phenomena.
5. Twinning was found to be active and played a dominant role during the first two passes, beyond which slip was the dominant grain refinement mechanism.

For processing using die with channel angle (Φ) of 90°

1. After first pass, the microstructure was heterogeneous with a mixture of mostly large elongated grains and some clusters of very fine grains ($\sim 1 \mu\text{m}$). Some fine grains were visible along the boundaries of large elongated grains, forming a so-called necklace structure. Moreover, EBSD analysis of the microstructure revealed presence of mainly $\{10\bar{1}2\}$ tensile twins.
2. Twinning activity was greatly suppressed in the subsequent passes due to grain refinement, along with the decrease in heterogeneity in the microstructure.
3. Extraordinary grain refinement leading to UFG structure was achieved after the fourth pass. The average grain size was reduced from 20 to $0.86 \mu\text{m}$, which was accompanied by 79% of the grain boundaries having a misorientation angle greater than 15° (HAGBs). The texture was also weakened significantly due to grain refinement.

Remarkable grain refinement was achieved in both cases. The majority of the grains converted into ultrafine grain (UFG) size having mostly HAGBs after the final pass. However, higher levels of grain refinement was achieved using the $\Phi = 90^\circ$ die with four passes compared to achieved using the $\Phi = 120^\circ$ die with six passes. Overall, the shear deformation characteristics of I-ECAP process was found to be similar to the classical ECAP process. It is concluded that I-ECAP process is an effective method in refining grain structure in CP-Ti.

Chapter 6

Effect of I-ECAP on the mechanical behaviour of CP-Ti

6.1 Introduction

I-ECAP has been used in the present study to refine the grain structure in titanium as presented in Chapter 5. This chapter presents the effects of grain refinement using I-ECAP process on the mechanical performance of CP-Ti. For this purpose, tensile tests were performed after different number of passes to observe the changes in strength and ductility. Fractography of the tensile samples was performed to investigate the fracture morphology. Finally, detailed microhardness study was carried out to understand the hardness evolution and to examine the homogeneity of strain distribution during I-ECAP processing. Results from both processing conditions are presented and compared, i.e. for die angle of 120 and 90°.

6.2 Processing using I-ECAP die with channel angle (Φ) of 120°

6.2.1 Loads during processing

Fig. 6.1(a) to (f) shows the experimentally recorded forces on punch and feeding rod, also known as deformation and feeding forces respectively, during the first, second, third, fourth, fifth and sixth pass of I-ECAP. The vertical axis of the graphs represents force in kN and horizontal axis represents the stroke length in mm of the feeding rod. Note that the overall stroke is 10 mm less than the actual billet length, this is to prevent flattening the tail end of the billets. For better visualization, the recorded data was sampled and is presented in such a way that each force reading represents every 25th cycle during each pass. Due to the cyclic nature of the I-ECAP process, both the deformation and feeding force rises to a peak (crest) value and then falls to a lower (trough) value. The crest represent the force during deformation and the trough represents the force during feeding.

During the initial stage of processing the peak deformation force in all passes can be seen to increase up to a certain stroke length, beyond which it becomes somewhat constant. This stage of force increase is mainly due to the gradual increase in the contact area between the oscillating punch and the billet top surface (parallel to Z plane). Once there is full contact between the punch surface and billet surface, the force becomes constant. Apart from this the deformation is also dependent on the friction developed in the outlet channel because of lubricant removal in the inlet channel and shearing zone. It is also dependent on the compression in plastic deformation zone because of slight increase in cross-section.

Moreover, the deformation force is also seen to increase after subsequent passes. As shown in Fig. 6.2(a), the maximum values of force required to deform the pair of billets, progressively increased from 68.8 kN during the first pass to 92.5 kN in the sixth pass. This strongly suggests that the strength of billets is increasing after each pass and therefore greater force is required to deform the billets.

In Fig. 6.1(a) to (f), the peak values of feeding force during any cycle represent the force required to support the billets during deformation stages. It increases with each pass, following the trend of deformation force as presented in Fig. 6.2. The link between two forces is explained in Fig. 6.2(b) with the red arrows indicating force applied by punch C to deform the pair of billets, which is counter balanced not only by the die A (shown as green arrows) but also by the feeding rod B (shown as blue arrows). The actual force required to push the pair of billets during the feeding stage is between 1~3 kN (indicated by arrows in Fig. 6.1(a)), so small that it is hardly visible in the graphs. As demonstrated by Fig. 6.1(a) to (f), the actual feeding force required to carry out the process is very small. Thus I-ECAP can be used to process very long or continuous CP-Ti billets and thereby, making it an attractive option for industrialization to commercially produce UFG CP-Ti.

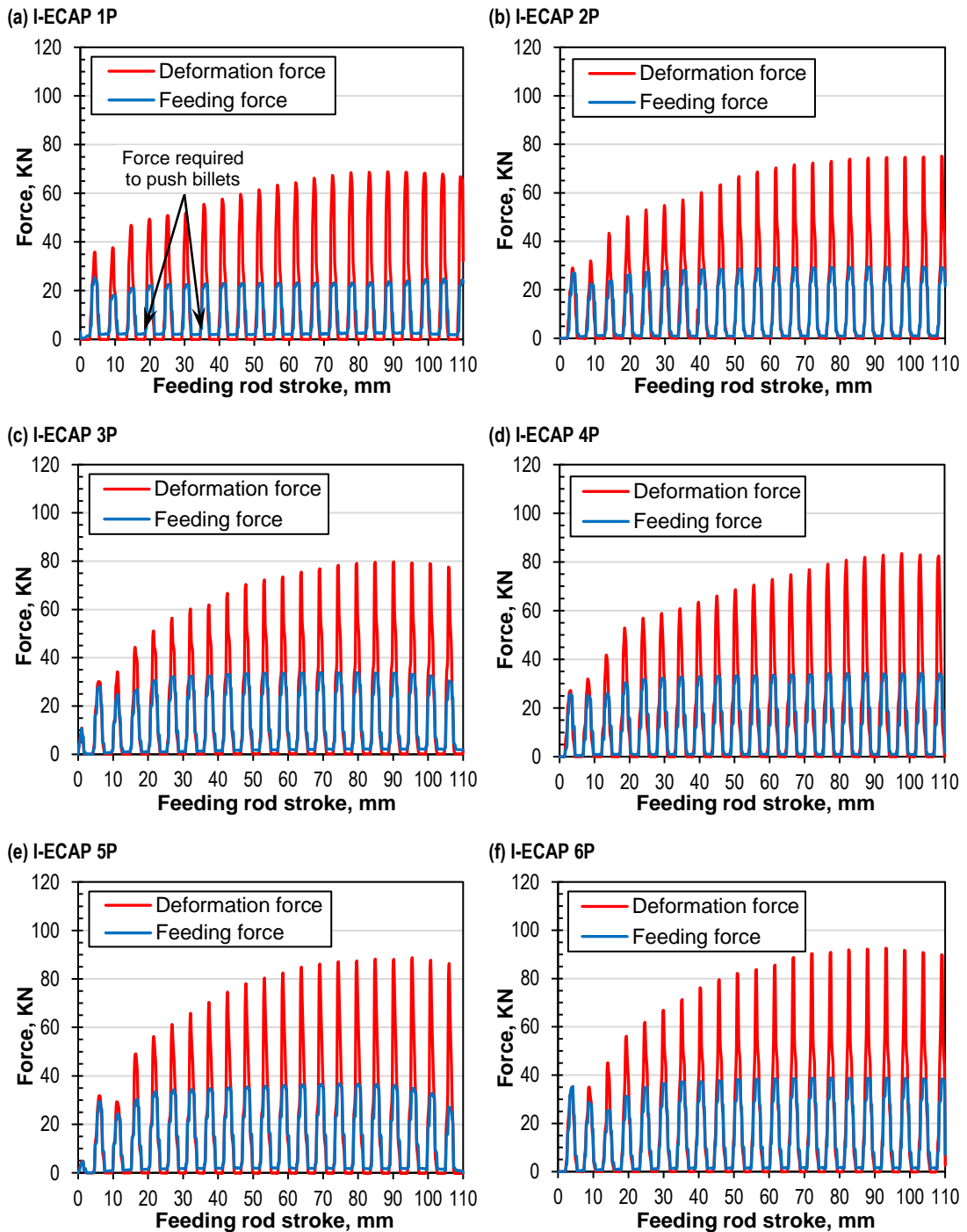


Fig. 6.1: Experimentally recorded deformation and feeding forces during (a) first, (b) second, (c) third, (d) fourth, (e) fifth and (f) sixth pass of I-ECAP processing at 300 °C using die with a channel angle (Φ) of 120°.

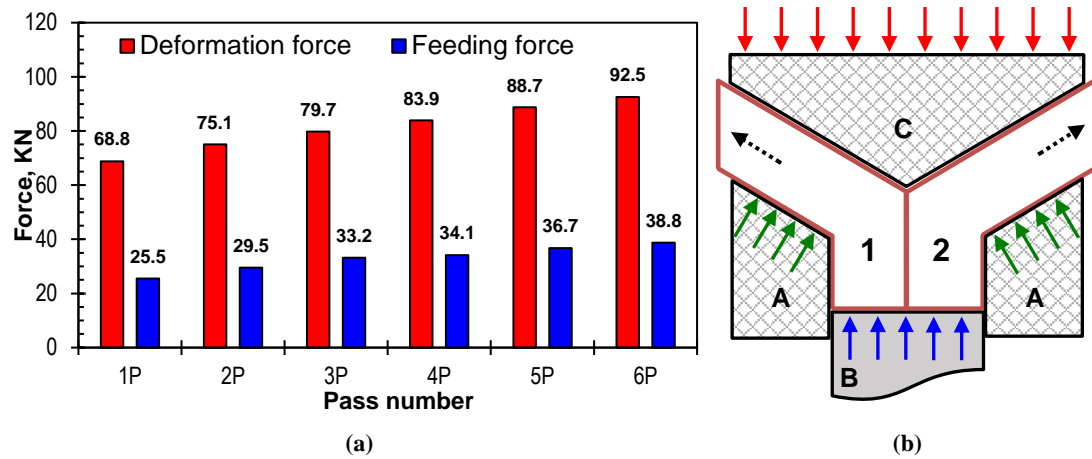


Fig. 6.2: (a) Values of maximum deformation and feeding forces during various passes of I-ECAP at 300°C using die with a channel angle (Φ) of 120° and (b) illustration of load distribution during the deformation stage.

6.2.2 Tensile properties

Fig. 6.3(a) shows the fractured tensile samples, after the room temperature tensile tests conducted at constant strain rate ($\dot{\epsilon}$) of 0.01 s^{-1} for the unprocessed condition and for first, second, fourth and sixth pass of I-ECAP using 120° channel angle die. Fig. 6.3(b) shows the corresponding stress-strain curves obtained from the tensile testing. The unprocessed material shows significant strain hardening beyond the yield point. For the processed material, it is seen that the level of yield strength (0.2% proof stress, σ_y) and ultimate tensile strength (σ_{UTS}) is greatly enhanced after the first pass and second pass compared to the unprocessed material. Although the level of strengthening is somewhat lower between second and fourth pass, this level improves again between fourth and sixth pass. Overall, it is apparent that the strength characteristic is gradually increasing due to the grain refinement taking place after each pass. In general, six passes of I-ECAP processing led to a significant increase in the values of yield strength and ultimate tensile strength in CP-Ti.

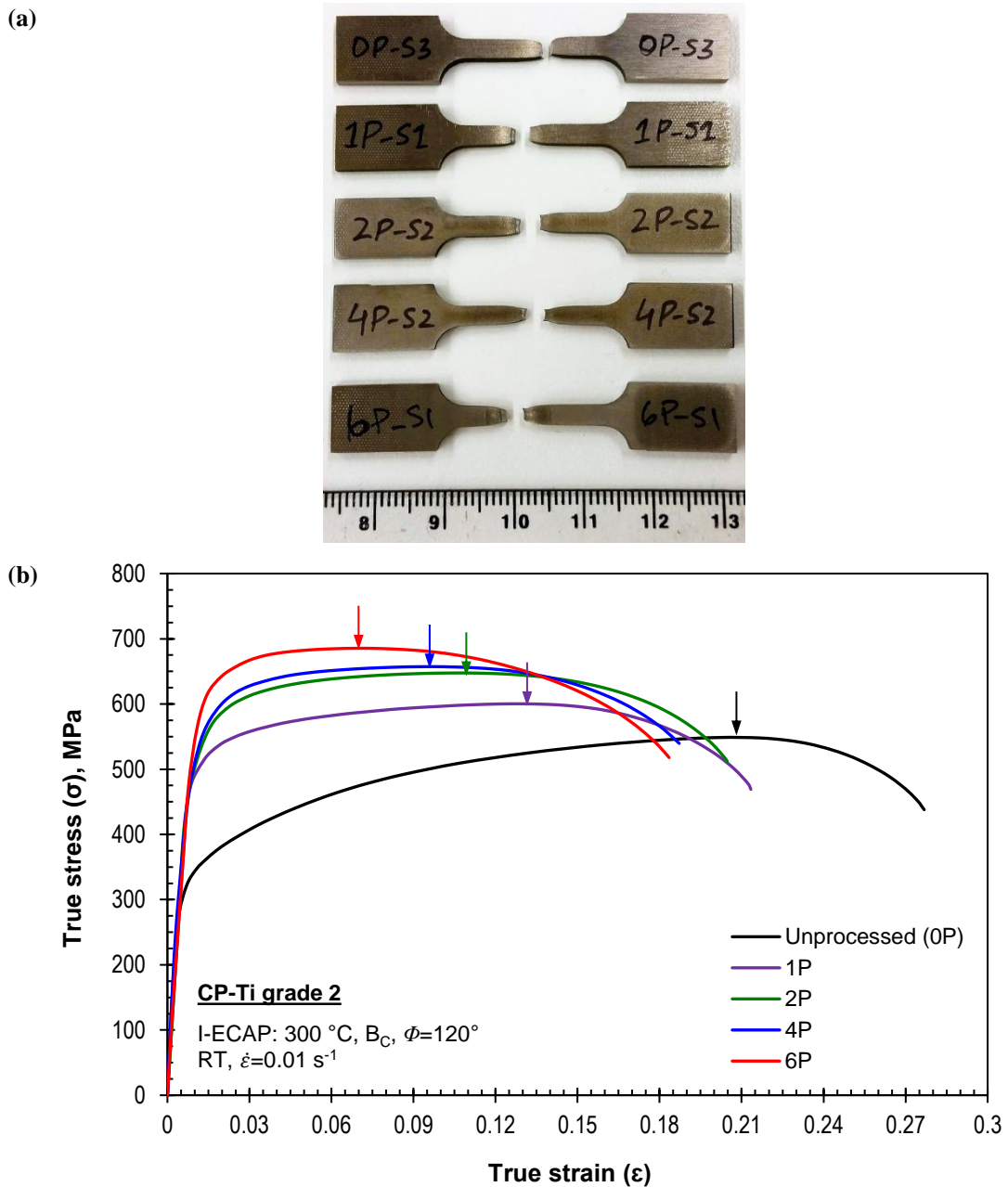


Fig. 6.3: (a) Fractured flat tensile CP-Ti test samples representing the unprocessed condition and after first, second, fourth and sixth pass of I-ECAP at 300 °C using $\phi = 120^\circ$ channel angle die and (b) stress-strain curves obtained from tensile testing at room temperature and at a strain rate of 0.01 s^{-1} . The arrow on each curve indicate the onset of necking.

Table 6.1 shows the individual values of strength and elongation derived from the stress-strain curves. Before and after six passes of I-ECAP, the yield strength of the material increases from 308 to 558 MPa and ultimate tensile strength increases from 549 to 685 MPa; this corresponds to 81% and 25% increase respectively. However, after I-ECAP processing, the ductility is somewhat reduced. The uniform

elongation (δ_{unif}), which is the elongation of the gauge length just before the onset of necking, decreases from the initial value of 22.3% to 8.80% after six passes. The elongation to failure (δ_{fail}) also decreases from 31.9% to 20.2%.

Table 6.1: Tensile properties of CP-Ti in unprocessed condition and after subsequent I-ECAP passes at 300 °C using $\Phi = 120^\circ$ channel angle die (0.2% σ_Y — yield strength, σ_{UTS} — ultimate tensile strength, δ_{unif} — uniform elongation, δ_{fail} — elongation to failure and Ψ — reduced cross-area at failure).

Pass #	Equivalent strain	0.2% σ_Y (MPa)	σ_{UTS} (MPa)	δ_{unif} (%)	δ_{fail} (%)	Ψ (%)
0P	-	308	549	22.3	31.9	63.9
1P	0.67	489	601	14.5	23.8	60.1
2P	1.34	502	648	12.7	22.8	59.6
4P	2.68	511	657	11.4	20.6	60.2
6P	4.02	558	685	8.8	20.2	59.5

It is interesting to note that the uniform elongation (δ_{unif}) achieved in all the processed material conditions is significantly lower than the elongation to failure (δ_{fail}). For visual purposes, the uniform elongation (δ_{unif}) is marked by arrows on the individual stress-strain curves in Fig. 6.3(b). Studies [184, 185] have shown that, in SPD processed material the onset of necking occurs in early stages of deformation during tensile testing. This is because SPD processed materials contain highly deformed structure, where dislocation density has reached a very high or to some extent a saturation level. Moreover, due to grain refinement occurring during SPD processing, the grain structure is in the UFG range, having mostly high angle grain boundaries. The UFG material tends to lose the strain hardening ability as the very fine grains lose their ability to further accumulate dislocations generated during tensile testing. Therefore UFG material are susceptible to plastic instability (early necking). Hence, in Fig. 6.3(b), the processed material exhibits lack of strain hardening behaviour compared to the unprocessed material. Since strain hardening is an important mechanism to sustain uniform elongation (δ_{unif}) during tensile loading, lack of strain hardening exhibited by SPD processed materials limits its ductility. In the present study, the processed material however exhibits increase in post necking elongation compared to the unprocessed material and therefore it displays acceptable levels of overall ductility (δ_{fail}). It is concluded from the data that, after six passes there is a significant increase in strength without considerable loss of ductility.

6.2.3 Fractography

Fig. 6.4(a) to (e) show SEM images of the fracture morphology of the tensile tested samples; (a) in the unprocessed condition and after (b) first, (c) second, (d) fourth and (e) sixth pass of I-ECAP. For each material condition, three images are shown; micrograph showing extend of necking at fracture (on the left), lower magnification micrograph (in the middle) and higher magnification micrograph of the dotted rectangular box (on the right).

Low magnification micrographs (middle figures) of all tested samples confirmed that the fracture surfaces are covered throughout by dimples. This suggests that in all cases, failure process is mainly occurring by nucleation and growth of voids and hence, the mode of fracture is entirely ductile in nature. Lower and higher magnification micrographs provided for each sample shows that size of the dimples is decreasing with increase in number of passes, which also confirms the occurrence of grain refinement process. The unprocessed material is dominated by large size dimples with some evidence of fine size dimples as seen in higher magnification micrograph in Fig. 6.4(a). After second pass of I-ECAP process, it is observed that the fraction of large size dimples has been reduced noticeably. After fourth pass, the fractured surface is covered by uniform sized dimples, with dimple size reducing even further after sixth pass. Moreover, it is seen that the fracture surface is somewhat smoother after sixth pass.

As listed in Table 6.1, regardless of the number of passes, the reduced area at failure (Ψ) is quite similar, having values between 60.1 to 59.5 %. As discussed earlier, although the onset of necking in processed material happens in the early stages of deformation, the area at failure (Ψ) values suggest resistance to fracture. This can be considered as a possible explanation for the area at failure (Ψ) having similar values for different passes.

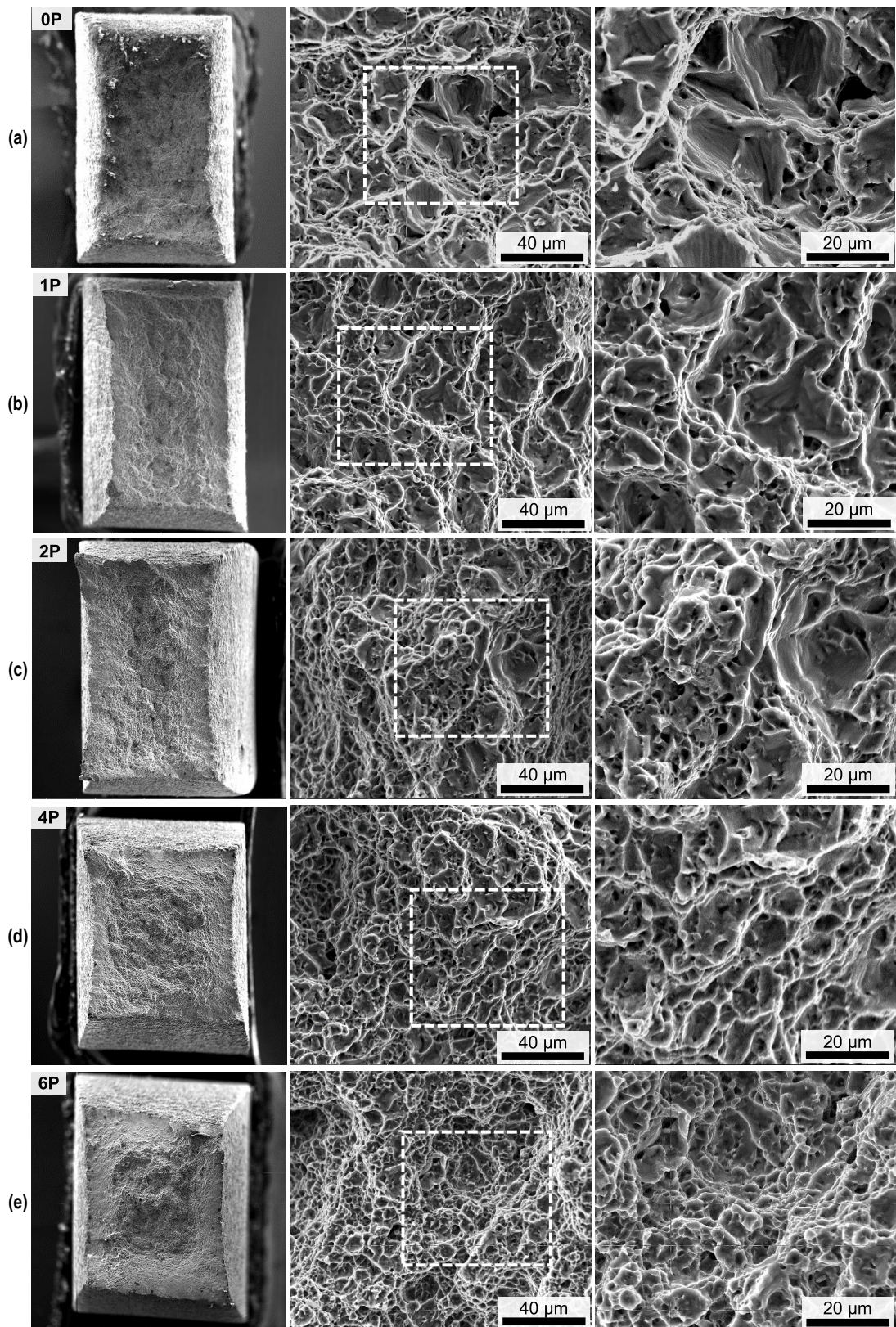


Fig. 6.4: SEM images of the fractured CP-Ti tensile samples showing the fracture morphology at three different magnifications for (a) unprocessed material and I-ECAPed material after (b) first, (c) second, (d) fourth and (e) sixth pass at 300 °C using $\Phi = 120^\circ$ channel angle die.

6.2.4 Hardness evolution

Numerous studies on ECAP have shown that it is essential to process the billet multiple times in order to induce the desired level of strain and thereby attain UFG structure. Microhardness measurement is considered a standard procedure for evaluating the induced strain after processing and also to study the level of billet homogeneity with respect to mechanical properties and corresponding microstructural changes. To examine the homogeneity of strain distribution and also to investigate the evolution of hardness with increasing number of I-ECAP passes, microhardness measurements were performed on the unprocessed material and the material subjected to I-ECAP passes. The individual values of microhardness (H_v) were measured on a 11 x 11 array of equi-spaced points across the transverse (X) plane.

For the purposes of providing a detailed visual representation, contour maps have been generated from the microhardness measurements across the X plane. Fig. 6.5(a) to (e) shows colour-coded contour maps for the (a) unprocessed material and for the (b) first, (c) second, (d) fourth and (e) sixth pass. For all maps, the values of microhardness are represented by a set of distinct colours. The corresponding microhardness value of each colour is shown by the legend given on the right, which ranges from 150 to 220 H_v in increments of 7 H_v . The horizontal and vertical axis of the plot represent the transverse direction (TD) and normal direction (ND), respectively, with flow direction (FD) pointing outward from the paper (X-plane).

It is evident from Fig. 6.5(b), that the microhardness increases significantly after the first pass and this increase is seen to occur over the entire surface of the sample. The increase in microhardness continues through subsequent passes; this is attributed to the fact that greater level of strain is induced in the material after each pass which causes reduction in grain size thereby increasing the strength characteristic of the material. However, upon close assessment of the contour plot, it is evident that the increase in the hardness distribution is not completely uniform across the entire surface. There is a region of lower hardness near the top surface of the billet after fourth pass. Although, after sixth pass the situation improves, as this region of lower hardness is somewhat shrunk. Nevertheless, this narrow region of lower hardness near the top (the surface of billet in contact with punch) remains even after six passes.

In order to examine the level of non-uniformity, Fig. 6.6 (a-d) shows the microhardness (H_v) values recorded in the transverse (X) plane along three horizontal lines; the centre line and at 1mm from the top and bottom surfaces after (a) one, (b) two, (c) four and (d) six passes. For all the plots, the dashed line represents the average microhardness in the unprocessed condition. Overall, it is fairly obvious that the microhardness values are increasing with increasing number of passes. After first pass, the average microhardness along the centre line increases to $\sim 180 H_v$ from $\sim 157 H_v$ in the unprocessed condition. The microhardness near the top surface was lower with a value of $\sim 175 H_v$, however near the bottom surface the average value was slightly higher with $\sim 182 H_v$. From pass two to six the hardness continues to increase gradually over subsequent passes and does not seem to saturate. The level of homogeneity improves after second pass since the microhardness near the top and bottom surfaces are relatively similar to microhardness measured along the centre line. Beyond pass two, the region near the bottom surface continues to maintain the same hardness level as the centre line. In contrast, the hardness near the top surface is somewhat lower. After six passes, average microhardness at the centre line and near the bottom surface are both roughly the same, at $\sim 218 H_v$, compared to a value of $\sim 210 H_v$ near the top surface.

Fig. 6.7 shows the mean values of microhardness evolution calculated from all the recorded measurements in the X plane of samples, for unprocessed condition and after first, second, fourth and sixth pass of I-ECAP. The error bars in the graph represent the standard deviation, which shows the level of dispersion in the hardness values from the mean value. In the unprocessed condition the mean value of microhardness is $\sim 156 H_v$, after first pass this value rises sharply to $\sim 181 H_v$, an increase of 16%. For subsequent second, fourth and sixth passes the microhardness value increases to 187, 199 and 215 H_v , this corresponds to an increase of 3.3%, 6.4% and 8.0% respectively. This increase in the mean microhardness also correlates qualitatively with the increase in yield and especially ultimate tensile strength observed in tensile test after subsequent I-ECAP passes. Overall, after six passes of I-ECAP, the average value of microhardness is increased from 156 to 215 H_v ; this corresponds to an increase of 38%.

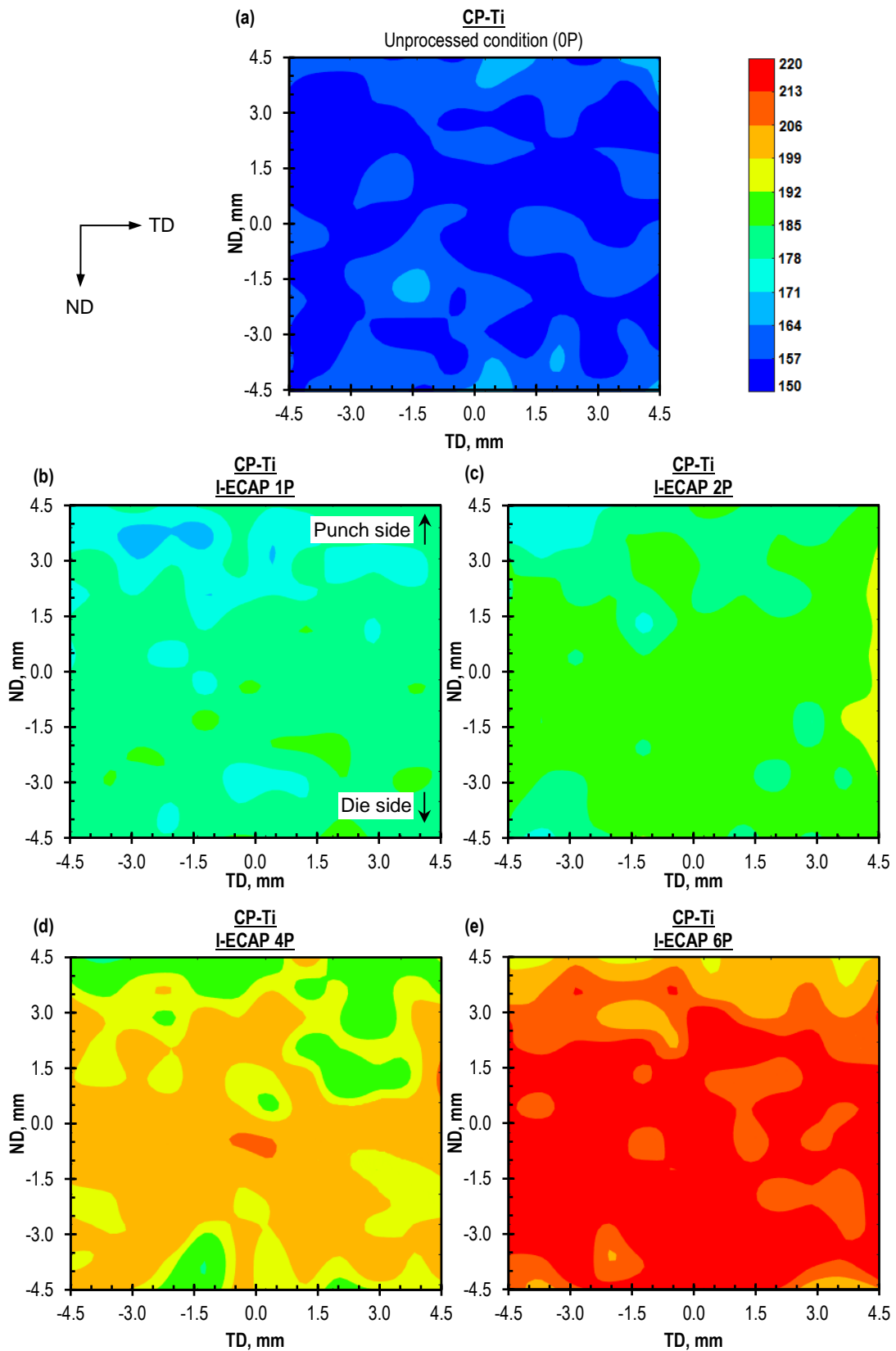


Fig. 6.5: Colour coded contour maps of the microhardness (H_v) recorded in the transverse (X) plane for (a) unprocessed condition, after (b) first, (c) second, (d) fourth and (e) sixth pass of the I-ECAP process at 300 °C using the die with channel angle (Φ) of 120°.

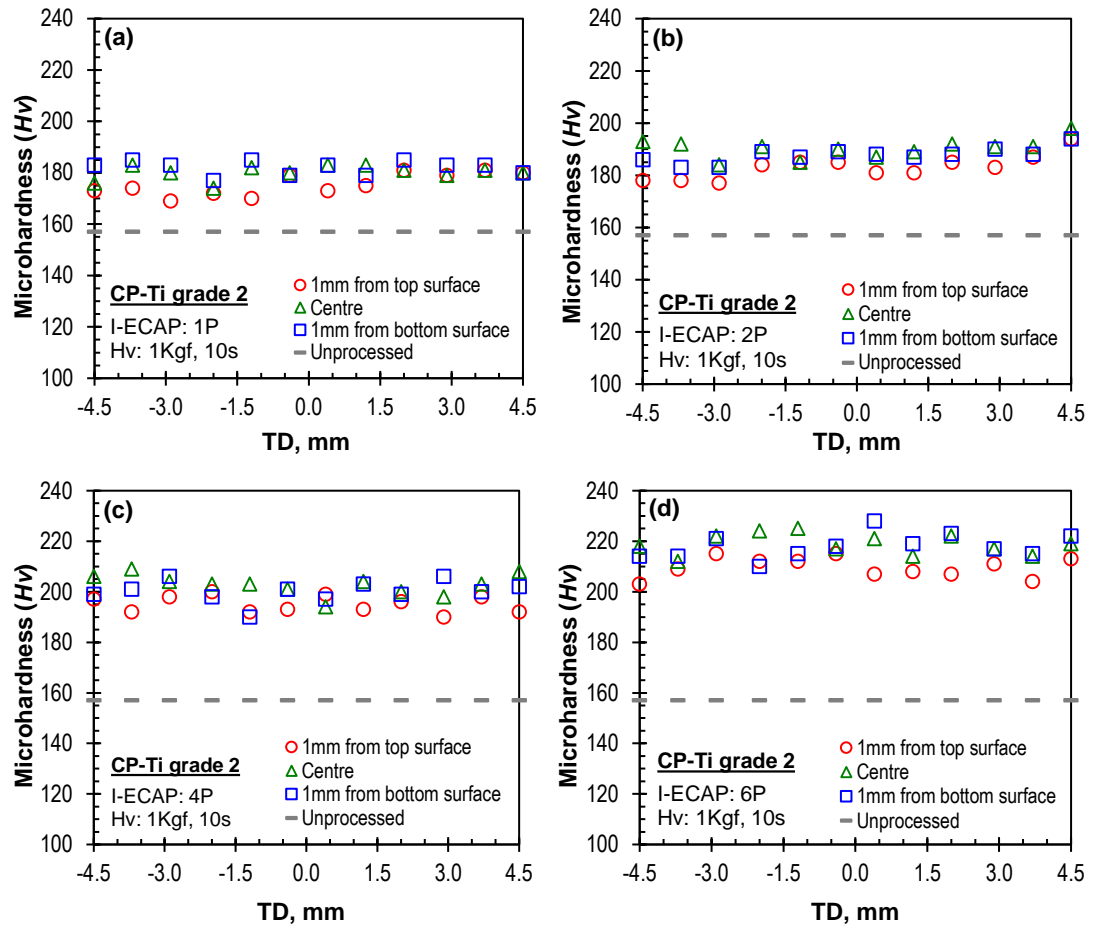


Fig. 6.6: Microhardness (Hv) recorded in the transverse (X) plane along three lines; the centre line and at 1 mm from the top and bottom surfaces after (a) first, (b) second, (c) fourth and (d) sixth pass of the I-ECAP process at 300 °C using the die with channel angle (Φ) of 120° (the dashed line shows average microhardness in the unprocessed condition).

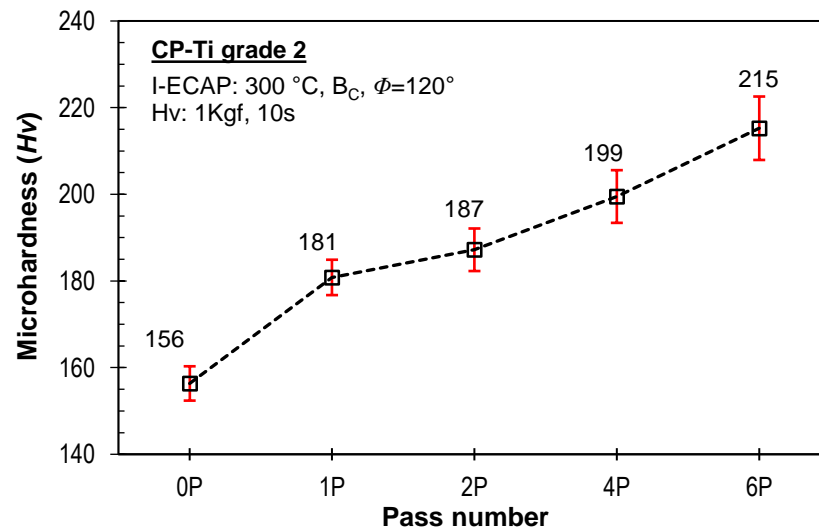


Fig. 6.7: Mean values of Vickers microhardness (Hv) recorded in the X plane before and after subsequent passes of I-ECAP at 300 °C using the die with channel angle (Φ) of 120°. The error bars represent the calculated standard deviation.

6.3 Processing using I-ECAP die with channel angle (Φ) of 90°

6.3.1 Loads during processing

Fig. 6.8(a) to (f) represent the graphs showing recorded forces on punch (deformation force) and feeding rod (feeding force); during the (a) first, (b) second, (c) third and (d) fourth pass of I-ECAP. The vertical axis of the graphs represents force in kN and horizontal axis represents the feeding rod stroke length in mm. Note that the overall stroke is again 10 mm less than the actual billet length; this is to prevent flattening of the billet at the tail end. For better visualization, the recorded data was sampled and is presented in such a way that each force reading represents every 25th cycle during each pass.

Similarly to the observations made in the $\Phi = 120^\circ$ study, here too, during the initial stage of processing the deformation force in all passes can be seen to increase up to a certain stroke length, beyond which it becomes rather constant or continues to increase but at a slow rate. As explained earlier, this stage of force increase is mainly due to the gradual increase in the contact area between the oscillating punch and the billet top surface (parallel to Z plane). Once there is full contact between the punch surface and billet surface, the force becomes constant. Moreover, the deformation force is also seen to increase in subsequent passes. As shown in Fig. 6.9, the maximum values of force required to deform the pair of billets, progressively increased from 185.8 kN during the first pass to 236.1 kN in the fourth pass. This strongly suggests that the strength of billets is increasing after each pass and therefore greater force is required to deform the billets. In general, the maximum feeding force during each pass is 55 ~ 60% of the deformation force value.

Compared to the channel angle (Φ) of 120° , the force required to deform a pair of billets increases by almost 2 to 2.5 times when the channel angle is lowered to 90° . This is because the induced strain during subsequent pass also increases from 0.67 per pass for $\Phi = 120^\circ$ to 1.07 per pass for $\Phi = 90^\circ$.

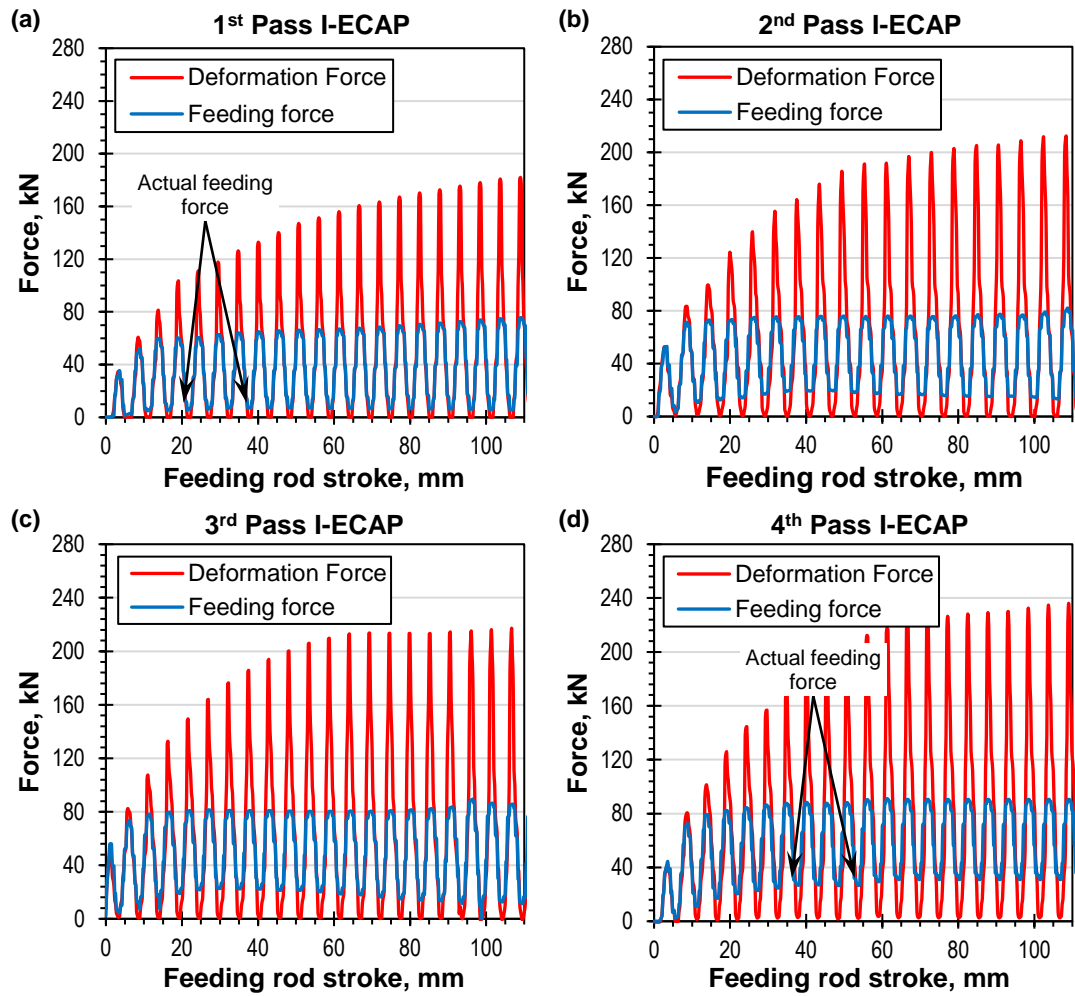


Fig. 6.8: Deformation and feeding forces recorded during (a) first, (b) second, (c) third and (d) fourth pass of I-ECAP at 300 °C using the die with channel angle (Φ) of 90°.

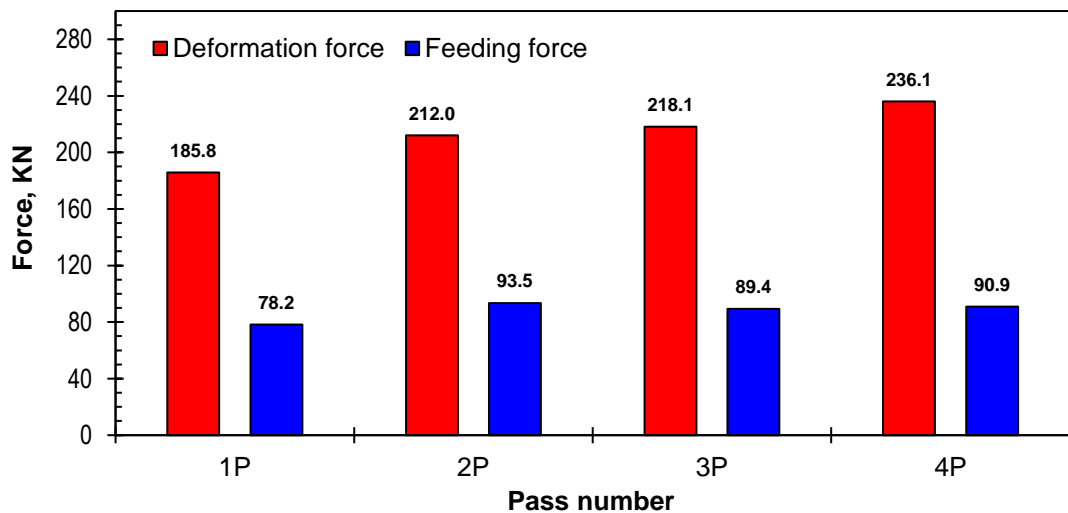


Fig. 6.9: Values of maximum deformation and feeding forces during consecutive passes of I-ECAP at 300 °C using the with channel angle (Φ) of 90°.

6.3.2 Tensile properties

Fig. 6.10 shows the stress-strain curves obtained from the tensile testing of unprocessed and I-ECAP processed samples after first, second, third and fourth pass. It is readily apparent from the curves that the strength characteristic is gradually increasing due to the grain refinement taking place in the billets after each pass of I-ECAP.

Table 6.2 shows the summary of tensile properties for the unprocessed and processed material. First pass of I-ECAP, significantly increased the yield strength (σ_Y) and ultimate tensile strength (σ_{UTS}) of the material. The σ_Y in particular was increased by almost double the initial value, i.e. from 308 to 610 MPa after the first pass. After second and third pass, the improvement is quite consistent and moderate levels of strengthening is achieved after each pass. However, after fourth pass it seems that the strengthening is reaching a saturation state, as the material does not exhibit any considerable improvement in strength compared to that after the third pass. Overall, due to the formation of UFG structure, the material subjected to four passes of I-ECAP, displayed a marked increase in the values of yield strength (σ_Y) and ultimate tensile strength (σ_{UTS}). The σ_Y was increased from 308 to 671 MPa and the σ_{UTS} was increased from 549 to 730 MPa; this corresponds to an increase of 118% and 33%, respectively.

Similarly to the $\Phi = 120^\circ$ study, although the severely deformed material displays increasing levels of strength (σ_Y and σ_{UTS}) after each pass of I-ECAP, the material suffers reduction in ductility due to the loss of strain hardening ability. The arrow on each curve in Fig. 6.10 indicates the uniform elongation (δ_{unif}) achieved. The stress-strain curve obtained after the second pass (see the green curve in Fig. 6.10) is an exception here. It displays some decent level of strain hardening. Consequently, according to the calculated values in Table 6.2, the second pass processed material displayed the highest values of ductility among all processed materials, with δ_{unif} at 13.1% and δ_{fail} at 23.1%. It is not clear, why the material regained its strain hardening ability after second pass. Such behaviour was not observed in the $\Phi = 120^\circ$ study. Beyond pass two, the material does not exhibit any noticeable strain hardening and therefore the ductility values continue to gradually decrease after subsequent passes.

It is interesting to note again that the processed material exhibits relatively high post necking elongation. As a result, despite the much reduced δ_{unif} , the processed

material still manages to display acceptable values of δ_{fail} in all cases. The room temperature tensile test shows that δ_{unif} after four passes of I-ECAP on CP-Ti decreases from an initial value of 22.3% to 8.9% and the δ_{fail} also decreases from 31.9% to 21.1%. The latter, is considered to be a reasonably good level of ductility exhibited by the severely deformed CP-Ti material after I-ECAP processing.

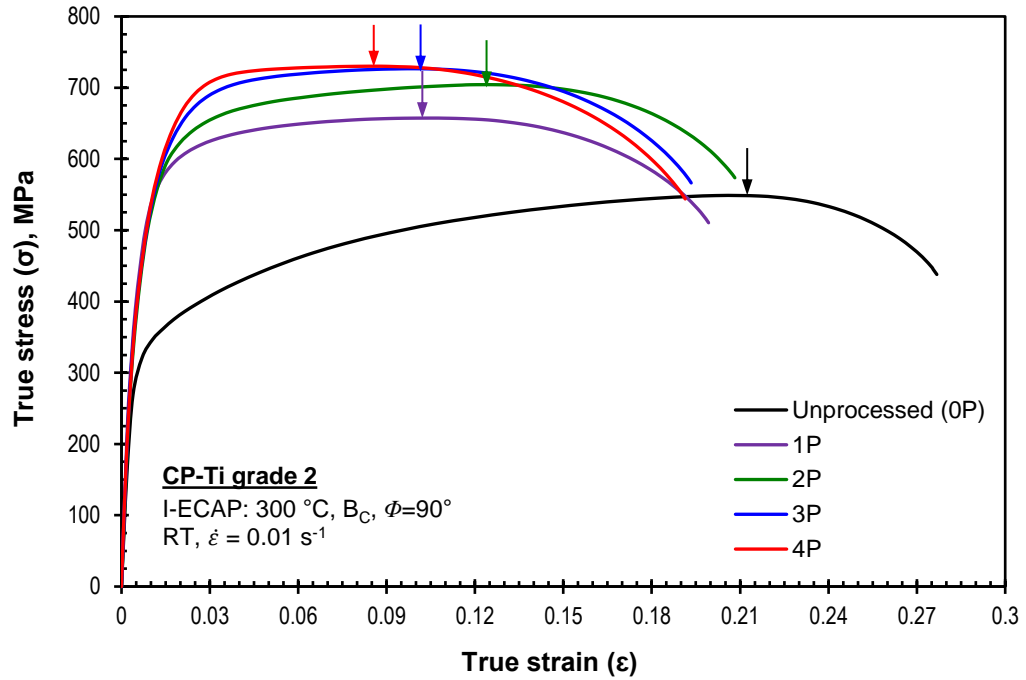


Fig. 6.10: True Stress-strain curves obtained from tensile testing at room temperature and at a strain rate of 0.01 s^{-1} of the unprocessed and processed CP-Ti samples after first, second, third and fourth pass of I-ECAP at 300 °C using $\Phi = 90^\circ$ channel angle. The arrow on each curve indicate the onset of necking.

Table 6.2: Tensile properties of CP-Ti in unprocessed condition and after subsequent I-ECAP passes at 300 °C using $\Phi = 90^\circ$ channel angle die ($0.2\% \sigma_Y$ — yield strength, σ_{UTS} — ultimate tensile strength, δ_{unif} — uniform elongation, δ_{fail} — elongation to failure and Ψ — reduced cross-area at failure).

Pass #	Equivalent strain	$0.2\% \sigma_Y$ (MPa)	σ_{UTS} (MPa)	δ_{unif} (%)	δ_{fail} (%)	Ψ (%)
0P	-	308	549	22.3	31.9	63.9
1P	1.07	610	657	11.1	22.0	61.4
2P	2.14	622	704	13.1	23.1	60.2
3P	3.21	657	726	10.7	21.3	60.1
4P	4.28	671	730	8.9	21.1	63.2

6.3.3 Fractography

Fig. 6.11(a) to (e) show the fracture morphology using SEM of the tensile tested samples: (a) in the unprocessed condition and after (b) first, (c) second, (d) third and (e) fourth pass of I-ECAP. Similar to the $\Phi = 120$ study, three images are shown for each material condition. On the left, there is a micrograph showing extend of necking at fracture, in the middle, a lower magnification micrograph and on the right, a higher magnification micrograph of the dotted rectangular box (on the right).

The lower and higher magnification micrographs show that for all tested samples, the fracture surface is covered throughout by dimples. This is a strong indication that for all cases the mode of failure is ductile fracture, as the failure process was initiated by the nucleation and growth of voids resulting in dimple formation upon fracture. These micrographs also clearly show the grain refinement after subsequent I-ECAP passes, as seen by the decreasing dimple pass after each pass. The unprocessed material is dominated by large size dimples as seen by the higher magnification micrograph in Fig. 6.11(a). After first pass, the dimple sizes has reduced, however, the dimples are not uniform in size. Beyond second pass, the dimple size continues to decrease and becomes uniform with the increase in number of passes. The fracture surface of the UFG CP-Ti sample after four passes of I-ECAP, shows a dramatic decrease in the dimple size and these very fine dimples are distributed uniformly across the fracture surface. As a result, compared to the unprocessed condition, the fracture surface is homogenous and rather smooth.

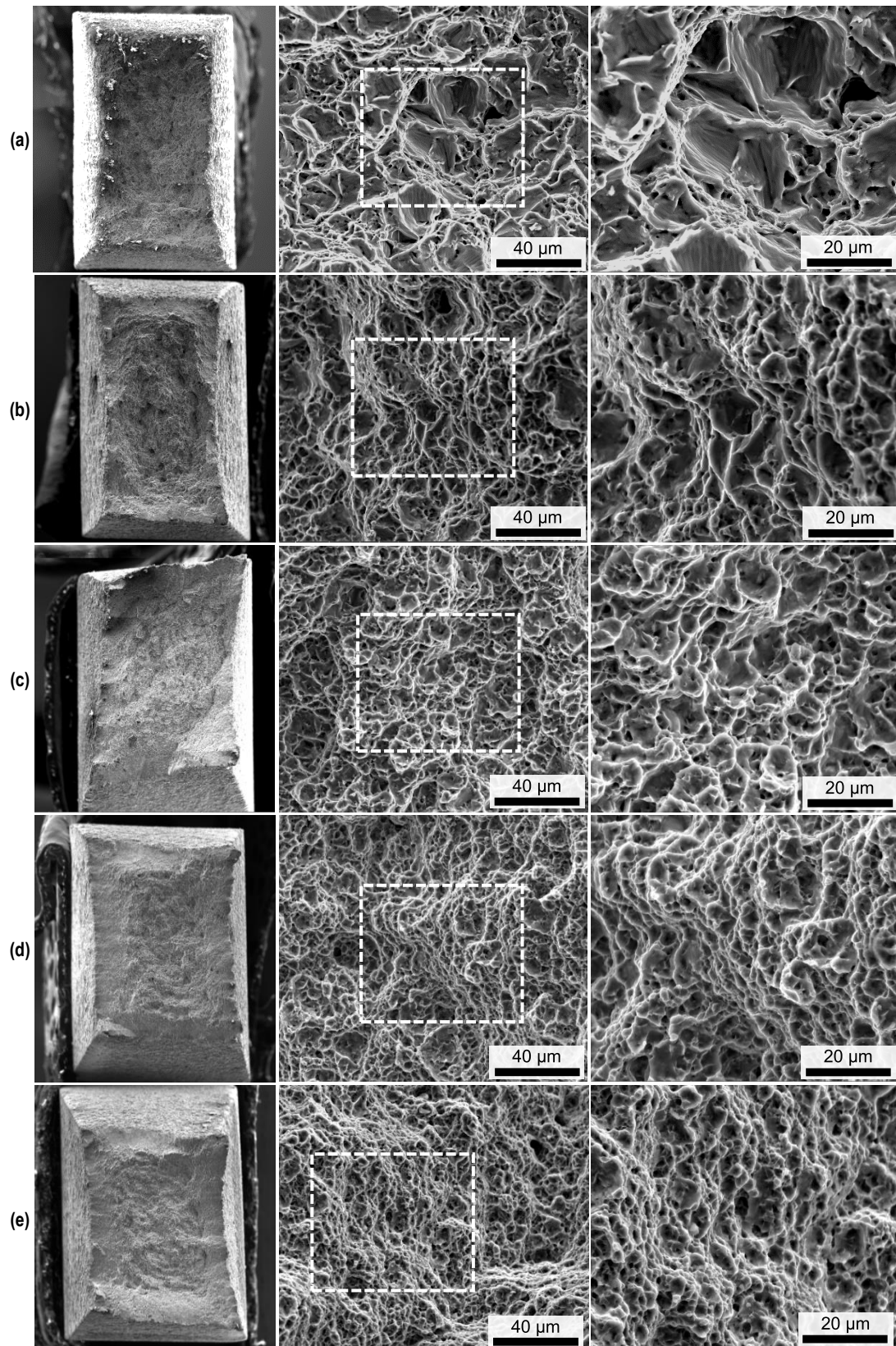


Fig. 6.11: SEM images of the fractured CP-Ti tensile samples showing the fracture morphology at three different magnifications for (a) unprocessed material and I-ECAPed material after (b) first, (c) second, (d) third and (e) fourth pass at 300 °C using $\Phi = 90^\circ$ channel angle die.

6.3.4 Hardness evolution

Fig. 6.12 shows the mean values of microhardness calculated from the recorded measurements in the transverse (X) plane of samples, for unprocessed condition and after first, second, third and fourth pass of I-ECAP. Twenty hardness measurement recordings were made at different locations in the X plane of each sample to calculate the mean value. The error bars in the graph represent the standard deviation, which shows the level of dispersion in the hardness values from the mean value. In the unprocessed condition, the mean value of microhardness is ~156 Hv, after first pass this value rises sharply to ~196 Hv, an increase of over 25%. For subsequent second, third and fourth passes the microhardness value increases to 200, 214 and 217 Hv, this corresponds to an increase of 2.6%, 6.5% and 1.4% respectively. This increase in the mean microhardness values also correlates qualitatively with the increase in yield and ultimate tensile strength observed in tensile test after subsequent I-ECAP passes. Overall, after four passes of I-ECAP, the average value of microhardness is increased from 156 to 217 Hv; this corresponds to an increase of 39.1%.

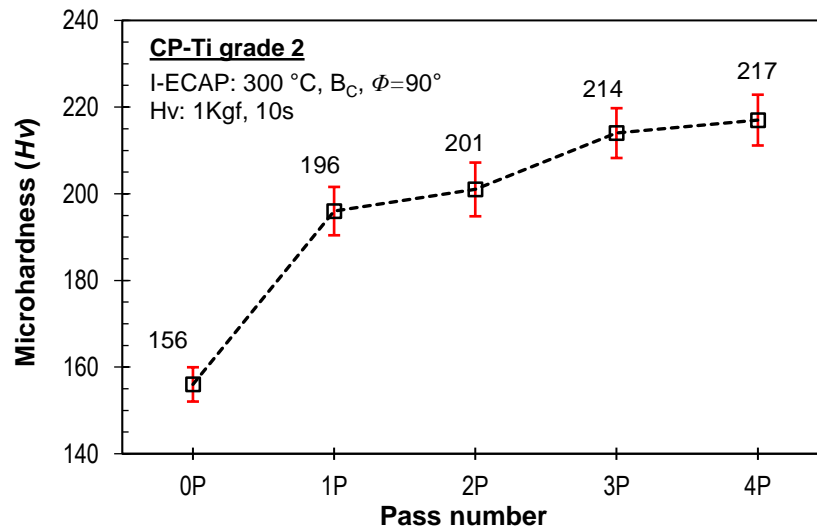


Fig. 6.12: Mean values of Vickers microhardness (Hv) recorded on the X plane before and after subsequent passes of I-ECAP process at 300 °C using the die with channel angle (Φ) of 90°. The error bars represents the calculated standard deviation.

6.4 Comparison of 120° and 90° channel angle cases

It is necessary to make a comparison of the improvements in tensile properties achieved in CP-Ti grade 2 material, after I-ECAP processing by using the 120° and 90° channel angle dies. Fig. 6.13(a-c) presents the yield strength, ultimate tensile strength (UTS) and percentage ductility (elongation to failure) values obtained from tensile testing at room temperature for the two studied cases. The properties are shown as a function of equivalent strain induced during I-ECAP processing. Recall that for 120° case the equivalent strain per pass is ~ 0.67 and for 90° case the strain is ~ 1.07 per pass. The billets are processed for six passes using the 120° die, inducing a total equivalent strain of ~ 4.02 . This value of strain induced is lower compared to the 90° case, where only four passes induce a total equivalent strain of ~ 4.28 , however are comparable.

In Fig. 6.13(a), for both cases, the first pass significantly improves the yield strength of the material. The original yield strength is increase from 308 MPa to 489 (58% increase) for 120° case and to 610 MPa (98% increase) for 90° case. The higher value of yield strength achieved in 90° case compared to 120° case is understandable, as the strain value induced during the first pass using the 90° die is $\sim 60\%$ higher than the strain induced using 120° die.

Beyond first pass in both cases, the yield strength is seen to increase, but at a much reduced rate. For the 120° case, after an initial sharp rise, the yield strength increases gradually to 558 MPa after the fourth pass. Although, compared to the original yield strength value, this represents a significant overall improvement; however, beyond first pass, the next five passes only contributed to 14% further increase in strength i.e. from 489 to 558 MPa. Similar trend is observed for the 90° case, where the next three passes only manages to increase the strength by just over 10% i.e from 610 to 671 MPa.

For the 120° case, it is interesting to note that the increase in yield strength is non proportional to the strain induced when compared to the 90° case. For example, after the second pass, the equivalent strain induced is ~ 1.34 (2×0.67) and the yield strength achieved is 502 MPa. This is much lower when compared to the 90° case where an induced strain of 1.07 results in a much higher yield strength value of 610 MPa. Consequently, even though the total equivalent strain induced in 90° case after

four pass is only ~6.5% higher compared to the strain induced after six passes in 120° case, the final increase in strength achieved is more than 20% higher for the 90° case. This shows that strain induced per pass has a bigger effect on the strength increase compared to the total equivalent induced strain.

Comparison of UTS is shown in Fig. 6.13(b) for the two cases. The unprocessed material displayed higher level of strain hardening in the room temperature tensile testing and reaches a UTS of 549 MPa. On the other hand, in both cases, the processed material suffered loss in strain hardening ability and therefore the improvement in UTS achieved after first pass is not at the same levels as increase in yield strength achieved. In 120° case, the UTS after first pass increases to 601 (9.5% increase) and in 90° case it increases to 657 MPa (20% increase). Beyond first pass, the UTS value increase by further ~14% in the next five passes to reach 685 MPa. In 90° case, the UTS increases by further ~11% in the next three passes to reach 730 MPa. Interestingly, here the 120° case displays rather proportional increase in UTS with respect to the induced strain at least up to the second pass. Beyond second pass the UTS increases gradually but non-proportionally to the strain induced.

It is important to compare the strength improvement achieved in the present study with Ti-6Al-4V, since the ultimate goal of the work is toward improvement in strength characteristics of CP-Ti to replace Ti-6Al-4V in bio-medical implants. The yield and tensile strength of Ti-6Al-4V is in the range of 840-90 MPa and 940-970 MPa, respectively [125]. To put it in perspective, the strengthening achieved in the present study for CP-Ti grade 2 using I-ECAP process with 90° degree die is around ~80% and ~75% of the yield and UTS of Ti-6Al-4V. This is considered to be a big achievement since this is the first time the material was processed on I-ECAP rig.

Finally, Fig. 6.13(c) compares the ductility (elongation to failure) for both cases. As seen by the graph, the loss in strain hardening ability also decreases the elongation to failure values. In both cases, the ductility decrease with the number of passes increases. The exception is however, second pass 90° case, where the ductility increases marginally compared to the first pass. In both cases the final ductility achieved is very similar 20.2% and 21.1% for 120° and 90°, respectively. Although, ductility is reduced in the processed CP-Ti, it is still considered reasonable.

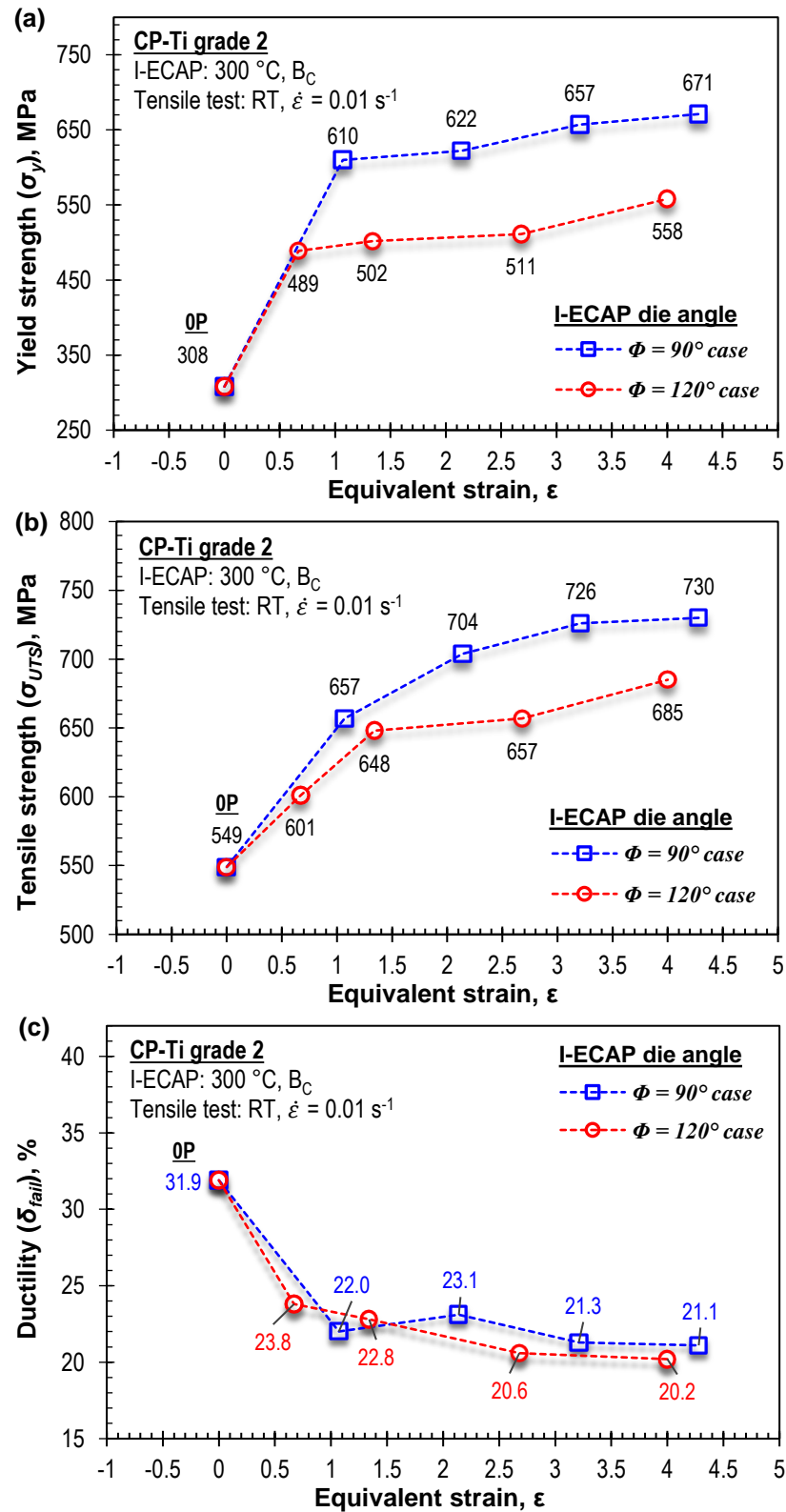


Fig. 6.13: Comparison of the room temperature tensile properties (a) yield strength, (b) ultimate tensile strength (UTS) and (c) percentage ductility (elongation to failure) as a function of induced equivalent strain during I-ECAP processing of CP-Ti using dies with channel angle (Φ) of 120° and 90° .

6.5 Comparison with ECAP

It is interesting to make a comparison with the earlier reports of processing CP-Ti (various grades) by ECAP for different die angles, processing speeds and temperatures. Table 6.3 presents the summary of processing parameters used in selected earlier ECAP studies and in the present study, along with the changes in grain size, hardness, strength and ductility. It is important to emphasize that the grain size and mechanical properties listed in the table are after ECAP process only and before any subsequent post ECAP deformation (such as cold extrusion, rolling etc.). The table has been arranged in the descending order of processing temperature.

As can be seen in the table, to facilitate processing of CP-Ti various techniques have been employed. These include processing at elevated temperatures, using higher die angles and by using lower grades of titanium. To activate more slip systems in titanium, almost all the studies listed in table have been performed at elevated temperatures (500 to 250 °C). Zhao et al. [129, 130] was however able to demonstrate ECAP at room temperature. This is because grade 1 was used in these studies, which has the lowest interstitial and substitutional elements among available commercial grades of titanium and therefore considered to be the most formable.

In the context of processing grade 2; for lower die angle of $\Phi = 90^\circ$, the lowest processing temperature used was 300 °C, similar to what is used in present study. However, it is seen that the processing temperature can be decreased to 250 °C, when higher die angles of 105 to 120° is used. It is evident from the table that the enhancements in mechanical properties by I-ECAP achieved in the present study are quite reasonably comparable with the previous ECAP studies. Although, by lowering the processing temperature, the enhancements in mechanical properties can be increased even further.

The study by Sordi et al. [135] is directly comparable with the $\Phi = 120^\circ$ case study, as it has identical processing conditions. It is seen that although the processing conditions are exactly the same, the mechanical properties are better to the ones obtained in the present study. However, the tensile flow stress curves in [135], it is clear that the material after subsequent ECAP passes, suffers a very high rate of flow softening beyond the onset of necking, which is not the case in the present study. Moreover, the uniform elongation achieved in the present study is much higher.

Table 6.3: Summary of CP-Ti processing parameters used in selected ECAP studies and present study, along with the changes in grain size, hardness, strength and ductility. The table is arranged in the order of decreasing processing temperature.

<i>Reference</i>	<i>Ti Grade</i>	<i>Die angle Deg</i>	<i>Speed mm/s</i>	<i>Temp °C</i>	<i>Route</i>	<i>N</i>	<i>Grain size μm</i>	<i>Hv</i>	<i>σ_y MPa</i>	<i>σ_{UTS} MPa</i>	<i>δ_{fail} %</i>
Stolyarov et al. [69]	3	90	-	450~500	Bc	7	0.30	240	520	540	16
Latysh et al. [138]	2	90	-	450	-	4	0.30~0.70	-	545	630	22
Chen et al. [118]	2	90	-	450	A	4	-	-	-	-	-
Kang and Kim [186]	2	90	2.0	450	A-C-C-A	5	0.96	-	530	665	26
Stolyarov et al. [108]	3	90	6.0	400-450	B _A , B _C , C	8	0.26~0.47	266~277	640~720	710~760	10~4
Hyun and Kim [187]	2	110	-	410	Bc	6	0.30	-	580	740	19.6
Rao et al. [188]	1	120	6	400	Bc	3	-	180	423	463	30
Ko et al. [124]	2	90	0.10	350	C	8	0.30	-	655	-	13
Bindu et al. [189]	2	90	-	350	Bc	4	0.24	-	418	-	-
<u>This study</u>											
Sordi et al. [135]	2	120	0.10	300	Bc	6	1.20	215	558	658	20.2
Pureck et al. [190]	2	90	0.10	300	Bc	4	0.86	217	671	730	21.1
Sordi et al. [135]	2	120	0.08	300	Bc	6	-	248	615	790	32
Pureck et al. [190]	2	90	1.27	300	E	8	0.30	-	620	760	21
Medvedev et al. [125]	2	90	1	300	Bc	4	0.25	-	750	850	18
Hajizadeh et al. [123]	2	105	1	250	-	10	0.21	280	750	892	20.5
Zhao et al. [129]	1	120	2.0	RT	Bc	8	0.20	-	710	790	19
Zhao et al. [130]	1	90	3.5	RT	C	4	0.15	236	-	765	48

6.6 Hall – Petch effect

The main objective of this research work is to refine the grain structure in titanium for the purposes of strength improvement. As discussed in Chapter 1, grain refinement in polycrystalline metals is one of the effective ways of improving the properties in particular the mechanical behaviour. In order to quantify the contribution from the grain size refinement to the strength enhancements, the Hall – Petch equation is commonly used. Hall-Petch effect is explained as a relationship between the average grain size and the yield strength. For the sake of convenience the equation is shown here again:

$$\sigma_y = \sigma_o + k_y d_g^{-1/2} \quad \text{Eq. 6.1}$$

Grain boundaries are considered as obstacles for dislocation movement. Grain refinement in SPD processes significantly increases the fraction of grain boundaries. Therefore, a greater force is required for plastic deformation to occur according to Hall – Petch effect. In order to quantify the strengthening contribution in the present study due to the Hall – Petch relationship, Fig. 6.14 is presented. It shows the plot of yield strength after subsequent passes of I-ECAP using $\Phi = 120^\circ$ and 90° angle die, against the $d_g^{-1/2}$. The average (d_g) size in the flow plane of the samples is used for both cases. In both cases, after the first pass the strength increase is significant and therefore the as-received (ASR) material point has a different slope from the I-ECAP processed material points beyond first pass. It is believed that in the initial passes of ECAP, dislocation strengthening or strain hardening plays a key role in the strength increase [123]. Here, formation of sub-grains and/or dislocations cells also contributes to the strength increase. After subsequent passes, fine grains are formed with high angle grain boundaries. Whereby, the contribution from grain refinement i.e. Hall – Petch relationship becomes the main role in strengthening. Therefore, it is worthwhile to consider the Hall – Petch relationship beyond first pass, similar trend was also observed in [187] during ECAP processing of CP-Ti grade 2 material. As can be seen, beyond first pass the slope of the linear fit is in excellent agreement with subsequent passes (notice the R^2 values).

For the $\Phi = 120^\circ$ case, the values of k_y and σ_o corresponds to $139 \text{ MPa}/\mu\text{m}^{1/2}$ and 437 MPa and for the $\Phi = 90^\circ$ case, the values of k_y and σ_o corresponds to 121

MPa/ $\mu\text{m}^{1/2}$ and 544 MPa. There is no evidence for the inverse Hall – Petch effect in the present study. It can safely be said that the primary strengthening in the present study is the Hall – Petch effect.

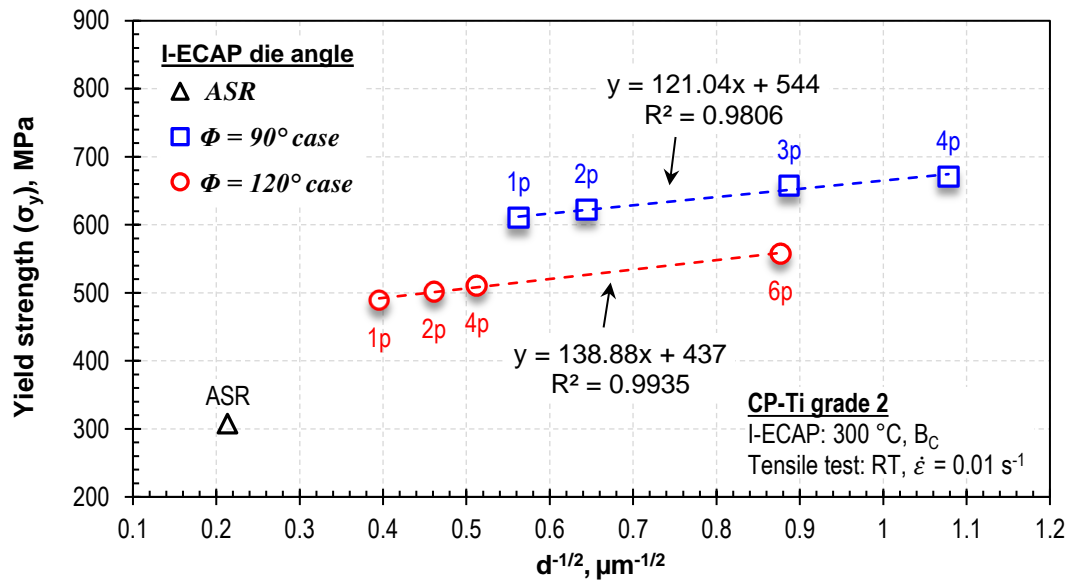


Fig. 6.14: Representation of yield strength as a function of average grain size to study the Hall – Petch effect in the present study.

Interestingly, when the yield strength and the grain size of the final pass (sixth pass for the $\Phi = 120^\circ$ and fourth pass for the $\Phi = 90^\circ$) are analysed, a better linear fit following the Hall – Petch effect is obtained (see Fig. 6.15). Here the k_y corresponds to 414 MPa/ $\mu\text{m}^{1/2}$ and σ_o corresponds to 211 MPa.

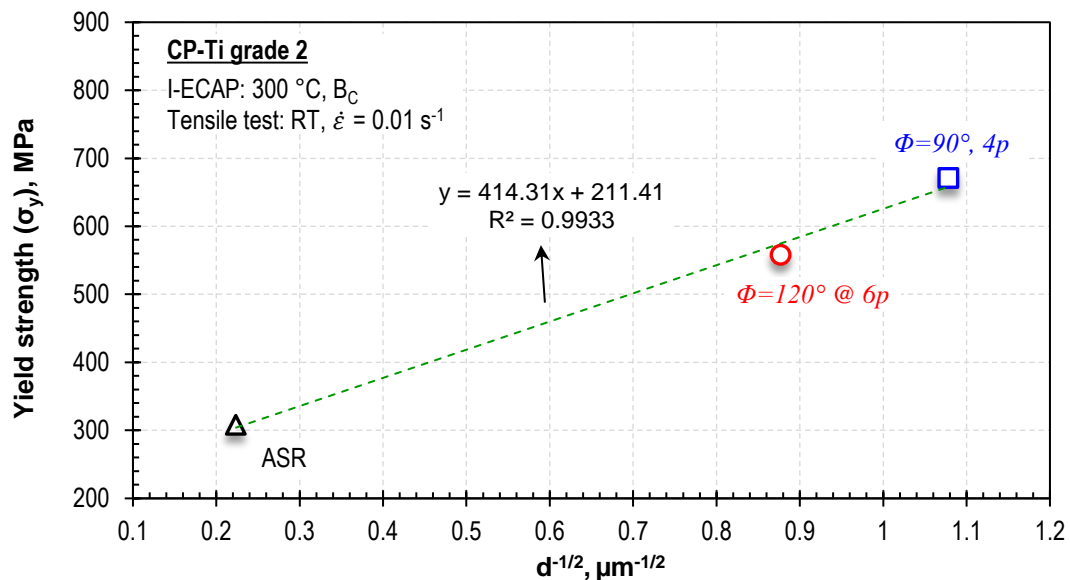


Fig. 6.15: Representation of yield strength as a function of average grain size to study the Hall – Petch effect during the final pass in the present study.

6.7 Conclusions

The effects of I-ECAP processing on the mechanical properties of the processed material presented in this chapter can be summarised as follows.

1. CP-Ti grade 2, was severely deformed using I-ECAP process. It exhibited significant improvements in its mechanical properties. During room temperature tensile testing, the yield strength increased from 308 to 558 MPa and ultimate tensile strength (UTS) increased from 548 to 685 MPa, for the material processed using die angle (Φ) of 120° . This corresponds to 81% and 25% increase, respectively. For the case of material processed using die angle (Φ) of 90° , the strength increase was even higher. The yield strength increased to 671 MPa and the UTS increased to 730 MPa, which corresponds to strength enhancements of 118% and 33%, respectively.
2. In both cases, ductility was somewhat reduced due to lack of strain hardening ability exhibited by the severely deformed material. The reduction was similar for both die angles and at ~20% elongation to failure, it is still be considered to be reasonable for practical applications.
3. The evolution of hardness during subsequent passes of I-ECAP was investigated by Vickers microhardness measurements in the transverse plane of the processed material. Hardness homogeneity was fairly good except for the narrow region at the top. The average value of microhardness was significantly increased from the initial value of 156 Hv. The hardness increments were different for the same amount of strain induced in both die cases, except the highest strain, for which the maximum hardness reached 215 to 217 Hv, an increase of ~40% after I-ECAP.

In general, for both cases, I-ECAP process has been shown as an effective method capable of producing defect free CP-Ti billets. The processing achieved remarkable improvement in strength due to grain refinement. In both cases, the strengthening mechanism is believed to be Hall – Petch effect. This promising technique requires very low feeding force therefore it is capable of processing very long or continuous billets.

Chapter 7

Workability characteristics of CG and UFG CP-Ti

7.1 Introduction

In order to improve the formability in CP-Ti, it is necessary to carry deformation at elevated temperatures. However, use of excessively high temperatures for UFG titanium can cause increased recovery, leading to significant grain growth. This will result in considerable loss of strength and hardness, especially if the deformation process is carried at a low strain rate. Deforming CP-Ti in the warm temperature range is therefore desirable, not only in terms of retaining the strength characteristics of UFG but also in terms of reducing the forming process energy requirements. Finding a good balance between formability and loss in strength is essential and can be achieved by developing a deeper understanding of the warm temperature range deformation behaviour of UFG CP-Ti. It is generally accepted that compression flow stress data can be used to simulate the deformation behaviour during bulk metal forming processes. The effective use of accurate flow stress data in simulations combined with the knowledge of grain growth at different temperatures and strain rates, will greatly help in establishing the optimal processing regimes of UFG CP-Ti.

The aim of this chapter is to study the workability characteristics of the unprocessed coarse grain (CG) and severely deformed UFG CP-Ti. This chapter has two parts: in the first part, effect of I-ECAP processing on the compression behaviour of CP-Ti is studied. For this purpose room temperature compression tests are carried out on CG and UFG CP-Ti at different strain rates. The compression behaviour, before and after I-ECAP is compared, which revealed a complex three stage hardening behaviour for all strain rates tested. This behaviour is analysed through the use of normalized strain hardening curves derived from flow stress curves for each test condition. Flow softening at higher strain rates and strain rate sensitivity are also compared before and after I-ECAP processing.

In the second part of the chapter, the workability characteristics of UFG CP-Ti is studied at warm temperature conditions. Here compression testing is carried out on UFG CP-Ti samples in the temperature range of 400 to 600 °C and at different strain rates. The flow stress and strain hardening behaviour is presented and discussed. Finally, microstructural changes, mainly the stability of the grains in the samples after compression testing is studied using EBSD analysis.

It is important to mention here that the UFG samples used in room temperature and warm temperature compression tests have been obtained from the billets after six passes of I-ECAP using the $\Phi = 120^\circ$ channel die. Refer to section 4.6 for I-ECAP experimental procedure and processing parameters. Geometric dimensions of the compression samples and other test details are mentioned in section 4.8.3.

7.2 Room temperature compression behaviour

To study the effect of I-ECAP processing on the compression behaviour of titanium, room temperature compression tests results are presented for the unprocessed coarse grain (CG) and severely deformed UFG CP-Ti.

7.2.1 True stress – true strain curves

Fig. 7.1 displays true stress as a function of true strain determined by uniaxial compression testing conducted at room temperature for (a) CG and for (b) UFG CP-Ti. To investigate any strain rate sensitivity at room temperature, tests was performed at three different strain rates ($\dot{\epsilon}$): 0.01, 0.10 and 1.00 s⁻¹. All tests were conducted up to 50% height reduction, resulting in a true strain value of ~0.70.

First, it is apparent from the obtained flow curves that the UFG material shows significant increase in compressive yield strength for all strain rates compared to the CG unprocessed material. This shows again that the material has strengthened due to the grain refinement process. However, the test results shows that the severely deformed material displays lower levels of strain hardening compared to the unprocessed CG material. It is interesting to note, that although the yield strength of the processed material is higher, the unprocessed material, due its greater strain hardening ability quickly strengthens during compression and displays a higher flow stress beyond the ~0.30 true strain value. For all strain rates, the unprocessed material

therefore manages to achieve slightly higher flow stress values at completion of compression tests at ~ 0.70 true strain.

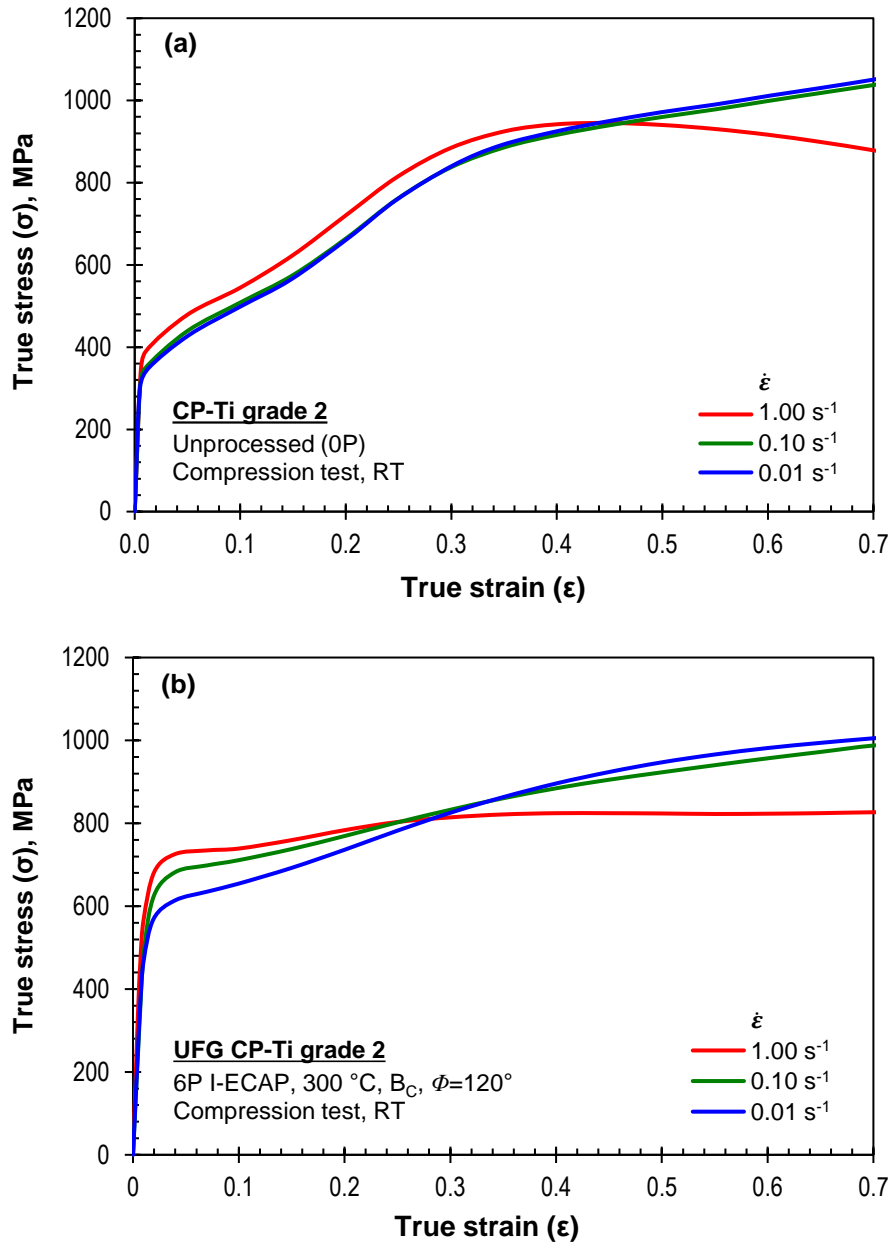


Fig. 7.1: Flow curves (true stress vs true strain) obtained from uniaxial compression testing at various strain rates for (a) unprocessed (CG) and (b) severely deformed (UFG) CP-Ti.

7.2.2 Strain hardening behaviour

In order to study the strain hardening behaviour during room temperature compression tests in detail, Fig. 7.2 present plots of normalized strain hardening rate ($d\sigma/d\varepsilon/G$) against true strain for (a) unprocessed (CG) and (b) severely deformed (UFG) material. Here, σ is the flow stress, ε is the true strain and G is the shear modulus (modulus of rigidity) for titanium. In general, both material condition exhibits a distinct three-stage strain hardening behaviour within the plastic regime.

Stage I is characterized by a decreasing rate of strain hardening and is similar to the dynamic recovery regime observed in many metals [191]. Upon reaching a certain strain, the hardening rate increases, representing the stage II deformation. This is then followed by considerable reduced rate of hardening or even flow softening (negative rate of hardening), denoting the stage III deformation. This three-stage hardening behaviour is consistent with earlier reports on compression testing of titanium at room and elevated temperatures [113, 191, 192].

Studies have shown that the increase in strain hardening behaviour in stage II is due to deformation twinning [112, 193]. Notice that the severely deformed CP-Ti in Fig. 7.2(b), exhibits much lower levels of stage II strain hardening compared to the unprocessed material. This is because the severely deformed material has a UFG structure; which causes twinning activity to be greatly suppressed as such. The results are consistent with Gray [194], who performed compression tests on fine and coarse grained titanium, which show that the rate of strain hardening increases with increase in grain size due to pronounced increase in deformation twinning.

Twinning increases the strain hardening in two ways, firstly, it causes reduction in average grain size, therefore contributes to strengthening via the Hall-Petch effect. Secondly, the twinned regions are much harder than the rest of the matrix (untwinned) regions. To confirm the later, Salem et al. [195] deformed CP-Ti under compression up to a strain of 0.05, this corresponds to the initiation of stage II hardening and onset of deformation twinning. Microhardness measurement on the twinned regions showed a 30% hardness increase compared to the matrix regions. The latter effect contributes to the mechanism proposed by Basinski et al. [196], whereby twinning results in increase in strength of a material.

Notice that the onset of stage II strain hardening in the present study also happens around ~ 0.05 true strain (see Fig. 7.2(a) and (b)). However in Fig. 7.2(a) it is seen that the initiation of stage II hardening for the fastest strain rate of 1.0 s^{-1} (red line) happens slightly earlier i.e. at a lower true strain value compared to the slower strain rates (green and blue lines). Similar results were obtained in [197], in which it was shown that deformation twins are generated at lower strains during compression as the strain rate is increased. However, this effect is not observed in the severely deformed material, where the onset of stage II hardening does not seem to be affected by the increase in strain rate.

For strain rates of 0.01 and 0.1 s^{-1} , the unprocessed material during stage III shows a rapidly decreasing strain hardening behaviour. However, beyond a true strain of ~ 0.40 both reach a steady state condition and there is no noticeable change in strain hardening rate. For the severely deformed material at these strain rates, the decrease in strain hardening in stage III is not as rapid. It decreases at a lower rate and continues to do so until test finishes.

The present compression tests show that the severely deformed material has still some tendency to strain harden compared to tensile tests, where a near steady state behaviour in flow stress was observed after initial yielding. Nevertheless, both the tensile and compression test results have shown that the processed material significantly loses its ability to strain harden compared to the unprocessed material. This is because the heavily deformed UFG structure in the processed material has a limited capacity to accumulate further dislocations and has a reduced tendency to generate twin boundaries during subsequent deformation [198].

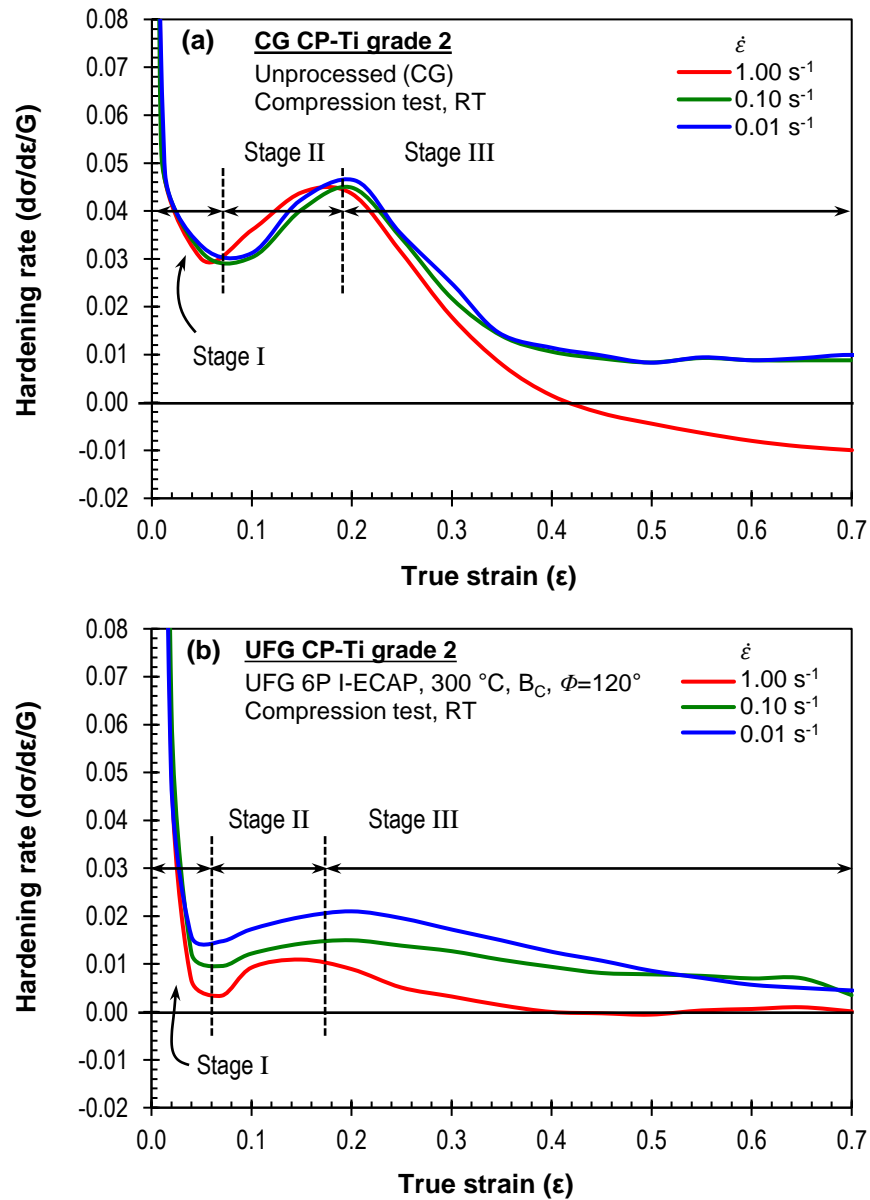


Fig. 7.2: Plots of normalized strain hardening behaviour obtained from room temperature compression testing at various strain rates for (a) unprocessed (CG) and (b) severely deformed material after six passes (UFG).

7.2.3 Flow softening due to adiabatic heating

For both material condition (CG and UFG) the flow stress obtained at the highest strain rate of 1.0 s^{-1} is particularly interesting, after an initial strain hardening behaviour (stage I and stage II), both materials exhibited flow softening (negative rate of hardening). However, this flow softening is much more prominent in the CG material. The observed flow softening is believed to be due to the temperature rise during deformation. Flow softening at a strain rate of 1.0 s^{-1} , has also been observed during compression tests on nanocrystalline titanium produced by mechanical milling followed by a consolidation process [199] and also in UFG titanium produced by ECAP [171]. Both studies concluded that flow softening is due to the heat generated during plastic deformation. The temperature rise during deformation can be calculated by the following relationship [200]:

$$\Delta T = \frac{\beta}{\rho C_p} \int_0^\varepsilon \sigma d\varepsilon \quad \text{Eq. 7.1}$$

where β is the factor which specifies the portion of plastic work converted into heat (Taylor-Quinney coefficient, normally taken to be 0.90), ρ is the material's density, C_p is the specific heat and the integral in Eq. 7.1 defines the work done by flow stress (σ) during deformation to strain ε . Using this equation, the temperature rise during compression testing is calculated for two strain levels: true strain where flow softening begins (ε_s) and the final true strain ($\varepsilon_f \approx 0.70$). Ideal conditions are assumed, i.e. no heat loss due to conduction or convection. For the CG material the equation predicts a temperature rise of 121°C at $\varepsilon_s = 0.45$ which increases to 219°C at ε_f . The predicted temperature rise for the UFG material is 81°C at $\varepsilon_s = 0.28$ and rises to 198°C at ε_f . The flow stress of titanium is very sensitive to temperature, the predicted temperature rise at strain rate of 1.0 s^{-1} for both material condition is assumed to influence the flow stress behaviour. However, further tests such as load-unload-reload tests performed in [199] are necessary to establish the exact role of temperature rise in flow softening.

7.2.4 Strain rate sensitivity

The flow stress of severely deformed material displays higher level of dependence on strain rate, whereby the flow stress increases with increase in strain rate. The unprocessed material only shows increase in flow stress at the highest strain rate of 1.0 s^{-1} . The effect of strain rate on the flow stress of the material can be further analysed by determining strain rate sensitivity of the material. The strain rate sensitivity value is denoted by m and calculated by Eq. 7.2:

$$m = \left. \frac{\partial \log \sigma}{\partial \log \dot{\epsilon}} \right|_{\epsilon, T} \quad \text{Eq. 7.2}$$

where σ and $\dot{\epsilon}$ are the flow stress and strain rate, respectively. It is important to note that m value has to be calculated for a certain strain value and temperature. Fig. 7.3(a) and (b) shows the variation of flow stress on various strain rates plotted on a semi-logarithmic form, where stress is measured at (a) 0.05 and (b) 0.10 true strain, respectively for coarse grain (0P) and UFG (6P) material tested in compression at room temperature. The values of strain rate sensitivity can be easily calculated from such graph, by determining the slope of the linear fit.

It is apparent that the m value at both selected strains shown in Fig. 7.3 for the UFG material is higher compared to CG material. From the flow stress observation and the m value calculation, it is shown that the UFG Ti exhibits a higher strain rate sensitivity in compression at room temperature. Although the UFG material exhibits increase strain rate sensitivity, this increase is not believed to improve the ductility of the material considerably during tensile deformations at room temperature. This is because the mechanisms such as grain boundary sliding which facilitates increase in ductility occurring in higher strain rate sensitive materials are not pronounced at room temperature [201].

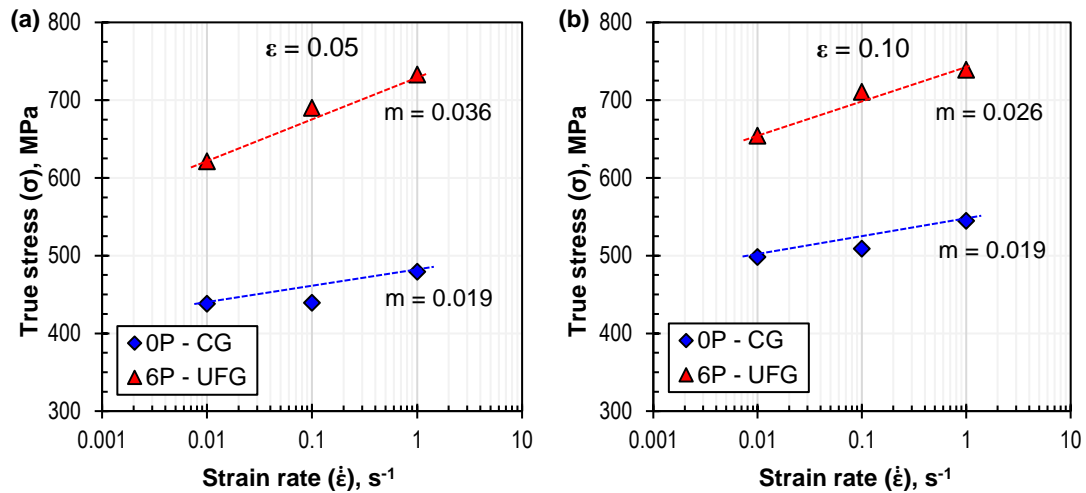


Fig. 7.3: Strain rate sensitivity of CG and UFG material compression tested at room temperature for (a) $\epsilon = 0.05$ and (b) $\epsilon = 0.1$.

7.3 Warm temperature deformation testing of UFG CP-Ti

To study the warm temperature deformation behaviour of UFG CP-Ti, a temperature range of 400 to 600 was selected for investigation. Similar to room temperature compression testing, the cylindrical samples were machined such that the axis of each sample was along the longitudinal axis of the billet. The method of lubrication was similar to room temperature testing, except graphite mixed with water was used instead of MoS_2 as lubricant.

A series of tests were conducted following the ASTM E209 – 00 (2010) standard, at three deformation temperatures of 400, 500 and 600 °C and at three different strain rates of 0.01, 0.1 and 1.0 s^{-1} . Tests were conducted under isothermal and constant strain rate condition. Temperature was monitored using two calibrated N-Type thermocouples, which were located near the deformation zone. When the temperature value was stable within ± 2 °C, compression test was initiated and the height of cylindrical sample was reduced by $\sim 50\%$ in a single loading step, achieving a true strain of ~ 0.70 . After the test, each sample was immediately quenched in cold water to arrest the microstructure and to stop any grain growth. A minimum of two tests were performed for each test condition to ensure repeatability of results.

7.3.1 True stress – true strain curves

Fig. 7.4 represents the true stress-strain curves for compression tests of UFG CP-Ti at warm deformation temperatures of (a) 400, (b) 500 and (c) 600 °C and for strain rates of 0.01, 0.1 and 1.0 s⁻¹. As expected, it can be observed that the flow stress of CP-Ti subjected to I-ECAP is dependent on both temperature and strain rate. In general, the flow stress is seen to increase with increasing strain rate. Moreover, at the same strain rate, it decreases with increasing temperature.

It is obvious from these graphs that compared to the room temperature results, the flow stress at warm temperatures for all strain rates is lower due to higher temperature effects. These figures also shows that UFG CP-Ti exhibits very low levels of strain hardening behaviour at these deformation temperatures. This is especially true for test temperatures of 400 and 500 °C. The flow stress at these test temperatures for all strain rates, quickly reaches a peak value near ~0.05 true strain, beyond which it exhibits a steady state response where there is not much appreciable strain hardening in general.

However, for all compression tests performed at 600 °C, the flow stress behaviour is different from the tests performed at 400 and 500 °C. Here all the stress-strain curves shows some strain hardening. Notice, how the flow stress is steadily increasing beyond a strain of 0.05. It is believed that at 600 °C significant grain growth has taken place and because of that the CP-Ti material has regained its strain hardening ability. On the other hand the flow stress curves has dropped to almost half, when compared to the flow stress obtained at 500 °C.

It is interesting to compare the flow stress behaviour of UFG CP-Ti at these temperatures with coarse grained CP-Ti. Zeng et al. [192] subjected CP-Ti grade 2 (with a starting grain size of 40 µm) to uniaxial compression at elevated temperatures ranging from 400 to 700 °C and strain rates of 0.001, 0.01, 0.1 and 1 s⁻¹. Compared to the flow stress obtained in that study which shows a pronounced three stage hardening behaviour for up to 500 °C, it is seen that UFG CP-Ti tested at 400 and 500 °C in the present study exhibits much higher compressive strength i.e. flow stress for 400 and 500 °C. At 600 °C the results from both studies becomes quite comparable i.e. the UFG CP-Ti loses its strength enhancements beyond this temperature.

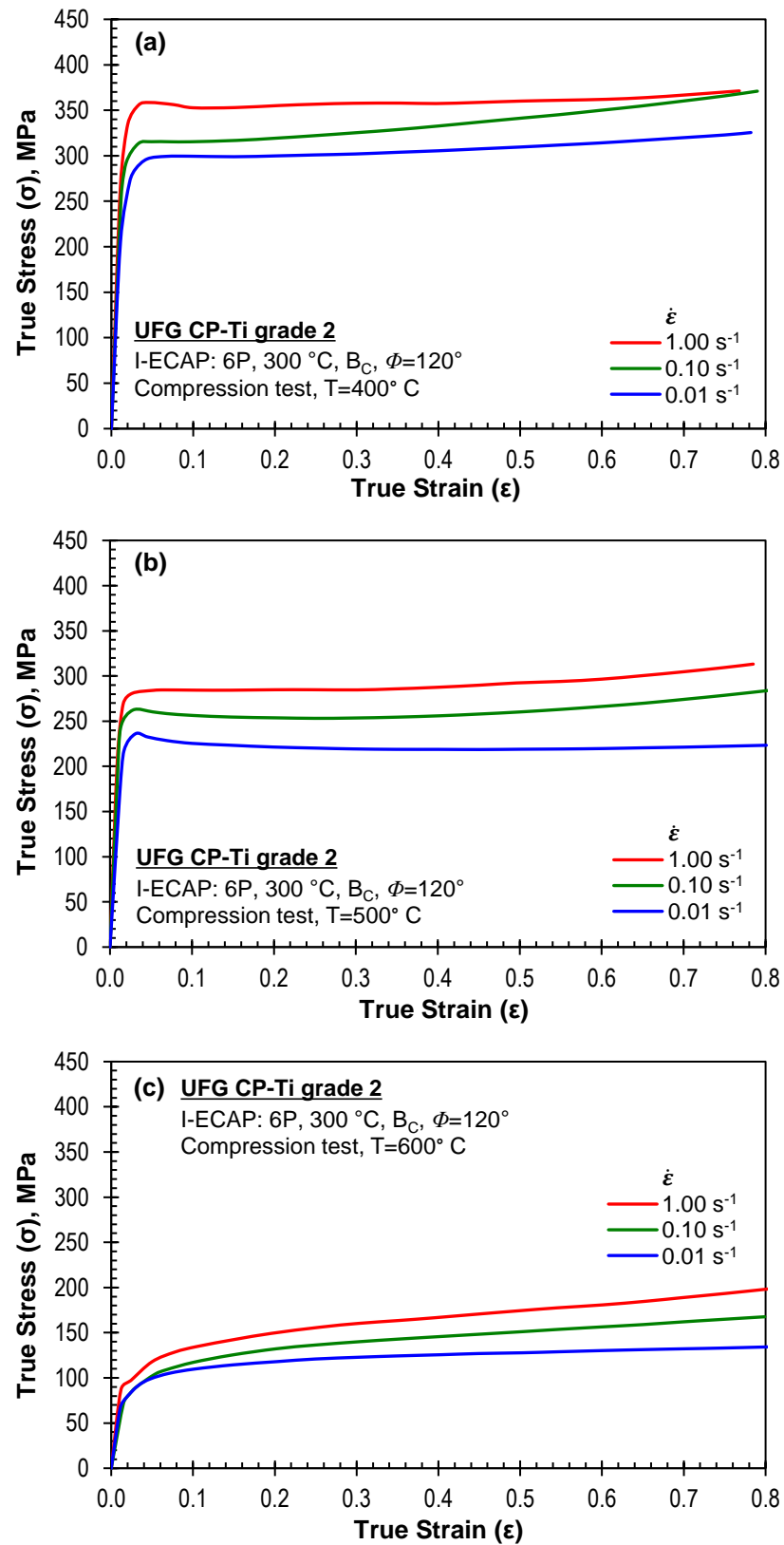


Fig. 7.4: True stress vs true strain plot obtained from the uniaxial compression testing at various strain rates and at temperatures of (a) 400, (b) 500 and (c) 600 °C.

7.3.2 Strain hardening behaviour

In order to study the strain hardening behaviour during warm temperature compression tests in detail, Fig. 7.5 present plots of normalized strain hardening rate ($d\sigma/d\varepsilon/G$) against true strain at various strain rates and at (a) 400, (b) 500 and (c) 600 °C. As clearly evident from these plots that the UFG CP-Ti at these warm deformation temperatures does not exhibit the distinct three stage hardening behaviour as exhibited by CG CP-Ti and to some extent exhibited by UFG CP-Ti at the room temperature testing.

For the 400 (Fig. 7.5(a)) and 500 °C (Fig. 7.5(b)), the hardening rate exhibits a sharp decrease at low strain levels (up to 0.05 and 0.1). For the 0.01 s⁻¹ at 400 °C and 0.10 and 0.1 s⁻¹ at 500 °C the hardening even goes to negative rates. Beyond these strain values, the hardening rate increases and reaches either a steady state condition (see blue line in Fig. 7.5(b)) or the hardening continues to increase but at a very low rate (see green in Fig. 7.5(b)).

In the case of 600 °C, the decreasing strain hardening rate continues up to ~0.35 strain values, however it does not go into negative rates. Beyond this strain value, the hardening rate reaches a steady state and does not changes much.

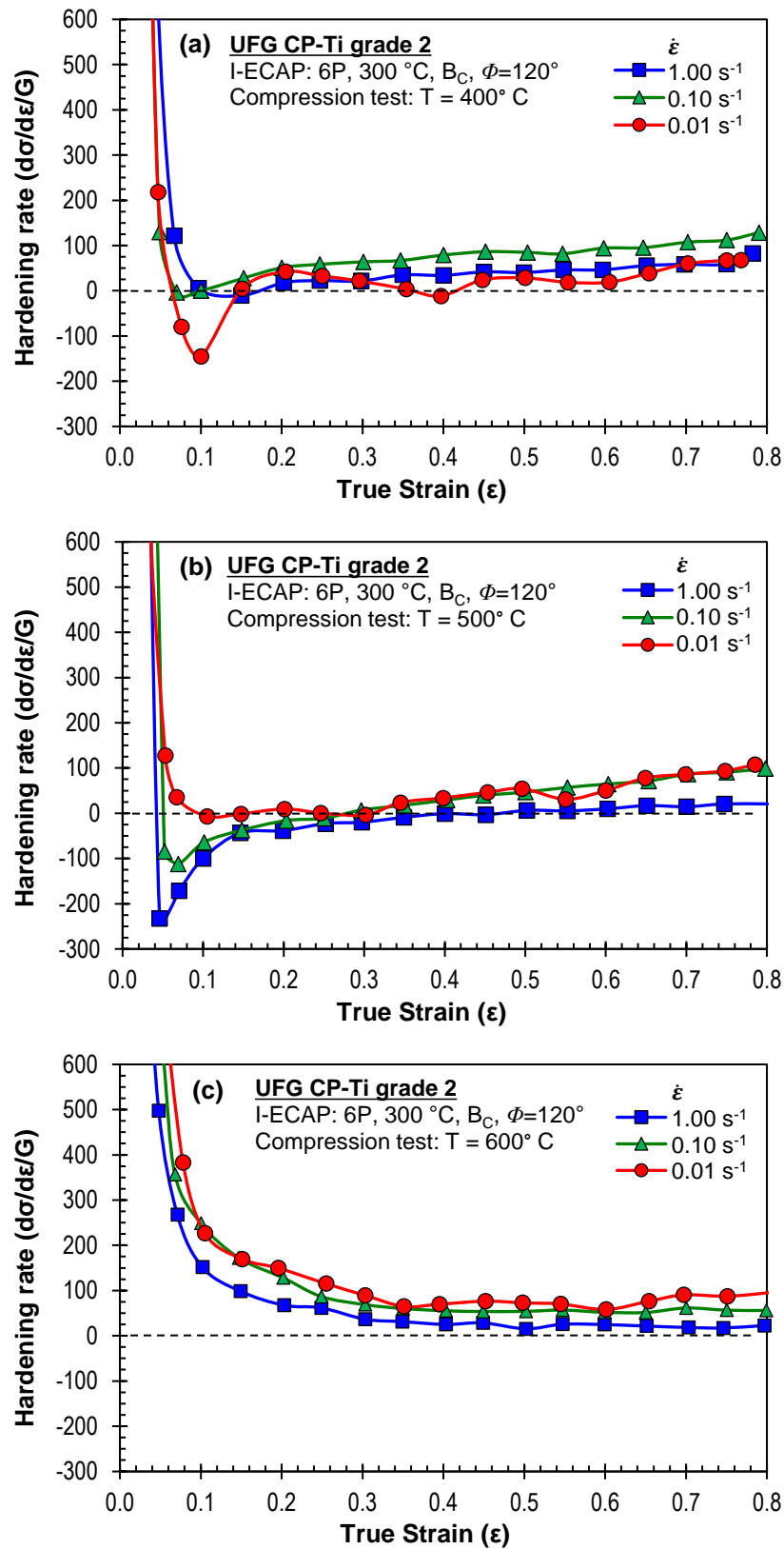


Fig. 7.5: Plots of normalized strain hardening behaviour obtained from warm temperature compression testing of UFG CP-Ti at various strain rates and at (a) 400, (b) 500 and (c) 600 °C.

7.3.3 Microstructures after deformation

In this section, microstructural changes occurring in the samples subjected to compression tests at three different temperatures of 400, 500 and 600 °C and at strain rates of 0.01, 0.1 and 1.0 s⁻¹ are analysed by IPF maps and shown in Fig. 7.6 to Fig. 7.8. The figures are arranged in the decreasing order of strain rate i.e. (a) 1.0, (b) 0.1 and (c) 0.01 s⁻¹; to better appreciate the grain growth. The IPF maps were generated in the central part of the compression tested samples which were cut along the longitudinal plane i.e. parallel to the loading axis. The figures also include the grain boundary map where the blue lines represents LAGB and red lines represents HAGB, along with the associated grain size histogram. The plots shows a complete picture showing the effects of tested temperatures and strain rates during compression testing of UFG CP-Ti.

In general it is seen that the microstructure is fairly stable for up to 500 °C for all strain rates and although some grain growth is evident, the average grain size is still below 2 µm. The microstructure even maintains its UFG form for 400 and 500 °C for the highest strain rate tested at 1.0 s⁻¹.

It is important to recall that the average grain size achieved after I-ECAP processing using the $\Phi = 120^\circ$ channel angle die was between 1.1 to 1.3 µm. However, it is seen that IPF maps shown in Fig. 7.6(a) and Fig. 7.7(a), the grain have been refined even further even though testing was done at higher temperature than I-ECAP. This is because after I-ECAP there exists many grain boundaries within the microstructure which are not fully enclosed. As soon as the material is exposed to slightly higher temperatures for a shorter duration such as during testing at 1.0 s⁻¹, it causes dynamically recrystallized nucleation preferentially at the incomplete HAGB and also close to grain boundaries. This leads to formation very fine equi-axed grains. These fine grains that are formed can promote grain boundary migration and grain rotation during the deformation. The deformation temperature is expected to affect the recrystallization kinetics, as it influences the stored energy. The stored energy is regarded as a driving force for recrystallization. Deformation at much higher temperature reduces the stored energy due to dynamic recovery and that is why for higher temperature of 600 °C and even at 1.0 s⁻¹ in Fig. 7.8(a) the refinement effects are not observed and there are pockets of regions where grain growth is significant.

When the strain rate is decreased, evidence for growth of grains i.e. elongated grains in the direction perpendicular to compression loading is observed (Fig. 7.6(b) and Fig. 7.7(b)). Grain growth is the process by which the average grain size of constituting grain increases. The driving force for this process results from the decrease in free energy which is due to the reduction in total grain boundary area [202]. Here most of grains start to grow by consuming fine grains along the grain boundaries, which lead to increase in the average grain size.

For samples tested at the slowest strain rate of 0.01 s^{-1} for 400 (Fig. 7.6(c)) and 500 (Fig. 7.7(c)), some grains have been seen to undergo an accelerated grain growth compared to surrounding grains. This causes noticeable increase in the overall average grain size in the final microstructure. Grain growth takes place by diffusion and is effected both by temperature and the time. Various clusters of very fine grain are seen across the scanned area, which retained their size and morphology (Fig. 7.6(c) and Fig. 7.7(c)). Grains in such clusters are believed to be thermodynamically stable enough to suppress the migration of their grain boundaries. It is interesting to see that the microstructure in Fig. 7.7(c) have a wavy grain boundaries nature. This kind of wavy grain boundary is the characteristics of microstructure after hot rolling [203].

Compression tests at $600 \text{ }^\circ\text{C}$ and at 1.0 s^{-1} (Fig. 7.8(a)), resulted in the microstructure similar to the one observed for $400 \text{ }^\circ\text{C}$ and at 0.1 s^{-1} . As the strain rate is high and there is not sufficient time to release deformation energy, some grains uses these energies to undergo accelerated grain growth at the expense of surrounding grains. Therefore, here again pockets of very fine grain clusters are observed. Notice the corresponding grain size histogram which shows $\sim 60\%$ of the area fraction below $1 \text{ }\mu\text{m}$ with $\sim 35\%$ below $0.4 \text{ }\mu\text{m}$. Microstructure of sample subjected to compression test at 600°C and 0.01 s^{-1} Fig. 7.8(c) is very interesting. Significant grain growth has taken place here as seen by occurrence of large grains. Moreover, within these larges grain twins are observed. This shows that the mode of deformation is slip as well as twinning. This may be due to formation twinned regions having different orientation as compared to the parent grain where they nucleated and extended.

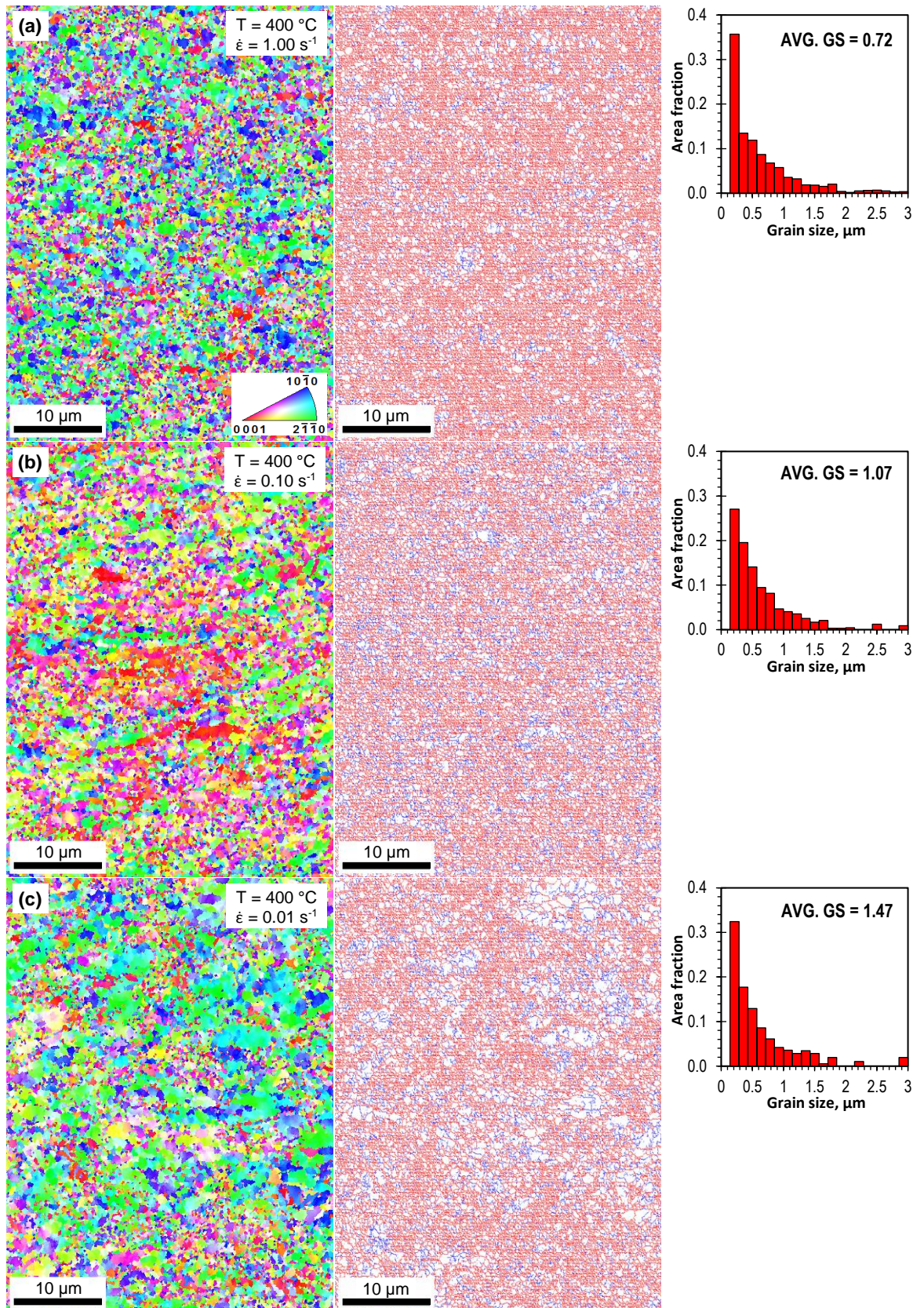


Fig. 7.6: EBSD based IPF map with the corresponding grain boundary map (blue and red lines refers to LAGB and HAGB) and the associated grain size histogram for the compression sample at 400 °C and at strain rates of (a) 1.0, (b) 0.10 and (c) 0.01 s⁻¹.

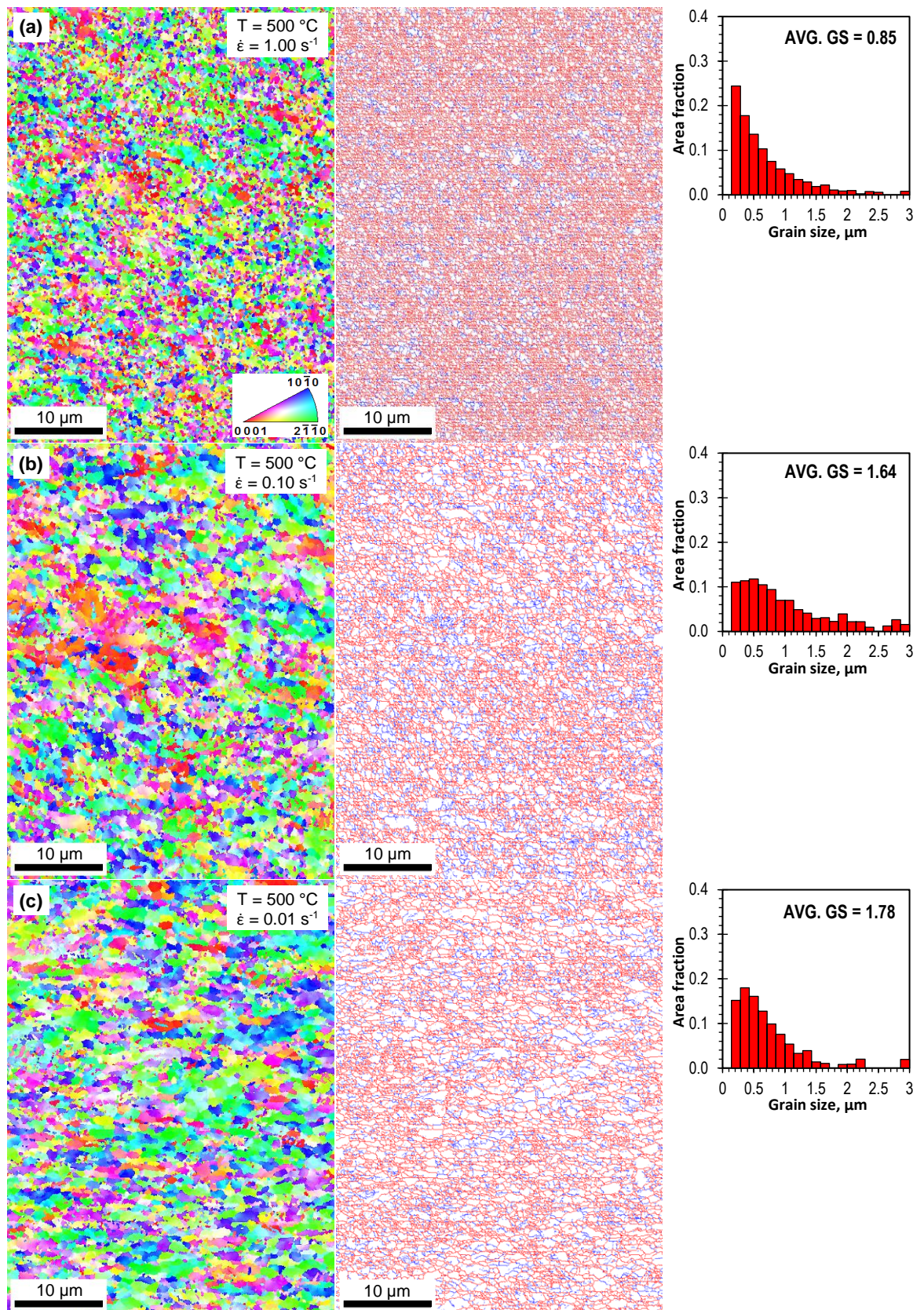


Fig. 7.7: EBSD based IPF map with the corresponding grain boundary map (blue and read lines refers to LAGB and HAGB) and the associated grain size histogram for the compression sample at 500 °C and at strain rates of (a) 1.0, (b) 0.10 and (c) 0.01 s⁻¹.

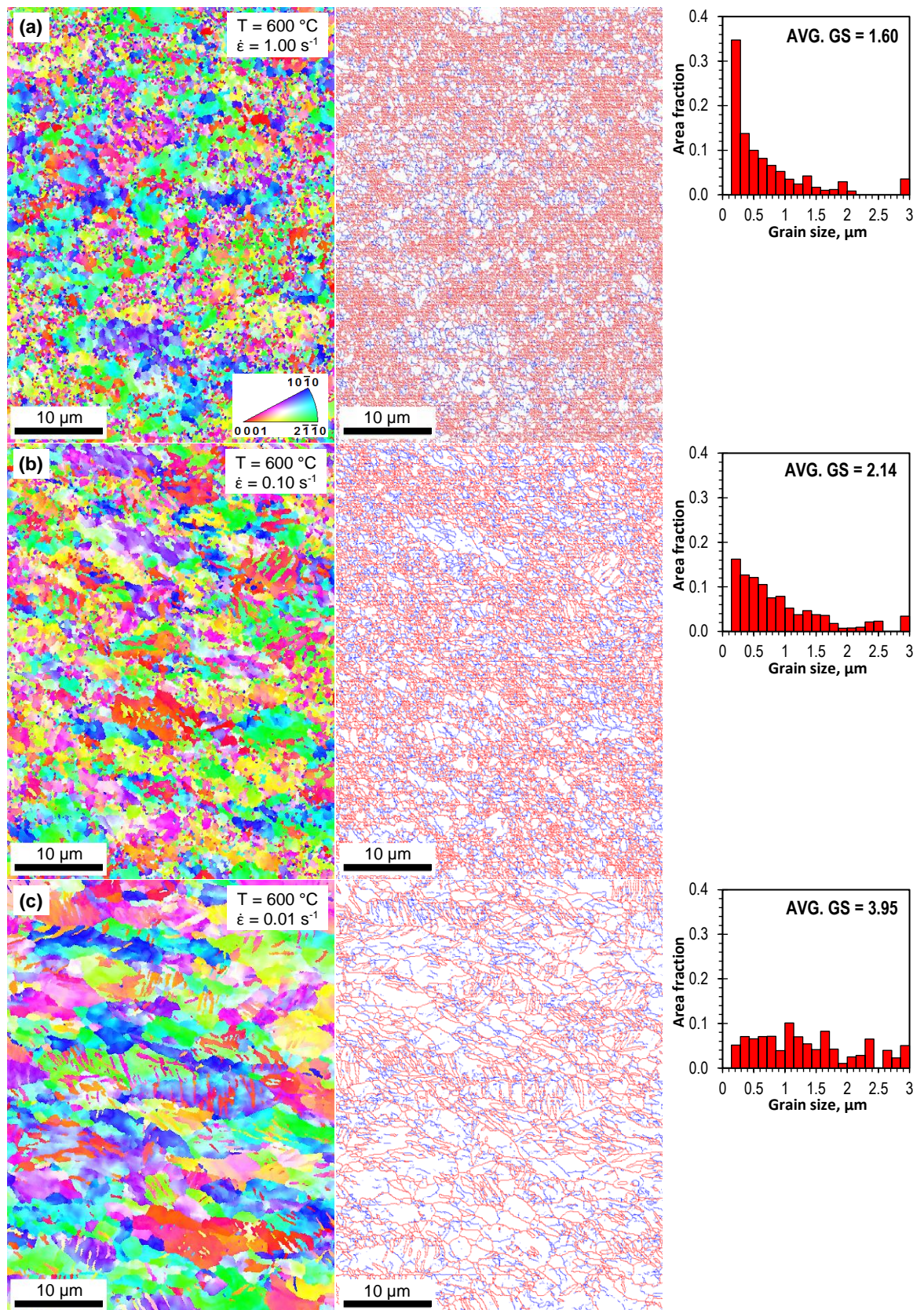


Fig. 7.8: EBSD based IPF map with the corresponding grain boundary map (blue and red lines refers to LAGB and HAGB) and the associated grain size histogram for the compression sample at 600 °C and at strain rates of (a) 1.0, (b) 0.10 and (c) 0.01 s⁻¹.

7.3.4 Dynamic grain size

Fig. 7.9 shows the average grain size calculated from the grain size histogram of the microstructure for the various temperature and strain rate conditions. The error bars represent the standard deviation from the average grain size. As predicted the average grain size increases with increasing temperature and decreasing strain rate. In general, the effect of temperature increase is greater on the grain growth than the deformation rate. Notice that the error bar is also increasing with increasing temperature and decreasing strain rate, this shows that the homogeneity in microstructure of the initial UFG material is being lost and it is moving towards heterogeneity. This increase in error bar with decrease in strain rate is gradual for 400 and 500 °C condition, whereas at 600 °C the microstructure is heterogeneous even for the fastest strain rate tested. This shows that the microstructure is highly unstable at 600 °C.

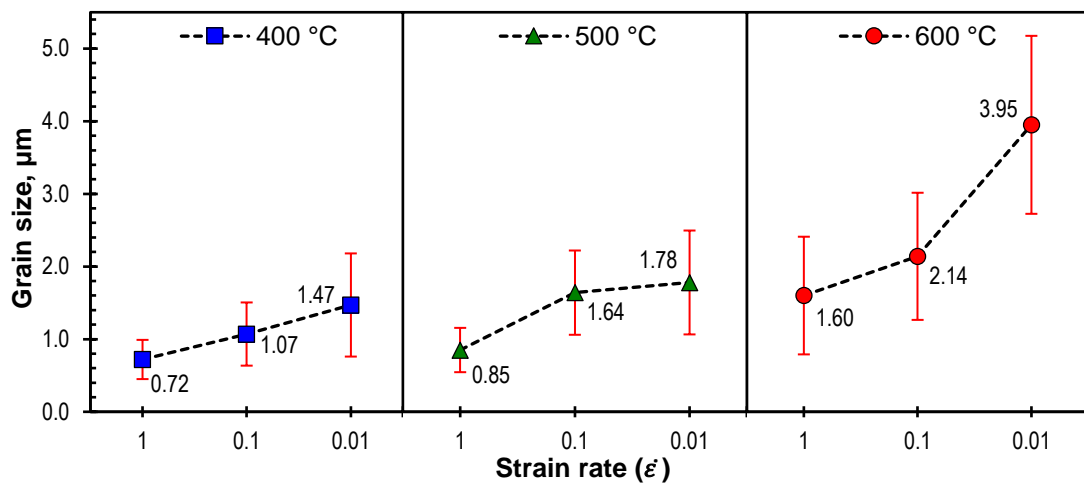


Fig. 7.9: Dynamic grain size observed during warm temperature compression testing as a function of temperatures and strain rates.

7.4 Conclusion

The chapter presented workability characteristics of CP-Ti at various conditions. To establish the workability characteristics, a series of compression testing were performed on the material. The tests include both room temperature and warm temperature conditions and at various strain rates. A compression was also done with coarse grained titanium to understand the changes in the compression behaviour. Following conclusions are drawn from the study:

1. Compression tests at room temperature and at various strain rates before and after I-ECAP processing revealed a complex three-stage strain hardening behaviour. However, the UFG CP-Ti due to its reduced tendency to generate deformation twins, showed a much lower strain hardening rate during stage II hardening. The severely deformed material displayed enhancement in compressive yield strength, as well as higher strain rate sensitivity compared to the unprocessed material.
2. Compression testing of UFG CP-Ti at warm temperatures of 400, 500 and 600 °C and at varying strain rates of 0.01, 0.1 and 1.0 s⁻¹, revealed that the flow stress was sensitive to temperature and strain rate. The flow stress increases with decreasing temperatures and increasing strain rates.
3. In compressions tests conducted at 400 and 500 °C, the flow stress quickly reaches a peak value, beyond which it exhibits a steady state response where there is no appreciable change in flow stress with increasing strain. The 600 °C tests however shows a strain hardening behaviour.
4. Microstructural observations using EBSD, exposed significant grain growth in the sample deformed at 600 °C and 0.01 s⁻¹. This also led to a considerable drop in flow stress during compression.

Chapter 8

Summary

The research work was undertaken to demonstrate the feasibility of the I-ECAP process to refine the grain structure in titanium for the purposes of improving its strength characteristics. The work also investigated in detail, the microstructural evolution and the mechanism of grain refinement during I-ECAP and its effects on the mechanical behaviour of the material. This work has a direct potential to replace the currently used Ti-6Al-4V (considered to be toxic in the long run) as a main material for bio-medical implants. The research work has yielded some interesting and useful insights into the I-ECAP processing of CP-Ti grade 2 material.

The first major task of the work was to improve the capability of the I-ECAP experimental rig and to demonstrate the I-ECAP as a viable method for commercialization purposes. Major upgrades and improvement were successfully carried out (as outlined in Chapter 4), to improve the operational efficiency of the I-ECAP rig. The upgrades such as automatic material feeding using a dedicated LabView application has greatly increased the processing efficiency of the rig. Moreover, high temperature processing capability added during the work, allows for a range of materials to be tested in future.

Using the improved I-ECAP rig, CP-Ti billets were successfully processed. For this purpose, new I-ECAP tooling was designed and manufactured following finite element simulations. To understand the effect of strain imposed during each pass of I-ECAP, experiments were performed for the first time using two new dies with channel intersection angles (Φ) of 120° and 90° . In this study, the as-received CP-Ti grade 2 billets were subjected to a total of six and four passes using the die angle of 120° and 90° , respectively. In both cases processing was done at 300°C following route B_C using the double billet variant of I-ECAP process. The billets obtained after processing were defect free without noticeable surface cracks and therefore it was shown

successfully that the new dies and the rig is capable of processing CP-Ti billets under the selected processing conditions.

To investigate the effect of I-ECAP processing on the grain refinement process, detailed microstructural investigations were carried out. The evolution of microstructure and deformation characteristics was studied and tracked by using relatively large scan areas obtained via EBSD. For the $\Phi = 120^\circ$ case, analysis was performed in both flow and transverse planes and for $\Phi = 90^\circ$ case, investigation was performed in the flow plane of processed billets. Moreover, for $\Phi = 120^\circ$ case, texture development through subsequent I-ECAP processing was also investigated using pole figures in both planes.

Effect of I-ECAP processing on the mechanical performance of the CP-Ti was determined by performing tensile tests and micro-hardness measurements. For the $\Phi = 120^\circ$ case, tests were performed after first, second, fourth and sixth pass and compared with the as-received properties. Whereas, for the $\Phi = 90^\circ$ case, test were performed after first, second, third and fourth pass. Finally, workability characteristics of CP-Ti is determined by compression testing at room and warm temperature conditions (400 to 600 °C).

According to the author's knowledge, this is the first time such detailed results regarding processing of commercially pure titanium using the I-ECAP process and its effects on the microstructural and mechanical behaviour is being reported. Also, this is the first time, an I-ECAP die with a channel intersection angle of 120° has been used such extensively on any metal or alloy. In all previous research work carried out on the I-ECAP rig, a channel angle of 90° has been used. Except only for one case [204], where the initial trial results obtained using the die angle of 120° on the Al-1050 alloy after first pass have been communicated by the current author as a co-author.

The work has contributed to the following research outputs:

1. **M.J. Qarni**, A. Rosochowski, and S. Boczkal, (2017), "Influence of incremental ECAP on the microstructure and tensile behaviour of commercial purity titanium", Procedia Engineering, xx, pp. xx-xx. (In press).
2. **M.J. Qarni**, G. Sivaswamy, A. Rosochowski, and S. Boczkal, (2017), "On the evolution of microstructure and texture in commercial purity titanium during multiple passes of incremental equal channel angular pressing (I-ECAP)", Materials Science and Engineering A, 699, pp. 31-47.
3. **M.J. Qarni**, G. Sivaswamy, A. Rosochowski, and S. Boczkal, (2017), "Effect of incremental equal channel angular pressing (I-ECAP) on the microstructural characteristics and mechanical behaviour of commercially pure titanium", Materials & Design, 122, pp. 385-402.
4. **M.J. Qarni**, A. Rosochowski, and S. Boczkal, (2017), "Warm deformation behaviour of UFG CP-Titanium produced by I-ECAP", IOP Conference Series: Materials Science and Engineering, 194, pp. 012038.
5. M.R. Salamati, S. Tamimi, S. Moturu, G. Sivaswamy, **M.J. Qarni** and A. Rosochowski, (2017), "Microstructure and mechanical properties of Al-1050 during incremental ECAP", IOP Conference Series: Materials Science and Engineering, vol. 194, pp. 012009.
6. M.R. Salamati, **M.J. Qarni**, S. Tamimi, and A. Rosochowski, (2016), "Effect of channel angle on the material flow, hardness distribution and process forces during incremental ECAP of Al-1050 billets", AIP Conference Proceedings, 1769, pp. 090004.
7. M. Gzyl, A. Rosochowski, S. Boczkal, and **M.J. Qarni**, (2015), "The Origin of Fracture in the I-ECAP of AZ31B Magnesium Alloy", Metallurgical and Materials Transactions A, 46, pp. 5275-5284.

Chapter 9

Conclusions

Detailed conclusions are listed at the end of each chapter. The following lists the important conclusions that are derived from this work.

1. The major upgrades implemented as part of this work on the I-ECAP rig which included the automation of material feeding, process control via LabVIEW application and elevated temperature processing capability; greatly improved the process efficiency and productivity.
2. Experiments conducted with die angle (Φ) of 120° and 90° , showed that I-ECAP requires very low feeding forces during experiments. In both cases, the process has been successfully demonstrated for obtaining defect free CP-Ti billets.
3. Remarkable grain refinement was achieved in both cases. After six passes using $\Phi = 120^\circ$ angle die, the average grain size in flow plane was reduced by 93.5% i.e. by 20 to $1.3 \mu\text{m}$. In transverse plane, the average grain size was reduced by 95% i.e. from 22 to $1.1 \mu\text{m}$. Using the $\Phi = 90^\circ$ angle die after four passes, the average grain size was reduced by 95.7% i.e. from 20 to $0.86 \mu\text{m}$. In both cases, the microstructure mostly consisted of high angle grain boundaries (HAGBs).
4. Twinning alongside continuous dynamic recrystallization (CDRX) were observed as the main mechanisms of deformation in CP-Ti during initial passes of I-ECAP.
5. Significant increase in strength was achieved after grain refinement in I-ECAP processing. In case of $\Phi = 120^\circ$ the yield strength was increased by 81% and ultimate tensile strength (UTS) was increased by 25%, respectively. In case $\Phi = 90^\circ$, the same were increased by 118% and 33%. However, the ductility was somewhat reduced in processed material due to reduced strain hardening.
6. A hardness increase of about 40% was observed after I-ECAP processing in both cases.

7. Although the total plastic strain induced in the $\Phi = 120^\circ$ case and $\Phi = 90^\circ$ case are comparable after 6 and four passes, respectively; the material processed via $\Phi = 90^\circ$ angle die yielded higher levels of grain refinement and which displayed higher strength enhancements compared to the material processed via $\Phi = 120^\circ$ angle die.
8. Room temperature compression tests on as received and severely deformed material condition showed marked improvements in the compressive yield strength and also some improvements in the strain rate sensitivity. A complex three stage strain hardening behaviour was revealed for both material condition.
9. Compression testing of UFG CP-Ti at warm temperatures of 400, 500 and 600 °C and at varying strain rates of 0.01, 0.1 and 1.0 s⁻¹, revealed that the flow stress was sensitive to temperature and strain rate. Analysis of the deformed microstructure shows that the UFG structure is fairly stable at 400 and 500 °C for 0.1 and 1.0 s⁻¹ strain rates.
10. Finally, the research work shows that grain refinement to achieve UFG structure using I-ECAP is very effective technique in improving the strength characteristics of titanium. In this way, the need for harmful alloying elements can be eliminated and unalloyed titanium can be introduced in bio-medical implants. This promising technique can be exploited for commercial purposes.

Chapter 10

Recommendations for future work

The present work has demonstrated that CP-Ti billets can be successfully processed using the improved I-ECAP rig under certain processing conditions. However, there is scope to carry out further investigations by building on the results presented here.

It will be interesting to determine the process operating window for CP-Ti billets. Experiments should be carried out to investigate the lowest possible temperature at which CP-Ti can be processed successfully without segmentations or failure. The current processing temperature of 300 °C was carefully selected based on the existing data available on processing titanium using ECAP. However, it is believed that processing temperature can be lowered, especially for the experiments with $\Phi = 120^\circ$ I-ECAP die. Lowering of the temperature will reduced the effect of grain growth and recovery, this will enhanced the strength even further.

In the present work the billets processed using $\Phi = 120^\circ$ I-ECAP die exhibited slightly bowing which prevented re-inserting them in the channel for the next pass. Consequently, straightening operation was performed on the billets which is an additional work and which requires access to separate equipment. This effects the productivity and adds to the overall cost in producing the billet. The present work has shown that optimized die design using detailed FE analysis can eliminate this problem effectively. It is suggested to perform similar FE analysis studies for the $\Phi = 120^\circ$ die to optimize the design and eliminate this problem.

Although UFG structure was achieved in the present research work and subsequently the strength characteristics of CP-Ti was significantly increased. However, the grain refinement ratio calculated for both cases (i.e. die angle of 120 and 90°) shows potential for further refinement and therefore further improvement in strength. It is recommended to increase the total induced equivalent strain in billets by

subjecting the billets to even greater number of passes. Also, while route B_C has been used here in all experimental, other routes should be explored and its effects on the grain refinement and strength characteristics. Post I-ECAP operations such as upsetting and rolling can also be explored as a means of introducing even further grain refinement and dislocations.

This work has considerably improved the process efficiency of the I-ECAP rig. Further work to investigate the productivity limits of the I-ECAP can now be performed much easily. Design of experiments (DOE) study is recommended on the productivity parameters such as feeding stroke, punch amplitude and oscillations. This will be highly desirable in determining the feasibility of the process for commercialization purposes in future.

The present study employed EBSD analysis to study relatively large areas of the microstructure. The technique proved very useful in determining the changes in the microstructure and texture on a global scale and shed light on important phenomenons such as twinning and CRDX. For future studies, it is recommended to characterize the microstructure in detail by combining EBSD with TEM (transmission electron microscopy). In particular, TEM can be a powerful technique in studying the twinning activity and its role as a grain refinement mechanism during I-ECAP processing.

The present results shows that although the yield strength, ultimate tensile strength and hardness was significantly improved in the processed severely deformed material, however, the ductility was reduced. Further research work can be performed to improve the ductility of the processed material without considerable changes in the strength characteristics. Annealing the processed billets can be a way of improving the ductility. Experiments should be performed to determine the processing window (temperature and soaking time) to achieve the best combination of strength and ductility.

This work has determined the warm temperature workability of the material in the strain range of 0.01 to 1 s⁻¹. It is recommended to perform higher strain rate testing to establish a full picture of the workability characteristics. Such data will be useful in the forgeability of the material for making implants.

It is recommended to develop some miniature implants using the billets processed via I-ECAP such as screws used in dental implants. Implants made with the high strength of UFG/nano titanium can be much smaller in the diameter. Smaller dental implants introduces less damages to any surrounding areas during surgery, it also means less trauma for the patient.

References

- [1] G. Lütjering, and J.C. Williams, (2003), Titanium, Springer.
- [2] M.J. Donachie, (2000), Titanium - A technical guide, ASM International.
- [3] M. Geetha, A.K. Singh, R. Asokamani, and A.K. Gogia, (2009), "Ti based biomaterials, the ultimate choice for orthopaedic implants – A review", *Progress in Materials Science*, 54, pp. 397-425.
- [4] D.M. Brunette, P. Tengvall, M. Textor, and P. Thomsen, (2001), Titanium in medicine: Material science, surface science, engineering, biological responses and medical applications, Springer-Verlag, Berlin Heidelberg New York.
- [5] S.J. Lugowski, D.C. Smith, A.D. McHugh, and J.C. Van Loon, (1991), "Release of metal ions from dental implant materials in vivo: Determination of Al, Co, Cr, Mo, Ni, V, and Ti in organ tissue", *Journal of Biomedical Materials Research*, 25, pp. 1443-1458.
- [6] V.K. Truong, R. Lapovok, Y.S. Estrin, S. Rundell, J.Y. Wang, C.J. Fluke, R.J. Crawford, and E.P. Ivanova, (2010), "The influence of nano-scale surface roughness on bacterial adhesion to ultrafine-grained titanium", *Biomaterials*, 31, pp. 3674-3683.
- [7] M.A. Meyers, A. Mishra, and D.J. Benson, (2006), "Mechanical properties of nanocrystalline materials", *Progress in Materials Science*, 51, pp. 427-556.
- [8] T.G. Langdon, (2013), "Twenty-five years of ultrafine-grained materials: Achieving exceptional properties through grain refinement", *Acta Materialia*, 61, pp. 7035-7059.
- [9] A. Balyanov, J. Kutnyakova, N.A. Amirkhanova, V.V. Stolyarov, R.Z. Valiev, X.Z. Liao, Y.H. Zhao, Y.B. Jiang, H.F. Xu, T.C. Lowe, and Y.T. Zhu, (2004), "Corrosion resistance of ultra fine-grained Ti", *Scripta Materialia*, 51, pp. 225-229.
- [10] N.P. Gurao, G. Manivasagam, P. Govindaraj, R. Asokamani, and S. Suwas, (2013), "Effect of Texture and Grain Size on Bio-Corrosion Response of Ultrafine-Grained Titanium", *Metallurgical and Materials Transactions A*, 44, pp. 5602-5610.

-
- [11] W.-J. Kim, C.-Y. Hyun, and H.-K. Kim, (2006), "Fatigue strength of ultrafine-grained pure Ti after severe plastic deformation", *Scripta Materialia*, 54, pp. 1745-1750.
- [12] I.P. Semenova, G.K. Salimgareeva, V.V. Latysh, T. Lowe, and R.Z. Valiev, (2009), "Enhanced fatigue strength of commercially pure Ti processed by severe plastic deformation", *Materials Science and Engineering: A*, 503, pp. 92-95.
- [13] Y. Estrin, E.P. Ivanova, A. Michalska, V.K. Truong, R. Lapovok, and R. Boyd, (2011), "Accelerated stem cell attachment to ultrafine grained titanium", *Acta biomaterialia*, 7, pp. 900-906.
- [14] S. Faghihi, F. Azari, A.P. Zhilyaev, J.A. Szpunar, H. Vali, and M. Tabrizian, (2007), "Cellular and molecular interactions between MC3T3-E1 pre-osteoblasts and nanostructured titanium produced by high-pressure torsion", *Biomaterials*, 28, pp. 3887-3895.
- [15] L. Mishnaevsky Jr, E. Levashov, R.Z. Valiev, J. Segurado, I. Sabirov, N. Enikeev, S. Prokoshkin, A.V. Solov'yov, A. Korotitskiy, E. Gutmanas, I. Gotman, E. Rabkin, S. Psakh'e, L. Dluhoš, M. Seefeldt, and A. Smolin, (2014), "Nanostructured titanium-based materials for medical implants: Modeling and development", *Materials Science and Engineering: R: Reports*, 81, pp. 1-19.
- [16] R.Z. Valiev, I.P. Semenova, V.V. Latysh, H. Rack, T.C. Lowe, J. Petruzelka, L. Dluhos, D. Hrusak, and J. Sochova, (2008), "Nanostructured Titanium for Biomedical Applications", *Advanced Engineering Materials*, 10, pp. B15-B17.
- [17] Y. Estrin, and A. Vinogradov, (2013), "Extreme grain refinement by severe plastic deformation: A wealth of challenging science", *Acta Materialia*, 61, pp. 782-817.
- [18] R.Z. Valiev, R.K. Islamgaliev, and I.V. Alexandrov, (2000), "Bulk nanostructured materials from severe plastic deformation", *Progress in Materials Science*, 45, pp. 103-189.
- [19] R. Valiev, (2004), "Nanostructuring of metals by severe plastic deformation for advanced properties", *Nature Materials*, 3, pp. 511-516.
-

-
- [20] V.M. Segal, S.V. Dobatkin, and Valiev R. Z., (2004), "Equal-channel angular pressing of metallic materials: Achievements and trends. Selection of articles: Part I", *Russian Metall*, 1, pp. 1-102.
- [21] A. Rosochowski, and L. Olejnik, (2007), "FEM Simulation of Incremental Shear", *AIP Conference Proceedings*, 907, pp. 653-658.
- [22] E.O. Hall, (1951), "The Deformation and Ageing of Mild Steel: III Discussion of Results", *Proceedings of the Physical Society. Section B*, 64, pp. 747.
- [23] N.J. Petch, (1953), "The cleavage strength of polycrystals", *Journal of Iron Steel Inst.*, 174, pp. 25-28.
- [24] K.S. Kumar, H. Van Swygenhoven, and S. Suresh, (2003), "Mechanical behavior of nanocrystalline metals and alloys¹", *Acta Materialia*, 51, pp. 5743-5774.
- [25] J. Schiotz, F.D. Di Tolla, and K.W. Jacobsen, (1998), "Softening of nanocrystalline metals at very small grain sizes", *Nature*, 391, pp. 561-563.
- [26] R. Armstrong, I. Codd, R. Douthwaite, and N. Petch, (1962), "The plastic deformation of polycrystalline aggregates", *Philosophical Magazine*, 7, pp. 45-58.
- [27] R. Armstrong, (1970), "The influence of polycrystal grain size on several mechanical properties of materials", *Metallurgical and Materials Transactions B*, 1, pp. 1169-1176.
- [28] N. Hansen, (2004), "Hall–Petch relation and boundary strengthening", *Scripta Materialia*, 51, pp. 801-806.
- [29] J.D. Embury, and R.M. Fisher, (1966), "The structure and properties of drawn pearlite", *Acta Metallurgica*, 14, pp. 147-159.
- [30] R.W. Armstrong[†], Y.T. Chou, R.M. Fisher, and N. Louat, (1966), "The limiting grain size dependence of the strength of a polycrystalline aggregate", *Philosophical Magazine*, 14, pp. 943-951.
- [31] S. Erbel, (1979), "Mechanical properties and structure of extremely strainhardened copper", *Metals Technology*, 6, pp. 482-486.
- [32] J.R. Bowen, P.B. Prangnell, and F.J. Humphreys, (2000), "Microstructural evolution during formation of ultrafine grain structures by severe deformation", *Materials Science and Technology*, 16, pp. 1246-1250.
-

-
- [33] P.B. Prangnell, J.R. Bowen, and A. Gholinia, (2001), "The formation of submicron and nanocrystalline grain structures by severe deformation Science of metastable and nanocrystalline alloys," Proc. Proceedings of the 22nd Riso International Symposium on Materials Science, Science of Metastable and nanocrystalline Alloys Structure, Properties and Modeling, A. R. Dinesen, et al., eds., Riso National Laboratory, Roskilde, Denmark, pp. 105.
- [34] E. Arzt, (1998), "Size effects in materials due to microstructural and dimensional constraints: a comparative review", *Acta Materialia*, 46, pp. 5611-5626.
- [35] R. Birringer, (1989), "Nanocrystalline materials", *Materials Science and Engineering: A*, 117, pp. 33-43.
- [36] J.B. Cohen, (1992), "The early stages of solute distribution below a transition temperature", *Metallurgical Transactions A*, 23, pp. 2685-2697.
- [37] Valiev R. Z., (2004), "Nanostructuring of metals by severe plastic deformation for advanced properties".
- [38] Y.T. Zhu, T.C. Lowe, and T.G. Langdon, (2004), "Performance and applications of nanostructured materials produced by severe plastic deformation", *Scripta Materialia*, 51, pp. 825-830.
- [39] H. Gleiter, N. Hansen, A. Horsewell, T. Leffer, and H. Lilholt, (1981), "Polycrystals: Mechanics and Microstructures", *Risø National Laboratory, Rackilde, Denmark*, pp. 15-21.
- [40] H. Gleiter, (1989), *Nanocrystalline materials*, Progress in materials science, Pergamon Press, Oxford; New York.
- [41] U. Erb, A.M. El-Sherik, G. Palumbo, and K.T. Aust, (1993), "Synthesis, structure and properties of electroplated nanocrystalline materials", *Nanostructured Materials*, 2, pp. 383-390.
- [42] N.Y.C. Yang, T.J. Headley, J.J. Kelly, and J.M. Hruby, (2004), "Metallurgy of high strength Ni–Mn microsystems fabricated by electrodeposition", *Scripta Materialia*, 51, pp. 761-766.
- [43] C. Suryanarayana, (1999), *Non-equilibrium processing of materials*, Pergamon, Amsterdam.

-
- [44] M. Luton, C. Jayanth, M. Disko, S. Matras, and J. Vallone, (1989), "Multicomponent Ultrafine Microstructures," Proc. Mater. Res. Soc. Symp. Proc, 132, pp. 79.
- [45] D.B. Witkin, and E.J. Lavernia, (2006), "Synthesis and mechanical behavior of nanostructured materials via cryomilling", Progress in Materials Science, 51, pp. 1-60.
- [46] G. Nieman, J. Weertman, and R. Siegel, (1990), "Tensile strength and creep properties of nanocrystalline palladium", Scripta Metallurgica et Materialia, 24, pp. 145-150.
- [47] C.J. Youngdahl, P.G. Sanders, J.A. Eastman, and J.R. Weertman, (1997), "Compressive yield strengths of nanocrystalline Cu and Pd", Scripta Materialia, 37, pp. 809-813.
- [48] R.Z. Valiev, O.A. Kaibyshev, R.I. Kuznetsov, R.S. Musalimov, and N.K. Tsenev, (1988), Proc. USSR Acad Sci (Dokl. Akad. Nauk SSSR), 301, pp. 864-866.
- [49] R.Z. Valiev, N.A. Krasilnikov, and N.K. Tsenev, (1991), "Plastic deformation of alloys with submicron-grained structure", Materials Science and Engineering: A, 137, pp. 35-40.
- [50] R.Z. Valiev, A.V. Korznikov, and R.R. Mulyukov, (1993), "Structure and properties of ultrafine-grained materials produced by severe plastic deformation", Materials Science and Engineering: A, 168, pp. 141-148.
- [51] R. Valiev, Y. Estrin, Z. Horita, T. Langdon, M. Zechetbauer, and Y. Zhu, (2006), "Producing bulk ultrafine-grained materials by severe plastic deformation", JOM Journal of the Minerals, Metals and Materials Society, 58, pp. 33-39.
- [52] G. Langford, and M. Cohen, (1969), "Microstructure of Armco-iron subjected to severe plastic drawing", Trans. ASM, 82, pp. 623-632.
- [53] F. Li, and P.S. Bate, (1991), "Strain path change effects in cube textured aluminium sheet", Acta Metallurgica et Materialia, 39, pp. 2639-2650.
- [54] V. Rybin, (1987), "Large plastic deformations and destruction of metals", Moscow: Metallurgia.
-

-
- [55] P.W. Bridgman, (1935), "Effects of High Shearing Stress Combined with High Hydrostatic Pressure", *Physical Review*, 48, pp. 825-847.
- [56] A. Rosochowski, and L. Olejnik, (2012), Chap 5: Severe plastic deformation for grain refinement and enhancement of properties - Microstructure Evolution in Metal Forming Processes, (Ed. D. Balint, et al.), Woodhead Publishing, 978-0-85709-074-4.
- [57] V.M. Segal, V.I. Reznikov, A.E. Drobyshevskiy, and V.I. Kopylov, (1981), "Plastic metal working by simple shear", *Russ Metally*, 1, pp. 99-104.
- [58] A. Korbel, M. Richert, and J. Richert, (1981), "The effects of very high cumulative deformation on structure and mechanical properties of aluminium," *Proc. Proceedings of Second RISO International Symposium on Metallurgy and Material Science*, Roskilde, September, pp. 14-18.
- [59] A.K. Ghosh, and W. Huang, (2000), *Investigations and Applications of Severe Plastic Deformation*, (Ed. T. C. Lowe, et al.), Springer Netherlands, Dordrecht, 978-94-011-4062-1.
- [60] J. Huang, Y.T. Zhu, D.J. Alexander, X. Liao, T.C. Lowe, and R.J. Asaro, (2004), "Development of repetitive corrugation and straightening", *Materials Science and Engineering: A*, 371, pp. 35-39.
- [61] Y. Beygelzimer, D. Orlov, and V. Varyukhin, (2002), *Ultrafine Grained Materials II*, (Ed. John Wiley & Sons, Inc., 9781118804537).
- [62] V.M. Segal, (1977), "The method of material preparation for subsequent working," Patent of the USSR No. 575892.
- [63] P. Berbon, M. Furukawa, Z. Horita, M. Nemoto, and T. Langdon, (1999), "Influence of pressing speed on microstructural development in equal-channel angular pressing", *Metallurgical and Materials Transactions A*, 30, pp. 1989-1997.
- [64] R. Valiev, R. Mulyukov, V. Ovchinnikov, and V. Shabashov, (1991), "Mossbauer analysis of submicrometer grained iron", *Scripta Metallurgica et Materialia (USA)*, 25, pp. 2717-2722.
- [65] N.A. Akhmadeev, R.Z. Valiev, V.I. Kopylov, and R.R. Mulyukov, (1992), "Formation of submicro grain structure in copper and nickel by extensive shear deformation", *RUSSIAN METALLURGY METAL*, 2, pp. 96-101.
-

-
- [66] J. Wang, Z. Horita, M. Furukawa, M. Nemoto, N.K. Tsenev, R.Z. Valiev, Y. Ma, and T.G. Langdon, (1993), "An investigation of ductility and microstructural evolution in an Al– 3% Mg alloy with submicron grain size", *Journal of Materials Research*, 8, pp. 2810-2818.
- [67] R.Z. Valiev, (1997), "Structure and mechanical properties of ultrafine-grained metals", *Materials Science and Engineering: A*, 234-236, pp. 59-66.
- [68] I.V. Alexandrov, Y.T. Zhu, T.C. Lowe, R.K. Islamgaliev, and R.Z. Valiev, (1998), "Microstructures and properties of nanocomposites obtained through SPTS consolidation of powders", *Metallurgical and Materials Transactions A*, 29A, pp. 2253 - 2260.
- [69] V.V. Stolyarov, Y.T. Zhu, T.C. Lowe, R.K. Islamgaliev, and R.Z. Valiev, (1999), "A two step SPD processing of ultrafine-grained titanium", *NanoStructured Materials*, 11, pp. 947-954.
- [70] R.Z. Valiev, and T.G. Langdon, (2006), "Principles of equal-channel angular pressing as a processing tool for grain refinement", *Progress in Materials Science*, 51, pp. 881-981.
- [71] Y. Iwahashi, J. Wang, Z. Horita, M. Nemoto, and T.G. Langdon, (1996), "Principle of equal-channel angular pressing for the processing of ultra-fine grained materials", *Scripta Materialia*, 35, pp. 143-146.
- [72] K. Furuno, H. Akamatsu, K. Oh-ishi, M. Furukawa, Z. Horita, and T.G. Langdon, (2004), "Microstructural development in equal-channel angular pressing using a 60° die", *Acta Materialia*, 52, pp. 2497-2507.
- [73] V.M. Segal, (1995), "Materials processing by simple shear", *Materials Science and Engineering: A*, 197, pp. 157-164.
- [74] T. Langdon, M. Furukawa, M. Nemoto, and Z. Horita, (2000), "Using equal-channel angular pressing for refining grain size", *JOM Journal of the Minerals, Metals and Materials Society*, 52, pp. 30-33.
- [75] M. Furukawa, Y. Iwahashi, Z. Horita, M. Nemoto, and T.G. Langdon, (1998), "The shearing characteristics associated with equal-channel angular pressing", *Materials Science and Engineering: A*, 257, pp. 328-332.
-

-
- [76] M. Furukawa, Z. Horita, and T.G. Langdon, (2002), "Factors influencing the shearing patterns in equal-channel angular pressing", *Materials Science and Engineering: A*, 332, pp. 97-109.
- [77] R.E. Barber, T. Dudo, P.B. Yasskin, and K.T. Hartwig, (2004), "Product yield for ECAE processing", *Scripta Materialia*, 51, pp. 373-377.
- [78] M. Avvari, and S. Narendranath, (2014), "Influence of Route-R on wrought magnesium AZ61 alloy mechanical properties through equal channel angular pressing", *Journal of Magnesium and Alloys*, 2, pp. 159-164.
- [79] V.P. Astakhov, (2015), *Modern Manufacturing Engineering*, (Ed. J. P. Davim), Springer International Publishing, Cham, 978-3-319-20152-8.
- [80] A. Rosochowski, and L. Olejnik, (2002), "Numerical and physical modelling of plastic deformation in 2-turn equal channel angular extrusion", *Journal of Materials Processing Technology*, 125-126, pp. 309-316.
- [81] Y.T. Zhu, and T.C. Lowe, (2000), "Observations and issues on mechanisms of grain refinement during ECAP process", *Materials Science and Engineering: A*, 291, pp. 46-53.
- [82] Y. Iwahashi, M. Furukawa, Z. Horita, M. Nemoto, and T.G. Langdon, (1998), "Microstructural characteristics of ultrafine-grained aluminum produced using equal-channel angular pressing", *Metallurgical and Materials Transactions A*, 29, pp. 2245-2252.
- [83] Y.T. Zhu, and T.G. Langdon, (2004), "The fundamentals of nanostructured materials processed by severe plastic deformation", *JOM*, 56, pp. 58-63.
- [84] T.G. Langdon, (2007), "The principles of grain refinement in equal-channel angular pressing", *Materials Science and Engineering: A*, 462, pp. 3-11.
- [85] D. Kuhlmann-Wilsdorf, (1997), "High-strain dislocation patterning, texture formation and shear banding of wavy glide materials in the LEDS theory", *Scripta Materialia*, 36, pp. 173-181.
- [86] D. Kuhlmann-Wilsdorf, (1989), "Theory of plastic deformation: - properties of low energy dislocation structures", *Materials Science and Engineering: A*, 113, pp. 1-41.
- [87] R.Z. Valiev, I. Sabirov, A.P. Zhilyaev, and T.G. Langdon, (2012), "Bulk Nanostructured Metals for Innovative Applications", *JOM*, 64, pp. 1134-1142.
-

-
- [88] Y. Saito, N. Tsuji, H. Utsunomiya, T. Sakai, and R. Hong, (1998), "Ultra-fine grained bulk aluminum produced by accumulative roll-bonding (ARB) process", *Scripta materialia*, 39, pp. 1221-1227.
- [89] R. Srinivasan, P. Chaudhury, B. Cherukuri, Q. Han, D. Swenson, and P. Gros, (2006), "Continuous severe plastic deformation processing of aluminum alloys", DOE Award Number: DEFC36-01ID14022, Technical report.
- [90] G.J. Raab, R.Z. Valiev, T.C. Lowe, and Y.T. Zhu, (2004), "Continuous processing of ultrafine grained Al by ECAP–Conform", *Materials Science and Engineering: A*, 382, pp. 30-34.
- [91] J.-C. Lee, H.-K. Seok, J.-H. Han, and Y.-H. Chung, (2001), "Controlling the textures of the metal strips via the continuous confined strip shearing(C2S2) process", *Materials Research Bulletin*, 36, pp. 997-1004.
- [92] Y. Saito, H. Utsunomiya, H. Suzuki, and T. Sakai, (2000), "Improvement in the r-value of aluminum strip by a continuous shear deformation process", *Scripta Materialia*, 42, pp. 1139-1144.
- [93] Y. Huang, and P.B. Prangnell, (2007), "Continuous frictional angular extrusion and its application in the production of ultrafine-grained sheet metals", *Scripta Materialia*, 56, pp. 333-336.
- [94] A. Rosochowski, (2017), Chapt 2: Incremental ECAP - Severe Plastic Deformation Technology, (Ed. A. Rosochowski), Whittles Publishing, ISBN: 978-1-84995-091-6.
- [95] A. Rosochowski, L. Olejnik, and M.W. Richert, (2008), "Double-billet incremental ECAP," *Proc. Materials Science Forum*, 584, pp. 139-144.
- [96] L. Olejnik, A. Rosochowski, and M.W. Richert, (2008), "Incremental ECAP of plates," *Proc. Materials Science Forum*, 584, pp. 108-113.
- [97] A. Rosochowski, M. Rosochowska, L. Olejnik, and B. Verlinden, (2010), "Incremental equal channel angular pressing of sheets," *Proc. Proc. 13th International Conference on Metal Forming, Japan 2010*, Steel Research International, 81, pp. 470-473.
- [98] V.M. Segal, (2004), "Engineering and commercialization of equal channel angular extrusion (ECAE)", *Materials Science and Engineering: A*, 386, pp. 269-276.
-

-
- [99] I.H. Son, Y.G. Jin, Y.T. Im, S.H. Chon, and J.K. Park, (2007), "Sensitivity of friction condition in finite element investigations of equal channel angular extrusion", *Materials Science and Engineering: A*, 445-446, pp. 676-685.
- [100] G. Lütjering, and J.C. Williams, (2007), *Titanium, Engineering Materials and Processes*, Springer, Berlin Heidelberg New York.
- [101] M.E. Weeks, (1932), "The discovery of the elements. XI. Some elements isolated with the aid of potassium and sodium: Zirconium, titanium, cerium, and thorium", *Journal of Chemical Education*, 9, pp. 1231.
- [102] R.W. Schutz, and D.E. Thomas, (1987), *Corrosion - Metals Handbook*, ASM, Metals Park, USA.
- [103] K. Sakurai, Y. Itabashi, and A. Komatsu, (1980), *Titanium '80, Science and Technology*, AIME, Warrendale, USA.
- [104] R. Boyer, G. Welsch, and E.W. Collings, (1994), *Materials Properties Handbook: Titanium Alloys*, ASM, Materials Park, USA.
- [105] N.E. Paton, and J.C. Williams, (1974), "Effect of hydrogen on titanium and its alloys", *American Society for Metals. Hydrogen in Metals*, pp. 409-32.
- [106] S.L. Semiatin, D.P. DeLo, V.M. Segal, R.E. Goforth, and N.D. Frey, (1999), "Workability of commercial-purity titanium and 4340 steel during equal channel angular extrusion at cold-working temperatures", *Metallurgical and Materials Transactions A*, 30, pp. 1425-1435.
- [107] S.L. Semiatin, and D.P. DeLo, (2000), "Equal channel angular extrusion of difficult-to-work alloys", *Materials & Design*, 21, pp. 311-322.
- [108] V.V. Stolyarov, Y.T. Zhu, I.V. Alexandrov, T.C. Lowe, and R.Z. Valiev, (2001), "Influence of ECAP routes on the microstructure and properties of pure Ti", *Materials Science and Engineering: A*, 299, pp. 59-67.
- [109] M.H. Yoo, (1981), "Slip, twinning, and fracture in hexagonal close-packed metals", *Metallurgical Transactions A*, 12, pp. 409-418.
- [110] N. Stanford, U. Carlson, and M.R. Barnett, (2008), "Deformation Twinning and the Hall–Petch Relation in Commercial Purity Ti", *Metallurgical and Materials Transactions A*, 39, pp. 934-944.
- [111] Y.B. Chun, S.H. Yu, S.L. Semiatin, and S.K. Hwang, (2005), "Effect of deformation twinning on microstructure and texture evolution during cold

-
- rolling of CP-titanium", *Materials Science and Engineering: A*, 398, pp. 209-219.
- [112] A.A. Salem, S.R. Kalidindi, and R.D. Doherty, (2003), "Strain hardening of titanium: role of deformation twinning", *Acta Materialia*, 51, pp. 4225-4237.
- [113] S. Nemat-Nasser, W.G. Guo, and J.Y. Cheng, (1999), "Mechanical properties and deformation mechanisms of a commercially pure titanium", *Acta Materialia*, 47, pp. 3705-3720.
- [114] I. Kim, W.-S. Jeong, J. Kim, K.-T. Park, and D.H. Shin, (2001), "Deformation structures of pure Ti produced by equal channel angular pressing", *Scripta Materialia*, 45, pp. 575-580.
- [115] I. Kim, J. Kim, D.H. Shin, X.Z. Liao, and Y.T. Zhu, (2003), "Deformation twins in pure titanium processed by equal channel angular pressing", *Scripta Materialia*, 48, pp. 813-817.
- [116] D.H. Shin, I. Kim, J. Kim, Y.S. Kim, and S.L. Semiatin, (2003), "Microstructure development during equal-channel angular pressing of titanium", *Acta Materialia*, 51, pp. 983-996.
- [117] I. Kim, J. Kim, D.H. Shin, C.S. Lee, and S.K. Hwang, (2003), "Effects of equal channel angular pressing temperature on deformation structures of pure Ti", *Materials Science and Engineering: A*, 342, pp. 302-310.
- [118] Y.J. Chen, Y.J. Li, J.C. Walmsley, S. Dumoulin, P.C. Skaret, and H.J. Roven, (2010), "Microstructure evolution of commercial pure titanium during equal channel angular pressing", *Materials Science and Engineering: A*, 527, pp. 789-796.
- [119] Y.J. Chen, Y.J. Li, J.C. Walmsley, S. Dumoulin, and H.J. Roven, (2010), "Deformation Structures of Pure Titanium during Shear Deformation", *Metallurgical and Materials Transactions A*, 41, pp. 787-794.
- [120] Y.J. Chen, Y.J. Li, J.C. Walmsley, S. Dumoulin, S.S. Gireesh, S. Armada, P.C. Skaret, and H.J. Roven, (2011), "Quantitative analysis of grain refinement in titanium during equal channel angular pressing", *Scripta Materialia*, 64, pp. 904-907.
-

-
- [121] C.S. Meredith, and A.S. Khan, (2015), "The microstructural evolution and thermo-mechanical behavior of UFG Ti processed via equal channel angular pressing", *Journal of Materials Processing Technology*, 219, pp. 257-270.
- [122] V.S. Zhernakov, V.V. Latysh, V.V. Stolyarov, A.I. Zharikov, and R.Z. Valiev, (2001), "The developing of nanostructured spd ti for structural use", *Scripta Materialia*, 44, pp. 1771-1774.
- [123] K. Hajizadeh, B. Eghbali, K. Topolski, and K.J. Kurzydowski, (2014), "Ultra-fine grained bulk CP-Ti processed by multi-pass ECAP at warm deformation region", *Materials Chemistry and Physics*, 143, pp. 1032-1038.
- [124] Y.G. Ko, D.H. Shin, K.-T. Park, and C.S. Lee, (2006), "An analysis of the strain hardening behavior of ultra-fine grain pure titanium", *Scripta Materialia*, 54, pp. 1785-1789.
- [125] A. Medvedev, H.P. Ng, R. Lapovok, Y. Estrin, T.C. Lowe, and V.N. Anumalasetty, (2015), "Comparison of laboratory-scale and industrial-scale equal channel angular pressing of commercial purity titanium", *Materials Letters*, 145, pp. 308-311.
- [126] P. Rodriguez-Calvillo, and J.M. Cabrera, (2015), "Microstructure and mechanical properties of a commercially pure Ti processed by warm equal channel angular pressing", *Materials Science and Engineering: A*, 625, pp. 311-320.
- [127] A.V. Sergueeva, V.V. Stolyarov, R.Z. Valiev, and A.K. Mukherjee, (2001), "Advanced mechanical properties of pure titanium with ultrafine grained structure", *Scripta Materialia*, 45, pp. 747-752.
- [128] Y. Zhang, R.B. Figueiredo, S.N. Alhajeri, J.T. Wang, N. Gao, and T.G. Langdon, (2011), "Structure and mechanical properties of commercial purity titanium processed by ECAP at room temperature", *Materials Science and Engineering: A*, 528, pp. 7708-7714.
- [129] X. Zhao, X. Yang, X. Liu, X. Wang, and T.G. Langdon, (2010), "The processing of pure titanium through multiple passes of ECAP at room temperature", *Materials Science and Engineering: A*, 527, pp. 6335-6339.

-
- [130] X. Zhao, X. Yang, X. Liu, C.T. Wang, Y. Huang, and T.G. Langdon, (2014), "Processing of commercial purity titanium by ECAP using a 90 degrees die at room temperature", *Materials Science and Engineering: A*, 607, pp. 482-489.
- [131] Y. Estrin, and A. Vinogradov, (2010), "Fatigue behaviour of light alloys with ultrafine grain structure produced by severe plastic deformation: An overview", *International Journal of Fatigue*, 32, pp. 898-907.
- [132] V.V. Stolyarov, Y.T. Zhu, T.C. Lowe, and R.Z. Valiev, (2001), "Microstructure and properties of pure Ti processed by ECAP and cold extrusion", *Materials Science and Engineering: A*, 303, pp. 82-89.
- [133] V.V. Stolyarov, L. Zeipper, B. Mingler, and M. Zehetbauer, (2008), "Influence of post-deformation on CP-Ti processed by equal channel angular pressing", *Materials Science and Engineering: A*, 476, pp. 98-105.
- [134] V.V. Stolyarov, Y.T. Zhu, I.V. Alexandrov, T.C. Lowe, and R.Z. Valiev, (2003), "Grain refinement and properties of pure Ti processed by warm ECAP and cold rolling", *Materials Science and Engineering: A*, 343, pp. 43-50.
- [135] V.L. Sordi, M. Ferrante, M. Kawasaki, and T.G. Langdon, (2012), "Microstructure and tensile strength of grade 2 titanium processed by equal-channel angular pressing and by rolling", *Journal of Materials Science*, 47, pp. 7870-7876.
- [136] J.-W. Park, Y.-J. Kim, C.H. Park, D.-H. Lee, Y.G. Ko, J.-H. Jang, and C.S. Lee, (2009), "Enhanced osteoblast response to an equal channel angular pressing-processed pure titanium substrate with microrough surface topography", *Acta Biomaterialia*, 5, pp. 3272-3280.
- [137] D. Rodríguez-Galán, I. Sabirov, and J. Segurado, (2015), "Temperature and strain rate effect on the deformation of nanostructured pure titanium", *International Journal of Plasticity*, 70, pp. 191-205.
- [138] V. Latysh, G. Krallics, I. Alexandrov, and A. Fodor, (2006), "Application of bulk nanostructured materials in medicine", *Current Applied Physics*, 6, pp. 262-266.
- [139] S. Li, M.A.M. Bourke, I.J. Beyerlein, D.J. Alexander, and B. Clausen, (2004), "Finite element analysis of the plastic deformation zone and working load in

-
- equal channel angular extrusion", *Materials Science and Engineering: A*, 382, pp. 217-236.
- [140] P.B. Prangnell, C. Harris, and S.M. Roberts, (1997), "Finite element modelling of equal channel angular extrusion", *Scripta Materialia*, 37(7), pp. 983-989.
- [141] J.R. Bowen, A. Gholinia, S.M. Roberts, and P.B. Prangnell, (2000), "Analysis of the billet deformation behaviour in equal channel angular extrusion", *Materials Science and Engineering: A*, 287, pp. 87-99.
- [142] V.P. Basavaraj, U. Chakkingal, and T.S.P. Kumar, (2009), "Study of channel angle influence on material flow and strain inhomogeneity in equal channel angular pressing using 3D finite element simulation", *Journal of Materials Processing Technology*, 209, pp. 89-95.
- [143] S. Dumoulin, H.J. Roven, J.C. Werenskiold, and H.S. Valberg, (2005), "Finite element modeling of equal channel angular pressing: Effect of material properties, friction and die geometry", *Materials Science and Engineering: A*, 410-411, pp. 248-251.
- [144] C.J. Luis-Pérez, R. Luri-Irigoyen, and D. Gastón-Ochoa, (2004), "Finite element modelling of an Al-Mn alloy by equal channel angular extrusion (ECAE)", *Journal of Materials Processing Technology*, 153-154, pp. 846-852.
- [145] A.V. Nagasekhar, and Y. Tick-Hon, (2004), "Optimal tool angles for equal channel angular extrusion of strain hardening materials by finite element analysis", *Computational Materials Science*, 30, pp. 489-495.
- [146] S.C. Yoon, and H.S. Kim, (2008), "Finite element analysis of the effect of the inner corner angle in equal channel angular pressing", *Materials Science and Engineering: A*, 490, pp. 438-444.
- [147] R.B. Figueiredo, M.T.P. Aguilar, and P.R. Cetlin, (2006), "Finite element modelling of plastic instability during ECAP processing of flow-softening materials", *Materials Science and Engineering: A*, 430, pp. 179-184.
- [148] H.S. Kim, M.H. Seo, and S.I. Hong, (2002), "Finite element analysis of equal channel angular pressing of strain rate sensitive metals", *Journal of Materials Processing Technology*, 130-131, pp. 497-503.
-

-
- [149] H. Jiang, Z. Fan, and C. Xie, (2009), "Finite element analysis of temperature rise in CP-Ti during equal channel angular extrusion", *Materials Science and Engineering: A*, 513-514, pp. 109-114.
- [150] F. Kang, J.T. Wang, Y.L. Su, and K.N. Xia, (2007), "Finite element analysis of the effect of back pressure during equal channel angular pressing", *Journal of Materials Science*, 42, pp. 1491-1500.
- [151] R.Y. Lapovok, (2005), "The role of back-pressure in equal channel angular extrusion", *Journal of Materials Science*, 40, pp. 341-346.
- [152] Q.X. Pei, B.H. Hu, C. Lu, and Y.Y. Wang, (2003), "A finite element study of the temperature rise during equal channel angular pressing", *Scripta Materialia*, 49, pp. 303-308.
- [153] I.-H. Son, J.-H. Lee, and Y.-T. Im, (2006), "Finite element investigation of equal channel angular extrusion with back pressure", *Journal of Materials Processing Technology*, 171, pp. 480-487.
- [154] T. Suo, Y. Li, Y. Guo, and Y. Liu, (2006), "The simulation of deformation distribution during ECAP using 3D finite element method", *Materials Science and Engineering: A*, 432, pp. 269-274.
- [155] W.J. Zhao, H. Ding, Y.P. Ren, S.M. Hao, J. Wang, and J.T. Wang, (2005), "Finite element simulation of deformation behavior of pure aluminum during equal channel angular pressing", *Materials Science and Engineering: A*, 410-411, pp. 348-352.
- [156] H.S. Kim, (2002), "Finite element analysis of deformation behaviour of metals during equal channel multi angular pressing", *Materials Science and Engineering: A*, 328, pp. 317-323.
- [157] T. Suo, Y. Li, Q. Deng, and Y. Liu, (2007), "Optimal pressing route for continued equal channel angular pressing by finite element analysis", *Materials Science and Engineering: A*, 466, pp. 166-171.
- [158] Y.-L. Yang, and S. Lee, (2003), "Finite element analysis of strain conditions after equal channel angular extrusion", *Journal of Materials Processing Technology*, 140, pp. 583-587.
-

-
- [159] A. Rosochowski, and L. Olejnik, (2007), "Finite element simulation of severe plastic deformation processes", Proceedings of IMechE, Part L: Journal of Materials: Design and Applications, 221, pp. 187-196.
- [160] D. DeLo, and S. Semiatin, (1999), "Finite-element modeling of nonisothermal equal-channel angular extrusion", Metallurgical and Materials Transactions A, 30, pp. 1391-1402.
- [161] H. Li, S. Li, and D. Zhang, (2010), "On the selection of outlet channel length and billet length in equal channel angular extrusion", Computational Materials Science, 49, pp. 293-298.
- [162] S.C. Yoon, A.V. Nagasekhar, and H.S. Kim, (2009), "Finite element analysis of the bending behavior of a workpiece in equal channel angular pressing", Metals and Materials International, 15, pp. 215-219.
- [163] "ASTM E209-00, (2010), "Standard Practice for Compression Tests of Metallic Materials at Elevated Temperatures with Conventional or Rapid Heating Rates and Strain Rates", ASTM International, West Conshohocken, PA, www.astm.org".
- [164] Z. Trojanová, P.A. Maksimiyuk, and P. Lukáč, (1994), "Temperature dependence of Young's modulus of α -titanium polycrystals", physica status solidi (a), 143, pp. K75-K77.
- [165] F. Zaïri, B. Aour, J.-M. Gloaguen, M. Naït-Abdelaziz, and J.-M. Lefebvre, (2006), "Numerical modelling of elastic-viscoplastic equal channel angular extrusion process of a polymer", Computational materials science, 38, pp. 202-216.
- [166] Y. Iwahashi, Z. Horita, M. Nemoto, and T.G. Langdon, (1998), "The process of grain refinement in equal-channel angular pressing", Acta Materialia, 46, pp. 3317-3331.
- [167] ASTM E8 / E8M-16a, (2016), "Standard Test Methods for Tension Testing of Metallic Materials", ASTM International, West Conshohocken, PA, www.astm.org
- [168] M. Rastegaev, (1940), "New method of uniform upsetting of specimens for determining the true deformation resistance and the coefficient of external friction (original in Russian)", Zavod Lab, 6, pp. 354.
-

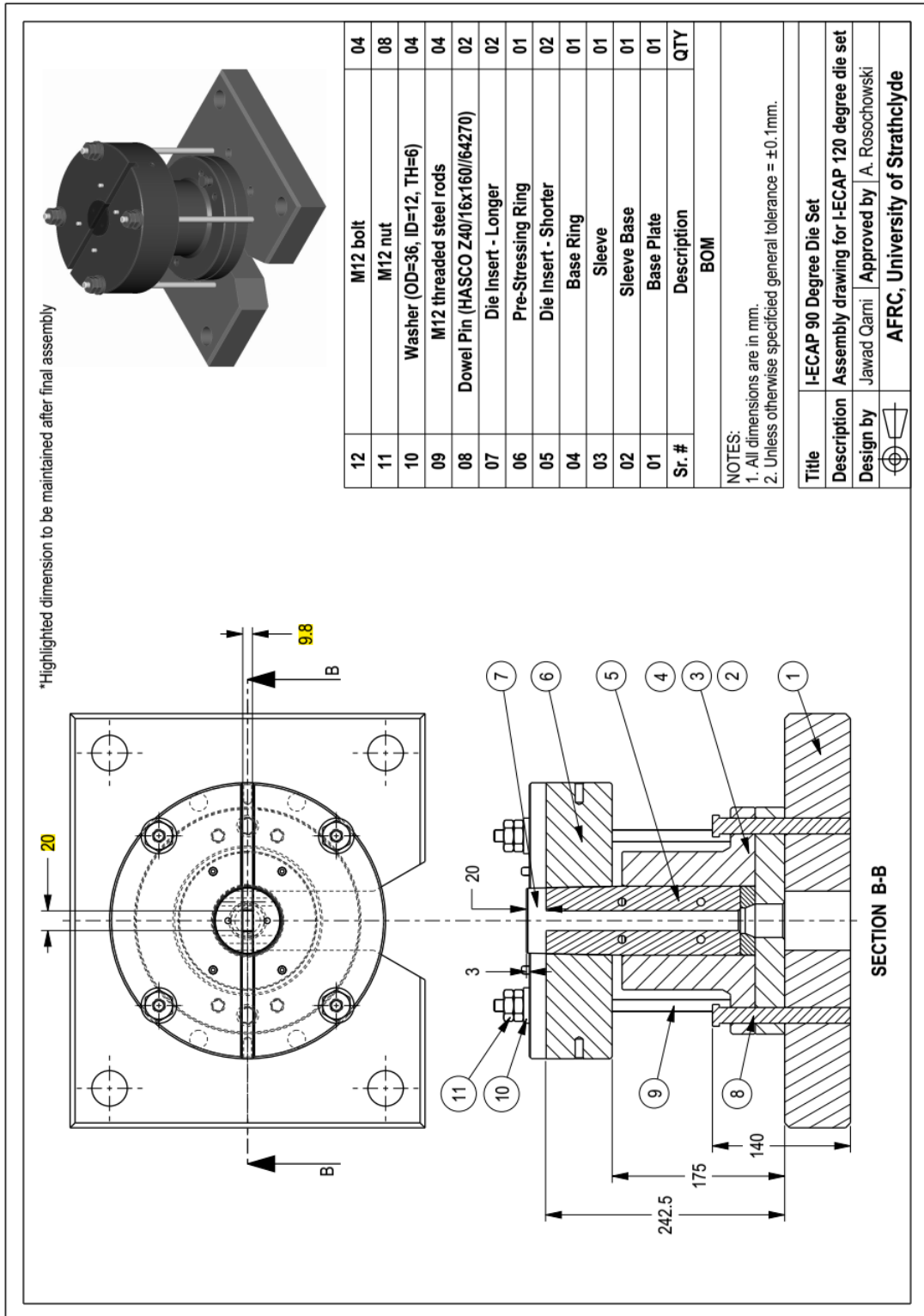
-
- [169] ASTM E9-09, (2009), "Standard Test Methods of Compression Testing of Metallic Materials at Room Temperature", ASTM International, West Conshohocken, PA, www.astm.org
- [170] J.W. Won, C.H. Park, S.-G. Hong, and C.S. Lee, (2015), "Deformation anisotropy and associated mechanisms in rolling textured high purity titanium", *Journal of Alloys and Compounds*, 651, pp. 245-254.
- [171] C.S. Meredith, and A.S. Khan, (2012), "Texture evolution and anisotropy in the thermo-mechanical response of UFG Ti processed via equal channel angular pressing", *International Journal of Plasticity*, 30–31, pp. 202-217.
- [172] Y.T. Zhu, X.Z. Liao, and X.L. Wu, (2012), "Deformation twinning in nanocrystalline materials", *Progress in Materials Science*, 57, pp. 1-62.
- [173] M.A. Meyers, O. Vöhringer, and V.A. Lubarda, (2001), "The onset of twinning in metals: a constitutive description", *Acta Materialia*, 49, pp. 4025-4039.
- [174] Y.N. Wang, and J.C. Huang, (2003), "Texture analysis in hexagonal materials", *Materials Chemistry and Physics*, 81, pp. 11-26.
- [175] B. Beausir, S. Suwas, L.S. Tóth, K.W. Neale, and J.-J. Fundenberger, (2008), "Analysis of texture evolution in magnesium during equal channel angular extrusion", *Acta Materialia*, 56, pp. 200-214.
- [176] B. Beausir, L.S. Tóth, and K.W. Neale, (2007), "Ideal orientations and persistence characteristics of hexagonal close packed crystals in simple shear", *Acta Materialia*, 55, pp. 2695-2705.
- [177] Y. Jiang, Z. Chen, C. Zhan, T. Chen, R. Wang, and C. Liu, (2015), "Adiabatic shear localization in pure titanium deformed by dynamic loading: Microstructure and microtexture characteristic", *Materials Science and Engineering: A*, 640, pp. 436-442.
- [178] J.W. Christian, and S. Mahajan, (1995), "Deformation twinning", *Progress in Materials Science*, 39, pp. 1-157.
- [179] M. Kawasaki, Z. Horita, and T.G. Langdon, (2009), "Microstructural evolution in high purity aluminum processed by ECAP", *Materials Science and Engineering: A*, 524, pp. 143-150.

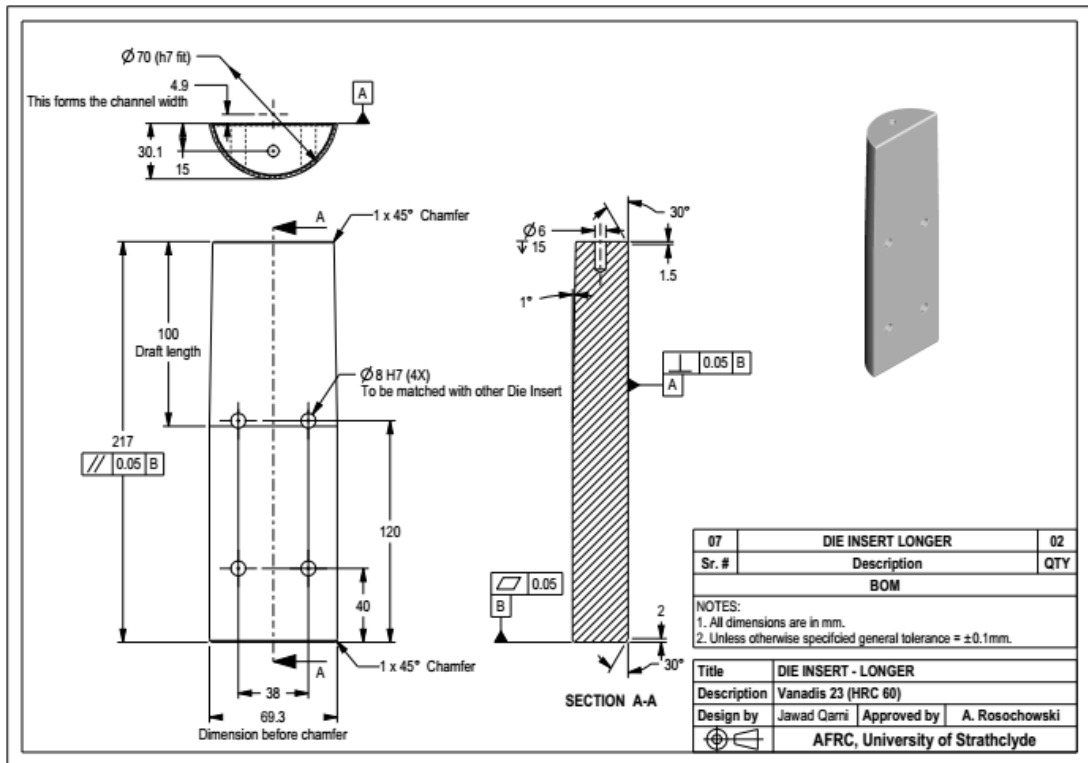
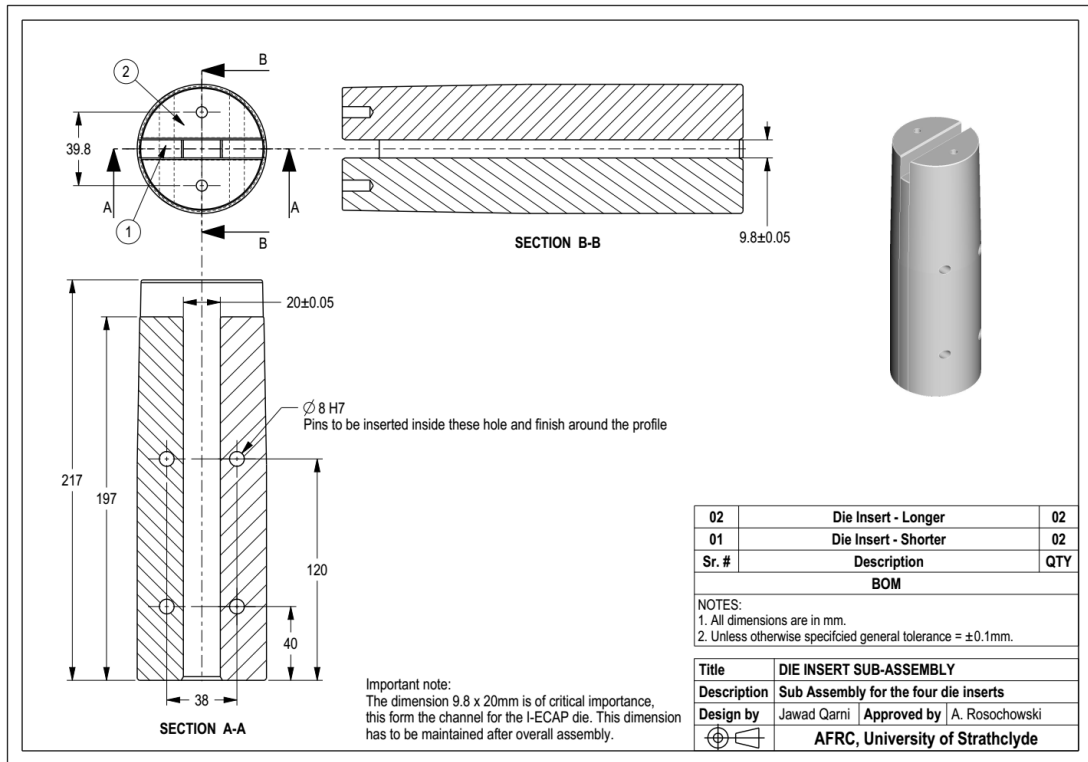
-
- [180] S. Suwas, B. Beausir, L.S. Tóth, J.J. Fundenberger, and G. Gottstein, (2011), "Texture evolution in commercially pure titanium after warm equal channel angular extrusion", *Acta Materialia*, 59, pp. 1121-1133.
- [181] I. Sabirov, M.T. Perez-Prado, J.M. Molina-Aldareguia, I.P. Semenova, G.K. Salimgareeva, and R.Z. Valiev, (2011), "Anisotropy of mechanical properties in high-strength ultra-fine-grained pure Ti processed via a complex severe plastic deformation route", *Scripta Materialia*, 64, pp. 69-72.
- [182] A. Ghaderi, and M.R. Barnett, (2011), "Sensitivity of deformation twinning to grain size in titanium and magnesium", *Acta Materialia*, 59, pp. 7824-7839.
- [183] F.J. Humphreys, and M. Hatherly, (2004), *Recrystallization and Related Annealing Phenomena (Second Edition)*, Elsevier, Oxford.
- [184] Y.M. Wang, and E. Ma, (2004), "Three strategies to achieve uniform tensile deformation in a nanostructured metal", *Acta Materialia*, 52, pp. 1699-1709.
- [185] Y. Wang, M. Chen, F. Zhou, and E. Ma, (2002), "High tensile ductility in a nanostructured metal", *Nature*, 419, pp. 912-915.
- [186] D.-H. Kang, and T.-W. Kim, (2010), "Mechanical behavior and microstructural evolution of commercially pure titanium in enhanced multi-pass equal channel angular pressing and cold extrusion", *Materials & Design*, 31, Supplement 1, pp. S54-S60.
- [187] C.-Y. Hyun, and H.-K. Kim, (2012), "Grain size dependence of flow stress in ECAPed Ti with constant texture", *Transactions of Nonferrous Metals Society of China*, 22, Supplement 3, pp. s673-s677.
- [188] M. Rao, U. Chakkingal, and T. Raghu, (2013), "Mechanical Behavior of Commercial Purity Titanium Processed by Equal Channel Angular Pressing Followed by Cold Rolling", *Transactions of the Indian Institute of Metals*, 66, pp. 357-362.
- [189] K.P.S. S. Bindu, K. Smetana, A. Balakrishnan, T.N. Kim, (2009), "An in vivo Evaluation of Ultra-fine Grained Titanium Implants", *J. Mater. Sci. Technol.*, 25, pp. 556-560.
- [190] G. Purcek, G.G. Yapici, I. Karaman, and H.J. Maier, (2011), "Effect of commercial purity levels on the mechanical properties of ultrafine-grained titanium", *Materials Science and Engineering: A*, 528, pp. 2303-2308.
-

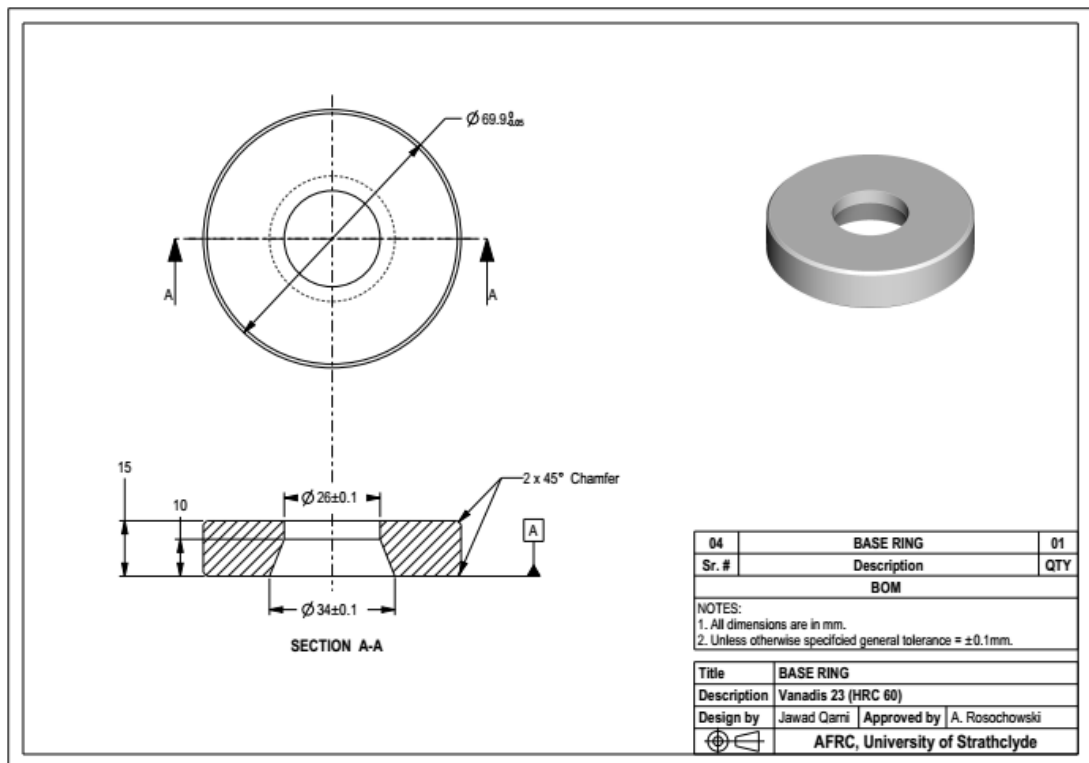
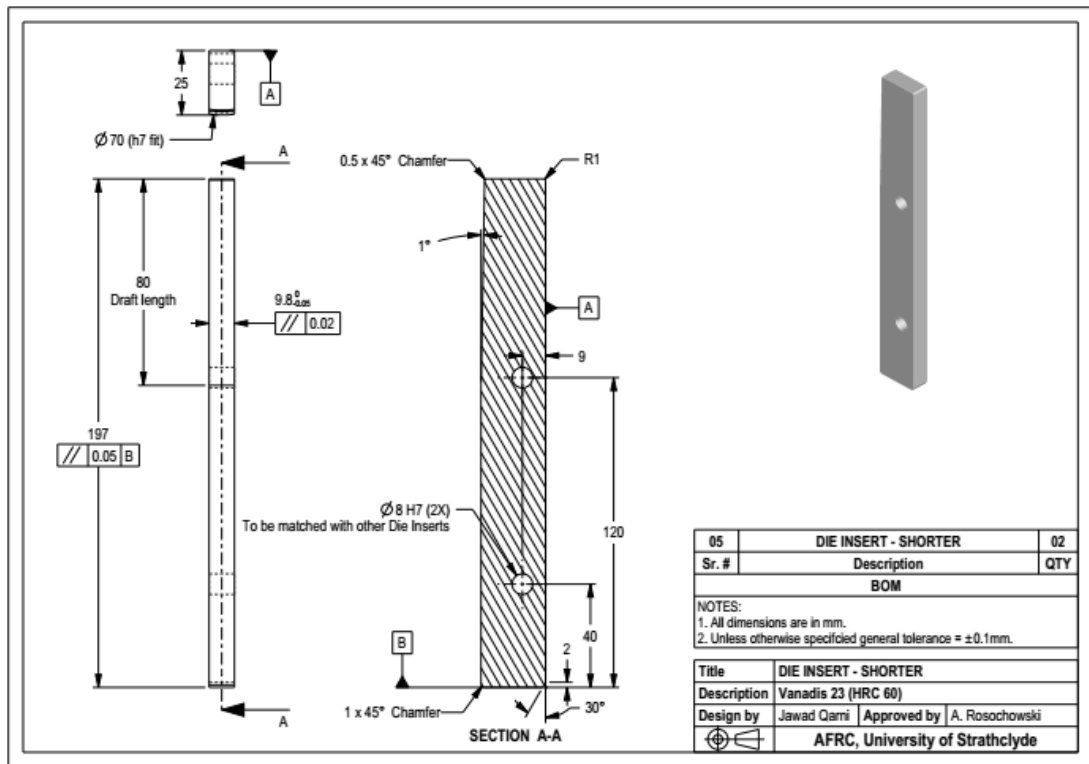
-
- [191] A.A. Salem, S.R. Kalidindi, and R.D. Doherty, (2002), "Strain hardening regimes and microstructure evolution during large strain compression of high purity titanium", *Scripta Materialia*, 46, pp. 419-423.
- [192] Z. Zeng, Y. Zhang, and S. Jonsson, (2009), "Deformation behaviour of commercially pure titanium during simple hot compression", *Materials & Design*, 30, pp. 3105-3111.
- [193] S.R. Kalidindi, A.A. Salem, and R.D. Doherty, (2003), "Role of Deformation Twinning on Strain Hardening in Cubic and Hexagonal Polycrystalline Metals", *Advanced Engineering Materials*, 5, pp. 229-232.
- [194] G. Gray, T., (1997), "Influence of Strain Rate and Temperature on the Structure. Property Behavior of High-Purity Titanium", *Le Journal de Physique IV*, 07, pp. 423-428.
- [195] A.A. Salem, S.R. Kalidindi, R.D. Doherty, and S.L. Semiatin, (2006), "Strain hardening due to deformation twinning in α -titanium: Mechanisms", *Metallurgical and Materials Transactions A*, 37, pp. 259-268.
- [196] Z.S. Basinski, M.S. Szczerba, M. Niewczas, J.D. Embury, and S.J. Basinski, (1997), "The transformation of slip dislocations during twinning of copper-aluminum alloy crystals", *Rev. Met. Paris*, 94, pp. 1037-1044.
- [197] K. Ahn, H. Huh, and J. Yoon, (2015), "Rate-dependent hardening model for pure titanium considering the effect of deformation twinning", *International Journal of Mechanical Sciences*, 98, pp. 80-92.
- [198] D. Jia, Y.M. Wang, K.T. Ramesh, E. Ma, Y.T. Zhu, and R.Z. Valiev, (2001), "Deformation behavior and plastic instabilities of ultrafine-grained titanium", *Applied Physics Letters*, 79, pp. 611-613.
- [199] J. Liu, A.S. Khan, L. Takacs, and C.S. Meredith, (2015), "Mechanical behavior of ultrafine-grained/nanocrystalline titanium synthesized by mechanical milling plus consolidation: Experiments, modeling and simulation", *International Journal of Plasticity*, 64, pp. 151-163.
- [200] J.-L. Pérez-Castellanos, and A. Rusinek, (2012), "Temperature increase associated with plastic deformation under dynamic compression: Application to aluminium alloy Al 6082", *Journal of theoretical and applied mechanics*, 50, pp. 377-398.
-

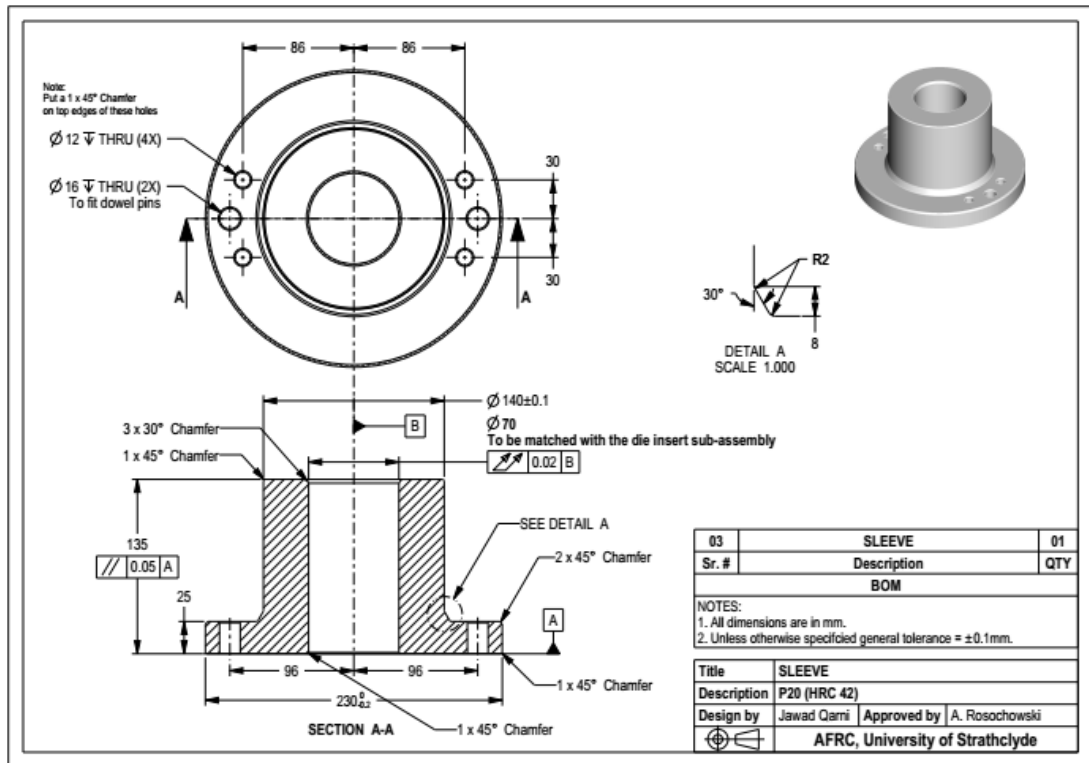
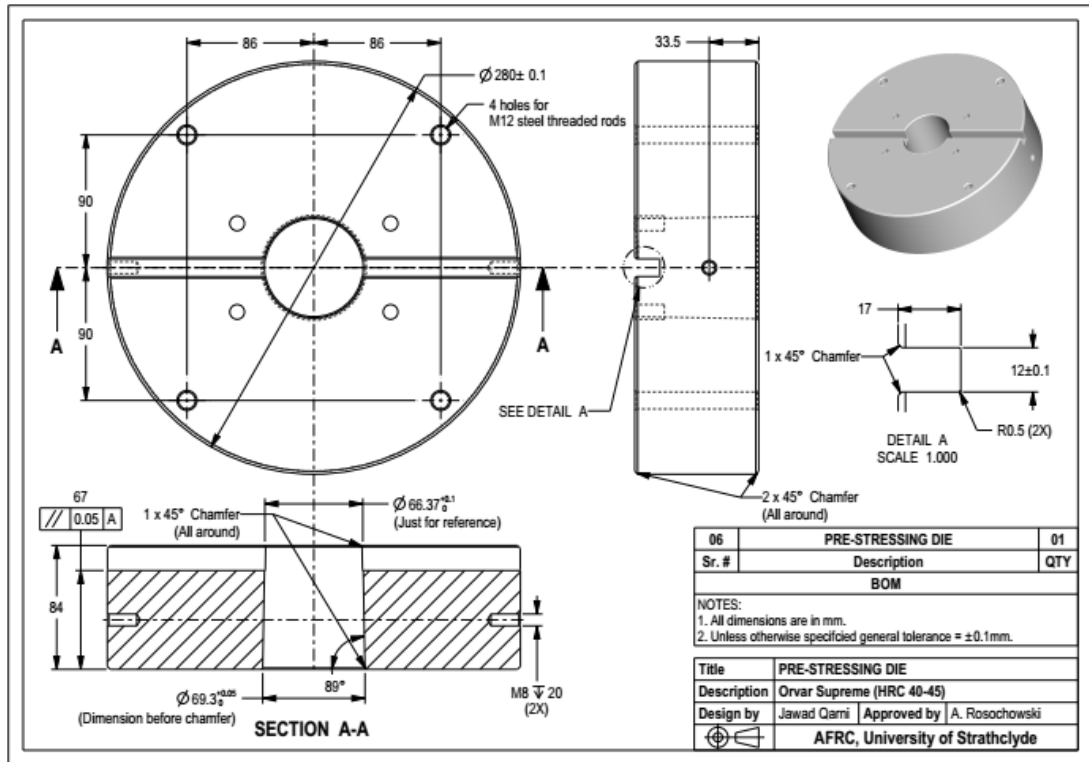
- [201] Y.M. Wang, and E. Ma, (2004), "Strain hardening, strain rate sensitivity, and ductility of nanostructured metals", *Materials Science and Engineering: A*, 375–377, pp. 46-52.
- [202] H.V. Atkinson, (1988), "Overview no. 65", *Acta Metallurgica*, 36, pp. 469-491.
- [203] Y.B. Chun, and S.K. Hwang, (2008), "Static recrystallization of warm-rolled pure Ti influenced by microstructural inhomogeneity", *Acta Materialia*, 56, pp. 369-379.
- [204] M.R. Salamati, M.J. Qarni, S. Tamimi, and A. Rosochowski, (2016), "Effect of channel angle on the material flow, hardness distribution and process forces during incremental ECAP of Al-1050 billets", *AIP Conference Proceedings*, 1769, pp. 090004.

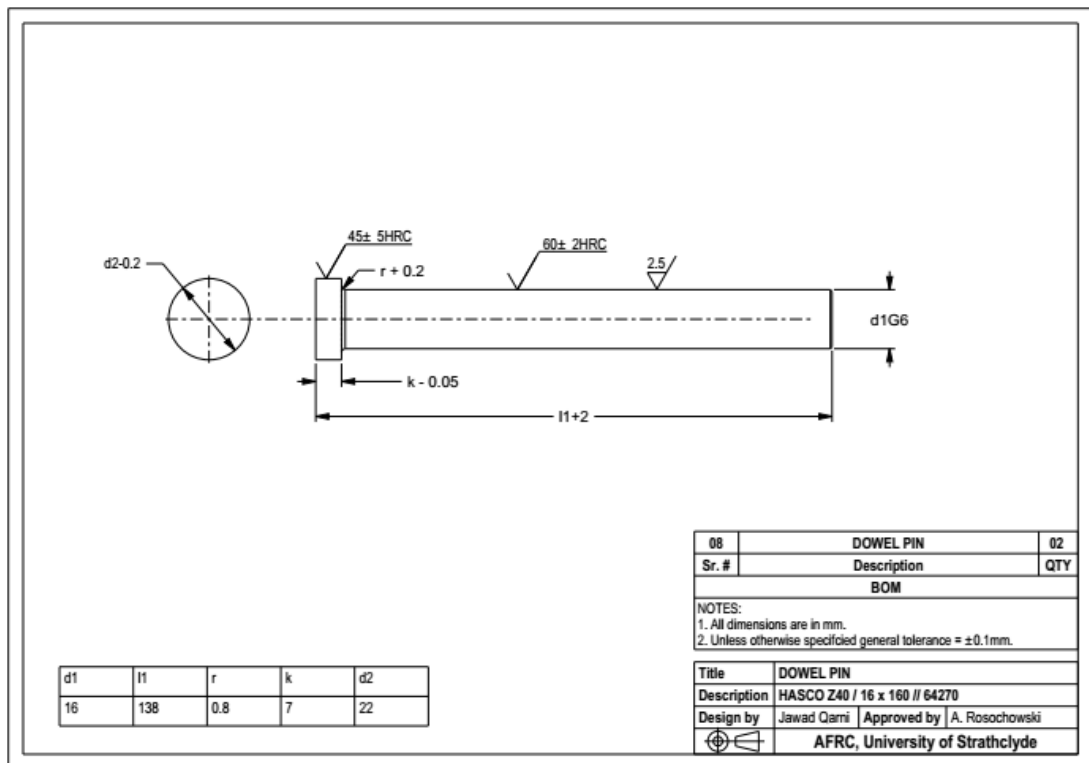
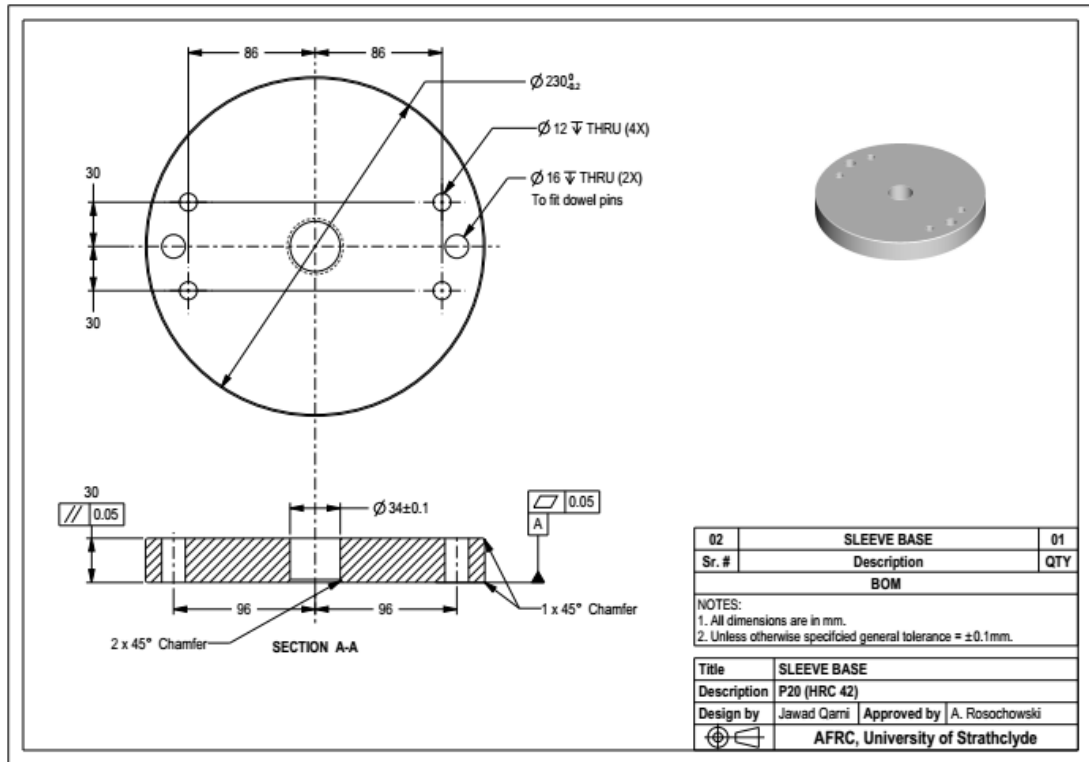
Appendix A – Engineering drawings for 90° I-ECAP die

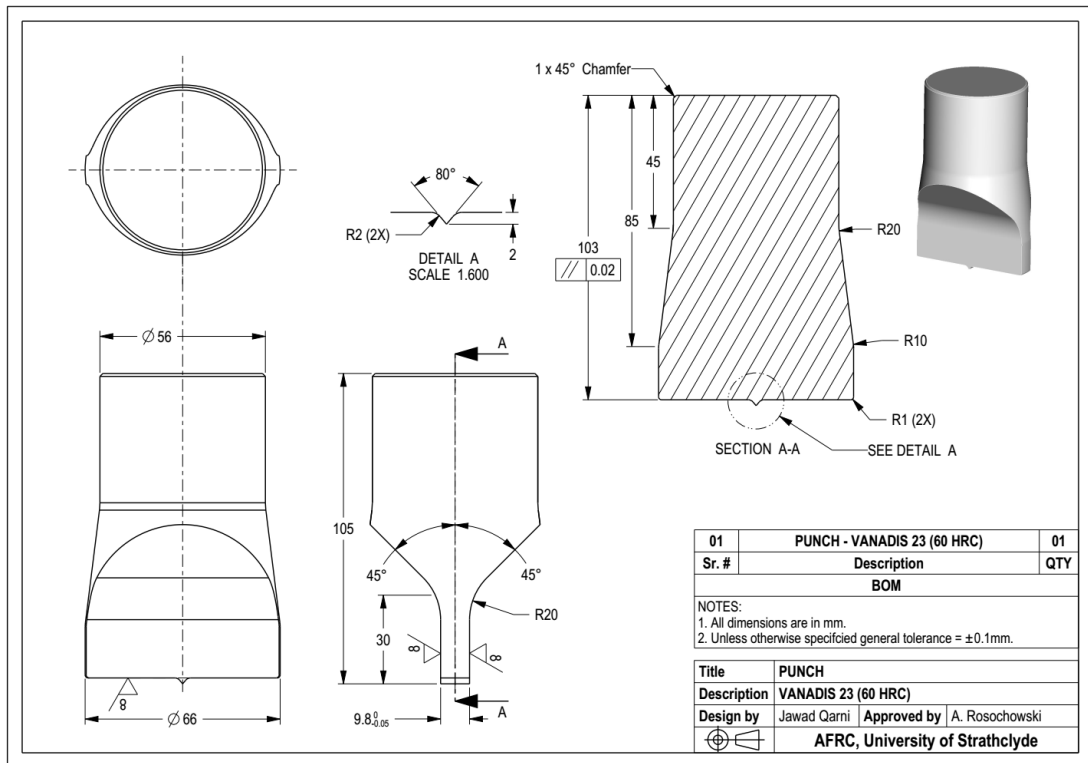
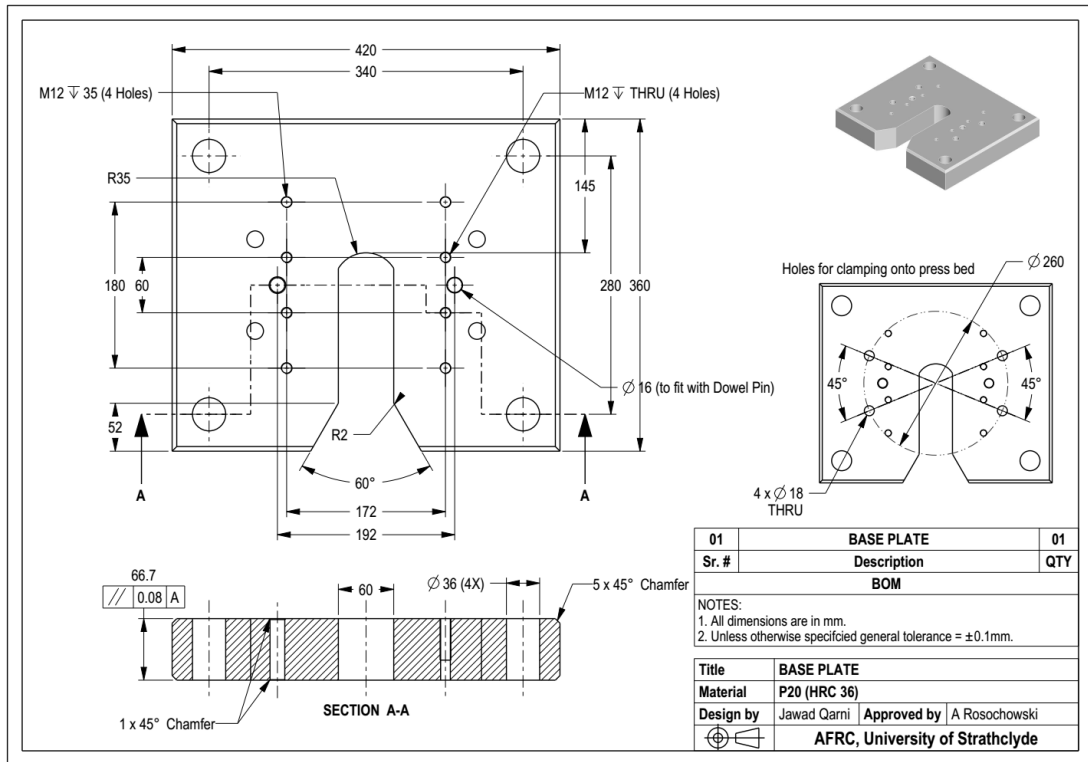




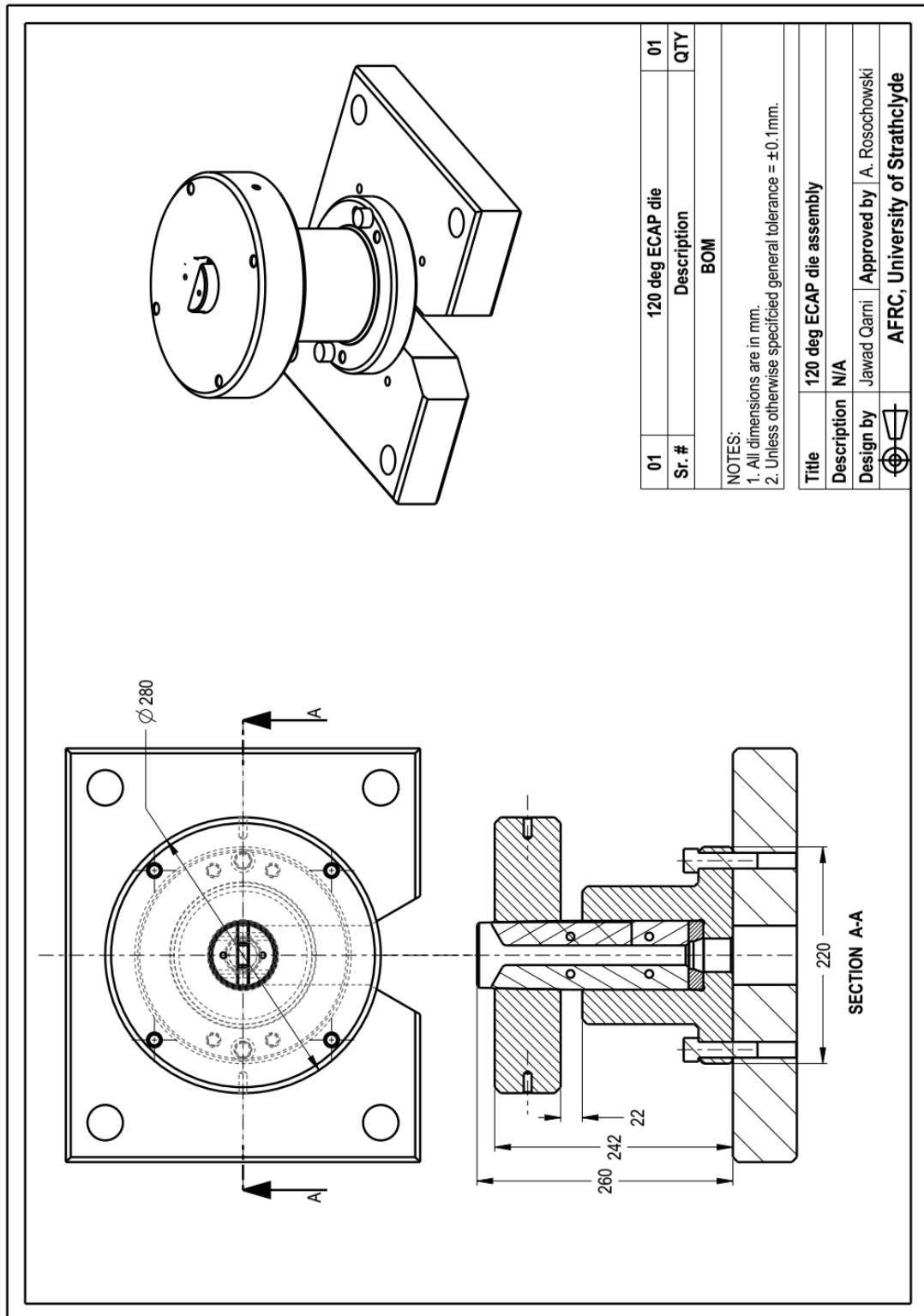


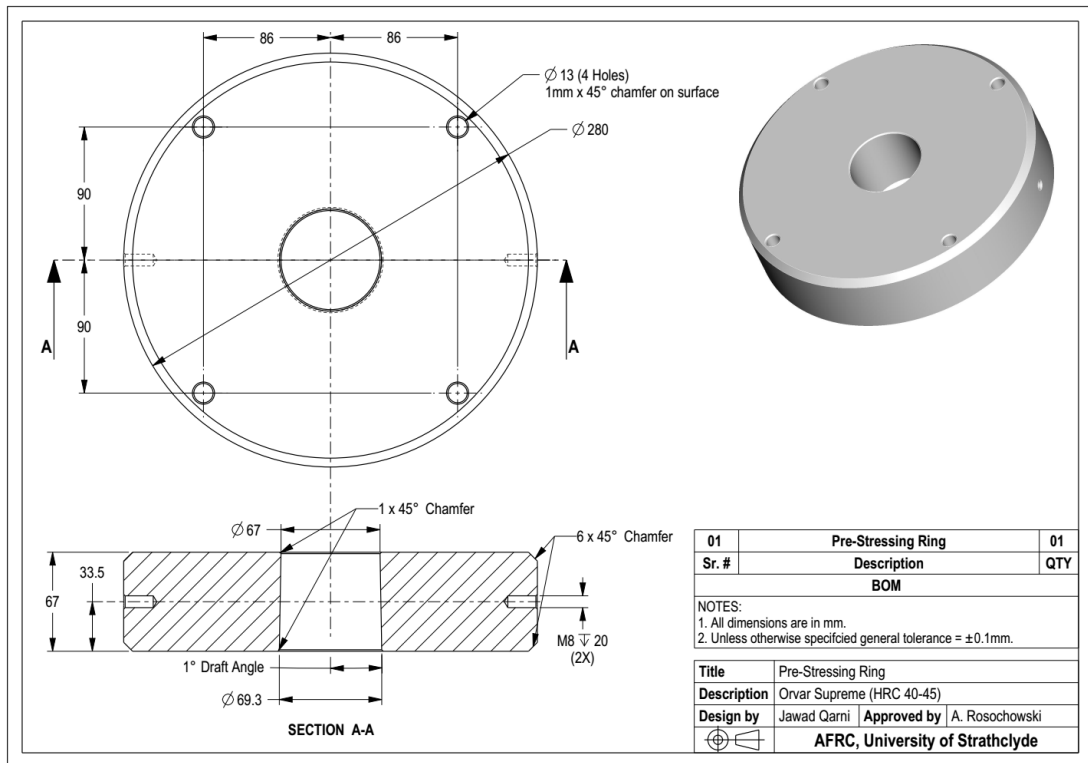
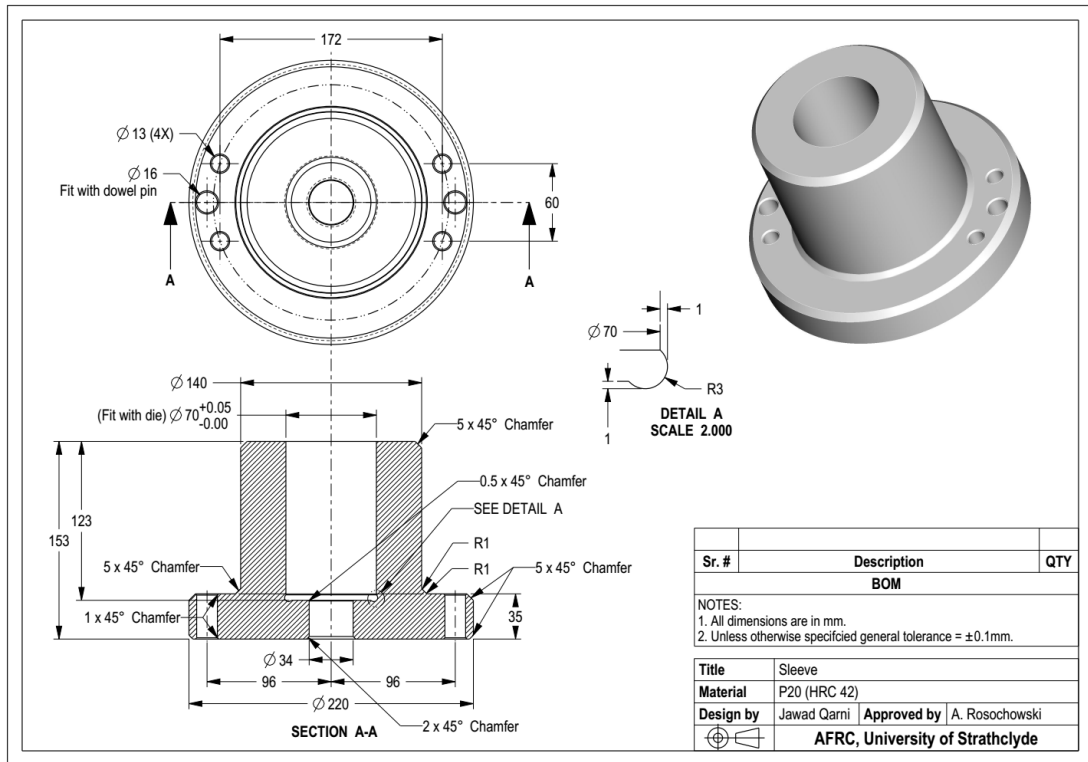


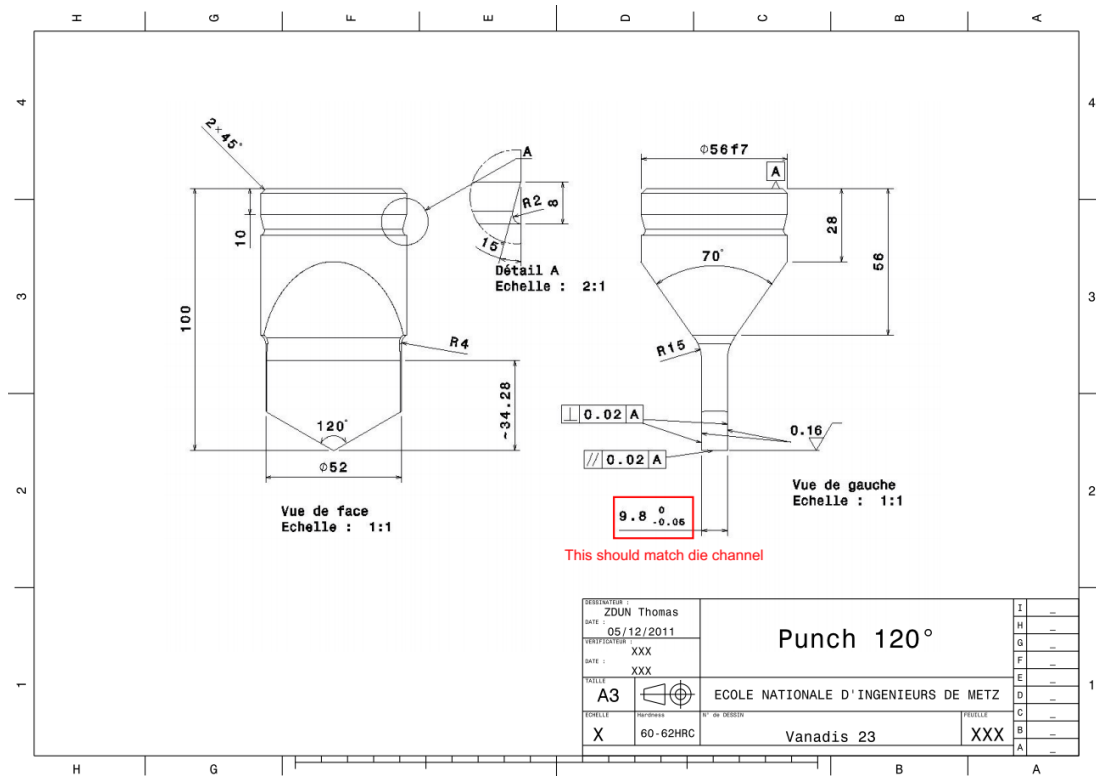
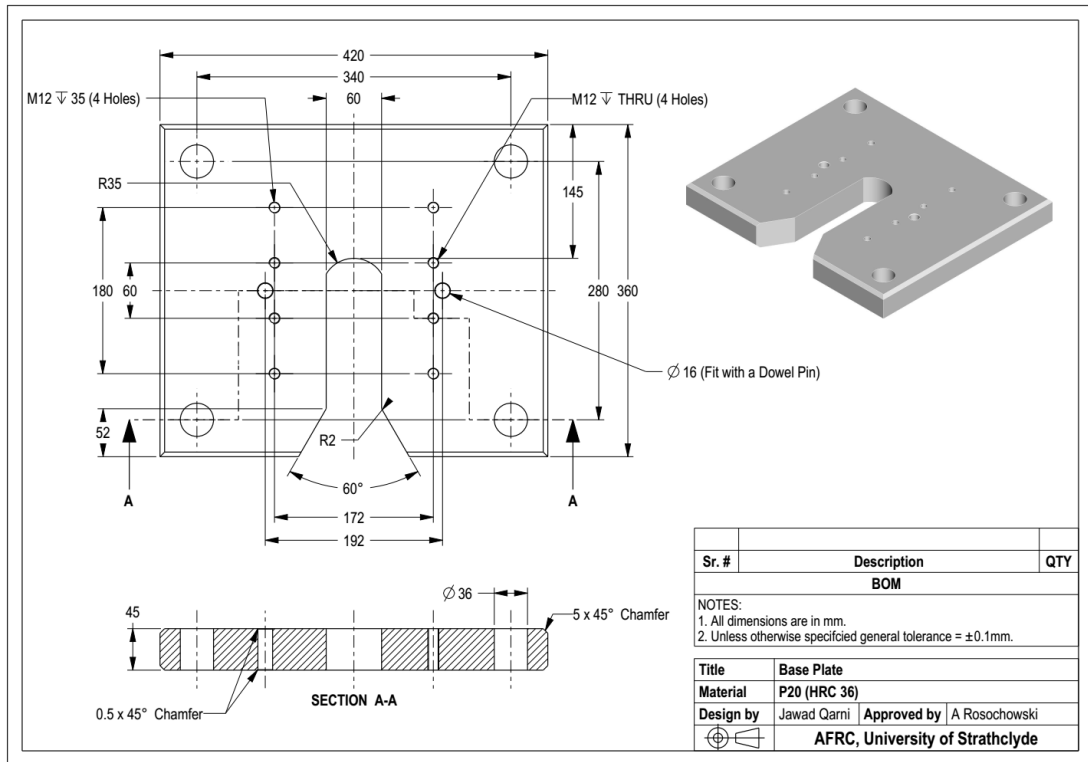


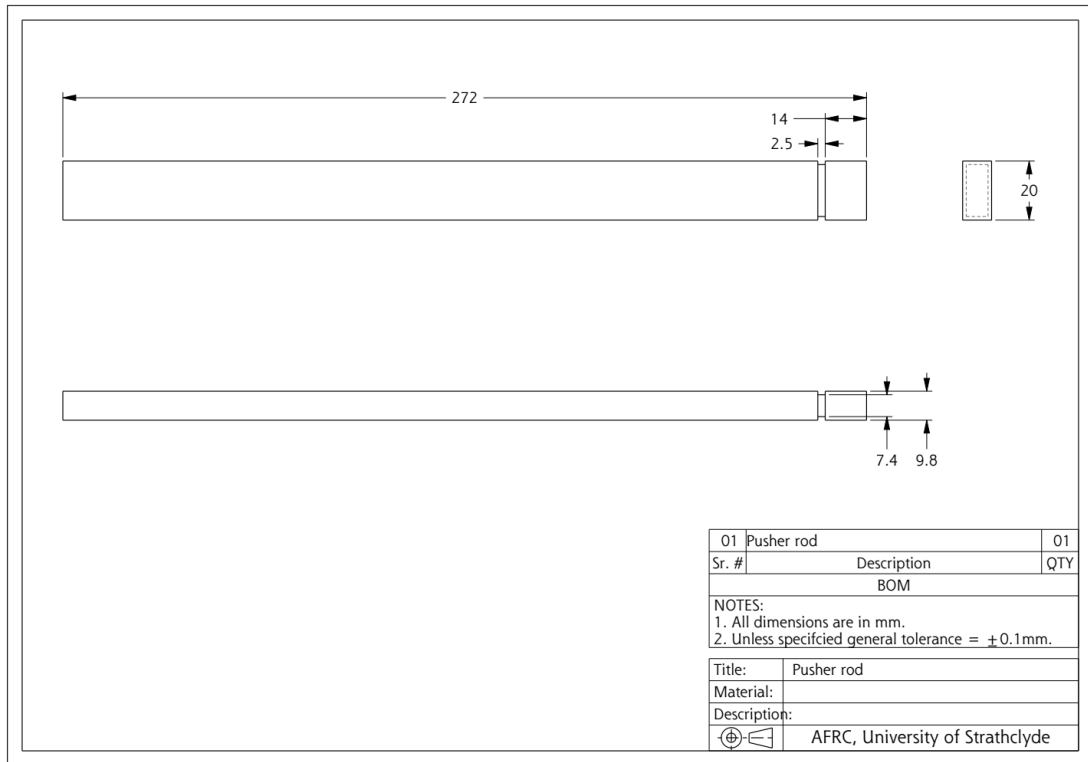


Appendix B – Engineering drawings for 120° I-ECAP die

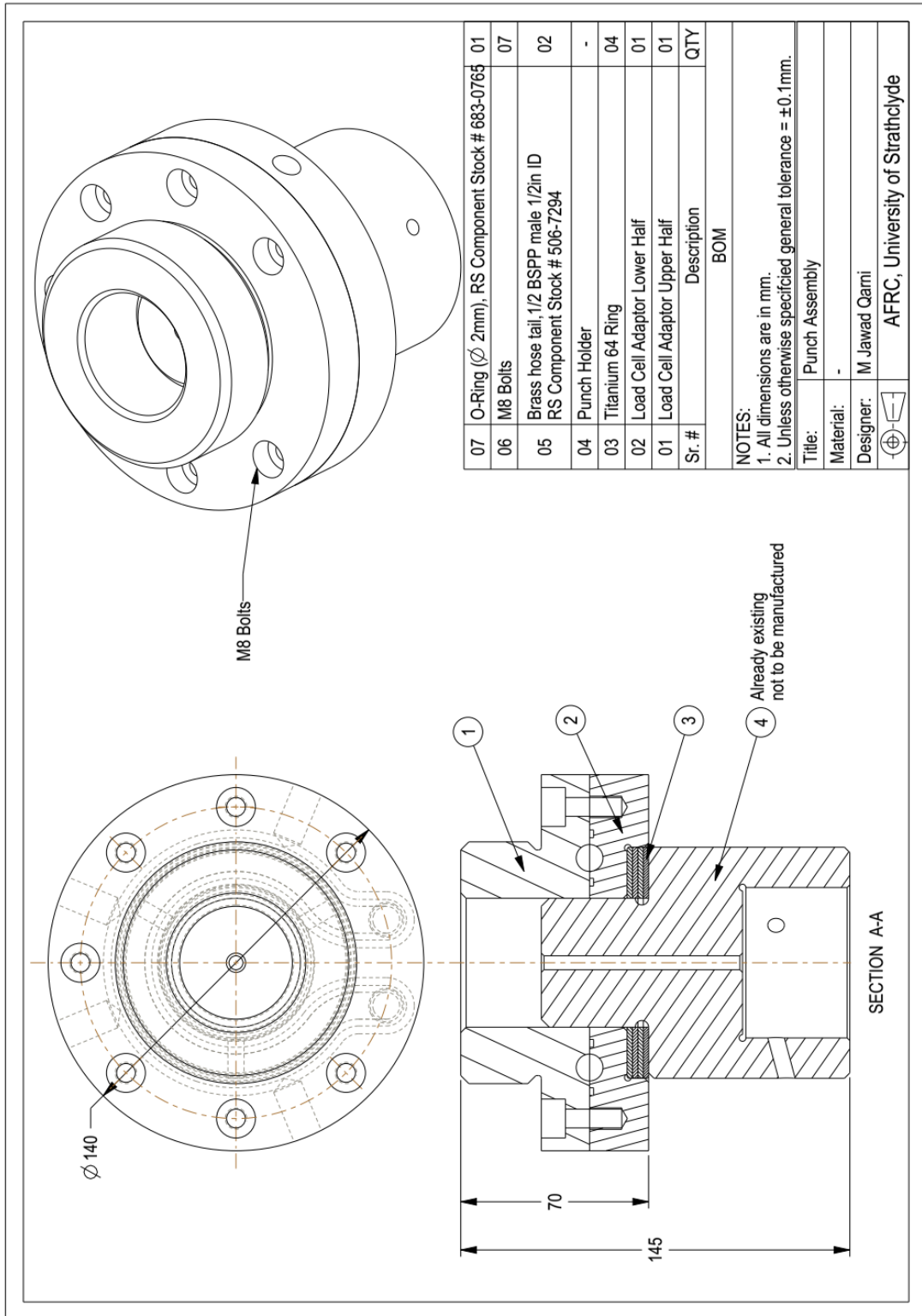


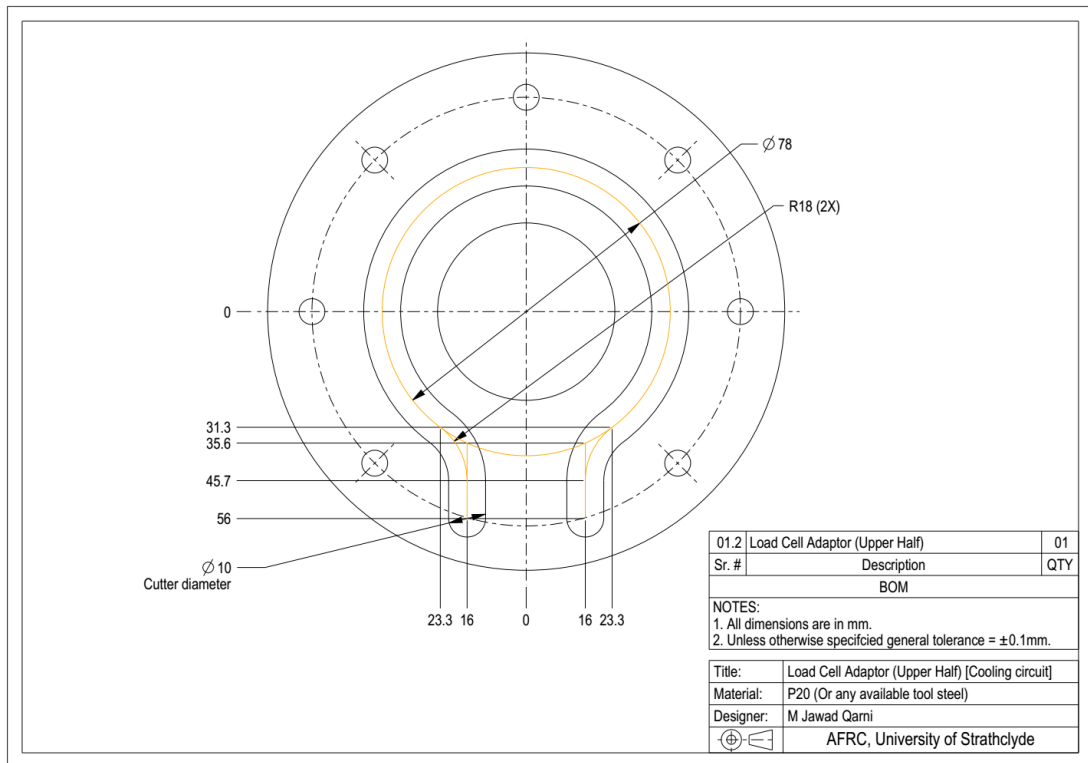
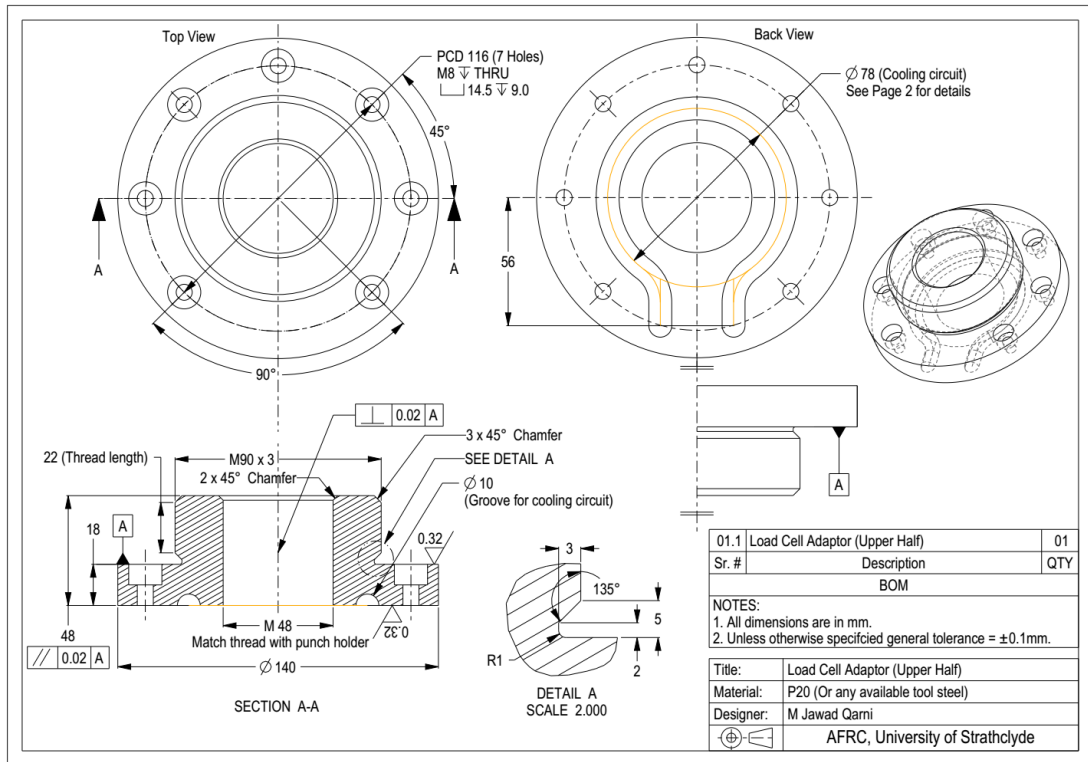






Appendix C – Engineering drawings for cooling system





Appendix D – Engineering drawing for test samples

